

# **Power Electronic System for Multi-MW PV sites**



**University of Southern Denmark**

Kasper Mayntz Paasch

The Maersk Mc-Kinney Moller Institute

Ph.D. thesis

February 2016

# **Power Electronic System for Multi-MW PV sites**

## **Author:**

Kasper Mayntz Paasch

## **Supervisor:**

Morten Nymand

## **The Maersk Mc-Kinney Moller Institute**

Campusvej 55  
DK-5230 Odense M  
Denmark

<http://www.sdu.dk/mmmi>

Tel: (+45) 65 50 16 95

Email: paasch@mci.sdu.dk

---

Publishing date: February 2016

Classification: Public

Edition: 1<sup>st</sup> Edition

Note: This thesis is submitted in partial fulfillment of the requirements for obtaining the Ph.D. degree at the University of Southern Denmark.

Copyright: Kasper Mayntz Paasch, 2016

## Preface

This thesis is submitted in partial fulfilment of the requirements for obtaining the Ph.D. degree at the University of Southern Denmark, The Maersk Mc-Kinney Moller Institute. The work was carried out during the period from January 2012 until February 2016 and was supervised by Associate Professor Morten Nymand at the University of Southern Denmark. This work was supported by Danfoss Solar Inverters A/S and in part by the Danish Sunrise-PV project, ERDFD-09-0069, financially supported by Syddansk Vækstforum and The European Regional Development Fund. This work is conducted as joint research cooperation between University of Southern Denmark and the company Danfoss Solar Inverters A/S.

## Acknowledgements

In the process of doing this PhD, I have become deeply grateful to all who have stood by me and helped me throughout this project.

My special thanks and love to my dear family, Lone, Thea and Alexander for their support, tolerance and patience with me during this project.

I would like to express my warmest gratitude to my supervisor Morten Nymand, to former Dean Per Michael Johansen as well as to Professor Horst-Günter Rubahn for giving me this opportunity.

Special thanks to Morten Nymand for his sustained help, constructive criticism, advices, guidance and patience with me.

Special thanks also goes to Dr. Cristina Cornaro and her colleagues Marco Pierro and Francesco Bucchi at the ESTER Outdoor PV monitoring station at the Tor Vergata University in Rome for their excellent guidance, access to the ESTER database and help during my pleasant stay there.

Without the support from Danfoss A/S and Danfoss Solar Inverter A/S would this project not have been possible and I would like to thank my co-authors Frerk Haase and Søren B. Kjær as well as R&D directors Hans Peter Ballegaard and Kim Petersen for their support and part funding of the project. I am indebted to Hans Aarhus Larsen, Martin Brander and Field Engineer Bjarne Sell for their assistance in accessing the Danfoss Solar Park and for permission to modify parts of it.

Thanks should also be extended to all my colleagues at the Mads Clausen Institute for their support and fruitful discussions and our students who implemented the data logging system and the industrialization of the developed IV-curve tracer prototype. A special thanks to Professor Stefan Matéfi-Témpfli for supporting this cooperation between the Maersk Mc-Kinney Moller institute and the Mads Clausen Institute.

I would also like to thank the project partners in the European Commission Project *Performance Plus* for possibility to join the project as Guest Partner.

Finally I would like to thank my brother Jesper M. Paasch as we as my colleagues Stephen Parsons and Søren Top as well as for the proofreading of the manuscript and for relevant suggestions. The errors and inconsistencies remain my own.

# Abstract

The work presented in this thesis addresses the optimization potential of large PV power plants with respect to energy production during periods of moving clouds. Presently the number and size of utility scale Photo Voltaic (PV) power plants in the megawatt range is increasing and the market for solar inverters is under a severe pressure regarding cost reduction. The main topic of this thesis is the investigation of the potential advantage of applying string inverters with multiple Maximum-Power-Point-trackers (MPPT) in large PV plants compared to the use of one large central inverter with one MPPT. The analysis is based on a comparative investigation of non-uniform irradiation events caused by moving clouds during a period of one year. A set-up for the long term recording of data from the 2.1 MW Danfoss Solar Park in Nordborg (DK) and the 62 kW PV plant at the University of Southern Denmark in Sønderborg (DK) was implemented. A total of 17 PV-inverters have been monitored during a period exceeding one year and the recorded data constitutes the basis of this investigation. A part of the 2.1 MW PV plant was reconfigured to emulate the behavior of a central-inverter and solar panels distributed over a distance of 160 m. In parallel a string based inverter configuration was established with solar panels at the same locations.

An analysis of irradiation data recorded during the test period showed that non-uniform irradiance due to moving clouds is expected to influence the PV plants for less than 4 % of their operational time. The resulting difference in energy production between a system with 3 MPPT and a system with 1 MPPT is calculated for all days where both systems had comparable operational conditions. It can be concluded that both the estimated and the calculated difference in the annual production of energy is in the range <0.3 % and around the limit of what can be registered in the PV plants. It has further been shown theoretically as well as experimentally that landscape variations result in energy production losses.

Two other methods were investigated by applying the recorded data from the 2.1 MW plant. The simulation of a dynamic string allocation concept for fast reallocation of PV strings in parallel show the potential of an increase in annual energy production of up to 0.6 %. The concept allocates PV strings in parallel during periods of low irradiation to avoid low inverter efficiency at low power levels. The effect of a sorting of the panels in the 2.1 MW park has been simulated to show the potential gain by applying PV sorting during the construction of a large PV plant. A sorting of the mounted PV panels is estimated to increase the annual energy production by approximately 0.4%.

A portable IV-scanning instrument for the fast long term characterization of solar panels was developed as part of the project. Each second a sweep of the IV-characteristics of a solar panel is performed and the result stored for later analysis. The instrument is based on an active load, is optimized for field use, is battery operated and has been applied for the characterization of a solar panel over a period of 6 months at the ESTER Outdoor PV monitoring station in Rome, Italy.

## Resumé (Danish)

Denne Ph.d. afhandling omhandler optimeringen af energiproduktion fra solcelleanlæg i megawatt-klassen under vekslende skydække. Der er de seneste år sket en kraftig forøgelse af sådanne solcelleanlæg og markedet for bl.a. de i markedet benyttede DC-AC omformere (invertere) er under et øget prispres med krav om kostoptimering. Formålet med afhandlingen er primært at undersøge, hvorvidt det med hensyn til energiproduktion er en fordel at anvende streng-omformere med flere ”Maximum-Power-Point-Trackers” (MPPT) frem for én central-omformer med én MPPT. Analysen er baseret på undersøgelsen af de forstyrrelser, som skyer forårsager, når de driver ind over anlæggene i løbet af et år. Et omfattende dataopsamlingssystem er installeret på hhv. det 2,1 MW store ”Danfoss Solar Park” i Nordborg (DK) samt det 62 kW store solcelleanlæg på Syddansk Universitet i Sønderborg (DK), hvorfra der er opsamlet data fra i alt 17 invertere i over ét år. Disse data udgør grundlaget for denne undersøgelse. En del af det store anlæg blev modifieret til at fungere som en central-inverter med 3 strenge af solcellepaneler fordelt over en 160 m lang strækning, parallelt med en streng-omformer med solcellepaneler placeret på samme måde.

En omfattende analyse af indstrålingsdata fra 2 solcelleanlæg viste at svingende lysintensitet pga. drivende skyer forventes at påvirke anlæggene i under 4 % af deres operative tid. Den deraf resulterende forskel i energiproduktion mellem systemer med én og flere MPPT blev beregnet for de dage, hvor begge testsystemer havde haft ens driftsbetingelser. Der kan konkluderes at både den estimerede og den målte forskel i årlig energiproduktion er i størrelsесordenen <0,3 % og på grænsen af, hvad der kan registreres i anlæggene. Det store solcelleanlæg følger landskabets konturer og det er opstillet en model for vinkelvariationernes indvirkning på energiproduktionen. Det er eksperimentelt eftervist at rækker af solcellepaneler, som har en stor variation i panelvinkel i forhold til vandret, producerer mindre energi i klart vejr end en tilsvarende flad række.

To andre metoder til øgning af den årlige energiproduktion er undersøgt med udgangspunkt i data opsamlet fra det store anlæg. Et koncept med hurtig parallel-kobling af solcellestrenge forventes at kunne forøge den årlige energiproduktion med op til 0,6 %. Dette opnås ved at samle solcellestrenge i parallel på færre omformere ved lav solindstråling for at øge omformerens virkningsgrad. Der er også vist at en sortering af det store anlægs paneler kunne have øget anlæggets energiproduktion med ca. 0,4 % pga. bedre tilpasning mellem de enkelte paneler i solcellestrenge.

En transportabel solpanel IV-kurvetester til langtidskarakterisering af solcellepaneler er udviklet som en del af projektet. Et solcellepanels strøm-spændingskurve måles i ét sekunds intervaller og lagres til senere analyse. Instrument er optimeret til feltbrug/batteridrift. Instrumentet blev anvendt til karakterisering af et solcellepanel gennem 6 måneder på ”ESTER Outdoor PV monitoring station” i Rom, Italien.

# Table of content

Preface .....	2
Acknowledgements .....	2
Abstract .....	3
Resumé (Danish).....	4
Table of content .....	5
1    Introduction .....	8
1.1  Scope .....	8
1.2  Project objectives .....	8
1.3  Background and motivation .....	8
1.4  Project plan and thesis outline.....	12
1.5  Thesis structure and content.....	14
2    State-of-the-Art analysis .....	16
2.1  Literature review .....	16
2.1.1 Dynamic switching schemes .....	16
2.1.2 Energy loss related to landscape topography .....	18
2.1.3 Energy loss due to moving clouds.....	18
2.2  Summary .....	19
2.3  The analysis of potential methods for optimization of energy yield.....	20
2.4  Research questions to address .....	21
3    Analysis.....	22
3.1  Estimation of difference in annual energy production .....	22
3.1.1 Estimated annual loss .....	22
3.2  PV utility plant layout and timing .....	23
3.2.1 String length and number of parallel stings .....	24
3.2.2 Estimated time of cloud passage .....	25
3.2.3 Conclusion regarding the weather profile .....	27
3.3  PV test park layout concept.....	28
3.4  Selection of main test park and resulting measurement plan .....	28
3.5  Measurement strategy .....	29
3.5.1 Inverter independent measurements / IV-sweep .....	30
3.6  Conclusion on the analysing section .....	31
4    Test plant related investigations.....	32
4.1  Danfoss Solar plant test layout.....	32
4.1.1 Recorded data sets .....	33
4.2  STC/NOCT data analysis .....	33
4.2.1 Air mass factor (AM) .....	33
4.2.2 Danfoss Solar Park and SDU Alsion PV plant .....	34

4.3	Panel sorting analysis .....	35
4.3.1	Effect of PV plant panel sorting.....	35
4.3.2	Conclusion on panel sorting .....	37
4.4	Panel temperature analysis.....	37
5	Energy estimation and test results.....	39
5.1	Test concept description.....	39
5.2	Estimation of irradiation dynamics .....	39
5.2.1	Occurrence of non-uniform irradiation .....	40
5.2.2	Conclusion on timing analysis .....	49
5.3	Dynamic panel allocation.....	50
5.3.1	Inverter efficiency .....	50
5.3.2	Case studies .....	52
5.3.3	Conclusion on case studies.....	54
5.4	Topography analysis .....	54
5.4.1	Irradiation model .....	55
5.4.2	Comparison of model and measurements .....	56
5.4.3	Central 60 kW inverter test .....	58
5.5	Energy loss estimation .....	59
5.5.1	Simulation of cloud induced difference in power generation .....	60
5.5.2	Variation in daily energy production .....	61
5.5.3	Full year DC level energy analysis .....	63
5.5.4	Full year AC level energy analysis .....	66
5.5.5	Conclusion on energy loss estimation.....	66
6	Conclusion and future work.....	67
6.1	Summary and Conclusion .....	67
6.2	Outlook and future work .....	68
	References.....	70
	Appendix A1-A7 .....	76
	Appendix A1 .....	77
	Appendix A2 .....	82
	Appendix A3 .....	87
	Appendix A4 .....	98
	Appendix A5 .....	105
	Appendix A6 .....	110
	Appendix A7 .....	120
8	Appendix A8 Selection of PV test plant .....	130
8.1	PV test plant requirements .....	130
8.2	Selection of primary PV test plant .....	131
8.2.1	Evaluated PV utility plants.....	131

8.2.2	Conclusion regarding selection of a test park .....	132
8.2.3	Danfoss Solar Park panel statistics.....	134
8.2.4	Energy storage/stabilization .....	136
8.3	Emulating a central inverter setup via string inverters.....	137
8.3.1	String modification.....	137
8.3.2	Inverter replacement to type MLX 60kW .....	138
8.4	High speed recording of inverter and weather parameters.....	138
8.4.1	Data logger system concept.....	138
9	Appendix 9 Irradiation statistics .....	143
9.1	Data set 1, SDU Alsion 150 days weather data.....	143
9.2	Data set 2, SDU Alsion one year weather data .....	144
9.3	Data set 3, Danfoss Solar Park one year weather data .....	145
9.3.1	Clouds speed estimation via time correlation between inverter data .....	146
10	Appendix 10 PV panel measurement.....	147
10.1	Panel under test .....	147
10.1.1	PV panel sweep data .....	147
10.2	STC/NOCT analysis.....	148
10.2.1	ESTER Outdoor PV monitoring station in Rome, Italy .....	148
10.2.2	Panel temperature analysis .....	149
10.2.3	Mapping of $V_{MPP}$ , $I_{MPP}$ and $P_{MPP}$ recording.....	151
10.3	Thermal effects due to fast change in irradiation .....	151
11	Appendix 11 PVSweep system evaluation, design and test.....	154
11.1	IV-curve tracer specifications .....	154
11.2	Design aspects .....	155
11.2.1	Thermal design.....	156
11.2.2	Active load & current sensing.....	158
11.2.3	Temperature sensor interface .....	160
11.2.4	Irradiance sensor analysis.....	160
11.2.5	Calibration at the ESTER sensor system.....	161
11.2.6	PVSweeper $P_{MPP}$ vs. panel temperature analysis .....	164
11.3	Temperature sensitivity analysis .....	165
11.3.1	Circuit temperature sensitivity .....	165
11.4	Conclusion on the construction and test of the IV-curve tracer.....	165

# 1 Introduction

This chapter illustrates the background and motivation of the work presented in this thesis. A short overview of the present status in inverter development is addressed with focus on the road towards decreasing Levelized Cost of Energy (LCOE) for string- and central inverters for MW-size PV utility plants [1]. The project objectives, limitations and the main contribution are presented.

## 1.1 Scope

The scope of this report is to present the results obtained in the PhD project “Power electronic system for multi-MW PV sites” as carried out by the author during the period from January 2012 to February 2016. Several of the results obtained in this project as well as developed test methodologies have been published in the form of peer reviewed conference papers and a journal paper. The published papers constitute an integral part of the thesis and are included in appendix [A1-A7]. The primary objective of this report is to supplement the information already listed in appendix [A1-A7] by placing the publications in a broader context and so create a more coherent and complete overview of the results obtained.

## 1.2 Project objectives

The primary objective of this project is to investigate the potential advantage of applying multiple Maximum-Power-Point-Trackers (MPPT) in a large PV utility power plant compared to applying a central inverter structure with only one MPPT. A difference in annual energy production between a PV utility scale power plant configured with string inverters and a plant equipped with a central inverter under varying irradiation conditions (clouds) is intuitively expected in areas with many moving clouds.

The study focusses on the changes in power production induced by non-uniform irradiation conditions in areas with a high degree of varying cloud cover, e.g. Northern Europe. Special focus has been given to the collection and analysis of irradiation and inverter data from a large PV utility plant with a high sampling rate and the high speed recording of IV-curves.

## 1.3 Background and motivation

The recently completed EC project “*Performance Plus*” [2] recommended several methods for improving the outcome of utility scale PV-plants:

- The assessment of the solar resource has been identified as the most important element in the contribution to the total uncertainty in the prediction of expected production.
- Short term / very short term irradiation forecast.
- Include additional tests to help to characterise the impact of degradation mechanisms.
- Diagnostics/systematic analysis of operational data to detect issues in underperforming PV plants, including measurement of dark IV-curve characteristics as a complement to light IV-curve measurements.
- Investigate the impact of non-ideal working conditions on the PV-inverter.

The assessment of the available solar resources in a given location does have a long term, a short term and a very short term aspect. The long term aspect is related to the overall energy planning of a given area. The short term aspect relates to the stability of the power grid / need for short term balancing/storage, while the very short term aspect relates to the detailed irradiation profile for a single PV-plant. The geographical size for a utility scale power plant, using standard fixed tilt mounting and modules with around 15% efficiency varies from around 1 hectare ( $10,000 \text{ m}^2$ ) per MW in tropical regions to above 2 hectare per MW in Northern Europe [3,4], see figure 1.1 for an example. Non-uniform irradiation patterns passing over the surface of such PV sites are expected to

occur on a noticeable time scale plants due to their geographical size. A high degree of variability at the minute-level during changing weather conditions is to be expected [5].



Figure 1.1 2.1 MW PV utility plant at Danfoss A/S, Nordborg, Denmark.  
Reprinted with permission.

A quality solar inverter incorporates internal max-Power-Point-Tracker (MPPT)-circuitry/software, as it has a control function with the purpose of continuously adjusting the operational point of the PV string to ensure maximum power production. The inverter market is expected in the future to be under a severe price pressure and future development is likely to focus on cost reduction in a competitive market [6]. Any additional functionality such as multiple MPPTs in an inverter system will add to the complexity and hence increased costs. The number of MPPT in a given PV plant depends on the type of inverter configuration applied. The commonly applied inverter topologies span from micro-inverter structures with a single MPPT per PV panel [7]<sup>1</sup> over string based solutions with one MPPT per PV-string, consisting of typ. 24 panels@72 cells [8] to large central inverters with hundreds of strings in parallel [9,10]<sup>2</sup>.

The maximum power point for a given panel and string of panels in series/parallel will primarily depend on panel/cell temperature and irradiation level as well as the aging of the panels and many concepts for MPPT control have been reported in the literature, e.g. [11-17].

In the recent years the energy conversion efficiency of commercial quality solar inverters, based on Silicon-technology, has increased and reached a level of maximum weighted efficiencies at approximately 98%. With the emerging Silicon Carbide (SiC) technology have 99% been reached [18,19]. The weighted efficiencies [20] of central inverters tend to be marginally higher [10], see table 1.1 for a selected representative range of inverters.

Table 1.1 Examples of commercial inverter with different power levels.

Inverter manufacturer/type	Power rating (kW)	$n_{max}$ (%)	$n_{EC}$ (%)	$n_{CEC}$ (%)
Danfoss/SMA FLX17k [21]	17	98.0	97.4	--
SMA Sunny Tripower 20000TLHE-10 [22,23]	20 (SiC)	99.0	98.6	--
Kago SunMaster CS30TL RP [24]	33	97.7	97.2	--
Danfoss/SMA MLX [25]	60	98.6	98.0	98.0
PowerOne AURORA PVI-400.0-TL [10]	400	98.0	97.7	97.4
AEG PROTECT PV.500-UL[10]	500	98.4	98.2	98.2
SMA Sunny Central 900CP-XT[10]	900	98.6	98.5	98.4
Bosch BPT-IS 1400[10]	1540	98.3	97.9	98.1

<sup>1</sup> Commercially available products from companies like SolarEdge and Solarmax Technology Inc..

<sup>2</sup> The definition of the terms string and central inverter are not clear. In [38] the term "string inverter" is used for inverters up to 100 kW, only possible to reach with multiple strings in parallel.

The emerging use of SiC-technology further enables a possible reduction in physical size /volume per kW as SiC transistors can be driven at high frequencies, thus allowing the use of smaller magnetic components and safe operation at higher junction temperatures [27-30]. A 5 kW solar inverter with SiC-transistors was demonstrated in 2010, reaching a world record of 99% [19]. The 20kW Sunny Tripower20000TLHE-10 with SiC technology was later marketed by the company SMA Solar Technology AG (see table 1.1).

The differences between the efficiencies of quality inverter can be considered small and the choice of inverter configuration often depend on installer preferences and are subject to non-technical factors such as ease/cost of replacement, cabling costs and operational cost as well as opinions held by the plant owner/installer/operator [31]. Studies of smaller sites in Italy have shown a small advantage for the central inverter in the range of 1% during shady conditions [32]. Plants in the MW class often have central inverters installed, but string inverters have to some extent been installed in large PV-plants due to the ease of service as well as the advantages regarding inter-row shading during winter periods.

An important input parameter for the financial model of the LCOE (Levelized Cost of Energy) calculation for a given utility plant is the estimated annual energy production [1]. Several studies have shown that the financial difference between installing string inverters vs. central inverters is very little over the expected lifetime of a PV-plant (20-25 years) [33]. For large PV plants the inverter related costs in 2014 were  $\approx 11\%$  of the total system costs (110 €/kWp out of 1000 €/kWp) [6], this is expected to decline to  $\approx 8\%$  (20-43 €/kWp) in 2015.

The most important factors regarding energy yield can be characterised by the tilted plane insolation/irradiation level, ambient temperature, rainfall and consecutive days without significant rainfall [34]. A major benefit is achieved by reducing daily soiling where there is a long period without significant rainfall. Similar results are reached after extensive monitoring of PV plants in Ukraine with an installed capacity of 700 MW<sup>3</sup>[35].

Depending on the site specific circumstances can PV utility parks be designed to allow inter-row shading in the morning and in the evening and during winter. In the event that each row consist of several (typical 2-3) sub-rows of stacked panels only the strings in the lowest sub-row will be exposed to a shadow from the front row, not all strings in the full width of the row, see figure 1.2. As an example it can be mentioned that a 84 MW PV power plant at Eggebek in Northern Germany is equipped with 5318 Danfoss TLX-type string inverters, having a total of 3x5318 strings of 23-24 PV-modules attached, each string having its own Max Power Point Tracker (MPPT). Comparable large parks have installed central inverters, each handling up to and above 1 MWp per section [36]. Each of the string inverters can easily be replaced by locally trained maintenance personnel and a malfunction of one inverter does thus not result in long periods of production losses.

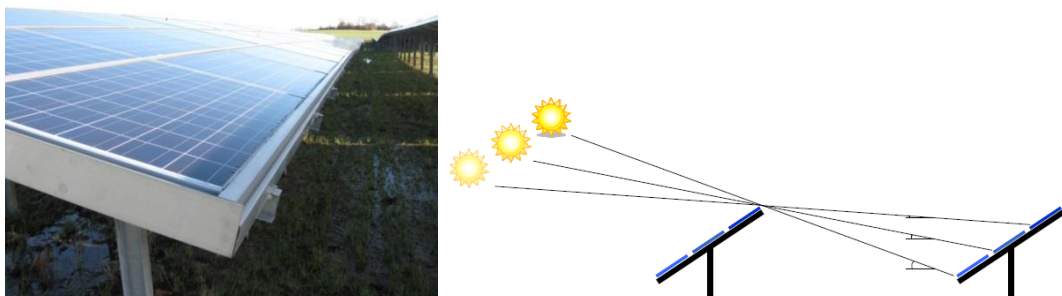


Figure 1.2 Left: Example of inter-row shading on the lowest sub row of a 3 panel wide row with panels mounted horizontally. The photo is taken 13 o'clock, February 5, 2016, Denmark. Right: Schematic illustration [8]. Reprinted with permission.

<sup>3</sup> Personal communications with the operator of MW PV-plants in Ukraine (Gerhard Mütter, Technical director at AES GmbH, Vienna (A)), via the EC Performance Plus project [57].

A decision to construct a large PV power plant depends on a long range of factors like local legislation, feed-in tariffs, base component costs (BOS) and general assumptions regarding expected annual energy yield (kWh/kWp) installed. Inverter costs are an important factor in the total BOS (Bill Of Sales) for a given PV plant project [37]. Recent studies performed by the Fraunhofer ISE Institute, DE, estimate the market share of central inverters to be rising to around 57.5% in 2015, see table 1.2.

Table 1.2 Estimated inverter type market shares and price/Wp, compiled from [6,38-40].

Inverter/ converter	Power level	Efficiency	Market share (est.) / price			Remarks
			2012	2013/14	2015	
String	<100 kWp	Up to 98%	≈90% ≈ 0.2-0.3€/Wp	≈50% ≈ 0.15€/Wp	≈41% ≈ 0.11€/Wp	Easy to replace
Central	>100 kWp	Up to 98.5%	≈9% ≈ 0.2-0.25€/Wp (+0.05€/Wp)*	≈48% ≈ 0.1€/Wp (+0.05€/Wp)*	≈57.5% ≈ 0.08€/Wp (+0.05€/Wp)*	High reliability Often sold only with service contract
Micro	Module power range	90-95%	<1% ≈ 0.5-0.8€/Wp	≈1.5% ≈ 0.4€/Wp	≈1.5% ≈ 0.35€/Wp	Ease-of-replacement concerns
DC/DC converters (Power Optimizer)	Module power range	Up to 98.8%	≈ 0.3% ≈ 0.4-0.8€/Wp	n.a. ≈ 0.4€/Wp	n.a. ≈ 0.1€/Wp	Ease-of-replacement concerns Output is DC AC-inv. needed

\* DC cabling (2014 level).

The recent study by Fraunhofer ISE, commissioned by the “AGORA Energiewende” organisation, estimates a further decline of inverter pricing to the level of 0.02-0.04 €/Wp in 2050, according to 4 different development scenarios [6], as illustrated in figure 1.3. The DC cabling for central inverters is expected to decline to the level of 0.03-0.045€/Wp in 2050, the same level as for the solar inverter itself.

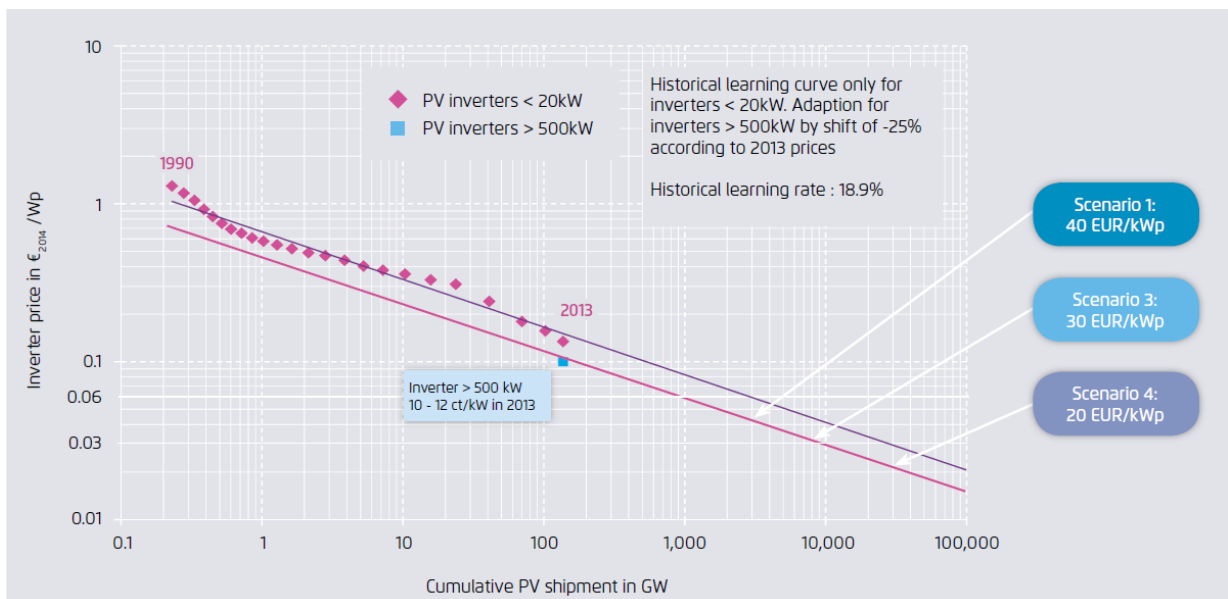


Figure 1.3 Extrapolation for the price experience curve for PV inverter [6]. Reprinted with permission.

The issues of operational conditions, service costs and lifetime estimations of a given inverter type have been excluded from this study due to its many variables including the detailed design of the inverters. However, any type of quality PV inverter requires some sort of MPPT and the complexity of a given inverter increase with the number of MPPTs implemented. An increased power output by applying many MPPTs via micro-inverters is claimed by manufacturers, i.e. [41] as well as intuitively expected when the PV panels experience different operational conditions, especially irradiation level and panel temperature. However, the potential benefit of applying many MPPTs by using string inverter configuration instead of a central inverter configuration under identical environmental conditions is not known to have been documented in the literature.

Micro (module) level inverters as well as other technologies such as cell level inverters and DC/DC string equalizers have been excluded from further study due to their low market share and relatively high price per rated Wp.

## **1.4 Project plan and thesis outline**

The work packages carried out in project are illustrated chronologically in figure 1.4. The flow chart further illustrates how the published articles and papers relate to the individual work packages. The present State-of-the-Art regarding the use on string- vs. central inverter structures in utility scale PV plants as well as the analysis of the effect of fast moving clouds on annual PV-production is analysed. It is initially documented that the inverter market is under an increasing pressure to reduce the inverter cost price per kW.

The concept of applying a dynamic switching concept to PV string in order to enhance the efficiency of the inverter at low irradiation levels is analysed and published as [A1]. A test structure for fast (second) long term monitoring of the performance of PV inverters is implemented at a small local PV plant in parallel with the identification and modification of a suitable utility scale PV site. The system is prepared for implementation on the large test plant, once identified. A battery operated system for the fast recording and storage of IV-characteristics for PV-panel has been developed and tested under field conditions in Denmark and in Italy. The initial design is published as [A2] and the application is published as [A3]. A suitable test plant was identified and the next step was to reconfigure/rewire parts of it to emulate the operation of a central inverter for comparison with the performance of string inverters under the same environmental conditions. The concept of using a modified string/central inverter layout is published as [A6]. A simulation platform to estimate the effect of fast moving shadow fronts is developed and published as [A4]. A structure for recording, storing and post processing of the GBytes of data obtained from the Danfoss Solar Park, the SDU Alsion PV plant and the developed PV sweeper units is implemented. A total of 17 string inverters were monitored and 31 parameters from each inverter were recorded each second. The concept of a novel gravitational energy storage system also relevant for utility PV plants is peripherally included and published as co-author in [A7].

Parts of the irradiation and inverter power/energy data recorded over a period exceeding one year are used to evaluate the potential gain of dynamic string allocation, the effect of landscape topography and the potential gain of using multiple MPPT by analysing the occurrence of fast variations in irradiation level and its effect on the annual energy production. A model for the effect of landscape topography on power production is developed and is published as [A5]. The initial plan of mounting IV-recording units at the large test plant was modified due to complications with infrastructure and the parallel use of the same plant as a test plant by Danfoss Solar Inverter A/S. A panel of the same type is monitored for 7 months in Italy to obtain higher irradiance levels than expected to occur in Denmark and to document the performance of the panel without any MPPT circuit involved. As only parts of the obtained results are included in the published material [A1-A7] new observations are included in the main part of this thesis.

## PhD project Overview

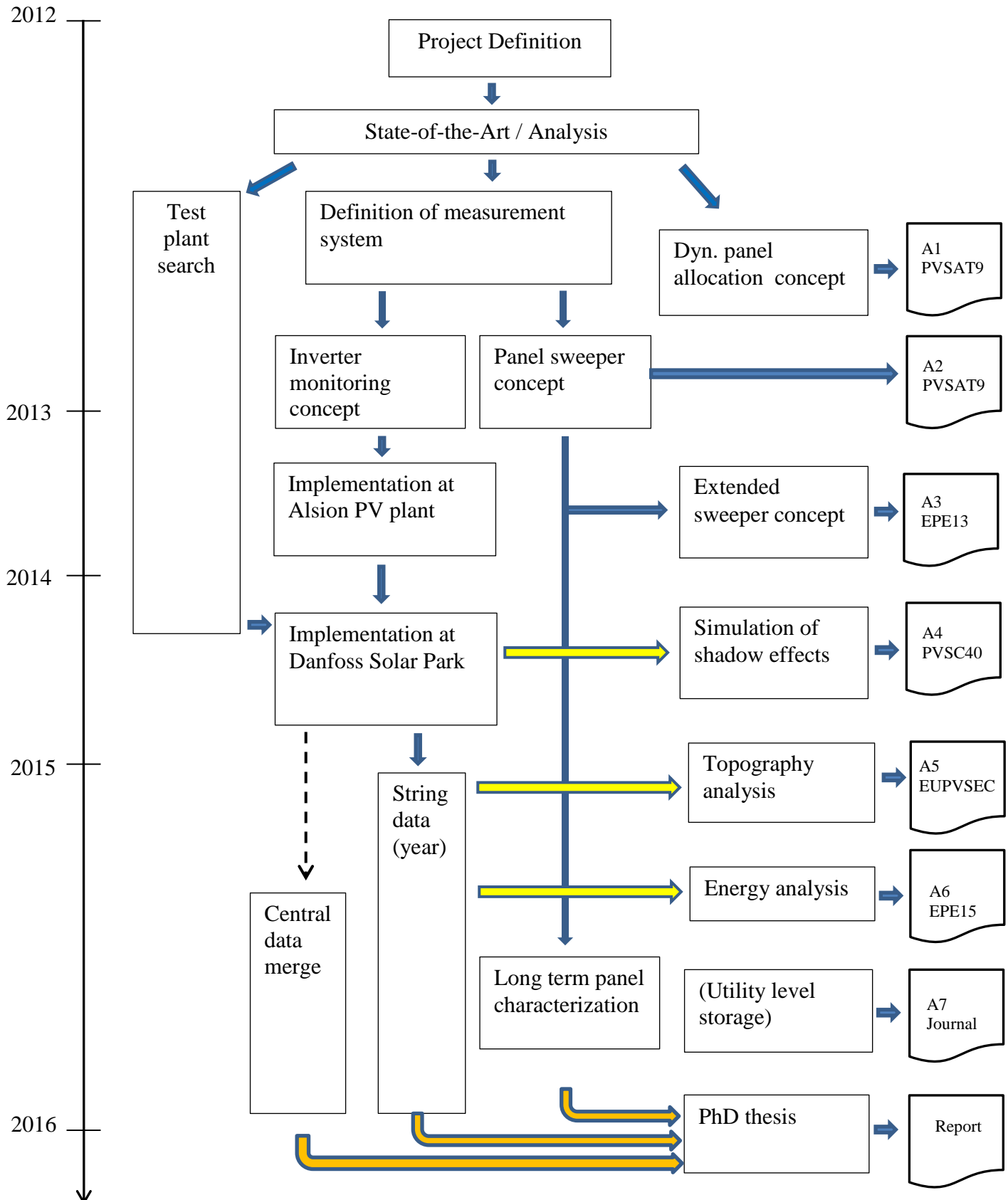


Figure 1.4 Chronological PhD project work plan.

## **1.5 Thesis structure and content**

This thesis is organized to reflect the approach adopted in the project i.e. defining an objective and motivation => analysis of State-of-the-Art => analysis of the problem => establishment of a suitable test environment => analysis of inverter and irradiation data => conclusion. The intention of this thesis organization is to present the project result in a condensed and straightforward manner.

The contents, organization and structure of this thesis are illustrated in the flow chart presented in figure 1.5.

The published conference papers and the journal article [A1-A7] constitute an integral part of the thesis and are therefore appended. The published work cover a part of the work performed in this project. This report will therefore both complement the published work and present new results in a coherent and concise way. Special focus will be on the coherent presentation of parts of the large amount of recorded data from the main PV test site.

Special attention will be on the analysis and presentation of results based on the sampled irradiation and inverter data not addressed in the published result.

Detailed descriptions about the construction, test and calibration of the developed measurement equipment as well as technical details about the file structure in the database, details regarding the choice of test plant and a description of the Danfoss Solar Park and the SDU Alsion PV plant are placed in the appendix sections [A8-A11].

## PhD project Structure

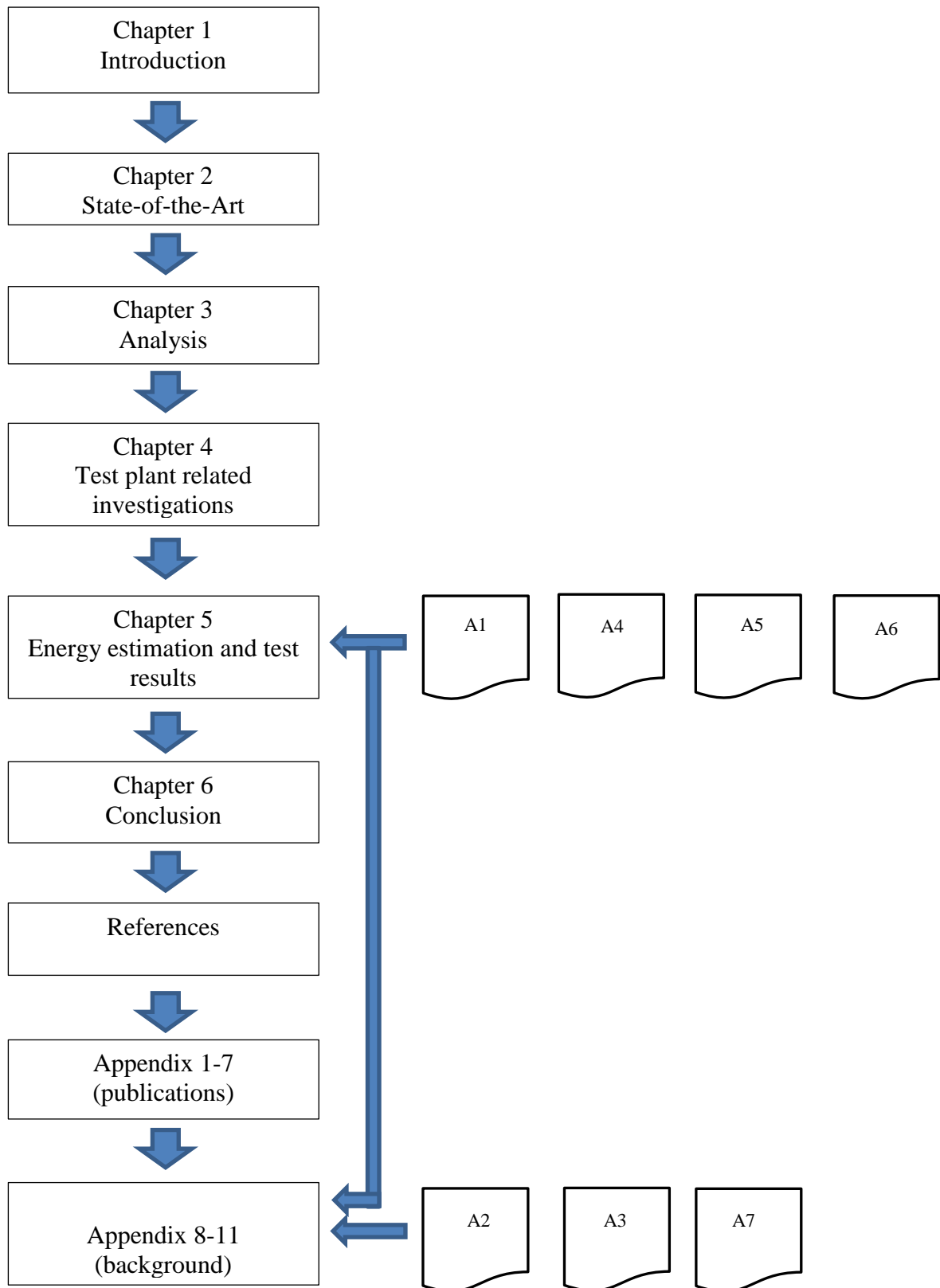


Figure 1.5 Ph.D. thesis structure.

## 2 State-of-the-Art analysis

The purpose of this chapter is to present an overview of the present State-of-the-Art of inverter related approaches for optimization of the performance of PV power plants. Focus is on the implementation in utility scale PV power plants, the short term prediction of fluctuations in energy production due to moving clouds and methods for optimizing the long-term energy generation from stationary large PV utility plants.

### 2.1 Literature review

Published literature in the form of conference papers, journal articles and technical literature have been investigated with focus on site specific conditions and potential for the improvement of the long-term optimization of the energy production from utility scale PV power plants.

Clouds can cause non-uniform irradiation patterns across large PV-plants and short term fluctuations in power production on the timescale below one minute due to panel mismatch are to be expected [42-44]. The individual PV panels/strings can thus not be expected to see the same physical operational conditions even with identical panel specifications ( $V_{oc}$ ,  $I_{sc}$ ,  $V_{MPP}$ ,  $I_{MPP}$ ) and this will result in mismatch losses (MML) as the panels then have varying operational conditions [45,46]. Furthermore, the production spread within a given production series of a PV-panel series will generate mismatch conditions in both string- and central inverter applications [47].

The topic of partially shadowed PV strings/arrays has been extensively studied and modelled in the literature, i.e. [48-50] as it is critical for residential applications, where shadows from for example trees often cannot be avoided. But for large utility level PV power plants sources for shadows are likely to be removed from the vicinity of the park. The actual plant design has been the subject of several studies, taking into consideration inter-row shading effects, i.e. [14,51].

Intuitively it is to be expected that multiple MPP during partial shading will occur, but it has been shown that this is not likely to happen during passing clouds for high-quality panels [52-53].

The effect of variation of panel parameters such as  $P_{MPP}$  and  $I_{MPP}$  have been investigated in the literature and it is concluded that a factory sorting and later mounting according to the sorting can generate in the order of 0.4% more power as mismatch losses are reduced [54]. It seems however not to be financially beneficial with present day production methods and logistics.

#### 2.1.1 Dynamic switching schemes

The inverter conversion efficiency under low irradiation levels be a degrading factor for both the string inverter concept and the central inverter concept, as the efficiency of a given solar inverter is not constant, but depends on the actual relative power levels as well as the PV string voltage. Dynamic switching techniques have therefore been developed in order to increase the conversion efficiency under low irradiance conditions. The principle is schematically illustrated in figure 2.1 for a switching concept at string level and at the inverter level.

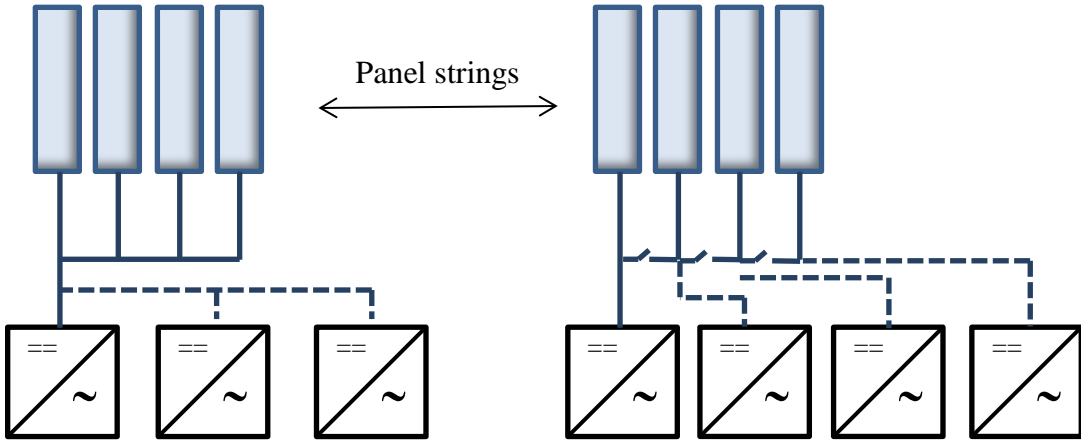


Figure 2.1 Switching techniques. PV strings connected to inverters. Left: Master-slave concept. Right: Team-concept with reconfigurable strings.

The Team-concept is a method for dynamic string allocation for (potentially) obtaining higher energy production from a selected inverter during periods of low irradiation levels, by allocating strings from other inverters in parallel to the said inverter [55]. The other inverters are then turned off. The active inverter then operates at a higher power level during the period of low irradiation, hence increasing its conversion efficiency. See figure 2.2 for an example of an efficiency curve for a 15 kW string inverter.

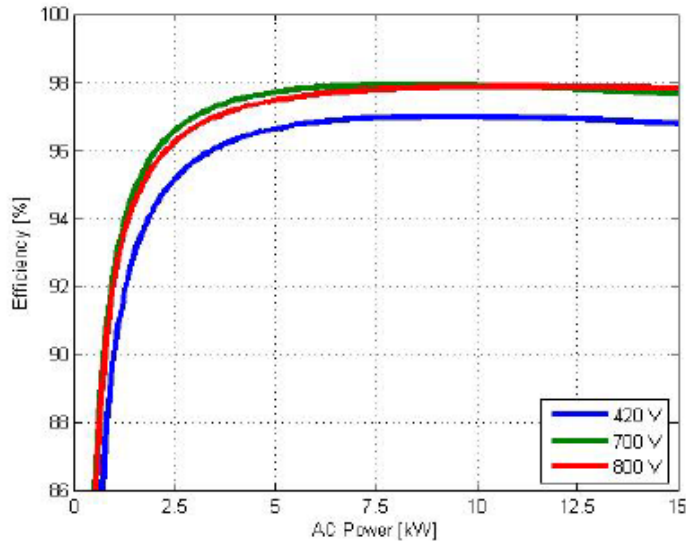


Figure 2.2 Illustration of a conversion efficiency curve for a string inverter of type Danfoss TLX15K [56]. Reprinted with permission.

A master-slave concept is applied in many brands of larger central inverters to increase the conversion efficiency under low irradiance conditions by keeping all incoming strings connected in parallel and internally switching power modules inside the central-inverter, depending on the irradiation level. The master-slave concept has its main advantage with inverters where the base losses are high and has in an early study (2003) demonstrated an increase in the weighted European efficiency  $n_{EC}$  in the area of 0.9%, compared to a central inverter without the Master-slave concept [55]. The string inverter technology in the same study reached an increase of 0.75%. A concept called the Team-concept was compared in the same study, showing an increase in efficiency in the order of 1.7% at that time. The mismatch losses in the central inverter configuration were in the order of 1-1.4% from the nominal panel ratings. The inverter efficiency of a quality inverter in 2003

was in the range of 95%, so there was some room for improvement. For present day inverters, reaching 98%, the net gain is expected to be lower.

The Master-Slave concept can only be used if it is designed into a given central inverter, but the multi-team concept of parallelizing strings acc. to the irradiance level can in theory be an add-on to existing string-inverters (however no such commercial product is known to be available).

### **2.1.2 Energy loss related to landscape topography**

The subject of panels mounted on curved surface roofs has been addressed by micro-inverter manufacturers, e.g. SolarEdge, for residential / small utility scale PV plants but documented studies of the effect of land topography on the energy production from utility scale PV power plants have not been identified in the literature. The use of a hilly area might force the developer either to flatten the area or to adjust the panel mounting structure to the ground curvature. Both possibilities generate extra cost. Another possibility is to let the rows follow the landscape curvature, giving an easier mounting but with an expected lower energy production due to varying panel angles.

### **2.1.3 Energy loss due to moving clouds**

As addressed above are PV utility parks not expected to be troubled by shadowing objects in the vicinity, however, moving clouds will generate periods of moving shadow fronts. The effect of cloud induced changes in irradiation level has been addressed in the literature as well as in recent research projects like the EC Performance Plus project [2,57], due to the fast increase in PV installations worldwide over the recent years. The US National Renewable Energy Laboratory (NREL) has reported that clouds can be a challenge to large PV power plants and has initiated activities related to this field [58].

An electricity supply system with a high degree of integrated renewable energy sources like wind and PV will experience increased fluctuations in the energy production, generating the need for short/medium/long term production forecasting, consumer/load control (Smart Grid) as well as utility level energy storage. Forecasting enables the energy provider to access other means of energy supply in order to secure a stable power grid. Forecasting in the minute/hour/day scale are the subject of a long range of research activities, i.e. [57,59-62] and minute forecasting (also called ‘nowcasting’) is relevant for small local energy grids [63,64]. Fluctuations in irradiation level are expected to have an effect on utility scale PV-plants due to the physical size of such plants and the influence on large PV plants in the MW range are expected to generating substantial fluctuations in power production [65,66].

String inverter based systems, being residential or utility scale, are distributed over large areas and will individually respond to a change in irradiation level, but a large PV utility plant with few central inverters or many PV-strings in parallel) is expected to have an additional loss due to the effect of the generated additional panel mismatch loss (MML) because of uneven irradiation level.

The effect of partial shading of PV-systems by obstacles such as trees and chimneys as well as for mobile applications is extensively studied in the literature, e.g. [20,50,67]. The net annual effect of the difference between applying string- or central inverters due to fast moving clouds therefore depends on the seasonal occurrence of partially clouded conditions, which will be very site dependent (for example desert vs. Northern Europe). Earlier studies related to a proposed redefinition of the European solar inverter efficiency  $n_{EC}$  have documented that the annual intensity distribution is very site-dependent [68]. A study in 2008 based on a year of irradiation data measured in intervals of 10 seconds showed that with correct sizing of the inverter and by applying a fast dynamic MPP-tracking algorithm in principle a few percent energy could be gained from the same PV array in case the nominal inverter size is a factor of 1:2-1.3 times the installed DC-power [69].

The effect of moving clouds on the energy production of PV plants has been the subject of research. For example, recent studies by the Tampere University of Technology in Finland have addressed the effect of moving clouds in Finland on the time scale of seconds under varying cloud directions. Simulations have shown that during the cloud transition period there is a visible effect on the mismatch loss (MML), with 1-8% loss for the tested series/parallel panel configurations [43]. Losses due to a long series of string configurations are the largest, up to 4% in Southern Finland under the given site specific weather conditions. The analysis of the meteorological data showed that non-uniform irradiation conditions were present 7% of the operational time during a 180 day period in the winter season [44].

Temperature differences between the panels in the strings have been shown to increase the MML for parallel strings more than for independent strings, as temperature has a larger effect on the voltage of a PV module than on the current, however the thermal time constant for panels is in the range of 5-10 minutes [70]. Simulations show that sharp shadow fronts and their direction has an substantial effect on the amount of mismatch losses in the level of up to 18% mismatch loss for parallel sharp shadow fronts on a 24 panel string for both single string and multi string operation [42]. It has further been shown that it is beneficial to apply a square-line layout instead of a string-like layout of the panels as the global MPP voltage of the generators then can be held within 80-110% of the MPP voltage under MPP [71]. The effect of combined system shading (% of panels shaded) and shading strength on the location of the MPP point have been analysed in [72]. A case study by the company SolarEdge claim an increase of 1.65% in energy production by using micro-inverters compared to a traditional inverter on days with dynamic cloudy conditions for a 5.25kWp system on a flat field, but no inverter data is presented [73 ].

## 2.2 Summary

The market review for utility scale inverter solutions and the State-of-the-Art analysis showed that a continuing competition in the PV inverter market generates a need for cost reduction. The level of efficiency of >98% reached is likely to shift the focus to a general cost optimization on the system level.

The main subject of the investigation is to clarify a possible advantage with respect to annual energy production of using multiple MPPT compared to a plant operated with a single MPPT (central inverter with parallel strings) and a setup with string inverters (large number of MPPTs). The effect of moving clouds on the annual energy production of a utility scale PV plant and the benefit of using multiple MPPTs/string inverters compared to a large central inverter is not well understood. Instant differences in the range of up to 20% during a passage of sharp shadow fronts are to be expected but the net annual occurrence of non-uniform irradiation conditions is estimated to be in the range below 7% of the operational time of a PV plant. The influence of the landscape topography on the annual energy production of large PV utility plants appears not to be well investigated.

The short term fluctuations in the power generation from PV plants caused by moving clouds are a possible source for instability in the electrical grid. The emerging use of energy storage technology is expected to contribute to the stabilization of the electrical grid as well as providing short to medium term supply/demand balancing, relevant for renewable energy sources.

## **2.3 The analysis of potential methods for optimization of energy yield**

The State-of-the-Art analysis identified 3 main areas of potential of optimization relevant to be addressed in this thesis.

- *Potential of fast dynamic allocation of panel strings.*

The SOA analysis revealed that dynamic switching of either panels or inverter modules inside a central inverter have shown potential for an increase in energy production. The Master-slave concept is well established in industrial central inverters, but the dynamic allocation of strings in a string inverter configuration has been only addressed by one manufacturer. The potential benefit of applying fast dynamic switching of PV-strings to follow rapidly changing weather conditions in steps of a few seconds is not known to have been published.

- *The influence of topography on the energy production.*

The analysis further revealed that the potential loss of power production due to topographical variations in the literature has been mainly addressed for micro/panel inverter types. The effect on topographical variations in a large PV power plant with string- or central inverters has not been identified in the published literature. The potential gain in annual energy production is also expected to relate to the design and construction of the individual PV plant, i.e. whether the panels are all mounted on the same horizontal level or whether they can have individual orientations due to landscape curvature.

- *Inverter configuration with single or multiple MPPT.*

There is a documented potential loss of energy because of induced mismatch losses by non-steady irradiation conditions. The induced loss is expected to depend on the actual inverter implementation, being a number of string inverters or a central inverter. The net gain in annual energy production by using of multiple MPPT compared to a central inverter solution with only one MPPT under identical operating conditions/MPPT-type is not known to have been published.

## **2.4 Research questions to address**

The main research questions to be addressed in this thesis are related to the number of MPPT in a system and the possible gain of applying fast dynamic switching on a string-inverter based system.

- What are the potential benefits with respect to annual energy production by applying PV-inverters with multiple Max-Power-Point-Trackers (MPPT) in a PV utility scale power plant, compared to applying a central-inverter with only one MPPT.
- What is the expected maximum achievable increase in annual energy production in a string-inverter based system with individual MPPT with dynamic allocation of strings?
- What is the influence of PV-plant topography on the power production?

In order to address the potential difference between a string inverter and a central inverter concept the following tasks have been identified:

- Analysis of timing related to the passage of cloud induced shadows front over a MW-size PV plant.
- Identification and implementation of means of determining the occurrence of dynamic weather conditions on an annual basis.
- Estimation of the annual effect of clouds on the energy production of a MW-size PV plant..
- Estimation of the effect of landscape topography on power production.

### 3 Analysis

The purpose of this chapter is to analyse the identified potential for optimizing the annual energy production from PV utility plants and the methods of investigation.

#### 3.1 Estimation of difference in annual energy production

The published results from University of Tampere showed that non-uniform irradiation conditions were present 7% of the operational time of a PV-plant during a 180 day period during a winter season [44]. Instant power losses of up to 8 % in a PV-string of 18 panels were recorded. Instant differences in power production between a string inverter and a central (multistring) inverter configuration during passage of a cloud have been reported to reach the level of 18% [42]. A case study by the company SolarEdge [73] claims an increase of 1.65% compared to string inverters in energy production from a PV plant following a curved roof, but detailed information has not been published.

##### 3.1.1 Estimated annual loss

An simple indication of the magnitude of an annual energy loss ratio  $E_{loss}$  from moving clouds over solar panel is based on the estimation of the energy occurrence of non-uniform irradiation profiles and their induced losses. The average loss factor  $loss_{av}$  of a non-uniform event is estimated as a ratio of the maximum loss factor  $loss_{max}$  found in the literature, see eq. 3.1.

$$\begin{aligned} E_{loss} &= nur \cdot loss_{av} \\ &= nur \cdot q \cdot loss_{max} \end{aligned} \quad (3.1)$$

where  
    *nur*     =rate of non-uniform irradiation over a year  
    *loss<sub>av</sub>*   =average loss factor per non-uniform incident over the whole year  
    *loss<sub>max</sub>* ≈ maximum recorded loss factor *loss<sub>max</sub>* for that year.  
    *q*        = ratio between *loss<sub>av</sub>* and *loss<sub>max</sub>* (<<1)

The estimated annual loss ratio  $E_{loss}$  for a given *nur* and *loss<sub>av</sub>* scenarios are shown in figure 3.1.

The following estimation of an annual loss in energy production is based on the data identified in the State-of-the-Art section:

- *nur* = 7% is valid for all year observations [44].
- the average loss per non-uniform occurrence equals 25% (very high) of the maximum recorded loss of 18% ( $q=0.25$ ,  $Loss_{max}=0.18$ ) [42].

Then

$$loss_{av} = 0.25 * 0.18 = 0.045$$

and

$$E_{loss} = 0.07 * loss_{av} = 0.003$$

The result is an estimated annual worst case loss in the range of 0.3%. Even if all non-uniform events would mean maximum loss (18%) the annual loss would still only reach around  $0.07 * 0.18 = 1.3\%$ .

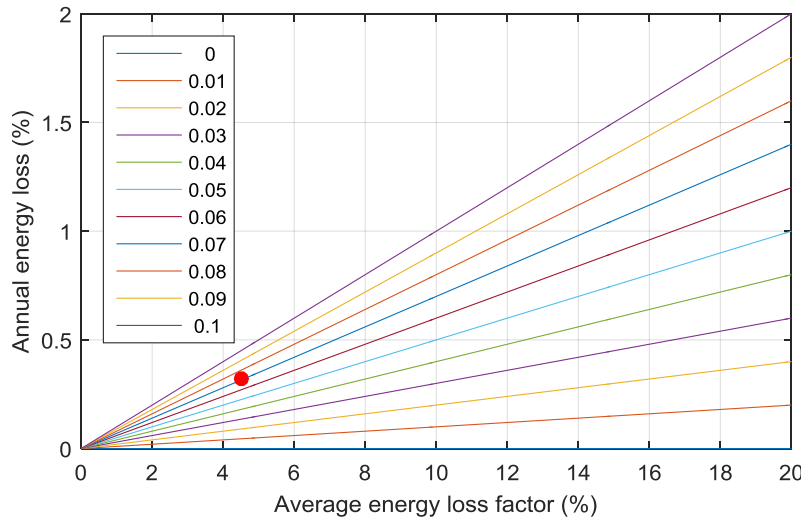


Figure 3.1 Estimated energy loss vs. average energy  $loss_{av}$  factors for different non-uniform annual irradiation ratios (see legend). The red dot indicate the location of the example shown (non-uniform level = 7%, estimated average loss = 4.5%).

The example shown above indicates that the expected annual loss in energy production as well as the difference in energy production between a string inverter concept and a central inverter concept due to moving clouds is likely to be very small even for locations considered as very cloudy.

### 3.2 PV utility plant layout and timing

The land area presently required to place a 1.5MWp PV power plant using standard fixed tilt mounting and modules with say 15% efficiency, varies from around 1 hectare in tropical regions to above 2 hectare in Northern Europe, depending on the actual row configuration, row spacing etc. and the adaption to the geographical constraints at the site of construction [75]. A general layout of a PV utility plant incl. the path of an incoming cloud is schematically illustrated in figure 3.2. A potential effect of moving shadow fronts will depend on the speed and direction of the said front as well as the physical distances of the in parallel connected PV strings.

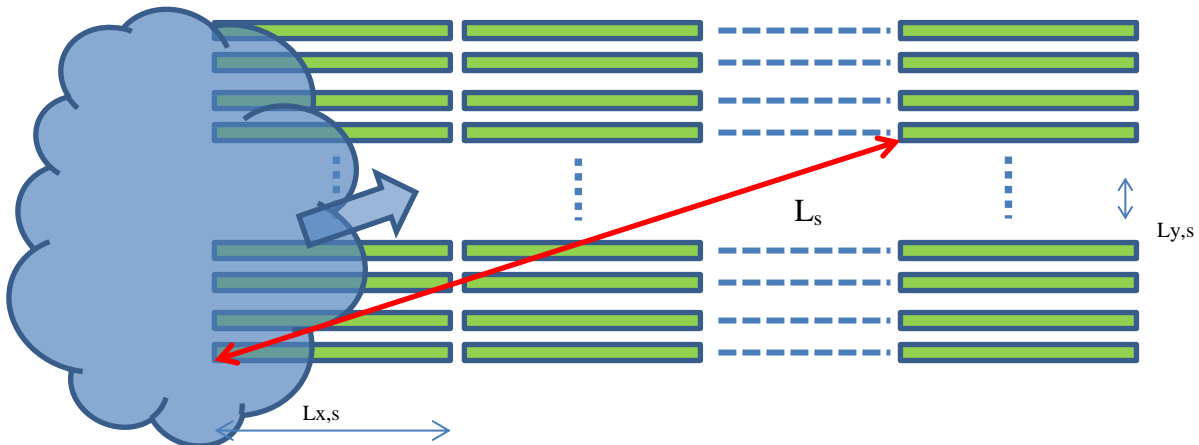


Figure 3.2 Plan of a generic PV utility plant with  $q$  strings in a row and a shadow front passing. The red arrow indicate the maximum length cloud path  $L_s$ .  $Ly,s$  : distance between strings.  $Lx,s$ : string length.

### 3.2.1 String length and number of parallel strings

The present normal operational voltage  $V_{max}$  in a PV plant is 1000V and imposes a limit to the  $n$  number of panels connected in series, taking the temperature dependency of the open circuit voltage  $V_{oc}$  of the PV panels into account. The linearized voltage temperature coefficient  $\delta = dV_{OC}/dT$  for a silicon solar cell can be approximated to -2.2mV/°C [76], resulting in a voltage temperature coefficient  $\beta$  for a Si-based PV panel in the range of -0.3%/°C.

An increased change to systems with 1500V string voltage instead of 1000V is foreseen in the near future giving longer strings, larger inverters, larger array blocks and fewer components and less labour costs and thus resulting in less overall costs [77,78]. The company GTM Research expects 1.500-volt systems to account for 9 percent (4.6 GW) of worldwide utility solar installations in 2016 [77]. A recent analysis published by the company ABB A/S estimate the saving in cable inductor material to be in the range of 15-85% and the saving related to combiner boxes to be in the range of 25-60% [79].

The number of panels  $n$  can be calculated by eq. 3.1, where  $T_{ref}$  refers to either STC (Standard Test Conditions, 25°C) or NOCT<sup>4</sup> (Normal Operating Cell Temperature, 20°C).  $T_{min}$  refers to the minimum operational temperature expected for a given PV plant.

$$n = \frac{V_{max}}{V_{oc}} = \frac{V_{max}}{V_{oc,Tref} * [1 + \beta(T_{min} - T_{ref})]} \quad (3.1)$$

The calculated maximum number of 60-cell panels in a string, for a standard 230W panel ( $V_{oc,STC}=36.6\text{V}$ ,  $\beta=-0.3\%$  and  $T_{ref}=25^\circ\text{C}$ ), as a function of minimum panel temperature is illustrated in figure 3.2. For a given central inverter of power level  $P$ , the number of strings in parallel  $m$  for a string length of  $n$  panels with a STC rating of  $Q$  watt can be calculated as

$$m = \frac{P}{Q*n} \quad (3.2)$$

The required number of parallel strings for 230W panels in series is illustrated in figure 3.3 as a function of nominal inverter input power.

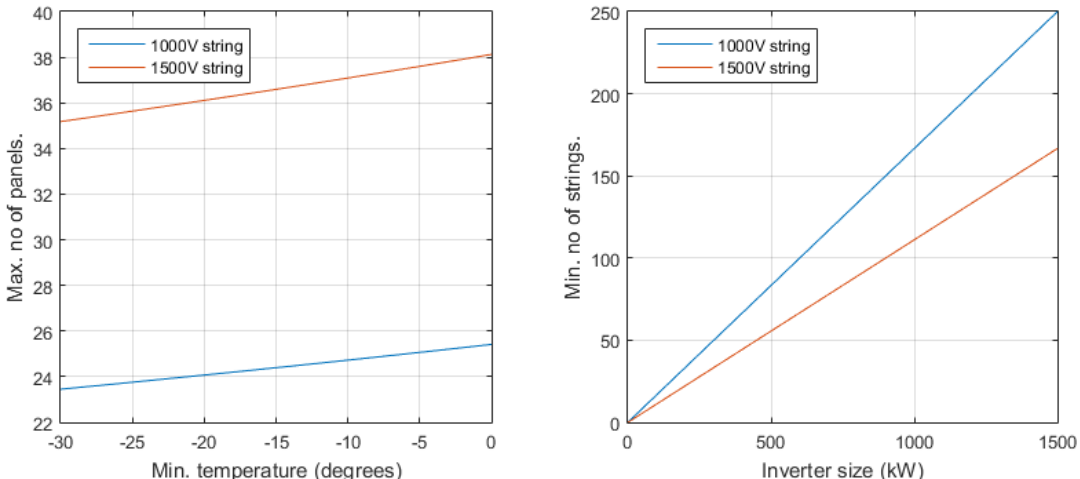


Figure 3.3 Left: Maximum panel number as a function of the minimum operating temperature for a 1000V and a 1500V PV string. Right: Minimum number of strings with 230W panels for 1000V and 1500V DC voltage.

<sup>4</sup> IEC/TS 61836, IEC61215

The maximum number of panels in a string operating at  $T_{min}=-20^{\circ}\text{C}$  equals 24 / 36 panels, for 1000V / 1500V systems respectively. Present industry guidelines recommend the number of 60-cell panels in a 1000V string to 24 [8]. The physical string lengths  $L_{x,s}$  will be  $\approx 40$  m for a 1000V system and 60 m for a 1500V system.

Panels with a power rating of 225-250W (60-cells) presently are a standard panel size range for mono/polycrystalline based PV utility plants and central inverters have a power range up to 1.5 MW [80]. The required number of strings and panels for a 1 MW utility scale plant is shown in table 3.1.

Table 3.1 String/panel number at 1000V and 1500V string voltage.

String voltage	1000V		1500V	
Panel rating	230W	250W	230W	250W
Strings	181	167	121	111
Panels*	2344	4008	2356	3996

\*The variation in panel number between 1000V and 1500V is due to the round off for an integer no of strings.

### 3.2.2 Estimated time of cloud passage

The estimated time for a cloud to pass a PV utility plant is investigated. Assuming a symmetrical layout, the longest distance  $L_{max}$  between two strings for a 1000V system will be in the order the order of 150m. The Speed-Over-Ground (SOG)  $v$  of a passing shadow determines the actual time delay between strings in a plant. The maximum time difference  $\Delta t_{max}$  between the arrival of the shadow front at the inverters can be estimated (eq. 3.3)

$$\Delta t_{max} = \frac{L_s}{v} \quad (3.3)$$

The estimated time delay between strings for string distances  $L=50\text{-}300\text{m}$  is illustrated in figure 3.4 as a function of an anticipated speed-over-ground of the shadow front.

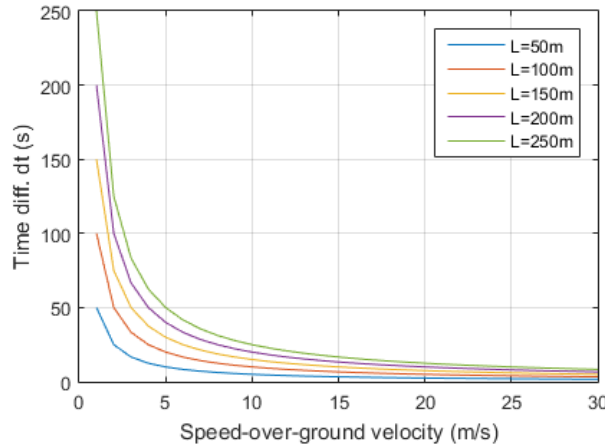


Figure 3.4 Estimated time delay between strings as a function of anticipated speed-over-ground of the shadow front for different distances between the strings.

#### 3.2.2.1 Estimation of the speed-over-ground (SOG).

The speed and direction of moving clouds is determined by higher altitude winds, not necessarily having the same direction and velocity as the ground speed. A weather station can provide information about wind speed and direction etc., but the speed and direction of moving clouds is determined by higher altitude winds, not necessarily having the same direction and velocity as the ground velocity. Sky-camera systems for the determination of cloud speed/direction are an ongoing

field of research, but were not available for this project. These cameras are intended for short term to midterm weather forecast scenarios [63].

The primary method for estimating the actual cloud speed considered in this work is based on the measurement of the low altitude wind speed by a weather station and calculating/estimating the wind profile in higher altitudes, up to the cloud base. The weather in Northern Europe is known to change fast and long periods of moving clouds are known to occur. Available weather data from Northern Europe is thus considered to be only representative. The cloud patterns generating distinct shadows on PV-fields are considered to be mainly within the lower atmospheric boundary layer of the troposphere (up to 2000 m). The SOG equals the actual wind speed at the altitude of the cloud base and is in general not equal to the measured wind velocity due to the ruggedness factor of the landscape/surroundings and will among atmospheric parameters like pressure, humidity and temperature depend mainly on the cloud altitude and the surface ruggedness factor [81], see figure 3.5.

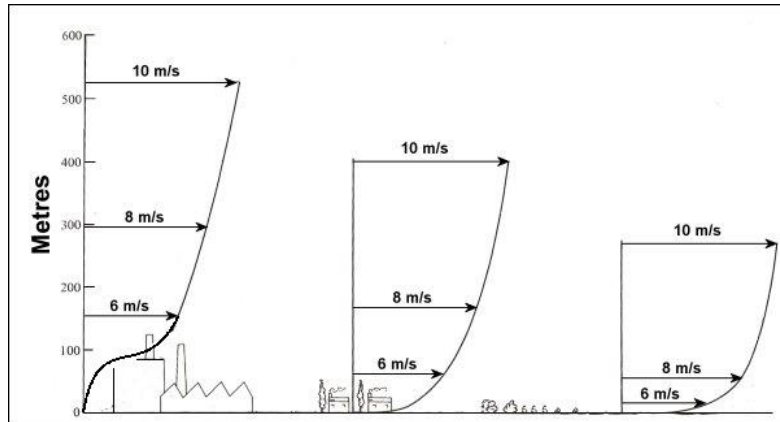


Figure 3.5 Wind speed gradients curves [82]. Reprinted with permission.

The estimation of wind profiles has been a field of extensive studies due to the wind turbine industry and the currently preferred approximation for the wind profile for heights between 120 and 500m is the wind power law (eq. 3.4) [16,83-84].

$$v_z = v_g \left( \frac{z}{z_g} \right)^{\frac{1}{\alpha}}, \quad 0 < z < z_g \quad (\text{eq. 3.4})$$

where

$v_z$ = speed of the wind at height  $z$

$v_g$ = gradient wind at gradient height  $z_g$

$\alpha$ = exponential coefficient

The ratio between the measured reference wind speed  $V_g$  and the estimated wind speed  $v_z$  is named the wind gain factor  $Q$ .

$$Q = \frac{v_z}{v_g} \quad (\text{eq. 3.5})$$

The wind profiles over ground can show a significant temporal variation, each preferably fitted by different functions [85]. The average wind speed might even become nearly constant above a certain height (150 m in the specific case described in [85]). For a base height  $z_g=10$  m the exponent  $1/\alpha$  equals the Hellmann constant  $\beta$  which for different surface conditions can be found in the literature [86,87]. Values of  $\beta \approx 0.2$  apply for farm land /rural areas and  $\beta \approx 0.3$  apply for neutral air above inhabited areas. During unstable conditions the power law exponent is mainly a function of surface roughness and only a weak function of stability [88].  $B \approx 1/7$  is in general a good approximation under stable conditions [83].

The height of the cloud base for low clouds is in the literature for Southern Denmark / Northern Germany and is estimated to be at the level of 100-500 m [89]. Height data recorded by a LIDAR system in Northern Germany (August 2013-August 2014, 1 hour intervals) shows a rather uniform distribution of the occurrence of base heights from 200-1500m, see figure 3.6.

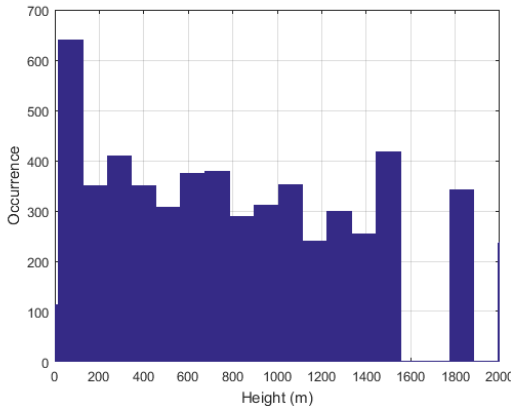


Figure 3.6 LIDAR height measurement statistics for August 2013-August 2014 from Friesoythe in Northern Germany<sup>5</sup>.

### 3.2.3 Conclusion regarding the weather profile

Based on the above listed arguments it is assumed for this study that the real wind velocity profile can be approximated by the wind profile power law (eq. 3.4). The approximate wind gain factor  $Q$  is in the literature approximated to 2 for a cloud base of 500 m [89], equivalent to  $\beta=0.2$  (flat farm land). The available data for the cloud base height of 300-400 m over inhabited areas suggests that  $Q<3$ . For a worst case scenario the speed over ground of a shadow front induced by a moving cloud is expected to be in the order of 3 times higher than data recorded from a weather station on-site. The wind speed in Northern Europe is very dependent on the location (coast, inland etc.). For Denmark the average wind speed is in the order of 5.8 m/s and the prevailing direction is west<sup>6</sup>. The number of days with strong winds (10.8-13.8 m/s) are between 30-170, dependent on location. Storms (over 24.5 m/s) occur during winter and are most frequent along coastal areas and occur 3 to 4 times per year on average.

The average speed over ground of a sharp (ideal) cloud front is expected to be approximately  $3*5.8\text{m/s}=17.4\text{ m/s}$  (eq. 3.5). The resulting time to pass the PV-plant will depend on the width of the transition zone. The estimated passage times for different widths of cloud transition zones pass a 160m wide PV plant are shown in table 3.2.

Table 3.2 Transition times for selected widths of a cloud transition zone.

Type of wind	Velocity [m/s]	Cloud SOG [m/s]	Passage time for different transition profiles [s]			
			Sharp	100m	250m	500m
Average	5.8	17.4	<b>9</b>	<b>17</b>	<b>27</b>	<b>47</b>
Strong	12	36	<b>4</b>	<b>8</b>	<b>13</b>	<b>22</b>
Storm	25	75	<b>3</b>	<b>4</b>	<b>7</b>	<b>11</b>

The transition times in table 3.2 are indicative only. It can be concluded that the time for cloud induced shadows to pass over a 1.5MW PV plant (side length 160m) plant are expected to be predominantly in the range of 4-50 seconds. A string of panels (length  $\approx 40$  m) is likely to be

<sup>5</sup> Data obtained from University of Oldenburg, Germany.

<sup>6</sup> <http://www.dmi.dk/en/klimaet-frem-til-i-dag/danmark/vind/> (accessed February 2016)

influenced by a passing cloud for approximately 1-20 seconds. The directions of the dominant cloud cover at the height of 300-400 m are anticipated to have the same direction as the wind monitored above ground level by a weather station.

### 3.3 PV test park layout concept

The investigation of the potential difference in energy production for plants with string and central inverter layout is based on a comparative analysis with operational data from an operational PV utility scale power plant. Such PV plant should ideally be equipped with both string and central inverters, having identical panel layout in the strings and comparable inverter characteristics. The expected annual difference in energy production between two inverter systems is expected to be <0.3%, thus requiring either detailed knowledge of the individual inverter efficiency characteristics in case different types of inverters are present. The test concept is illustrated in figure 3.7, combining string- and central inverter functionality in one PV plant.

The ability to monitor selected inverters distributed over a large area give the possibility to estimate the through speed-over-ground of the shadows passes via time correlation of the DC power values.

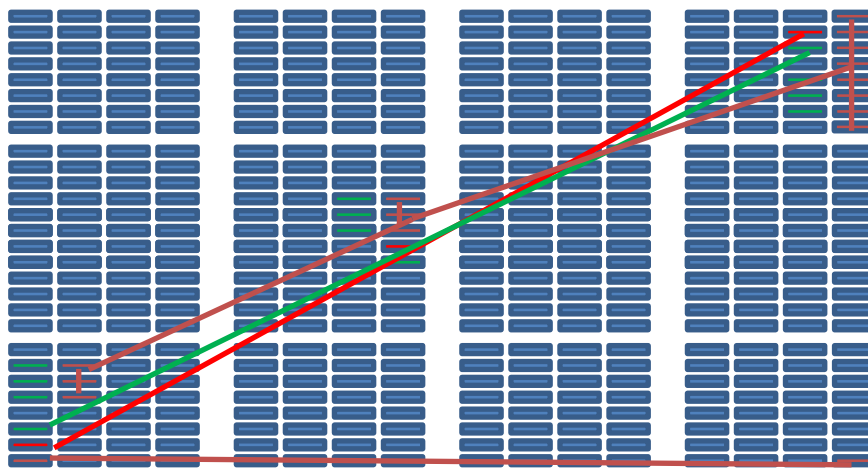


Figure 3.7 PV test plant concept. Green: Individual string inverters. Brown: Parallel/central inverter. Red: Parallel/central inverter with spaced strings. The drawing does not show exact inverter positions.

### 3.4 Selection of main test park and resulting measurement plan

The evaluation of possible PV utility test plants is described in detail in Appendix [A8], where the new Danfoss Solar Park in Nordborg, Denmark, is identified as the most suitable test plant available, see figure 3.8. The park was accessible for experiments / data logging from June 2014.

The new 2.1MW PV utility plant was selected as the primary test plant due to the possibilities for reconfiguration of a specific row (row 21), the possibility of data recording via the inverter communication port and ease of access. The park imposed both practical and analytical challenges, as the part at the same time was used also as a primary test plant for Danfoss Solar Inverters A/S (in 2014 acquired by SMA Solar Technology AG) and also is located on a hilly area.



Figure 3.8 Areal view (left) and topography (right) of a section of the 2.1 MW Danfoss Solar Plant in Nordborg, Denmark.

A 62 kWp PV plant at the University of Southern Denmark Campus in Sønderborg, Denmark, hereafter called “SDU Alsion PV plant”, was added as a secondary test plant. Details are given in appendix [A8].

A detailed description of the implemented data recording platform for the data retrieval from the inverters regarding their DC and AC performance and calibration is given in appendix [A8]. 31 parameters per inverter were for a period of more than one year retrieved from 12 selected inverters at an approximate rate of 1 Hz.

### 3.5 Measurement strategy

For the identification and recording of fast changes in power and energy production from a series of PV strings / inverters it is necessary to obtain data with a high temporal resolution. The analysis of the passage time for clouds showed that sharp shadow fronts with a passage time  $> 3$  seconds for strong winds are to be expected. It was decided to implement measurement systems with an update rate of 1 Hz as a compromise between expected irradiation dynamics and amount of sampled data. The parameters listed in table 3.3 are to be measured / obtained per monitored inverter.

Solar inverters performance can be monitored via external instrumentation, giving freedom to operate regarding accuracy and sampling speed but at increased costs as each inverter requires its own measurement system. It is possible to read data from the FLX-type inverters from their internal measurement circuitry via a communication link. As solar inverters in general are not designed to comply with the standards for energy metering must the AC power levels measurement be performed with, or calibrated against, external measurement equipment / energy meters for reaching a sufficient accuracy.

Table 3.3 Primary parameters to be obtained for an inverter system.

Inverter		
DC	AC	Ambient
Voltage per string	Voltage per string	Irradiation level
Current per string	Current per phase	Air temperature
Energy per string	Power per phase	Panel temperature
	Energy per phase	

The string parameters recorded during operation are the apparent MPP values for each string, determined by the dynamic response of the inverter MPPT performance. In case a fast shadow moves the MPP of the attached PV string it is possible that the apparent MPP value is lagging

behind the true MPP, due to a finite response time in the MPPT circuitry/software. The dynamic MPPT efficiency  $n_{MPPT,dyn}$  can acc. to [16] be defined as:

$$n_{MPPT,dyn} = \frac{\int_0^{T_M} v_{DC}(t) i_{DC}(t) dt}{\int_0^{T_M} P_{MPP}(t) dt} \quad (3.1)$$

where

$v_{DC}(t)$	=	voltage at the DC input of the inverter
$i_{DC}(t)$	=	current at the DC input of the inverter
$P_{MPPT}(t)$	=	available maximum power of the PV array
$T_M(t)$	=	measurement duration (start at t=0)

The integral in the denominator represents the whole MPP energy that can be absorbed under optimum conditions by the inverter. Dynamic MPPT is tested according to the European Standard EN50530. The standard use ramps of up to  $100W/m^2/s$  for testing [16]. Changes in the order of  $30 W/m^2/s$  are in [68] considered to be very fast and faster changes and thus do not need to be considered in inverter design. The tracking capability of an inverter will depend on the implemented type of MPPT-algorithm of which a wide range is known from the literature [13]. The “Incremental Conductance” method is claimed to be well suited for rapidly changing atmospheric conditions [90]. Recent studies by Kjaer document that the “Incremental Conductance” and the “Hill-climbing” method are almost similar in performance [15].

### 3.5.1 Inverter independent measurements / IV-sweep

To obtain inverter independent MPPT and reference measurements of panel performance under operational conditions it is preferable to continuously monitor selected panels with an IV-curve measuring instrument. To obtain inverter independent data/information about the characteristics of the PV-panels in a test park as well as in general should the IV-curves of at least one PV-panel of the same type as in the selected test park be recorded under operational conditions. The sweep repetition frequency should be the same as for the inverter data (1 Hz). Irradiation level, air and panel temperatures must be included. No identified commercially available IV-scanners were able to comply with the requirements regarding required sweep time, sweep interval and number of sweeps. Therefore a custom *low cost battery operated fast IV-curve tracer* IV-curve recording system for the fast measurement of IV-curves of selected panels was designed. The evaluation of available IV-curve tracers and the developed system is described in detail in appendix [A11]. However, the curvature of the rows in the Danfoss Solar Park and the access to only one row complicated the mounting of IV-curve tracers on selected panels distributed around the plant. The curvature generates different operational conditions for each panel under test and as only one row could be modified only one direction (East-West) could be monitored.

Due to the specific mounting and operational issues (other independent tests were run in parallel on multiple strings/inverters) it was decided *not to implement multiple IV-curve tracers on the Danfoss Solar Park*, but instead to test one panel externally to determine the temperature characteristics of the panel during extreme operating conditions. A panel of the same type as mounted in the Danfoss Solar Park therefore was tested at the ESTER Outdoor PV monitoring station at the Tor Vergata University in Rome, Italy, during several months because of the expected higher irradiation levels during summer periods. The focus of the tests performed were the measurement/verification of the Maximum-Power-Point temperature coefficient and the recording of data at other weather conditions than in Denmark. An IV-curve tracer was also installed at the SDU Alsion PV plant. The purpose was to monitor IV characteristics of a panel independent of any MPPT-circuitry and to compare the response with the tracking ability of the installed inverters. Inverter data is retrieved in

a similar way for both the Danfoss Solar Park and the SDU Alsion PV plant, see figure 3.9 and appendix [A8].

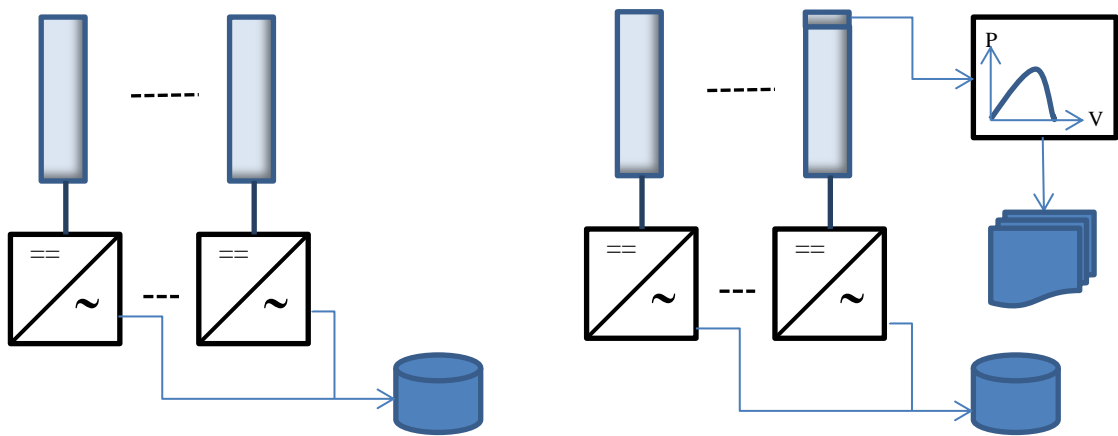


Figure 3.9 Measurement scheme. Left: Recording of inverter data at Danfoss Solar Park to a server. Right: Recording of inverter data to server and IV-sweep data at SDU Alsion PV plant to local files via an IV-curve tracer.

### 3.6 Conclusion on the analysing section

- Distributed PV strings over a larger area should be connected to groups of string inverters to emulate the functionality of a central inverter with a many parallel string input.
- The analysis of the estimated time difference likely to occur in a utility scale PV plant estimates the annual difference in energy production between systems with central inverters and string inverter to be <0.3%.
- The sampling rate for an intended measurement system, in order to capture instant differences in irradiance and DC power level is in the order of 1 second due to the time differences occurring in such parks.
- For the acquisition of inverter independent measurement IV-curves tracers should be installed on selected panels. Due to the topographical and operational conditions of the selected main test plant, the Danfoss Solar Park, it was decided not to install IV-curve tracers in that park but to test panels at other locations.

## 4 Test plant related investigations

The specific character of the Danfoss Solar Park presented 2 areas related to the construction of the site and the variation of PV panel data:

- The park has a quite uneven topography, due to the landscape curvature and the 9216 mounted panels have a production related variation in the basic panel parameters in the range of 5%.
- The PV plant is equipped with 9216 PV panels of 4 different types in the range of 225-230 Wp. The potential gain by sorting of the panels PV panel is analysed.

The occurrence of the *Standard Test Conditions* (STC) and *Normal Operating Cell Temperature* (NOCT) are investigated by analysing the occurrence of specific combinations of irradiation level, panel and ambient temperature in the recorded data set.

### 4.1 Danfoss Solar plant test layout

The layout of the 2.1 MW Danfoss Solar Park is shown in figure 4.1. A detailed description of the Danfoss Solar Park can be found in appendix [A8]. Basic data of the park are listed in table 4.1.

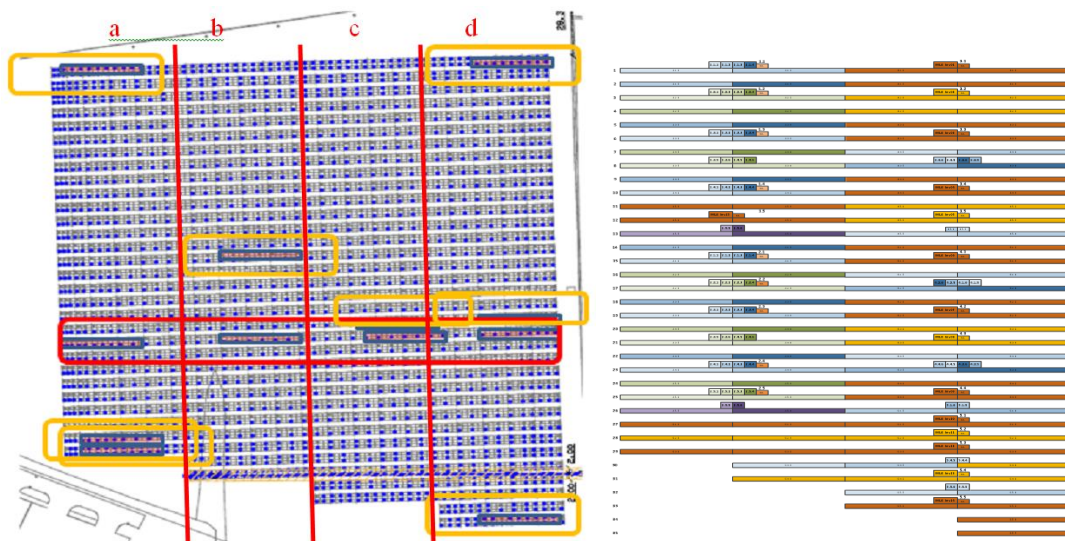


Figure 4.1 Danfoss Solar Plant string configuration, 35 rows. a,b,c,d indicate panel sections. Left: Dark areas indicate monitored string groups of 3x24 panels. The red box show the placement of the 4 primary FLX test inverters. The yellow boxes shows the location of additionally monitored test inverters. Right: Park layout medio 2015 after replacement of several FLX string inverters with MLX type 60 kW inverters.

Table 4.1 Basic parameters for the Danfoss Solar Park.

Parameter	Danfoss Solar Park
Inverter capacity	1,920kW
Module capacity	2,076,840Wp
Plant area	4 ha
Panel area	2.45 ha
Inverters (until spring 2015)	128 x FLX 15kPro (3 MPPT)*
Module rating	8568x225W; 648x230W

Cell type	Polycrystalline
Total no. of modules	9216
Est. production	Est. 1.957 MWh/year
Panel angle	15°
Panel orientation	SSE, 3° from S
Topography	Uneven, up to ±7° tilt
No of panels per inverter MPPT	24
No of rows	36 (uneven length)
No of panels per row (row 1-29)	3x96

\*approximately 50 % replaced during 2015 with 60kW MLX inverter.

#### 4.1.1 Recorded data sets

The data sets recorded and applied in this investigation are listed below.

- Data set 2: SDU Alsion PV plant recordings (October 2014 to October 2015, 415 variables)
- Data set 3: Danfoss Solar Park recordings (October 2014 to October 2015, 415 variables)
- Data set 4: IV-sweep data (March 2015 to October 2015)

The data are recorded at 1 second intervals, whenever possible. The recording, variables, structure and post the post processing of the data sets is described in detail in appendix [A8].

#### 4.2 STC/NOCT data analysis

In this analysis the recorded time stamps, panel and ambient temperature data, the irradiation data and the average wind speed are applied.

When comparing panel specifications and test results STC or NOCT are almost universally applied. The long term high speed irradiation measurements over a year obtained in this project have been analysed with respect to the occurrence of the STC and NOCT conditions. The irradiation levels recorded during the test of the developed IV-curve tracer platform in Rome have been included in the analysis.

Table 4.2 STC and NOCT conditions.

Parameter	STC	NOCT
Irradiation level	1000 W/m <sup>2</sup>	800 W/m <sup>2</sup>
Air mass (AM)	1.5	1.5
Cell temperature	25°C	47.5°C
Air temperature	---	20°C
Wind velocity	0 m/s	1 m/s
Mounting	---	Back side open

##### 4.2.1 Air mass factor (AM)

An air mass factor of 1.5 is part of the STC and represents the attenuation through the atmosphere and therefore will depend on the position of the Sun for each data recording in each data set. The air mass is a function of the solar angle and therefore the time of measurement can be used to calculate the position of the Sun and thereby the angular height /elevation  $h$  of the Sun at that specific time. The modified procedure described by [91] for obtaining AM values for angles close to the horizon was applied. The air mass (AM) factor relates to the path length of the solar irradiation through the atmosphere and can be approximated as [92]

$$AM \approx \frac{1}{\cos z} \quad (4.1)$$

where  $z$  is the zenith angle relative to the normal of the surface of the Earth.  $h$  is given as

$$h = (90^\circ - z) \quad (4.2)$$

For angles close to the horizon higher precision can be reached by applying eq. 4.3 instead of eq. 4.1 [91].

$$AM \approx \frac{1}{\sin(h + \frac{244}{165 + 47h^{1.1}})} \quad (4.3)$$

The air mass corresponding to all measured data in data set 1 and 2 were calculated, as well as for the data recorded at the ESTER Outdoor PV monitoring station in Rome (presented in appendix [A10]).

#### 4.2.2 Danfoss Solar Park and SDU Alsion PV plant

The occurrence of combinations of irradiation level and panel temperature for the Danfoss Solar Park and the SDU Alsion PV plant is shown in figure 4.2. It can be observed that the STC condition is outside the main area of operation for both sites.

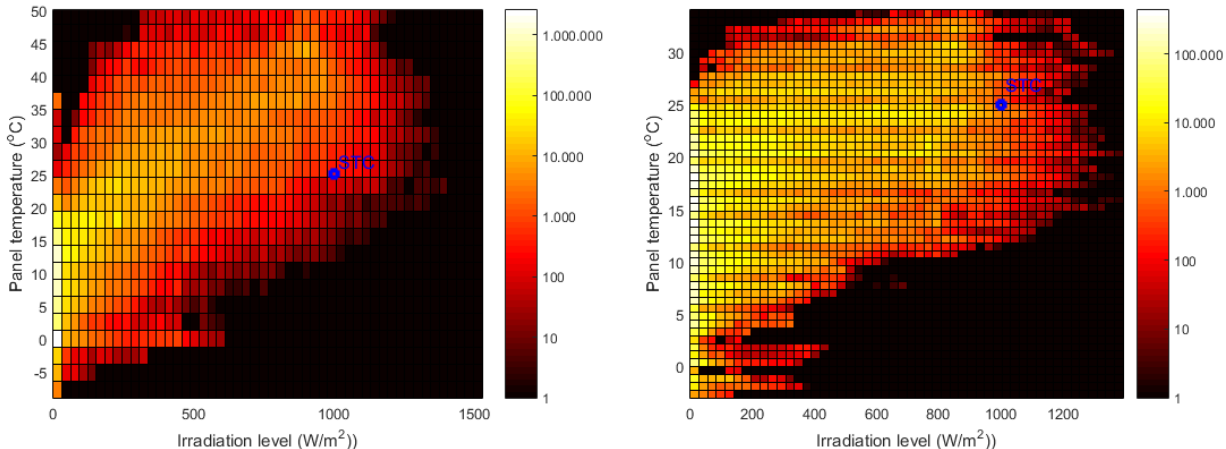


Figure 4.2 Occurrence plot of Irradiation levels vs. panel temperature. Left: Data set 2 (SDU Alsion PV plant). Right: Data set 3 (Danfoss Solar Park).

The analysis showed that no data point in the two data sets occurred at STC when considering the air mass requirement ( $AM=1.5$ ) or for NOCT, when the wind speed and cell/panel temperature requirements were added. Only by widening the acceptance intervals could some data points (<10 out of >10 mill. per plant) be registered. See table 4.3.

It must be concluded that STC and NOCT events are extremely rare events and that those specific test conditions do not represent the working conditions for the tested panel during the long period of investigation.

Data from the tests performed with the developed IV-curve tracer system at the ESTER Outdoor PV monitoring station in Rome shows a slight improvement in modified NOCT occurrences. See appendix [A10] for details regarding the distribution. For Rome 0.04% of the data points occurred around STC ( $\pm 5\text{W/m}^2, \pm 1^\circ\text{C}$ ) without considering the air mass (AM). No point occurred at NOCT, even when rejecting the wind speed requirement of 1 m/s. Rejecting also panel (cell) temperature requirement of  $47.5^\circ\text{C}$  ( $\pm 1^\circ\text{C}$ ) resulted in a NOCT of around 0.02%.

Table 4.3 Detected STC and NOCT events.

Site of observation	STC (%)	NOCT ((%)
SDU Alsion PV plant	<0.001	<0.001
Danfoss Solar Park	<0.001	<0.001
ESTER PV station, Rome*	<0.001	0.02

\*Appendix [A10].

### 4.3 Panel sorting analysis

The Danfoss Solar Park is as described in appendix [A8] equipped with 4 different types of PV panels (table 4.4), rated 225W and 230W. Flash test data ( $P_{MPP}$ ,  $V_{MPP}$ ,  $I_{MPP}$ ) for each panel of the 9216 panels mounted have been applied in this analysis.

Table 4.4 Module types mounted

Type	Number
ND225R1J	7308
NDR225A2	1260
NDR230A2	198
ND230R1J	450

#### 4.3.1 Effect of PV plant panel sorting

The distribution of the  $P_{MPP}$  values is illustrated in figure 4.3 together with the sorted values.

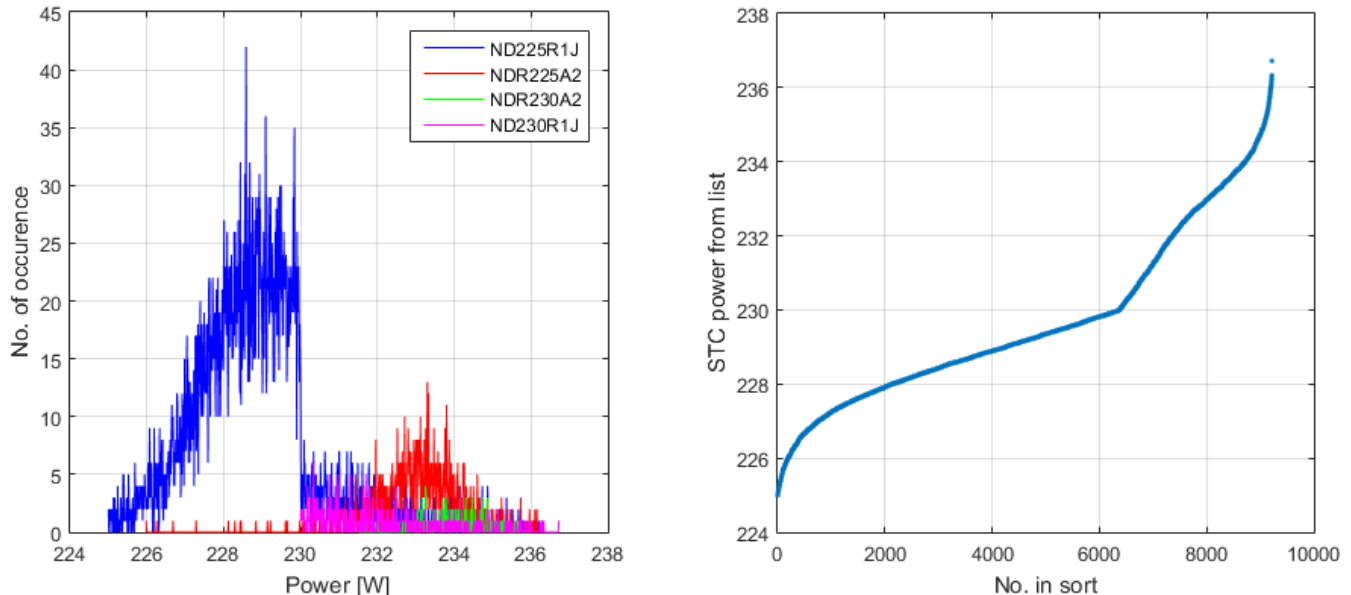


Figure 4.3 Left: Panel distribution histogram, acc. to panel type. Right: Sorted panel  $P_{MPP}$  values.

Of the total of 9216 panels are 8568 panels rated at 225W. The flash test data however showed that several of the 225W panel in have an  $P_{MPP}>230W$ . The plant has a total of 384 MPPT input. An analysis has been performed to calculate the change (loss) of power under STC conditions for a random number of panel combinations.

The random distribution of all 225W rated panels has been simulated for 10,000 events and the resulting DC mismatch loss is shown in figure 4.4. The  $I_{MPP}$  parameter was selected as the sorting parameter, as it is known from the literature that the variation of  $I_{MPP}$  has the highest influence on

the panel mismatch in series connected string [54]. It has been assumed that the panels are mounted in a flat area, without any varying panel tilt.

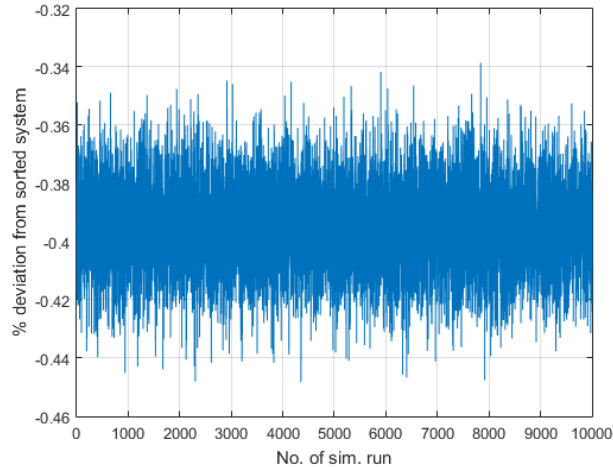


Figure 4.4 The simulated loss in DC power under STC conditions for 10,000 runs of random selection of the 9216 PV-panels in the Danfoss Solar Park, for the 384 inverters relative to a sorted mounting with 24 panels per string. STC conditions apply. Flat mounted rows are assumed.

A comparison between the installed power sum of all panels, the power after sorting after  $I_{MPP}$  and the additional average loss due to random placement of the panels are shown in table 4.4. In the event that the same panels are placed in strings of 36 panels in a future 1500V system (to benefit from the higher string voltage) the mismatch loss is expected to increase, even for sorted panels.

Table 4.4 DC loss due to panel mismatch of all 225W rated panels.

<b>Power generation</b>	<b>24 panels in string</b>		<b>36 panels in string</b>	
$P_{plant,STC}$ , nominal	1.967.324	100.0%	1.967.324	100.0%
$P_{plant,STC}$ , sorted after $I_{MPP}$	1.945.185	98.9%	1.942.181	98.7%
$P_{plant,STC}$ random placement*	1.938.106	-0.36%	1.935.842	-0.32%

\*Average of 10,000 simulations

It can be observed that  $P_{plant,STC}$ , sorted after  $I_{MPP}$  is about 1.1% lower than the nominal panel ratings and that the random placement of all panels on average add another loss in the range of 0.4%. The placement of 36 panels in a 1500V string marginally increases the losses for the sorted plant and additional loss from a random placement on average is comparable. A random distribution of all panels will increase the average loss by <0.1%, as shown in table 4.5.

Table 4.5 DC loss due to panel mismatch of all 225W and 230W rated panels.

<b>Power generation</b>	<b>24 panels in string</b>		<b>36 panels in string</b>	
Sum of all STC power	2.116.740 Watt	100.0%	2.116.740 Watt	100.0%
Sorted after $I_{MPP}$	2.092.880 Watt	98.9%	2.089.782 Watt	98.7%
Random placement*	2.084.840 Watt	-0.41%	2.082.677 Watt	-0.34%

\*Average of 10,000 simulations

It can be concluded that the random distribution of the PV panels will result in a nominal power loss in the range of 0.4% compared to a PV plant with sorted panels, regardless of string length. The use of individual module inverters would increase the power available under STC by approximately 1%.

Changes of the panel data induced by aging of the individual panels and potentially varying panel temperatures over the park area have not been included in this study.

All available flash test data is obtained on flasher equipment mounted in the production lines at the manufacturer of the panels. Comparison tests of flashers available at several European test laboratories showed that the tolerance of the power  $P_{\text{flash}}$  of a flasher measurement is about -1,5/+2.6% [93]. It was further assumed that the tolerance of production line flashers is no better than laboratory flashers. It is further stressed that it is very important to consider (and improve!) the error of STC power measurements for comparing the performance of different PV technologies and PV sites [93,94].

#### 4.3.2 Conclusion on panel sorting

The analysis of the flash data for all panels showed that a gain in the range of 0.4% can be achieved via sorting. This is consistent with a study published by TÜV Rheinland, Germany, reporting 0.4% gain for polycrystalline panels via sorting by  $I_{\text{MPP}}$  [54]. However, the associated cost-benefit analysis concluded that the estimated additional costs for sorting/handling/logistics ( $15\text{€}/\text{kW}_p$ - $30\text{€}/\text{kW}_p$ ) cannot repay itself during a 25 year expected lifetime of a PV-plant and the investment is decidedly not economically beneficial. Payback time was estimated to 25-49 years.

#### 4.4 Panel temperature analysis

A detailed temperature analysis of a panel of same type as mounted in the Danfoss Solar Park was performed at the ESTER Outdoor PV monitoring station, Italy. The developed IV-curve tracer has recorded approximately 13 mill. IV-scans under varying irradiation and temperature conditions. The  $I_{\text{MPP}}$  and  $V_{\text{MPP}}$  values together with irradiation level and panel temperature are detected in each scan. The details of the analysis are presented in appendix [A10]. The main results of the analysis are presented below.

The extracted  $P_{\text{MPP}}$  values from recorded data around specific temperature intervals are presented in figure 4.5 as a function of the measured irradiance together with a fitted power law function for each temperature interval. It has been accepted that an extended air mass (AM) interval of 1.0-3.0 is sufficient to obtain the required data points for the analysis, even if the variation is solar elevation / air mass introduces a potential spectral dependency due to varying atmospheric absorption spectra. The STC location is marked with a red dot.

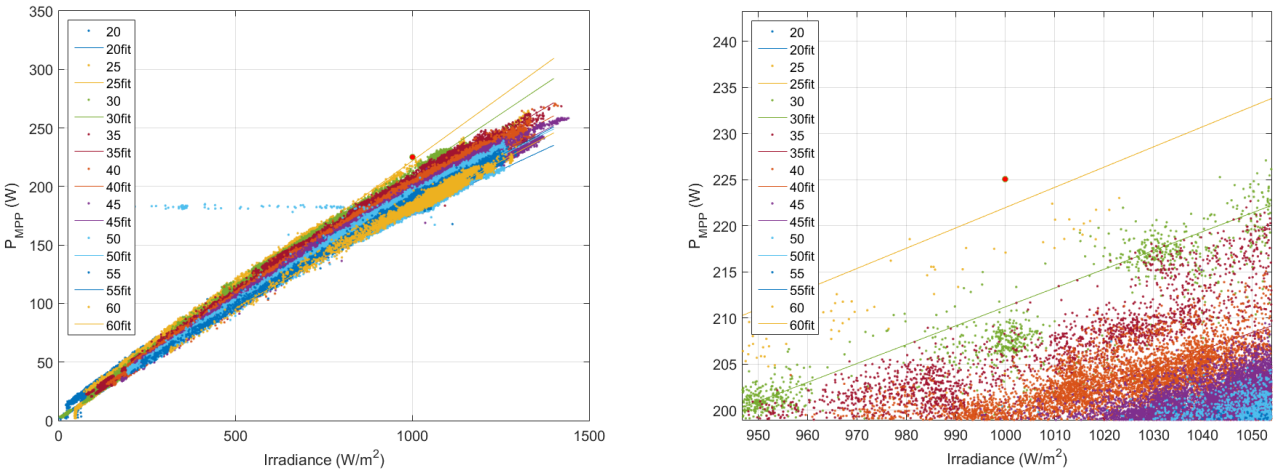


Figure 4.5 Left: Calculated PMPP levels as function of solar irradiance in steps of 5°C. The AM interval is 1-3. A total of approximately 418,000 out of 13 mill. Data points are shown. Right: Zoom on location around STC. The red dot indicated the location of the STC regarding irradiance, temperature and panel P<sub>MPP</sub>-rating.

The average  $P_{\text{MPP}}$  value of the few data in the data close to STC was 218W. The linear fit for  $T_{\text{panel}}=25^{\circ}\text{C}$  for the interval 100-1400  $\text{W}/\text{m}^2$  indicate for STC conditions a  $P_{\text{MPP}}$  level of 222W. This

is 1.4% below the nominal  $P_{MPP}$  level of 225.0W, but the power loss due to aging of the panel is not known and the data sheet guarantees max. 4% of loss during the first year of operation. The panel has been in operation for approximately 1.5 years in total and no clear aging effect could be identified for the 100 day period where panel temperature data were available.

Based on the recorded data an average temperature coefficient  $\tau$  has been estimated. Irradiance values below 200 W/m<sup>2</sup> were discarded due to a low number of actual measurements in that area at several temperature intervals.

The average temperature coefficient, estimated on the basis of the fitted functions for the interval 200-1200 W/m<sup>2</sup>, is  $-0.43 \pm 0.07\%/\text{°C}$ , close to the data sheet value of  $-0.440\%/\text{°C}$ . A dependency of the irradiation level as well as temperature is observed which is to be expected as  $P_{MPP}$  is the product of  $I_{MPP}$  and  $V_{MPP}$ , both of which vary with temperature and irradiance [76].

The estimated values are average values over all temperatures steps for irradiation levels >200 W/m<sup>2</sup> interval and the data sheet specification of a temperature coefficient of  $-0.440\%/\text{°C}$  is only to be seen as an average coefficient. The subject is discussed in more detail in appendix [A10].

## 5 Energy estimation and test results

### 5.1 Test concept description

The purpose of this chapter is to document the test concept and the main results obtained from the analysis of the recorded data from the Danfoss Solar Part and at the ESTER Outdoor PV monitoring station at the Tor Vergata University in Rome, Italy.

The string configuration concept applied to a row in the Danfoss Solar Park is illustrated in figure 5.1. Strings that are physically separated from each other are connected to the same inverter, but one inverter (inverter 2.3.5, logged as inverter 9) still operates with 3 independent MPPT where the other inverter (inverter 2.3.6, logged as inverter 10) has the 3 strings in parallel and therefore operates with only one MPPT and is subject to mismatch losses.

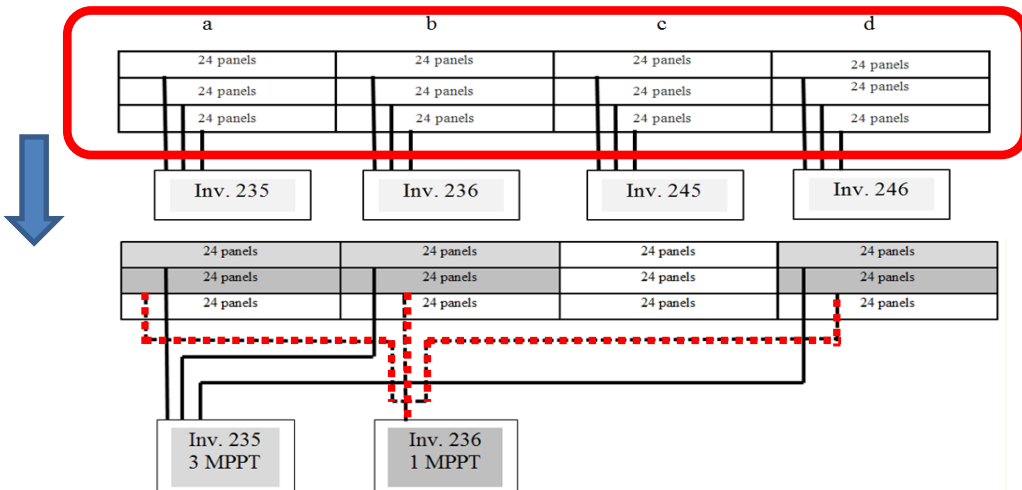


Figure 5.1 Concept of modified inverter configuration, implemented in row 21 of the Danfoss Solar Park.

The data from a total of 12 FLX-inverters are recorded with 1 second intervals, whenever possible. The basic logged parameters are listed in table 5.1. The recording, structure and the post processing of the data sets is described in appendix [A8].

Table 5.1 Logged inverter parameter per inverter.

PV voltage 1	PV voltage 2	PV voltage 3	PV current 1	PV current 3	PV current 3
PV power 1	PV power 2	PV power 3	Grid voltage L1	Grid voltage L2	Grid voltage L3
Grid volt L1-L2	Grid volt L2-L3	Grid volt L3-L1	Grid current L1	Grid current L2	Grid current L3
Grid power L1	Grid power L2	Grid power L3	Grid power sum	Grid freq. L1	Grid freq. L2
Grid freq. L3	Grid freq. mean	kWh today	kWh total		

### 5.2 Estimation of irradiation dynamics

The data sets recorded and applied in this investigation are listed below. The irradiation dynamics of data set 1-3 are investigated to estimate the loss in power production due to a non-uniform irradiation pattern during a year of operation.

- Data set 1: SDU Alsion PV plant recordings (October 2013 to February 2014, 184 variables)
- Data set 2: SDU Alsion PV plant recordings (October 2014 to October 2015, 415 variables)
- Data set 3: Danfoss Solar Park recordings (October 2014 to October 2015, 415 variables)
- Data set 4: IV-sweep data (March 2015 to October 2015, full IV-sweep data, 100 points/sweep)

### 5.2.1 Occurrence of non-uniform irradiation

The recorded irradiance data recorded from the 60 kW plant at SDU Alsion and the Danfoss Solar Park has been analysed with respect to the occurrence of a variation in irradiation level. The distribution of the recorded irradiance and the non-uniformity / change in irradiance for data set 1-3 is illustrated in figure 5.2.

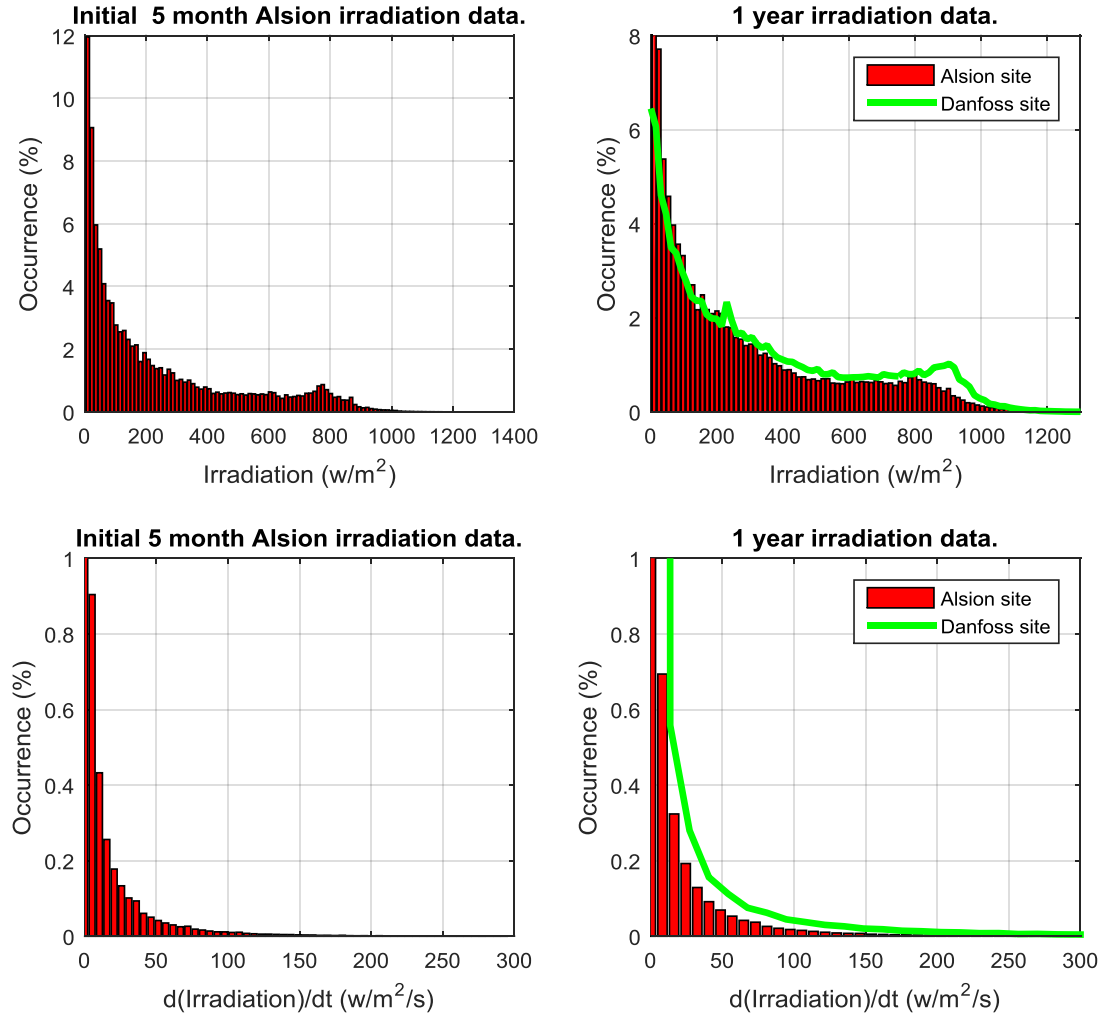


Figure 5.2 Distribution of irradiation levels from the Alsion site and the Danfoss Solar Park. Top row: Distribution of irradiation level. Bottom row: Distribution of calculated change in radiation. Left column: Data from the initial 150 day test period. Right column: Data from 1 year measurement campaign from both PV plants.

The PV plants are located approximately 20 km apart and it can be observed that all 3 analysed data sets have a similar distribution of the change in radiation. A change in irradiance is considered to be a **non-uniform situation** and can basically have two sources, the rotation of the Earth as well as moving clouds. The non-uniformity of the irradiation generated by the rotation of the Earth around its axis will be below 6 W/m<sup>2</sup>/s [44], determining the lower threshold for the detection of moving clouds. Measurements between 1.2 W/m<sup>2</sup> are considered as noise and only non-uniform irradiation changes of measurement >5 W/m<sup>2</sup>/s are seen as induced by moving clouds (and potential other local phenomena like flocks of birds). This threshold is applied in this study.

### 5.2.1.1 Data set 1: SDU Alsion PV plant (150 days)

The sampled irradiation data are analysed with respect to apparent wind speed/direction, irradiation distribution, the size and timing of variation, wind speed, and wind angle. The irradiation statistics are shown in figure 5.3.

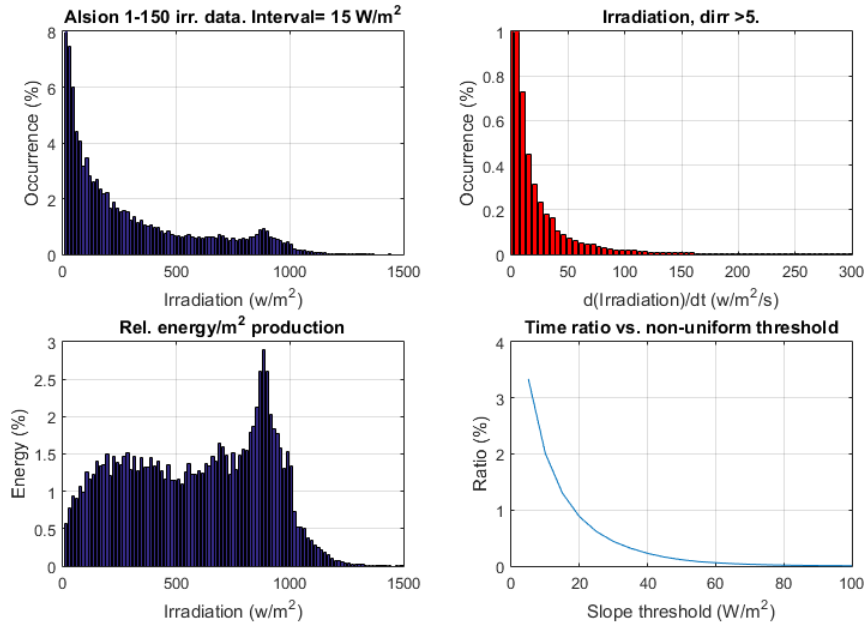


Figure 5.3 SDU Alsion irradiation data October 2013 to February 2014 statistics. Top left: Distribution of irradiation. Top right: Distribution of change of irradiation  $> 5 \text{ W/m}^2/\text{s}$ . Bottom left: Received energy/ $\text{m}^2$  as a function of irradiation level, Bottom right: non-uniform ratio as a function of slope threshold value.

It can be observed that the measured irradiation level for the region of Southern Denmark is distributed mainly below  $800 \text{ W/m}^2$  (figure 5.3 right) and that the rate of change  $d(\text{Irr})/dt > 5 \text{ W/m}^2/\text{s}$  is below 1% for all value-segments, accumulating to approximately 3.4% (figure 5.3 left), meaning that for 96.5% of the recordings the non-uniformity stays below  $6 \text{ W/m}^2/\text{s}$ . The highest continuous slope in the dataset is shown in figure 5.4, rising from  $600 \text{ W/m}^2$  to  $1200 \text{ W/m}^2$  within 10 seconds and thus giving a continuous slope of  $60 \text{ W/m}^2/\text{s}$ , but these events are considered as very rare.

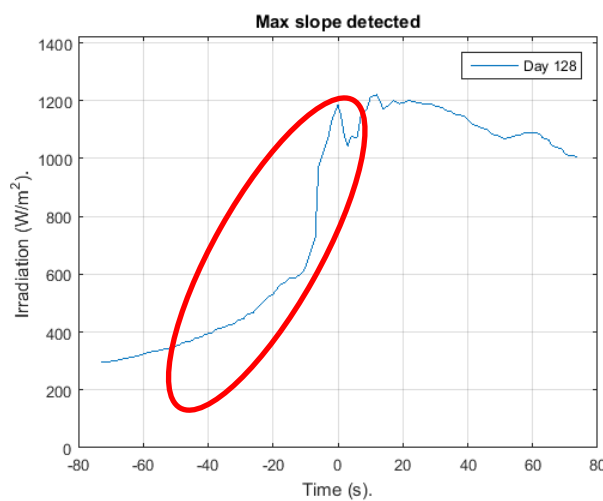


Figure 5.4 Maximum detected slope in dataset 1. Red circle: Detected slope.

The maximum  $d(\text{Irr})/dt$  as a function of wind speed and direction (measured approximately 20 m over ground level) is shown in figure 5.5 (left). The occurrence maps in figure 5.5 (right) illustrate

that the wind direction is dominantly from around  $100^\circ$  and  $230-250^\circ$ . The average  $d(Irr)/dt$  in that direction/speed combination is in the order of  $4-10 \text{ W/m}^2/\text{s}$ .

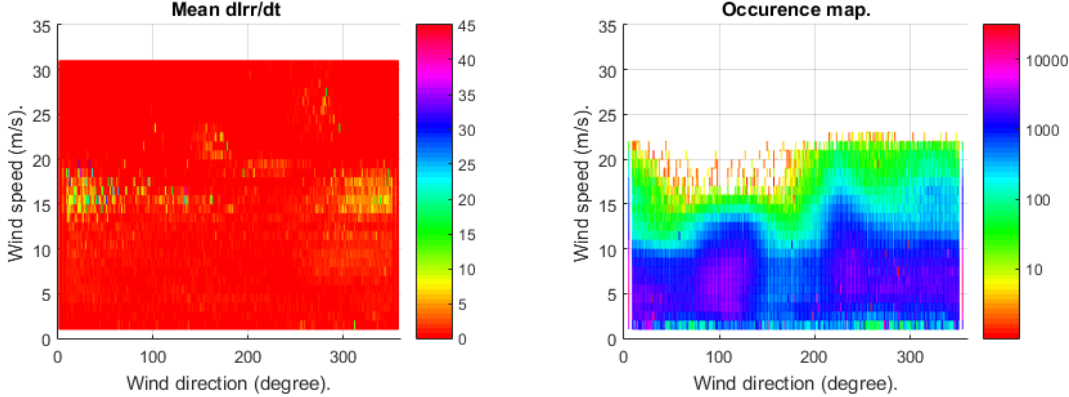


Figure 5.5 Occurrence map from data set 1. 150 days of data from the SDU Alsion test plan. Left: Mean recorded as a function of recorded wind speed and direction. Right: Occurrence of wind speed as a function of wind direction and change in irradiation level.

It can be observed that the measured wind speed slightly above ground level is dominant in the range of 4-12 m/s, equivalent to a SOG in the order of 12-36 m/s, based on an estimated cloud height of 500 m altitude. The perturbation amplitudes (slopes) and durations of the irradiance data induced by atmospheric conditions have been analysed with respect to the duration of the detected slopes. The detection is based on the identification of consecutive rising/falling events where  $abs(d(Irr)/dt) > 5 \text{ W/m}^2/\text{s}$  until a change in sign appears. The results are shown in figure 5.6

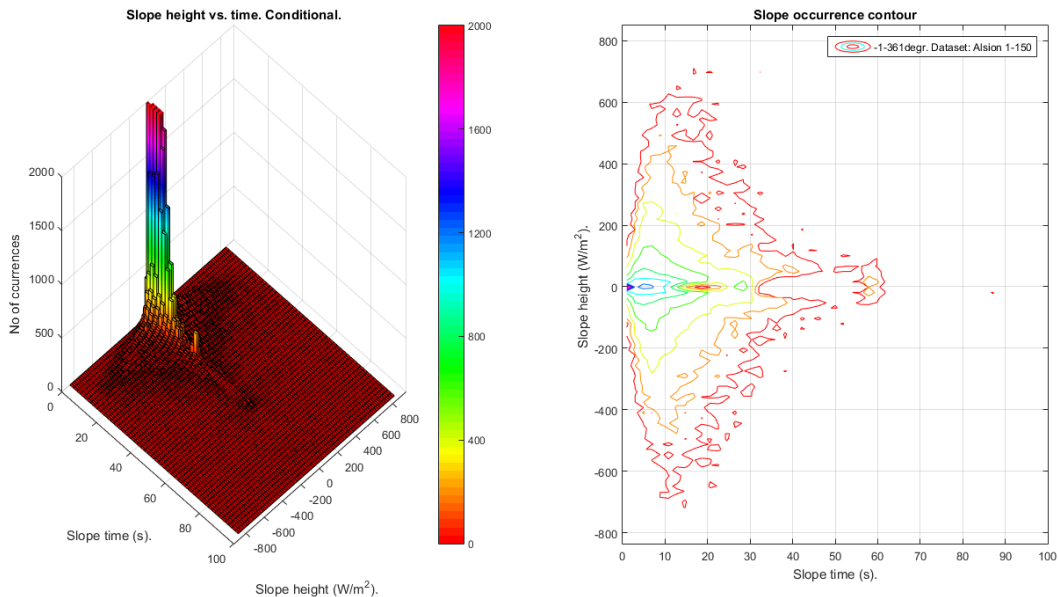


Figure 5.6 Contour maps of data set 1: SDU Alsion test data vs. slope time and slope height. Left: Slope time vs. slope height. Right: Slope time vs. slope time vs occurrence.

It can be observed that the slopes are mainly in the interval  $\pm 100 \text{ W/m}^2$  and the duration is typically  $< 12 \text{ sec}$ . The dominating slopes are centred around  $\pm 50 \text{ W/m}^2$  within 12 seconds. Longer slopes have been observed, but occur rarely, as can be seen in figure 5.7, showing a polar plot of the slope length vs. wind direction.

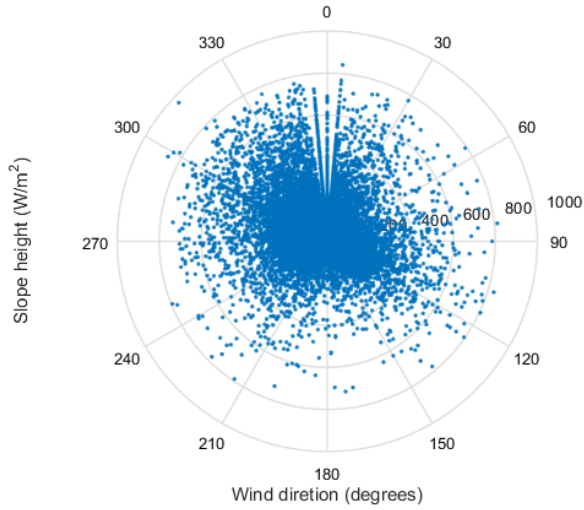


Figure 5.7 Polar plot of the recorded slope height vs. apparent wind direction.

The dominant SOG wind speed  $v_{SOG}$  for the -100 to 100  $\text{W/m}^2$  slope occurs in the interval  $\approx 10\text{-}35 \text{ m/s}$ . The slope length  $L_s$  of passing shadow  $s$  can be estimated by means of the SOG wind speed  $v_{SOG}$  and the slope passage time  $t_s$  (eq. 5.1).

$$L_s = t_s * v_{SOG,s} \quad (5.1)$$

The distribution of the calculated slope length  $L_s$  is illustrated in figure 5.8. It can be observed that a few slope lengths above 500 m have been identified but the dominant slope lengths are in the range below 100 m.

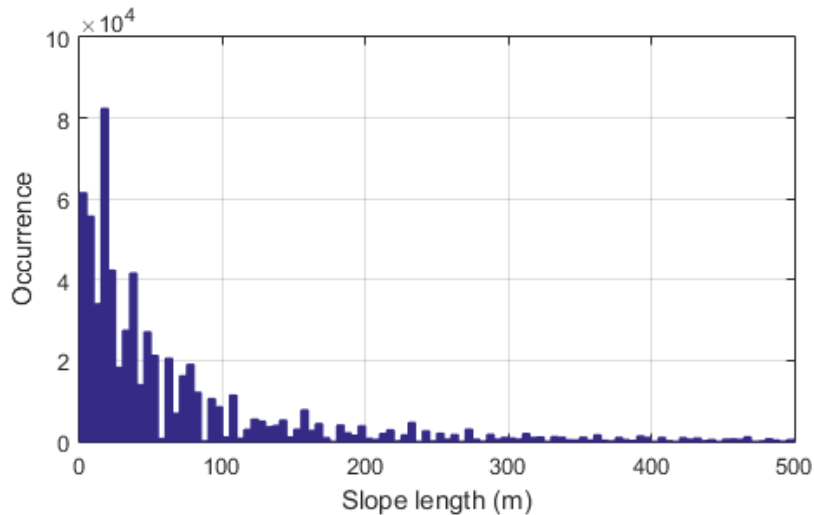


Figure 5.8 Histogram of calculated slope lengths for data set 1 up to 500 m. The 10% level is 100 m.

### 5.2.1.2 Data set 2: SDU Alsion PV plant (one year)

The 1 year irradiation data from the SDU Alsion PV plant are analysed as in the previous section. The sampled irradiation data are analysed with respect to apparent wind speed/direction, irradiation distribution, the size and timing of variation, wind speed, and wind angle. The irradiation statistics are shown in figure 5.9.

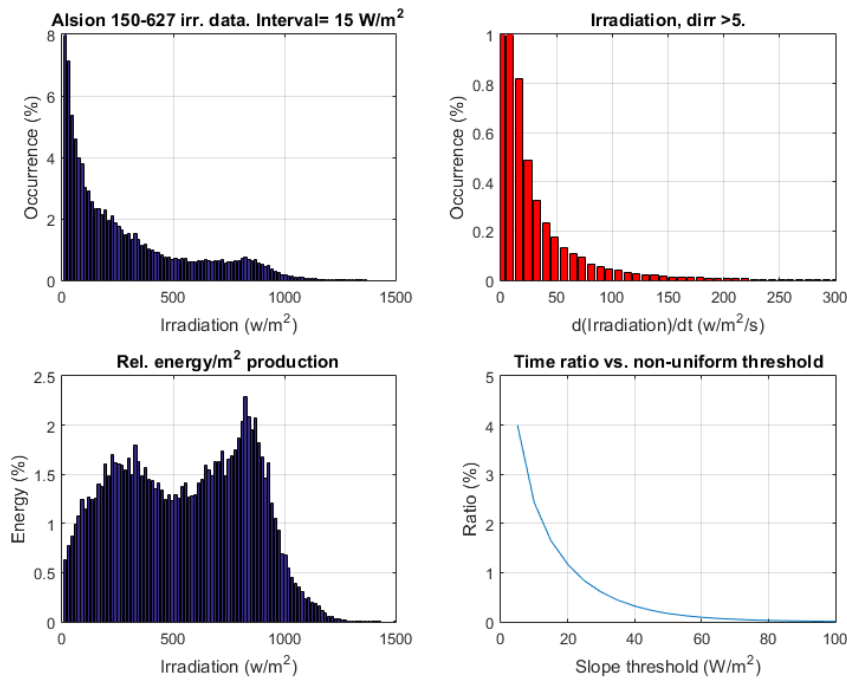


Figure 5.9 SDU Alsion plant irradiation data from data set 2. Top left: Distribution of irradiation. Top right: Distribution of change of irradiation  $> 5 \text{ W/m}^2/\text{s}$ . Bottom left: Received energy/ $\text{m}^2$  as a function of irradiation level, Bottom right: non-uniform ratio as a function of slope threshold value.

It can also be observed in this data set that the measured irradiation level is distributed mainly below  $800 \text{ W/m}^2$  (figure 5.9 upper-right) and that the rate of change  $d(\text{Irr})/dt > 5 \text{ W/m}^2/\text{s}$  is below 1% for all value-segments, but it accumulates to approximately 4%, meaning that for 96% of the recordings the non-uniformity stays below  $6 \text{ W/m}^2/\text{s}$ . This was expected as the data set covers a whole year of data. The highest continuous slope in the dataset is shown in figure 5.10, falling from  $1250 \text{ W/m}^2$  to  $700 \text{ W/m}^2$  within 10 seconds and thus giving a continuous slope of  $55 \text{ W/m}^2/\text{s}$ .

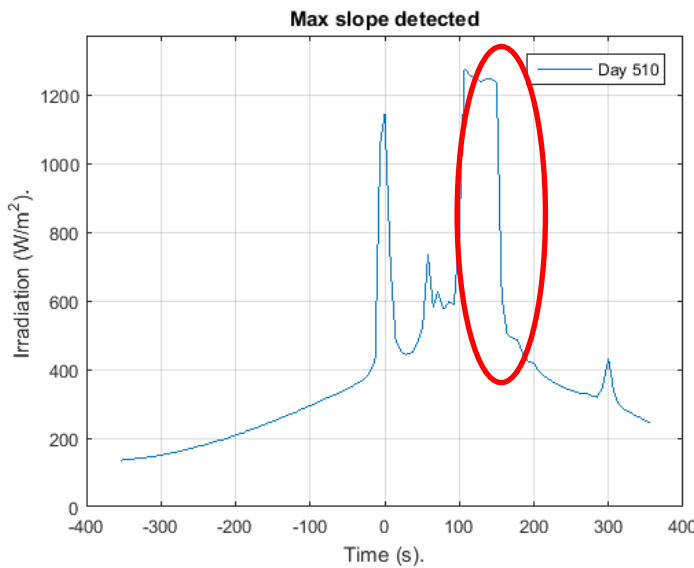


Figure 5.10 Maximum detected slope in dataset 2. Red circle: Detected slope.

The maximum  $d(\text{Irr})/dt$  as a function of wind speed and direction is shown in figure 5.11 (left). The occurrence maps in figure 5.11 (right) illustrate that the wind direction is dominantly in the interval  $270^\circ\text{-}100^\circ$ . The average  $d(\text{Irr})/dt$  in that direction/speed combination is in the order of  $8\text{-}15 \text{ W/m}^2/\text{s}$ .

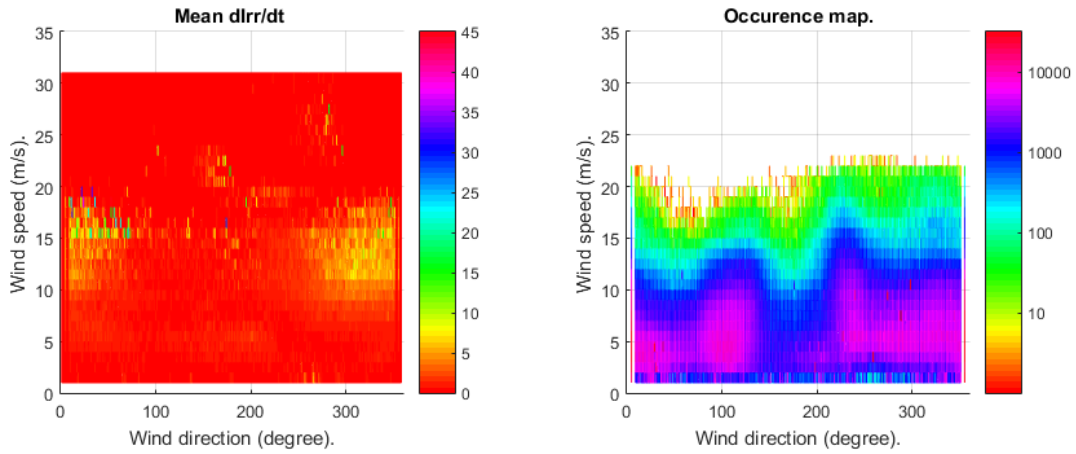


Figure 5.11 Occurrence map from data set 2. One year of data from the SDU Alsion test plan. Left: Mean recorded  $dIrr/dt$  as a function of recorded wind speed and direction. Right: Occurrence of wind speed as a function of wind direction and change in irradiation level.

It can be observed that the measured wind speed slightly above ground level is dominant in the range of 10-20 m/s, equivalent to a worst case SOG in the order of 30-60 m/s, based on the estimated cloud height of 500 m altitude. The calculated perturbation amplitudes (slopes) and durations of the irradiance data are shown in figure 5.12

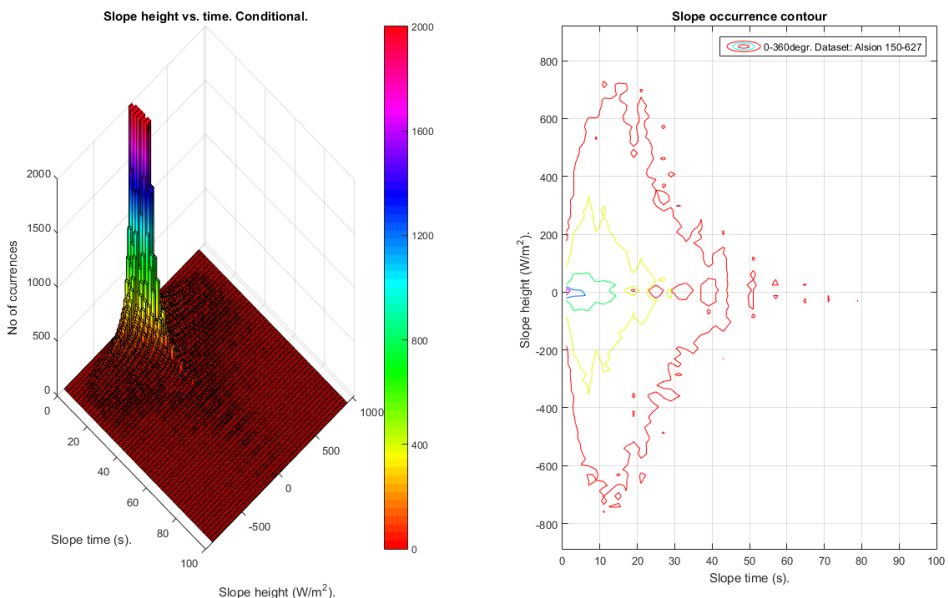


Figure 5.12 Contour maps of data set 1: SDU Alsion test data vs. slope time and slope height. Left: Slope time vs. slope height. Right: Slope time vs. slope time vs occurrence.

It can be observed that the slopes are mainly in the interval  $\pm 75 \text{ W/m}^2$  and the duration is typically  $< 12$  sec. The dominating slopes are again centred at  $\pm 75 \text{ W/m}^2$  within 10 seconds. Larger slopes have been observed, but occur very rarely, as can be seen in figure 5.13, showing a polar plot of the slope length vs. wind direction.

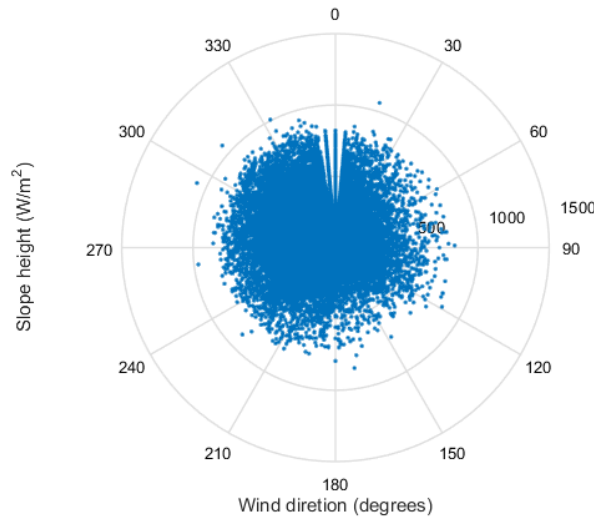


Figure 5.13 Polar plot of the recorded slope height vs. apparent wind direction.

The dominant SOG wind speed  $v_{SOG}$  for the  $\pm 100 \text{ W/m}^2$  slope interval occurs in the interval 0-30 m/s. The slope length  $L_s$  of passing shadow  $s$  can be estimated by eq. 5.1.

The distribution of the calculated slope length  $L_s$  is illustrated in figure 5.14. It can be observed that a few slope lengths above 500 m have been identified but the dominant slope lengths are in the range below 75 m.

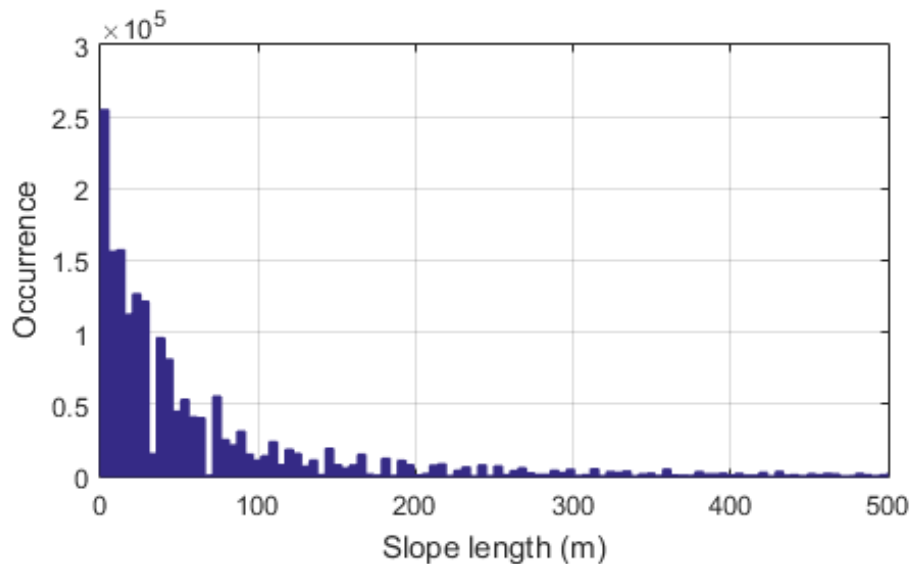


Figure 5.14 Histogram of calculated slope lengths for data set 2 up to 500 m. The 10% level is 80 m.

### Data set 3: Danfoss Solar Park (one year)

The 1 year irradiation data from the Danfoss Solar Park are analysed as in the previous section. The sampled irradiation data are analysed with respect to apparent wind speed/direction, irradiation distribution, the size and timing of variation, wind speed, and wind angle. The irradiation statistics are shown in figure 5.15.

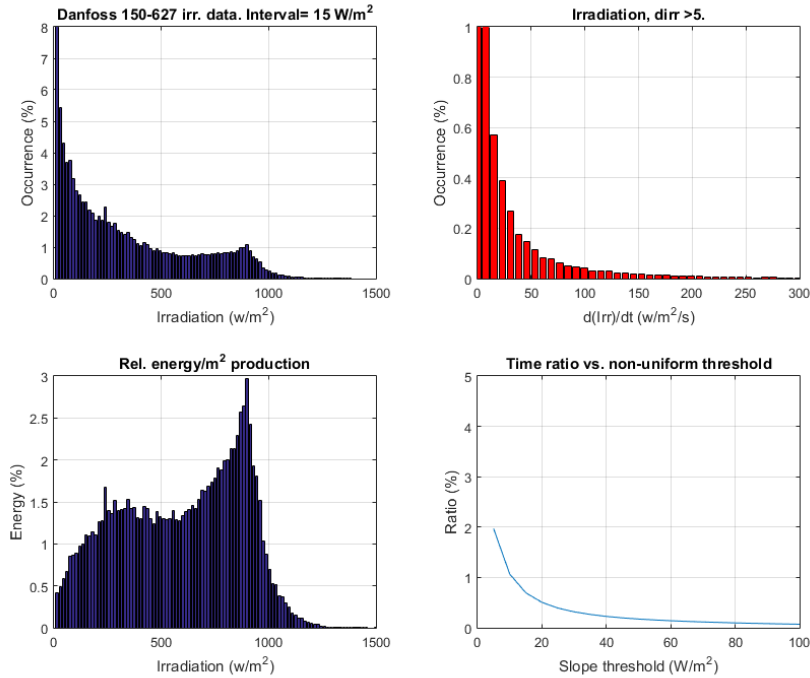


Figure 5.15 Danfoss Solar Park irradiation data for data set 3. Top left: Distribution of irradiation. Top right: Distribution of change of irradiation  $> 5 \text{ W/m}^2/\text{s}$ . Bottom left: Received energy/ $\text{m}^2$  as a function of irradiation level, Bottom right: non-uniform ratio as a function of slope threshold value.

It can be observed that the measured irradiation level is distributed mainly below  $800 \text{ W/m}^2$  (figure 5.15 right, however with a more clear peak around  $80 \text{ W/m}^2$ ), and that the rate of change  $d(\text{Irr})/dt > 5 \text{ W/m}^2/\text{s}$  is below 1% for all value-segments, accumulating to approximately 2% (figure 5.15 left), meaning that for 98% of the recordings the non-uniformity stays below  $6 \text{ W/m}^2/\text{s}$ . The highest continuous slope in the dataset is shown in figure 5.16, rising from  $500 \text{ W/m}^2$  to  $1300 \text{ W/m}^2$ .

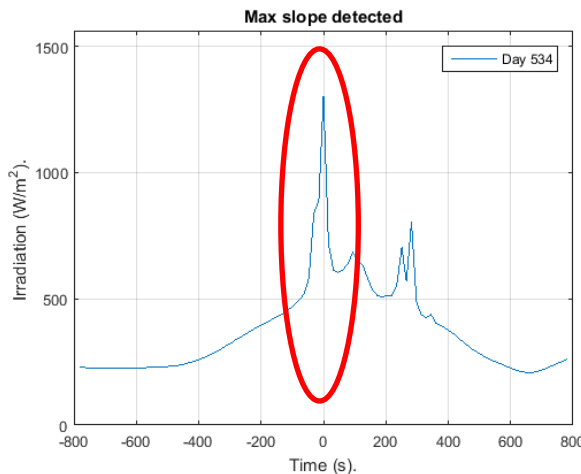


Figure 5.16 Maximum detected slope in dataset 3. Red circle: Detected slope.

The measured wind speed 6 m above ground level is dominant in the range of 5-15 m/s, equivalent to a worst case SOG in the order of 15-45 m/s. The result is shown in figure 5.17.

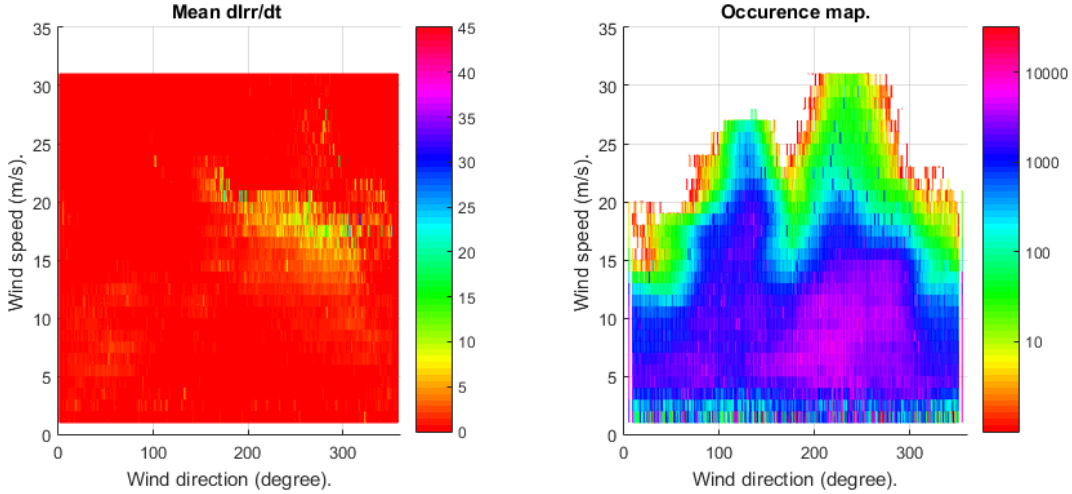


Figure 5.17 Occurrence map from data set 3. One year of data from the Danfoss Solar Park. Left: Mean recorded  $dIrr/dt$  as a function of recorded wind speed and direction. Right: Occurrence of wind speed as a function of wind direction and change in irradiation level.

It can be observed that the measured wind speed dominant in the range of 15-22 m/s, equivalent to a worst case SOG in the order of 45-64 m/s, based on the estimated cloud height of 500 m altitude. The calculated perturbation amplitudes (slopes) and durations of the irradiance data are shown in figure 5.18

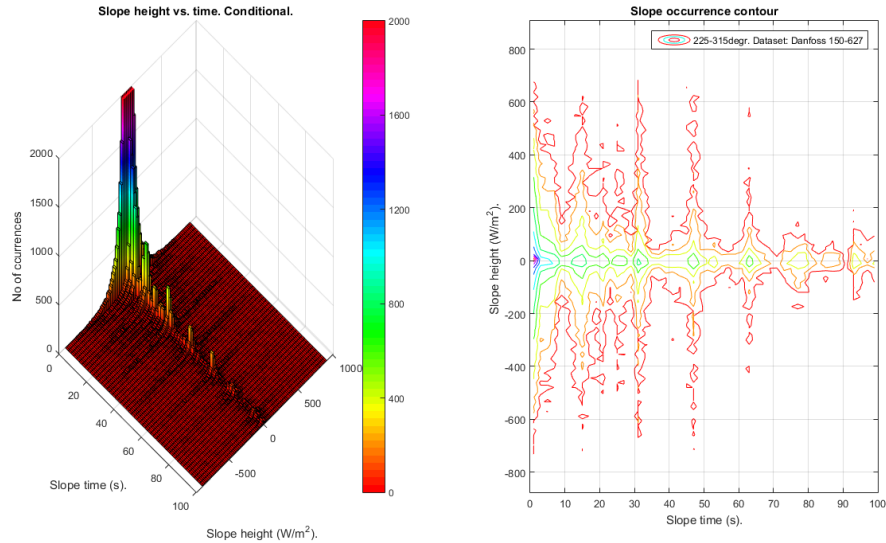


Figure 5.18 Contour maps of data set 3: SDU Alsion test data vs. slope time and slope height. Left: Slope time vs. slope height. Right: Slope time vs. slope time vs occurrence.

The slopes are mainly in the interval  $\pm 100 \text{ W/m}^2$  and the duration is typically  $< 12 \text{ sec}$ . The dominating slopes are centred around  $\pm 50 \text{ W/m}^2$  within 12 seconds. The periodic structure visible at very low levels and around  $0 \text{ W/m}^2$  is believed to be caused by irregular sampling during some day and has no effect on the analysis. Larger slopes have been observed, but also occur very rarely, as can be seen in figure 5.19, showing a poplar plot of the slope length vs. wind direction.

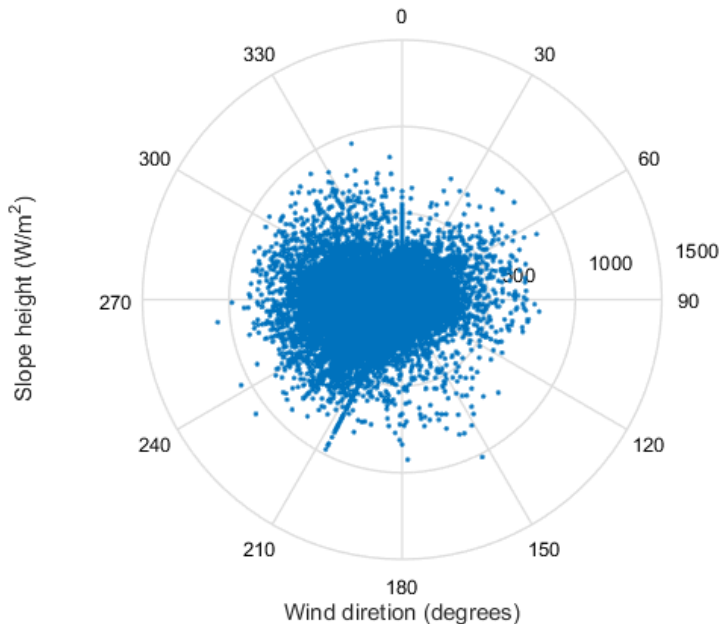


Figure 5.19 Polar plot of the recorded slope height vs. apparent wind direction.

The dominant SOG wind speed  $v_{SOG}$  for the  $\pm 100 \text{ W/m}^2$  slope interval occurs in the interval 0-30 m/s. The slope length  $L_s$  of passing shadow  $s$  can be estimated by eq. 5.1.

The distribution of the calculated slope length  $L_s$  is illustrated in figure 5.20. It can be observed that a few slope lengths above 500 m have been identified but the dominant slope lengths are in the range below 70 m.

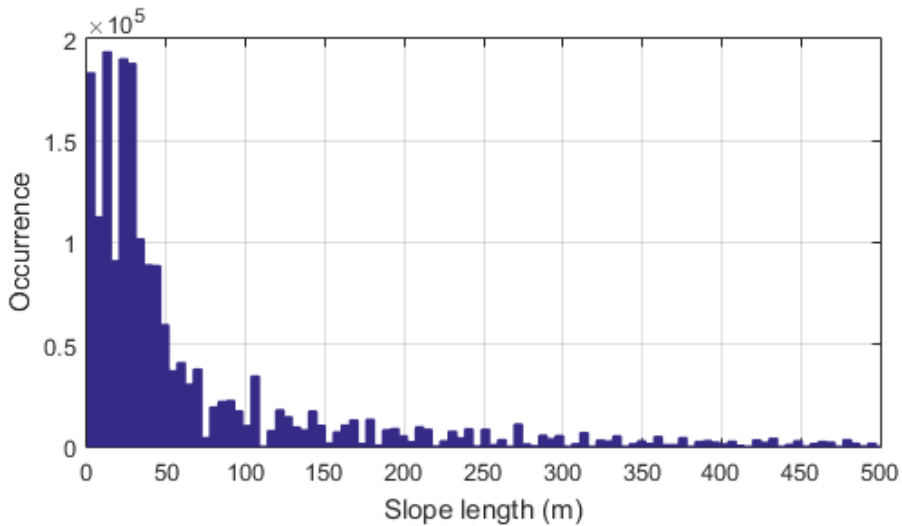


Figure 5.20 Histogram of calculated slope lengths for data set 3 up to 500 m. The 10% level is 70 m.

### 5.2.2 Conclusion on timing analysis

The varying irradiation conditions for a PV plant in Denmark are expected to have the dominant characteristics listed in table 5.2, which is based on the data sets analysed and the correction of the measured wind speed by the worst case wind speed factor Q. For the SOG range of 4-12 m/s  $\Delta t_{max}$  for L=150m be in the range of 13-40 seconds. It is thus anticipated that the dominant delays occurring in a 1 MW PV plant is in the range of 10-40 seconds.

Table 5.2 Dominant values

Parameter	Data set 1	Data set 2	Data set 3
Time period	Oct. 2013-Febr. 2014	Sept. 2014-Sept. 2015	Sept. 2014-Sept. 2015
Dominant change in irradiation during passage	-100 to 100W/m <sup>2</sup>	-70 to 70W/m <sup>2</sup>	-50 to 50W/m <sup>2</sup>
Length of shadow front passing (10%)	< 100 m	<75m	<70m
Dominant cloud direction (°)	[300-100, 230-250]	[270-100]	[180-300]
Dominant cloud speed	12-36 m/s	30-60 m/s	15-45 m/s
Non-uniform condition period	3.3%	2.4%	2.0%

The higher non-uniform condition period for data set 1 is caused by the length of the analysed time period, as the cloud cover for October-February is higher than the annual average. The data sets 2 and 3 have approximately the same non-uniform condition time over a one year period, which was expected as the distance between the locations is only 22 km. The percentages for non-uniformity are comparable to the data from long-term measurements (180 days) in Southern Finland, reaching up to 7% non-uniformity [44].

On the basis of the available measurement data obtained over one year of monitoring two PV plants in Southern Denmark it must be concluded that non-uniform irradiation conditions cloud induced partial shading from clouds are likely to take place **< 4 % of the time of operation of the plants**. This confirms the initial analysis in chapter 3, indicating that partial shading is expected to have a low effect on the differences on annual energy production between string based systems and central inverter based systems. The difference is estimated to be around/below the detection limit of certified energy meters for consumer applications [95].

Extended irradiation plots are presented in appendix [A9] for all 3 data set. An ongoing activity with the aim of extraction of the speed-over-ground velocity of clouds via a time correlation of inverter power measurements from the outer rim of the Danfoss Solar Park is briefly addressed.

### 5.3 Dynamic panel allocation

Adaptive photovoltaic inverter topologies for dynamical reallocation of PV-panels have been suggested in the literature [96]. Focus has been on the compensation for shadow effects due to obstacles like trees and houses, but in a PV utility plant such obstacles are typically removed and in any case would only affect a small area of the park with negligible impact in the annual energy production [35].

A method for dynamic string allocation was patented by the company SMA Solar Technology AG and in 2002 implemented in their Sunny Boy Multi String inverter series [55]. The Multi-Team concept connects PV-strings in parallel to gain a more favourable operation point on the efficiency curve of the active inverter. A measured gain in the range of 1% was reported for a one-year test period and up to 3.5% for 4<sup>th</sup> Quarter 2002 at a test site in Dimbach/Germany [55]. However, the influence of the threshold/switching level on the gain was not published. The possible gain to be obtained from applying the concept in northern countries with fast changing weather conditions is not known. The Team-concept was applied at a time where an inverter efficiency of 95% was considered being good, where today 97-98% are common values (table 1.1) and the effect of applying the technique to the new generations of inverters is anticipated to be lower.

#### 5.3.1 Inverter efficiency

The efficiency curve of a given inverter is the parameter of key importance regarding dynamic panel allocation. The efficiency parameter of a PV-inverter is often used for marketing purposes as

a major sales parameter and the parameter stated can be either a peak efficiency (at a given power level and voltage) or a weighted parameter obtained by applying specific weighting functions, being defined by the European Commission (EC) and the Californian Energy Commission (CEC) for measurement of overall inverter efficiency. Both procedures use a weighted ratio between efficiencies at specified power levels, relative to the nominal power, see eq. 5.2-5.3 [20].

$$h_{EC} = 0.03h_{5\%} + 0.06h_{10\%} + 0.13h_{20\%} + 0.1h_{30\%} + 0.48h_{50\%} + 0.2h_{100\%} \quad (5.2)$$

$$h_{CEC} = 0.04h_{10\%} + 0.05h_{20\%} + 0.12h_{30\%} + 0.21h_{50\%} + 0.53h_{75\%} + 0.05h_{100\%} \quad (5.3)$$

Mathematical models for the modelling of the characteristics of PV inverters are known from the literature. A quadratic function of the form shown in eq. 5.4 provides according to [69,97] a good fit for empirical data.

$$P_{loss} = a_0 + a_1 \cdot P_{out} + a_2 \cdot P_{out}^2 \quad (5.4)$$

The physical meaning of the 3 terms can to a certain level be understood as “self-consumption” ( $a_0$ ),  $a_1$ : losses proportional to  $I_{out}$  as  $V_{out}$  is fairly constant ( $a_1$ ) and ohmic losses proportional to  $I_{out}^2$  ( $a_2$ ). The efficiency is then calculated as

$$n = \frac{P_{out}}{P_{out} + P_{loss}} \quad (5.5)$$

Each  $a_i$  coefficient can be expanded to include a quadratic function of voltage

$$a_i = a_{i,0} + a_{i,1} \cdot V_{in} + a_{i,2} \cdot V_{in}^2 \quad (5.6)$$

That model however is not practical to implement (having 9 parameters) and other models have been developed to accommodate the wish for applying partial information and progressively improving the model [97].

For this study it was not possible to obtain such detailed inverter information to be published from any PV-inverter manufacturers contacted. Detailed information about the efficiency of an inverter vs. the power level ( $P_{rel}$ ) and the string voltage ( $V_{string}$ ) transfer matrix are considered internal (classified) information by inverter manufacturers and are in general not available for public access.

Inverter data published by a technical magazine [98] were used to generate an efficiency transfer matrix  $\bar{n}$ , including both power level and string voltage as input variables (eq. 5.7). The matrix  $\bar{n}$  is to be considered as representing a general 3-phase inverter in the 10-15 kW range. See figure 5.21.

$$\bar{n} = f(P_{rel}, V_{string}) \quad (5.7)$$

A transfer matrix  $\bar{n}$  has been obtained by 2D-interpolation of a mesh of points manually obtained and stored in a lookup table, compared to much slower direct 2D-interpolation.

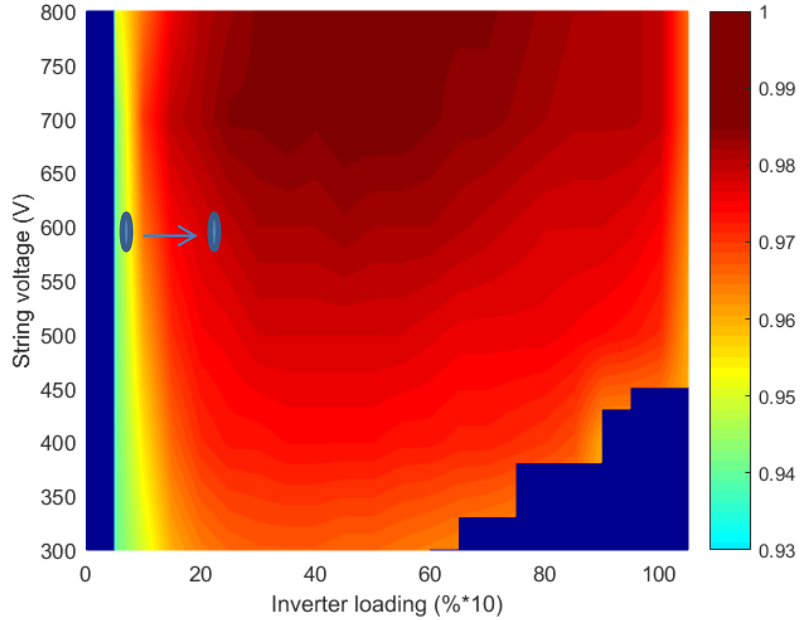


Figure 5.21 Efficiency of a generalized 3-phase inverter in the 10-15 kW range (TLX15KPro inverter, based on [98]). The implemented transfer matrix is a function of string voltage and inverter load, down to 300V string voltage. The arrow indicate shift in operating point.

The change in operation point is marked with the arrow, showing a change from 10% inverter loading to 20% inverter loading during a change in operation point, increasing the conversion efficiency.

### 5.3.2 Case studies

2 case studies with 3 data sets were performed, using the following data sets as input data for the simulation of the potential gain via dynamic string allocation:

1. Normal solar year 2002 from Denmark (1 minute resolution)
  2. Data set 1: One year of high temporal DC power level recordings from a PV-string at SDU Alsion PV plant
- Data set 2: one year of high temporal DC power level recordings from a string at Danfoss Solar Park

#### 5.3.2.1 Case study1. Danish normal year

The case study no. 1 used data for a Danish normal year. The 2002 normal solar year was recorded by the Danish Metrological Institute (DMI) and contained information about diffuse light level, normal light level and the Sun azimuth and elevation with 1 minute resolution. The power level on a PV string was estimated by calculating the plane-of-array (POA) irradiation level for a simulated PV plant of 20x230W panels. This analysis has been published and showed an annual potential energy gain in the order of 1.1% when applying one minute switching to a system containing 3 string inverter input in parallel; see appendix [A1].

#### 5.3.2.2 Case study 2&3: Danfoss Solar Park and Alsion PV plant one year data

The concept of dynamic switching has been tested on a set of DC input power data from data set 2 and 3, covering one year of power production from a PV-string from the SDU Alsion PV plant and Danfoss Solar Park.

A one second response to the DC power level data from test inverter 9 as a function of switching threshold / inverter loading has been simulated after the same concept as described in appendix [A1]. The calculated annual maximum gain under ideal switching conditions (no loss in the switching circuit and no delay in the MPPT circuit) are shown in figure 5.22 as a function of inverter switching threshold level, together with the seasonal dependency of the maximum gain. 3 inverters have been combined in this study.

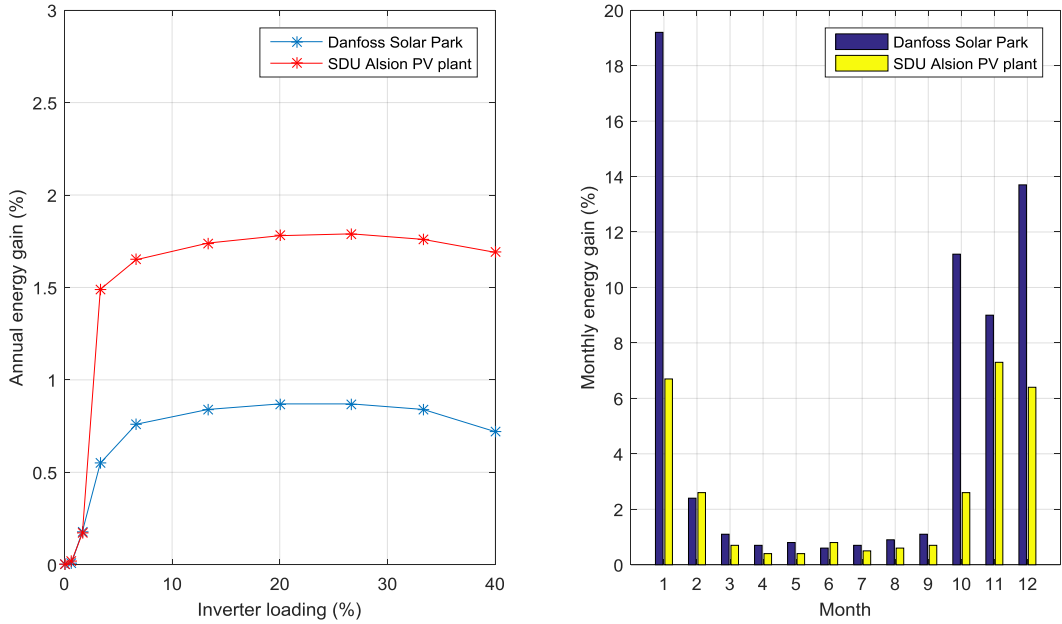


Figure 5.22 Estimated annual maximum energy gain for two PV sites. Left: Gain after approximately one year of operation as a function of inverter threshold level in % of full load. Right: Monthly gain for the two PV sites investigated.

It can be observed that the annual energy gain has a maximum of approximately 0.9% at a threshold around 30% for the Danfoss Solar Plant and approximately 1.8% for the Alsion PV plant. The seasonal variation of the irradiance generate a comparably strong gain over the winter months, due to the low irradiance level / energy production.

The gain at the SDU Alsion PV plant is higher than for the Danfoss Solar Park, as the average irradiance level is lower due to the orientation of the panels (Danfoss Solar Park oriented 3° from South, SDU Alsion PV plant facing 45° from South (see appendix [A8])).

The annual effect of applying the switching scheme to multiple inverters is illustrated in figure 5.23 for the Danfoss Solar Park, where the effect of a full year of operation with data set 3 is shown.

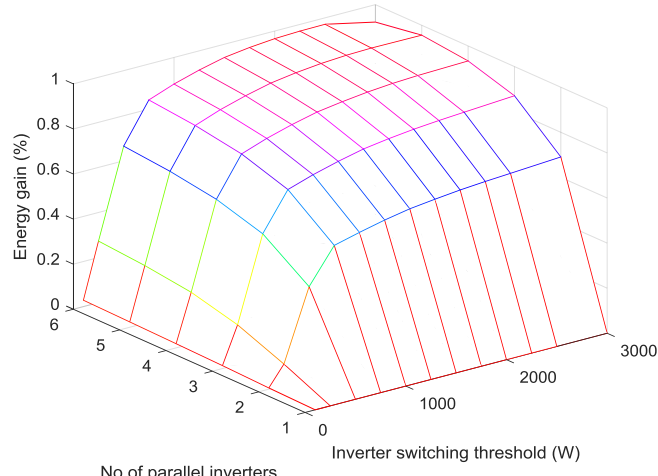


Figure 5.23 Simulation of theoretical gain by paralleling of inverters strings as a function of parallel string units (1-6 shown) and inverter switching threshold for a 5kW inverter unit.

### 5.3.3 Conclusion on case studies

The analysis showed that the maximum gain to be obtained over a full year of operation is below 1% and that the highest increase in gain (from 0% to 0.6%) is obtained when switching two inverters in parallel at a threshold level above 750 W for the type of inverter simulated. Increasing the number of inverters only increases the gain by 0.1-0.2% for up to 20 strings in parallel. More inverters in parallel will generate more energy during low light conditions, but the effect on the annual gain is very low. The above results are obtained with real string power values, but under ideal conditions meaning no switching loss, indicating that the effective gain is lower and on the same level / below the effect coming from the sorting of panels.

## 5.4 Topography analysis

The tilt of individual panel in a PV plant has been obtained by extraction from surveying CAD data and via the measurement by an inclinometer for the 5 first rows. Both methods have been applied here, as surveying data were not available for row 1-5, see figure 5.24. The maximum horizontal tilt variation for the analysed rows is shown in table 1. The calculated and measured horizontal tilt for row 21 are shown in figure 5.24 (left) together with the elevation above sea level (right).

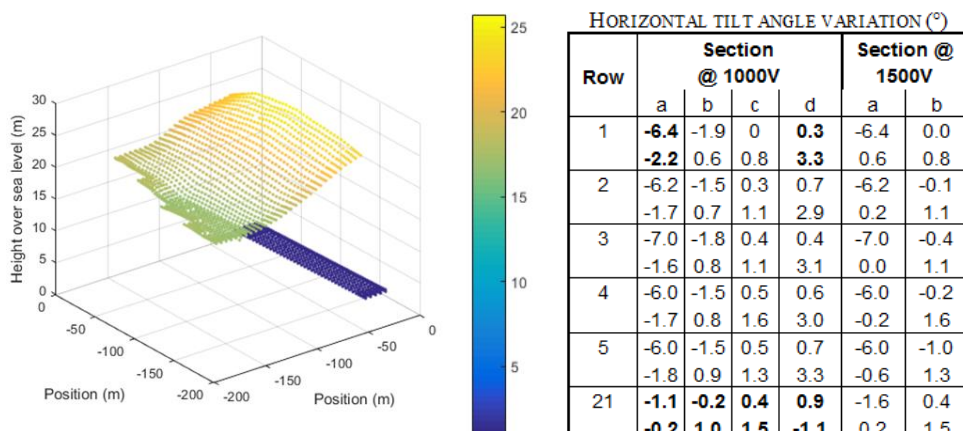


Figure 5.24 Left: Plant topography, obtained from surveying data. Right: The table shows angular variations in selected rows with high horizontal tilt angle variations for the present 1000V layout and a potential future 1500V layout. The values for row 1-5 are obtained manually.

The tilt angles and absolute height over sea-level for the panels in row 21 are shown in figure 5.25. A clear position dependent tilt of the pans is visible.

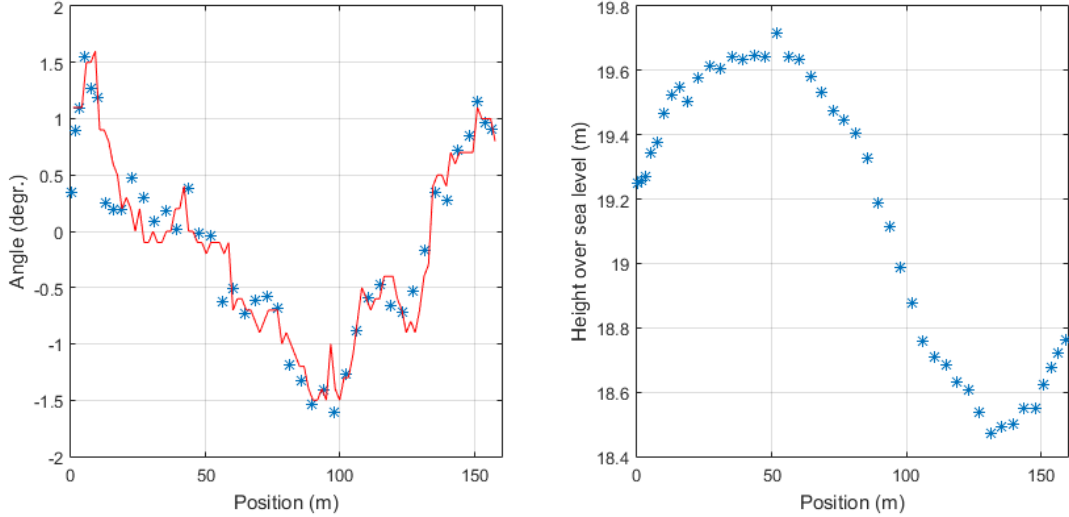


Figure 5.25 Left: Comparison of tilt angle measurements (\*) and calculation from CAD data (-) for row 21, section a. Right: Height variation over test row 21.

### 5.4.1 Irradiation model

The irradiation model is in detail described in appendix [A1] and [A6]. The model is based on the calculation of the angular position of the Sun at any given time and its effect on a curved string of 24 panels. Each panel with varying angular orientation to the Sun will receive different irradiation levels.

It can further be shown that the direct sunlight irradiation on the surface of solar panel  $x$  can be expressed as

$$I_{surface,x}(t) = I_{direct}[\cos(h(t)) \sin(\beta) \cos(\psi_x - \theta(t)) + \sin(h(t)) \cos(\beta)] \quad (5.8)$$

where  $h$ =solar elevation angle,  $\Theta$ =solar azimuth angle,  $\beta$ =panel elevation,  $\psi_x$ =panel azimuth for panel  $x$  ) [99].

The irradiation  $I_{direct}$  is calculated by introducing the elevation dependent air mass (AM).

$$I_{direct} = 1.353 (0.7^{AM(h)^{0.678}}) \quad (\text{kW/m}^2) \quad (5.9)$$

The air mass (AM) is as in section 4.2.1 estimated via an interpolative function as a function of the solar elevation angle  $h$  [91].

$$AM \approx \frac{1}{\sin(h + \frac{244}{165+47h^{1.1}})} \quad (5.10)$$

The panel elevation angle  $\beta$  is held constant, but each panel on a hilly surface has its own horizontal tilt angle  $\psi_x$ , where  $x$  identifies the individual panel. For each time  $t$  the irradiation (and thus the generated DC current  $I_x(t)$ ) for each of the panels in a string is calculated, forming a current vector  $\bar{I}_{panel}(t)$ . The effective string current  $I_{string}$  is determined by the minimum current of any of the panels in the string.

$$I_{string}(t) \approx \min(\bar{I}_{panel}(t)) \quad (5.11)$$

The generated string power  $P_{string}(t)$  is calculated via the IV-characteristic of the panel, giving the panel voltage  $V_x(t)$  at current  $I_x(t)$ .

### 5.4.2 Comparison of model and measurements

The simulated response of the 24 panel strings in section *a* of row 1 for the very sunny day of July 29 2014 is shown in figure 5.26 (green markers), together with the measured ratios for the same day between row 1 and row 21.

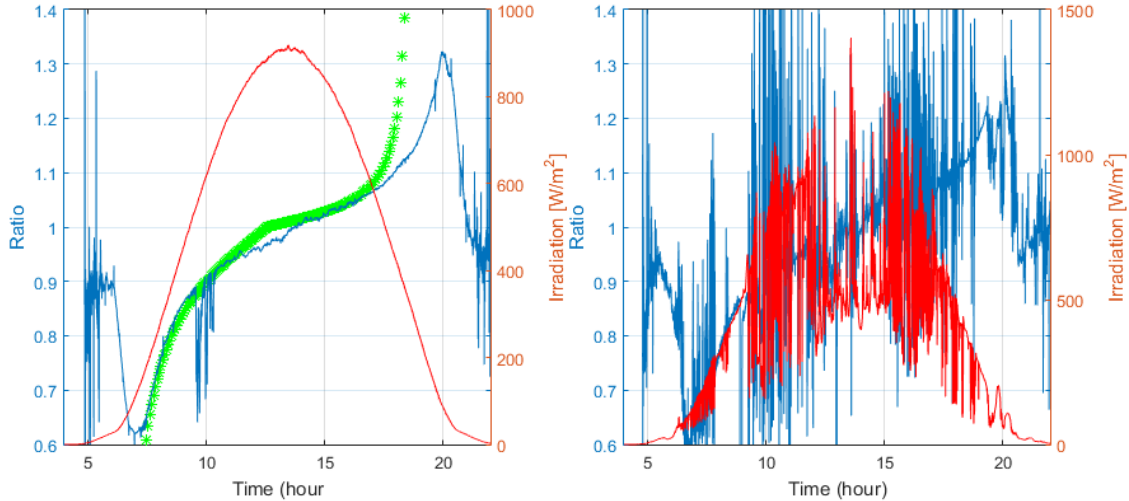


Figure 5.26 Irradiation level and ratio in power production between a curved segment of row 1 (inverter 11) and the more flat segment row 21 (inverter 9). Left: For a sunny day (July 29, 2014). Green markers: Theory according to eq. 5.8-5.11. Constant 20% diffuse light is assumed. Right: For a cloudy day (July 9, 2014).

The developed theory for the angular dependency of the power production, represented by the green markers, closely follow the measured ratio between a curved row section (row 1a) and an (almost) straight row section (Row 21a) until late afternoon. 20% constant level of diffuse light has been assumed in the simulation. It can also be observed that the trend is visible also for a day with many clouds, as shown on figure 5.26 (right).

The phenomenon is also visible in the more flat test row 21, as illustrated in figure 5.27.

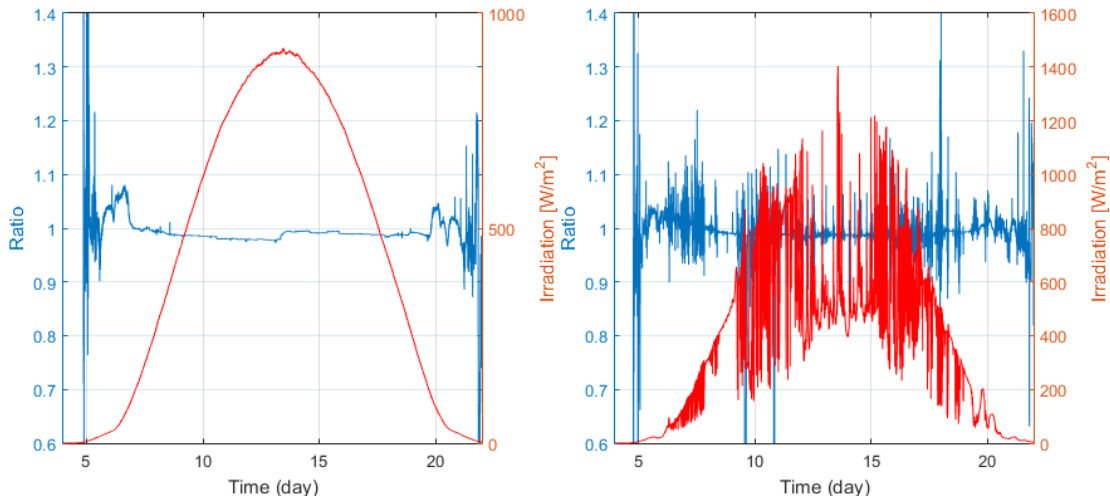


Figure 5.27 Topography induced effect measured on test row 21 for a sunny day (left) and a cloudy day (right), as in figure 5.26. The difference in power produced is shown.

The measured accumulated energy difference for inverter 9 and inverter 10 with all strings included is <0.2% for the investigated sunny day. The induced energy loss due to mismatch loss will be even lower in total, as cloudy days will lower the difference due to the presence of more diffuse light.

During a clear day (left) as well as during a cloudy day (right) the ratio between the test inverters is dependent on the position of the sun. The effect is in power level <1% during a clear day and <0.5% loss during a cloudy day. This variation must be included in the analysis/calibration of the inverter system, see appendix [A8] for details.

It can be observed that the loss in energy during the morning hours is not compensated by the gain in energy during afternoon hour so the accumulated power production by row 1 with a high variation in tilt angle during a sunny day in total is lowered. The energy loss for the clear day analysed is in the range of 2.5%.

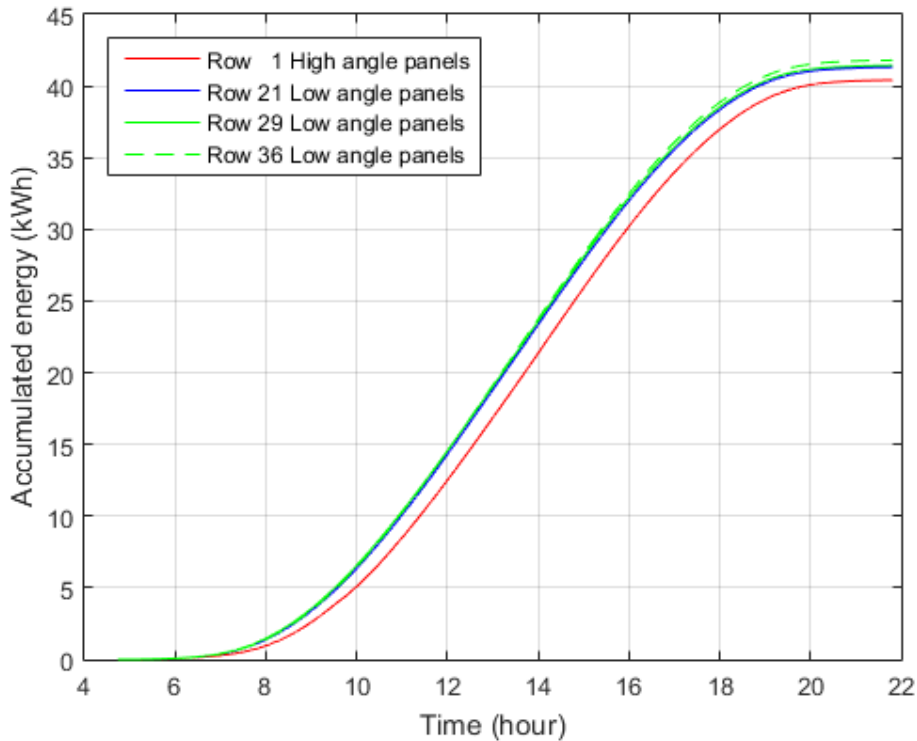


Figure 5.28 The accumulated energy per string from 4 selected inverters.

The topographical effect is further demonstrated in figure 5.29, showing the ratio for row segments with high topographical variation (row 1a) and for the test inverters (row 21a) for 7 days.

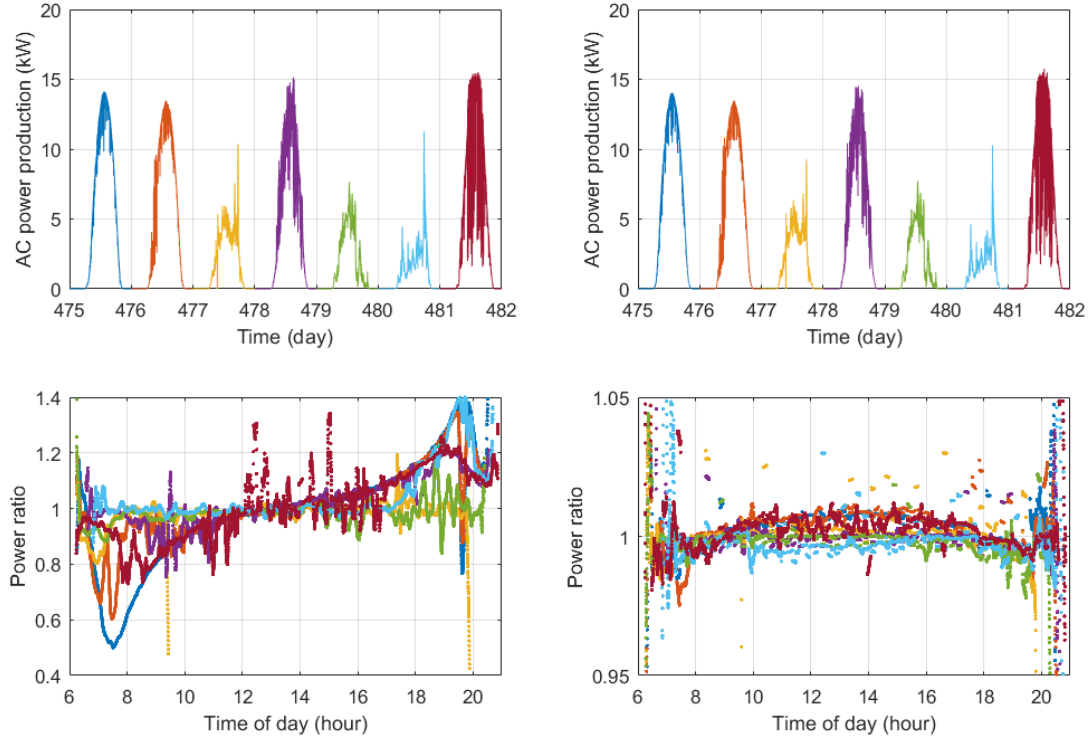


Figure 5.29 Topographical effect for 7 days on the AC production. Left column: Inverter 1 vs. inverter 9. Right column: Inverter 9 (3 MPPT) vs. inverter 10 (1 MPPT), different scaling applied. 1 min. averaging applied.

The topographical effect is clearly visible for the panel section with high angular variation (left column) and it can be observed that the presence of clouds, meaning increased level of diffuse light, lower the effect. For the two test panels with the same topographical variation on the strings the effect is again visible, but at a lower scale.

### 5.4.3 Central 60 kW inverter test

The replacement of several FLX inverters during 2015 replaced with 60 kW MLX central inverters (12 input strings, 1 MPPT) in the Danfoss Solar Park (1 MLX replaces 4 FLX) gave the possibility to study the effect on larger scale. The new layout of a small section in the northeast corner of the park is shown in figure 5.30.



Figure 5.30 Part of the PV plant layout with MLX inverters. Red boxes indicate the location of MLX inverter 1-4, each covering 4 strings in parallel.

The measured DC power for 2 MLX inverters (covering section c-d of row 3-4 and 9-10) and a reference MLX inverter on a flat section (covering section c-d of row 19-20) for a sunny day are shown in figure 5.31 (right). Inverter MLX 8 (not shown) acts as a reference inverter, due to the relative flat curvature of the strings attached. The relative DC power ratio for the MLX inverters

relative to inverter 8, is shown in figure 5.31 (left).

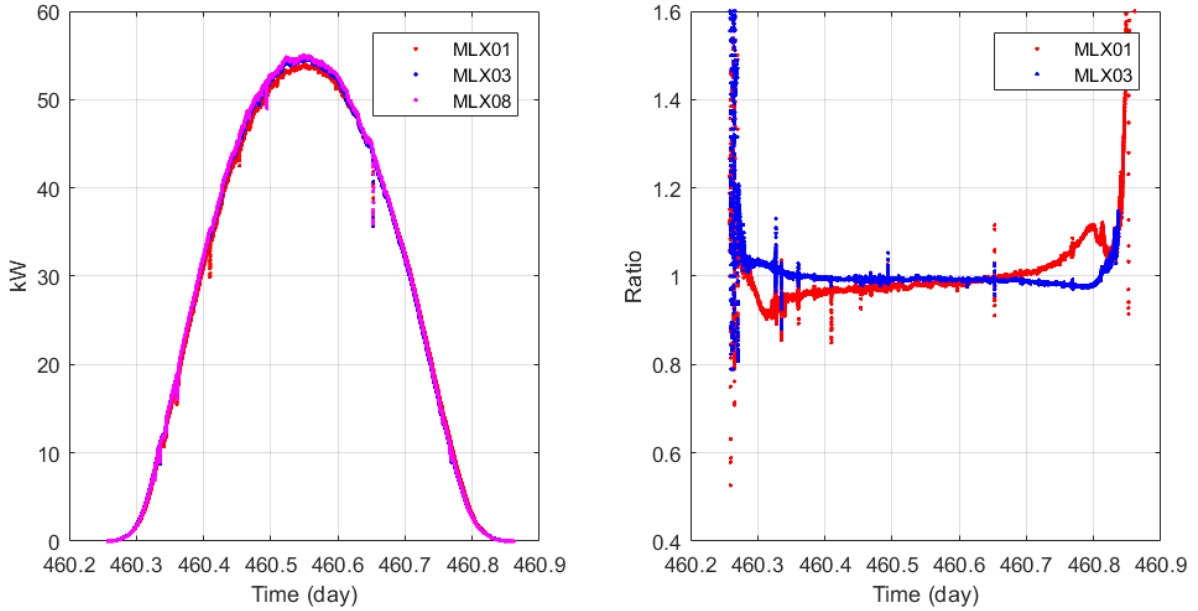


Figure 5.31 Left: MLX inverter DC power levels for April 25, 2015 (day 460). Right: MLX inverter 1-3 DC energy levels relative to MLX 8 reference inverter for the same day.

It can be observed that the ratio is centred around 1 and that a variation of up to 3% (MLX03) and 10% (MLX01) during morning and evening is present. The deviations have different directions as the panel groups have an angular tilt in different direction.

## 5.5 Energy loss estimation

A series of inverters in the Danfoss Solar Plant Row 21 as described in section 5.1 / figure 5.1 have been monitored during a period of one year. The parallel use of the test park as a test area for an inverter manufacturer implies that the recorded energy production for the test inverters are filtered for periods of non-normal use, being service, testing etc.. Only periods where all strings and inverters have been operational under the same conditions are valid for the energy analysis. The internal measurement of accumulated energy inside the inverters could therefore not always be used.

The energy loss is estimated via a comparative analysis of recorded data from 2 inverters:

- an inverter connected to 3 independent strings distributed over 160 m (inverter 9).
- an inverter connected to 3 parallel strings distributed over 160 m (inverter 10).

All string pairs are as far as possible identical regarding panel type, orientation, curvature and environmental influence. Both inverters are of same type (FLX15K).

The minimum  $I_{MPP}$  rating for the panels in each string, obtained from the panel distribution/sorting analysis in appendix [A8], table A8.3, are shown in figure 5.32. It can be observed that the rated current limiting panels in the individual strings have  $I_{MPP}$  values very close to each other.

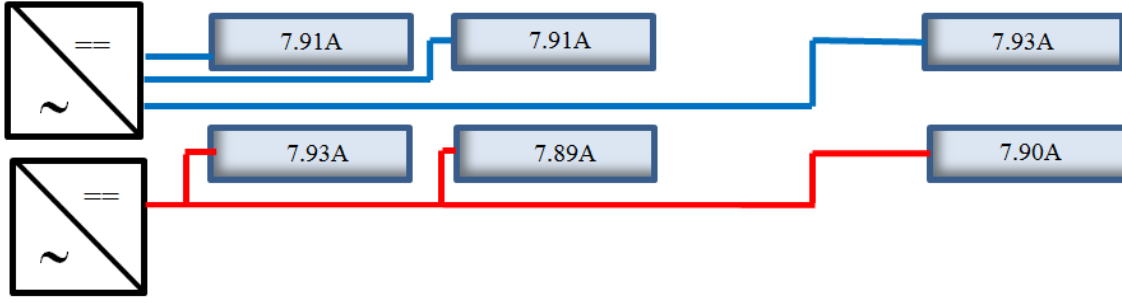


Figure 5.32 Minimum  $I_{MPP}$  in each string. Blue: 3 independent MPPT. Red: 1 MPPT / parallel.

The  $I_{MPP}$  difference between the strings in each section is 0.02A for all 3 sections, equivalent to 0.25%, however these are label-values and do not take into account aging of the panels, neither short term or long term). There will be a difference between the DC level of each inverter, so a DC calibration is needed but this difference will be small. Based in the IMPP is it estimated that the difference will be in the range < 0.5%.

### 5.5.1 Simulation of cloud induced difference in power generation

A simulation platform for the investigation of the effect of shadow front passing over large PV-arrays was developed and published as [A4]. The platform has been used to estimate the effect of a moving sudden increase/decrease in irradiation over a large group consisting of 20 strings of 24 250W PV panels each, equivalent to a 120 kW PV plant. The approach is based on the work presented in [100] and applies the classical single diode model of a solar cell [50]. A simulation of a combined system of string- and central inverter configurations with 10x24 PV-panels showed a difference in the power level during the passage of an increasing irradiation profile from 410 W/m<sup>2</sup> to 840 W/m<sup>2</sup> and back during approximately 50 seconds. The event is illustrated in figure 5.33.

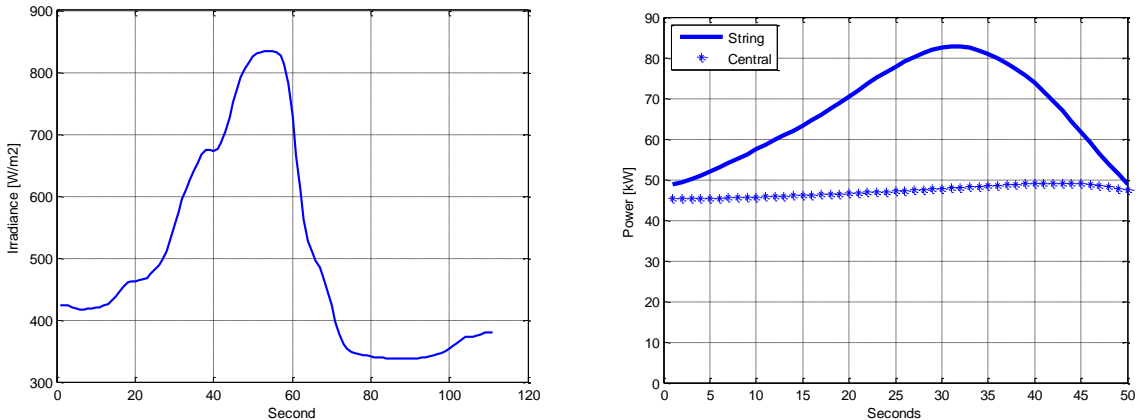


Figure 5.33 Simulation of the effect of a diagonally passing increase in irradiation. Left: Recorded event. Right: Simulated power production for string inverter and central inverter configurations.

The maximum simulated differential energy loss during the 50 seconds of passage is in the order of 25%, comparable to the levels reported by [42] as identified in the State-of-the Art analysis. This shows that even during the passage of shadow fronts with high slopes the energy loss is rather limited.

## 5.5.2 Variation in daily energy production

The differential energy loss  $\Delta E_{DC}$  in the energy production between the two test inverters has been calculated by analysing the DC and the AC energy production per day over the whole test period.

The difference in DC energy production is calculated as

$$\Delta E_{DC} = \sum_a^b \frac{\int (P_{DC,inv9}(t) - P_{DC,inv10}(t)) dt}{\int P_{DC,inv9}(t) dt} \quad (5.1)$$

where

- a = First day of analysis
- b = Last day of analysis
- $P_{DC,inv9}(t)$  = Available DC power of the PV arrays on inverter 9
- $P_{DC,inv10}(t)$  = Available DC power of the PV arrays on inverter 10

A number of constraints were applied to the available data sets.

- A total of 75 days were judged as being of non-operational quality, as disruptive conditions appeared during those days, being service, other tests etc.). Those days were removed from the analysis.
- The DC energy supplied from the PV strings to the inverters was calculated by numerical integration (trapezoidal integration) of the recorded power levels as the inverters do not measure DC energy. The validation of the method is described in appendix [A8] (section A8.4.1.1).
- The DC levels between the inverters were calibrated during a sunny day and the identified difference due to the topology (section 5.4) is compensated. The method is described in appendix [A8] (section A8.4.1.2).
- The AC energy supplied to the power grid from the inverters was recorded via the internal measurement circuit of the inverters, calibrated against external class 0.2% AC energy meters. The method is described in appendix [A8] (section A8.4.1.1).

### 5.5.2.1 Effect on inverter DC power production

The spatial distribution of the PV strings in the test row 21 over 160 m (east-west) was expected to generate temporal dependent losses during the passage of cloud fronts due to the non-uniform irradiation of the different PV strings. This effect has been recorded in the measurement, but the effect is very weak, as described below.

The dynamics of the two inverters is shown in figure 5.34 (top plot 1-2; bottom plot 3-4).

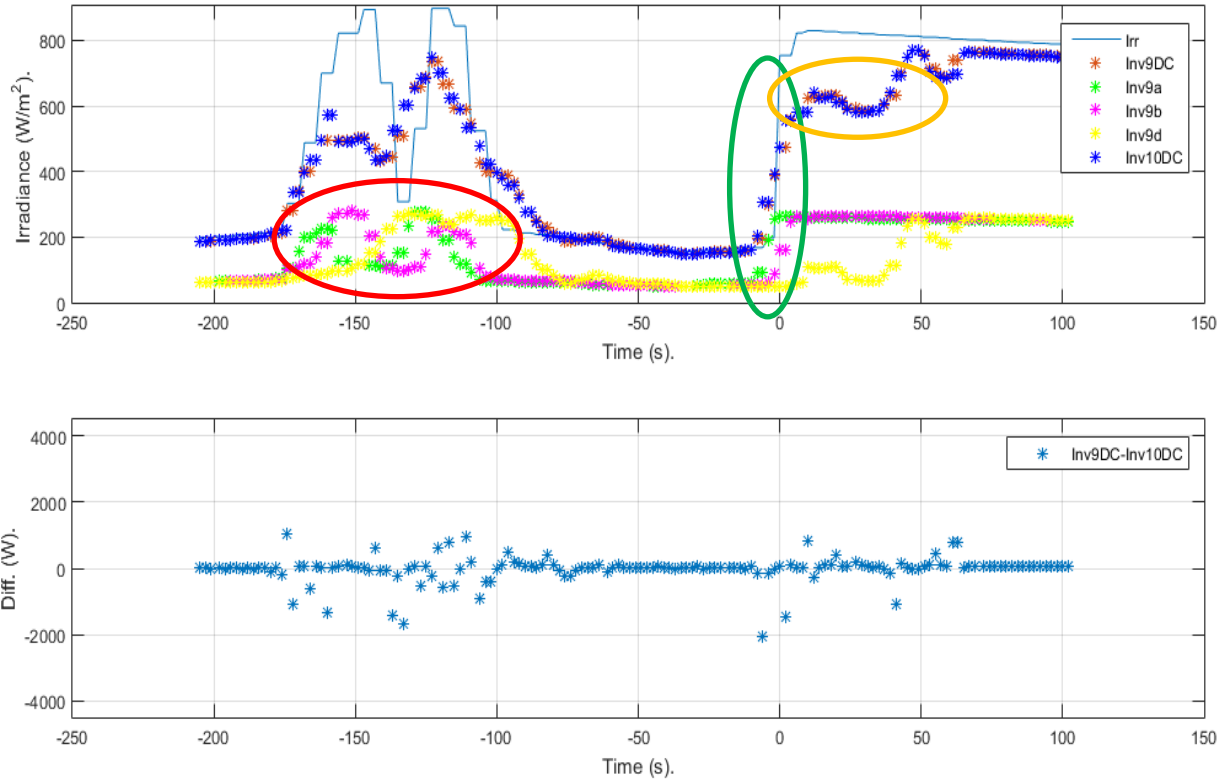
#### Wind from 270° (W):

Inverter no 9 (with 3 independent MPPT) reacts on the approaching intensity increase by independent increase in power generation for each MPPT (red circle). A very fast increase in intensity (green circle) generates only a small delay between section a and b, but section d is almost unaffected for the first 10 seconds.

#### Wind from 215 ° (SSW):

Inverter no 9 (with 3 independent MPPT) reacts not on the approaching small intensity decrease (purple circle) and a small decrease in intensity generates an apparent difference between section a and b/d resulting in a difference of 4 kW for a few seconds.

(1+2):



(3+4):

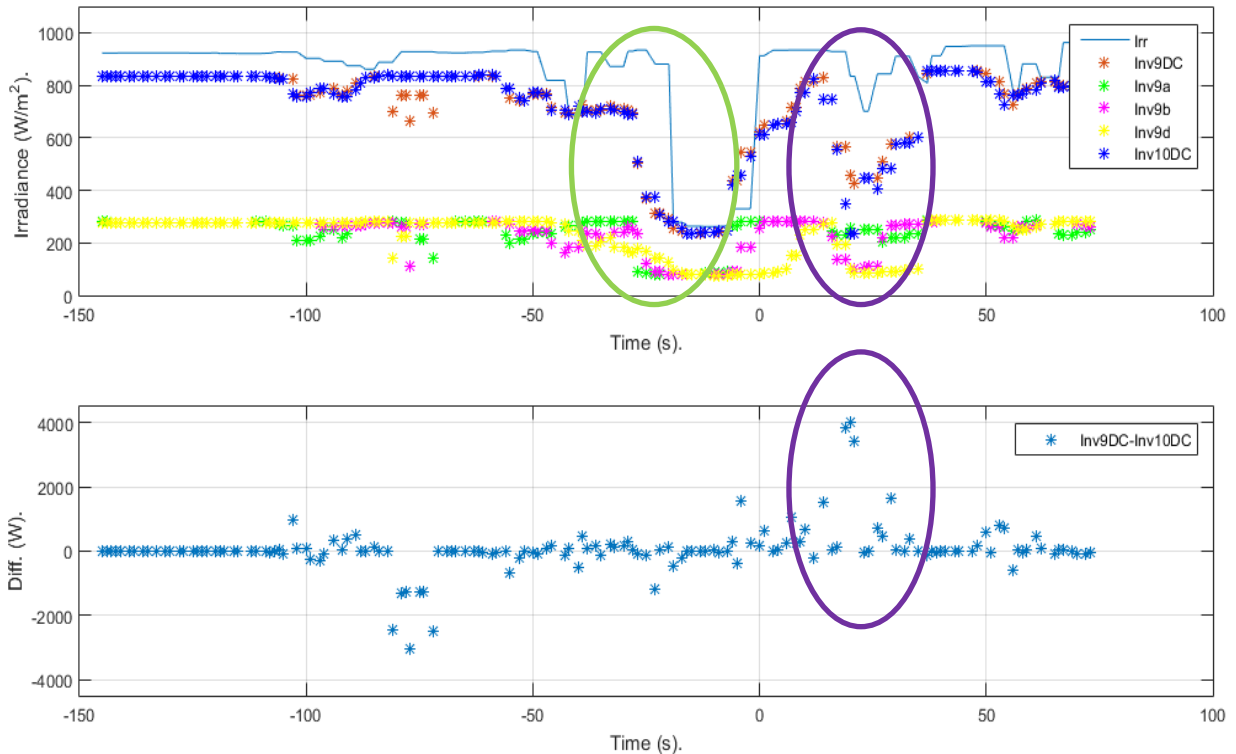


Figure 5.34 Example of slopes detected and the corresponding DC levels and energy differences. Top (1+2): Day 79, Wind direction 270 degrees (West). Bottom (3+4): Day 139, Wind direction 215 degrees (SSW). The inverter values are not to scale in (1+3). Inv9a,b,d indicates the individual strings.

The difference in power production during wind from west between the inverter 9 (with independent MPPT) and inverter 10 (with 1 MPPT) is barely noticeable (orange circle, expanded in figure 5.35). For a shadow front approaching from the south (figure 5.34, bottom 3+4), meaning perpendicular to the direction of the strings, it is observed that all strings react almost simultaneously (light green circle). The small difference indicates that the shadow fronts should not be seen as perfectly straight fronts.

The apparent time lag between the power levels and the irradiance is due to the placement of the irradiance sensor.

An apparent difference in power production during uneven irradiation of the PV strings is observed. The power from section c is lower than the power from section a and b) for the situation shown in figure 5.35 (wind from west). The difference is below 2% and only present for few seconds (circle).

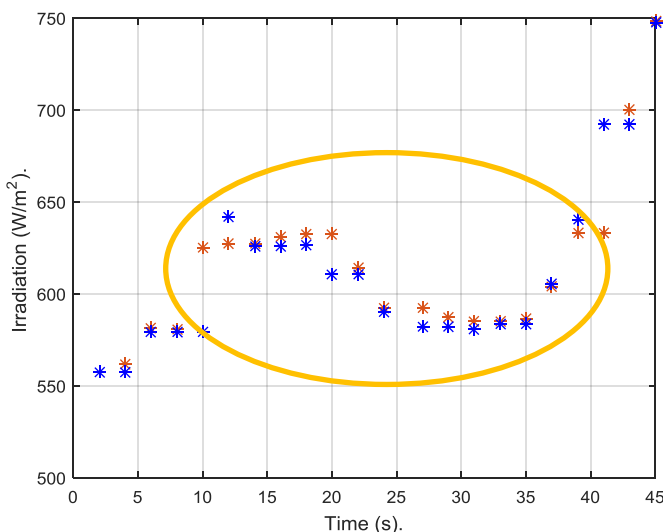


Figure 5.35 Expanded orange circle area of figure 5.34. DC power generated from the two test inverters during uneven irradiation conditions (circle).

The difference in energy production between the two test inverter due to irregular irradiation on the PV strings is very small and with the available test setup difficult to detect.

### 5.5.3 Full year DC level energy analysis

The calculated DC energy produced per day for all monitored days and both test inverters is presented in figure 5.36 (left). The accumulated energy production for the valid days (non-operational days were removed) is shown in figure 5.36 (right).

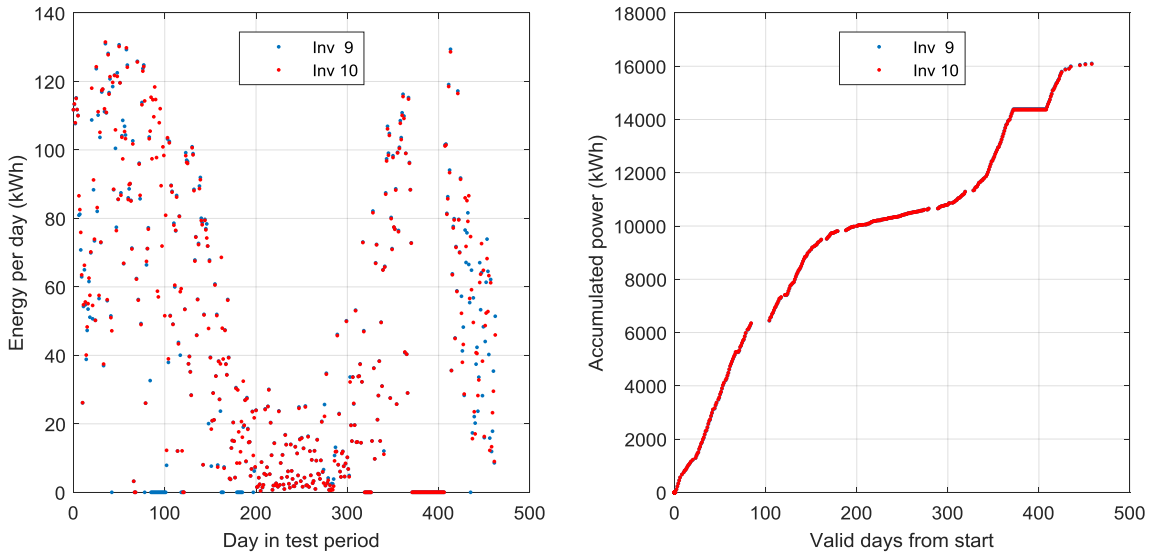


Figure 5.36 Left: Calculated energy production per inverter for all day in the test period for both test inverters. Right: Accumulated energy production for a valid test days (non-operational days are removed).

The calculated differences for each valid day is shown in figure 5.37 (left) together with the accumulated differences in energy production (right). For illustration of the influence of non-operational days was one such day included in the data set, a day where the inverters for test purposes were limited in output power to 1/3 of their normal operating range. The effect due to saturation is marked with a red circle.

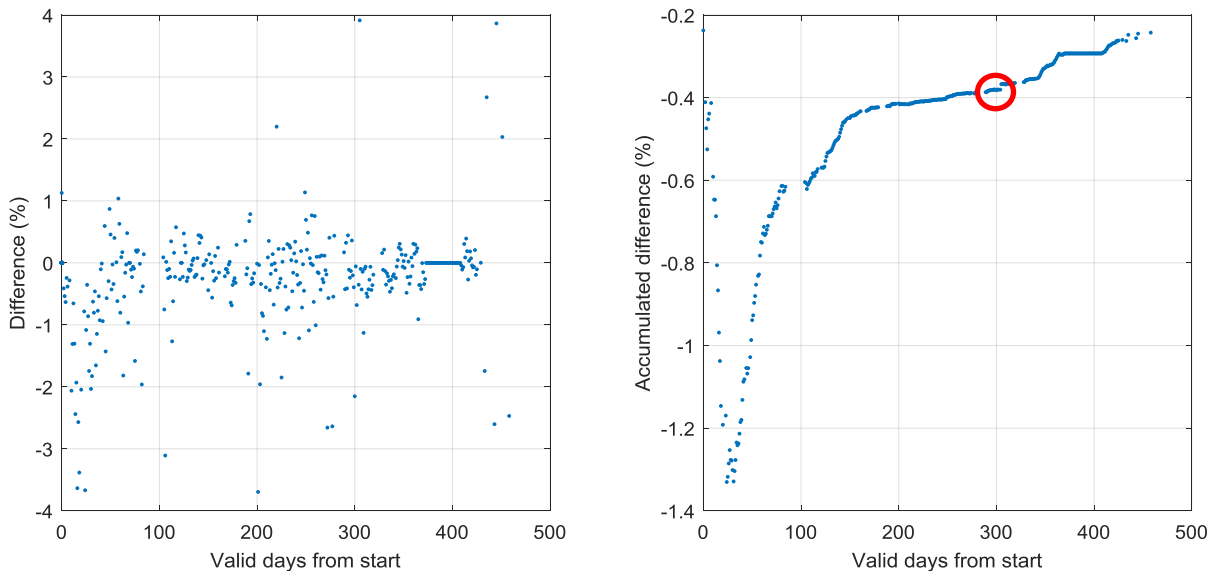


Figure 5.37 DC energy productions. Left: Energy difference for all valid days. Right: Accumulated energy difference. Red circle indicate effect of a non-valid day due to inverter saturation.

A small drift in the accumulated energy difference is noticed in figure 5.37 (right). During start of the test period did the difference increase to -1.3% for then apparently to turn and after more than one year to reach <0.1%. These numbers are obtained with non-calibrated circuitry, where the only calibration made was a relative calibration of the DC side of the inverters during a very clear day. The cause of the small “jump” in the accumulated DC difference visible around day 305 (red circle) is shown in figure 5.38, where the saturation effect is visible and the inverters saturate at different

levels. It can be observed that even this drastic event only changes the accumulated energy production by apparently <0.01% (far below a realistic detection limit). The saturation effect is shown in figure 5.38 (left). Figure 5.38 (right) shows the effect of a fast change in power production for the same day (green circle).

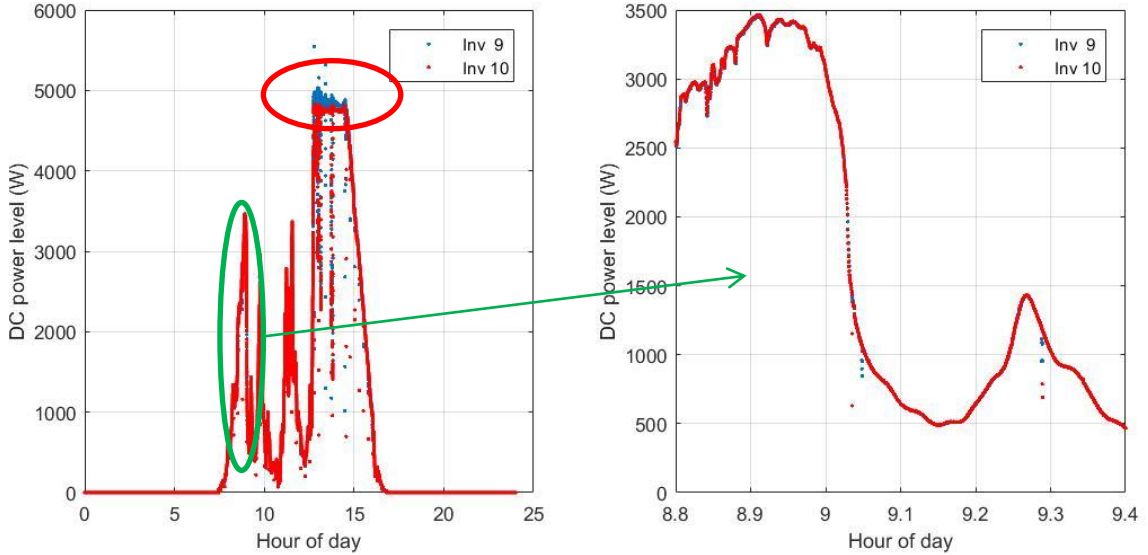


Figure 5.38 Example of a non-operational day, where the inverters for external test reasons were limited in output power. Left: Full day power production; red circle indicate saturation; green circle show fast event. Right: Amplified fast event.

### 5.5.3.1 Weather conditions

The influence of the average weather direction and wind speed on the produced energy difference for each day has been investigated, see figure 5.39.

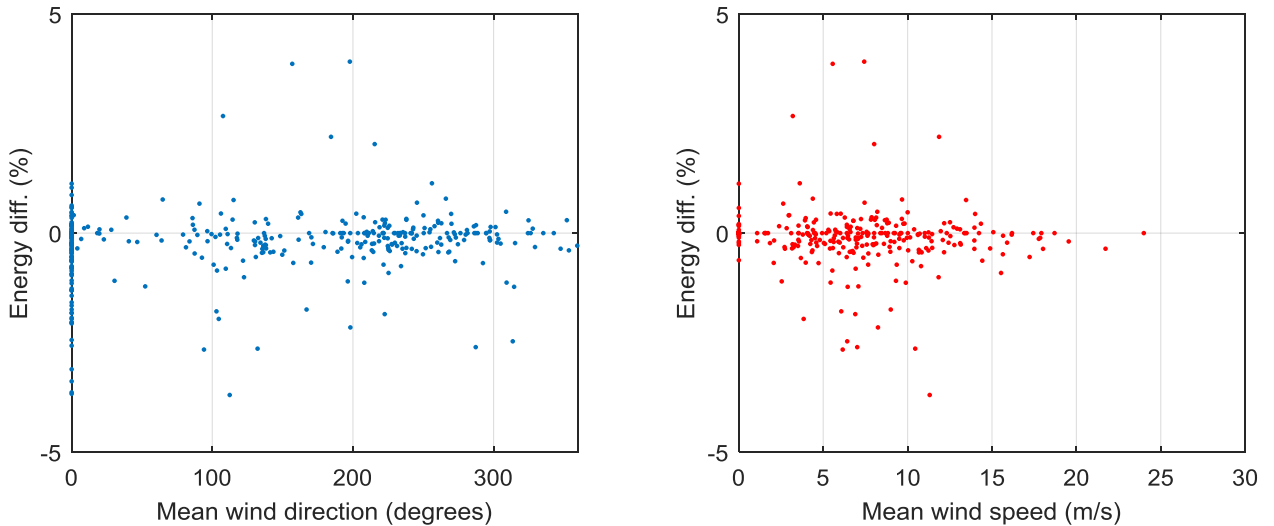


Figure 5.39 Calculated difference in energy production for the two modified test inverters for all days over the test period of approximately one year. Left: Mean wind direction. Right: Mean wind speed from the ground based sensor.

No correlation between the differences in the daily energy production and the weather data can be identified. It must be concluded that the effect of moving clouds on the DC energy production over a period of a year is very low, below the detection limit of this experiment, where a relative calibration between the two test strings were made during a sunny day.

### 5.5.4 Full year AC level energy analysis

The internal AC circuitry of the test inverters have been calibrated against certified energy meters (class 0.2%), as described in appendix [A8]. The resulting AC energy differences and the accumulated energy differences for the valid days are shown in figure 5.40.

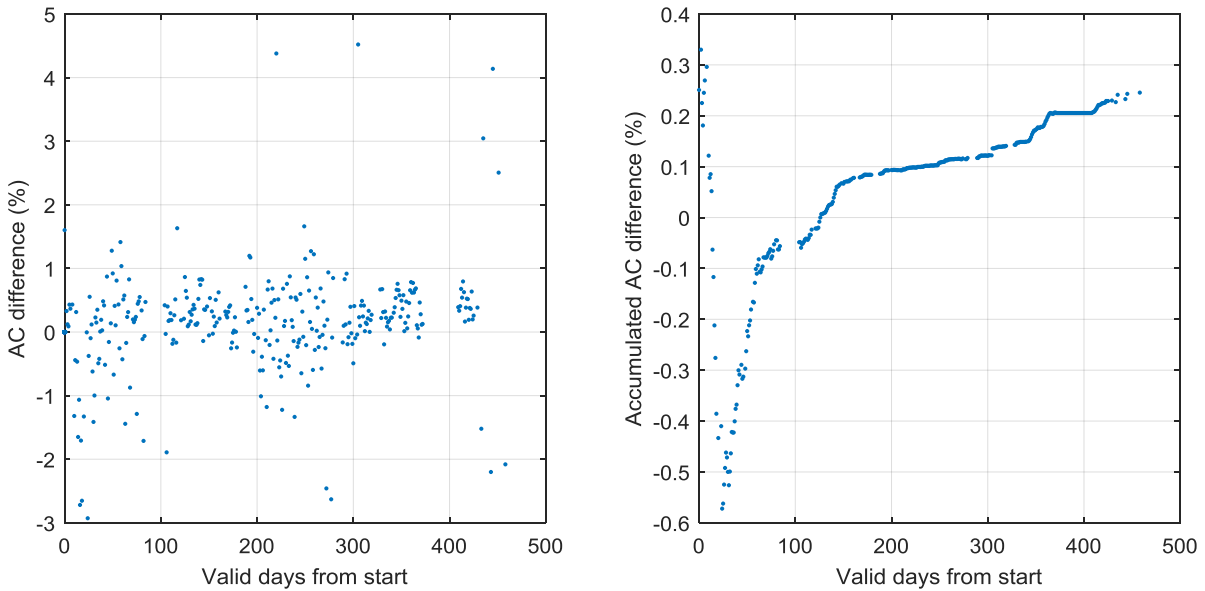


Figure 5.40 AC energy productions. Left: Energy difference for all valid days. Right: Accumulated energy difference. Red circle indicate effect of a non-valid day due to inverter saturation.

It can be observed that the trend matches the trend for DC measurements, but that there is an offset present, so that the accumulated difference after a year has reached the 0.2% level, which is the detection limit for the instrumentation.

### 5.5.5 Conclusion on energy loss estimation

The analysis of the data recorded from the two modified test rows at the Danfoss Solar Park in order to emulate the behaviour of a larger central inverter showed that the difference in energy production between the system with 3 spaced strings and 3 MPPT and a system with 3 strings in parallel and 1 MPPT is negligible /below the detection accuracy of the measurement system. Care has been taken to exclude days influenced by non-operational inverter conditions from the analysis.

The effect on moving clouds on the energy production from the two modified test inverters with distributed panels is below the detection limit even after one year of operation and it must be concluded that energy differences caused by moving clouds on a yearly basis are of little concern.

## 6 Conclusion and future work

### 6.1 Summary and Conclusion

A state-of-the-art analysis has been performed to create an overview of current activities and results achieved in the field of optimization of large PV utility scale power plants with regards to the influence of moving clouds on the annual energy production. The main focus has been on the potential gain in energy production achieved by applying many string inverters, resulting in many independent max-power-point-trackers over the field, vs. the use of a large central inverter with only one max-power-point-tracker. The PV inverter market is a competitive market under strong pressure for price reduction and a substantial reduction in inverter costs is foreseen until 2050. Therefore a simplified design with fewer maximum-power-point-trackers could potentially reduce costs.

Utility scale PV plants are in general not subject to shadows from ground based objects but only by moving clouds, causing fluctuations in the power production by direct shading and by induced mismatch losses. The induced mismatch loss during the passage of clouds was estimated on the basis of published literature and the use of a developed simulation platform, showing a reduced energy production for PV strings in parallel in contrast to strings controlled individually. An attempt was made to verify the effect experimentally by emulating a “central inverter” behavior in a PV plant equipped with string inverters. The Danfoss Solar Park was after a screening process selected as the primary PV test park and a high speed data recording setup was implemented to retrieve data at one second intervals from a series of inverters and a weather station for over a year. One row of PV panels was modified to emulate the behavior of a small central inverter with PV-panels distributed over a distance of 160 m. A comparative analysis was applied to detect the potential difference between this central inverter and a string inverter with comparable panel layout and composition.

The analysis of the irradiance and weather data obtained from two different test sites further showed that the occurrence of non-uniform irradiation conditions caused by moving clouds is below 4% of the operational time of the monitored PV plants. An occurrence in the range of 4% indicates that the effect of moving clouds on the difference in energy production between a string and a central inverter concept is likely to be <0.3% for a large PV plant located on a flat area. This level is at the limit of detection for certified energy meters and thus problematic to verify experimentally.

The accumulated DC and AC energy produced over a year of operation were monitored via the internal inverter measurement circuits of the test inverters. The AC energy measurements were calibrated with external class 0.2% certified energy meters. Days when the recording of the power production were influenced by non-operational events such as external testing, inverter malfunction and communication issues were removed from the analysis. Some events, indicating a difference between a string inverter and a central inverter setup, were identified but the accumulated effect on the annual energy production was in the limit of detection.

It can be concluded that both a string inverter based concept and a central inverter concept in the present test setup are comparable regarding the influence of shadows caused by moving clouds which have a negligible effect on the accumulated energy production for PV plants in flat areas.

The use of the Danfoss Solar Park as a test park imposed challenges such as the effect from landscape topography on the measurements due to the undulating rows. A model was developed to estimate the effect on undulating rows as function of the solar position and showed good agreement with measurement. A daily energy loss of up to 2.5% was experimentally observed during a sunny day for a sloping segment of a row showing a variation of tilt angle of 4°, compared to a flat row of similar length. The landscape topography of a given PV site will be an influencing factor in the

decision to install string inverters or central inverters. For PV plants located in a hilly area with varying slopes string inverters will be beneficial, depending of the actual variation in the panels horizontal tilt in a string.

The work presented showed that the decision of whether to install string inverters or central inverters should not be based on an assumption that string inverters are less influenced by moving clouds than central inverters if the ratio of non-uniform irradiance over a year is as low as in these test cases.

The available test site gave the opportunity to evaluate two other methods related to the optimization of the energy yield of large power plants:

- The operation of a dynamic combination of PV strings during periods of low irradiation level was simulated and showed a potential annual increase in energy production in the range of 0.6% by paralleling two string inverters. Connecting more in parallel only generated a marginal additional gain. The estimated financial benefit of the implementation of such devices as external units over an expected lifetime of 25 years for a PV park is therefore questionable.
- A sorting of panels prior to mounting after the  $I_{MPP}$ -value in a park of 2.1MW is shown to result in an expected annual gain in power production in the range of 0.4%. The financial benefit of sorting panels for a large PV plant will depend on improved methods for sorting of panels during production as well and handling logistics.

A portable battery operated IV-curve tracing instrument was developed and 3 operational prototypes were constructed to be able to scan IV-curves of selected PV panels at a rate of 1 scan per second. This enables high speed monitoring of max-power-point-levels without any influence from an attached inverter. IV-scanners were used to characterize panels in Rome, Italy, and at the University of Southern Denmark. A panel of the same type as mounted in the Danfoss Solar Park at the ESTER Outdoor PV monitoring station at the Tor Vergata University in Rome over a period of 6 months. The characterization showed a power temperature coefficient of the panel depending on the irradiation level.

An analysis of the irradiance data recorded for a year at the Danish test sites and for several months in Rome showed that the occurrences of Standard Test Conditions (STC) and Normal Operating Cell Temperature (NOCT) conditions are extremely rare.

## **6.2 Outlook and future work**

A large database containing a total of 499 logged parameters for over a year of recording at high speed from a total of 17 monitored inverters and two weather stations from two PV plants is available for future research. The recording of all parameters will continue as long as allowed by the plant owners.

The planned future activities include the following activities

- An extended analysis of the available data from the MLX 60kW inverters with regard to cloud induced shading patterns and area topography.
- The frequency stability of the generated AC power in connection with storage solutions is to be investigated.

- An extended simulation platform to include the topography of a given area for all positions of the Sun and the direct/diffuse ration for an arbitrary number of strings in series/parallel.
- The developed IV-curve tracer prototype will be further developed and ways of commercialization will be investigated as the prototype has caused considerable interest.
- The tests at the ESTER Outdoor PV monitoring station in Rome are planned to continue with the same panel to further investigate the influence of irradiance on the power temperature coefficient.
- The characterization of several other types of PV panels, incl. concentrating PV, is planned together with ESTER by applying a modified version of the IV-curve tracer in the near future.
- The estimation of speed-over-ground via time difference estimation between several inverters will be continued.

Planned publications:

- Extended test results from the ESTER Outdoor PV monitoring station in Rome is planned to be published at the *32<sup>th</sup> European Photovoltaic Solar Energy Conference and Exhibition* (EUPVSEC 2016).
- IV-curves recorded at the SDU Alsion plant is shared with the IMEC institute in Belgium to investigate/verify a temperature model for PV-panels. An abstract is submitted to the *32<sup>th</sup> European Photovoltaic Solar Energy Conference and Exhibition* (EUPVSEC 2016).
- Inverter data recorded from the SDU Alsion plant is shared with the Austrian Institute of Technology (AIT) to verify a model for inverter efficiency. An abstract is submitted to the *European Power Electronics Conference* (EPE'2016).
- Journal papers are planned to be submitted to *Journal of Photovoltaics, Solar Energy* and *IEEE transactions of Energy Conversion*.

## References

- [1] Fraunhofer ISE (2015): Levelized cost of electricity renewable energy technologies. Study 2013. *Fraunhofer Institute for Solar Energy Systems ISE*, Freiburg, Germany.
- [2] Mauricio Richter et al., "Best Practice Guide On Uncertainty in PV Modelling", public deliverable 2.4 from the *EC Performance Plus project* (EC no. 308991).  
[http://www.perfplus.eu/frontend/files/userfiles/files/308991\\_PerfPlus\\_Deliverable\\_D2\\_4\\_20150205.pdf](http://www.perfplus.eu/frontend/files/userfiles/files/308991_PerfPlus_Deliverable_D2_4_20150205.pdf) (acessed February 2016)
- [3] P. Wolfe, "Solar photovoltaic projects in the mainstream power market". Oxford: Earthscan; Routledge. Routledge. ISBN: 978-0-415-52048-5
- [4] Large-Scale Photovoltaic Power Plants Ranking 1-50.  
<http://www.pvresources.com/en/pvpowerplants/top50pv.php> (viewed 20160130)
- [5] Andrew Mills and Ryan Wiser," Implications of Wide-Area Geographic DIversity for Short-Term Variability of Solar Power, Ernest Orlando Lawrence Berkeley National Laboratory, Environmental Energy Technologies Division. Report LBNL-3884E, September 2010.
- [6] Fraunhofer ISE (2015): Current and Future Cost of Photovoltaics. Long-term Scenarios for Market Development, System Prices and LCOE of Utility-Scale PV Systems. Study on behalf of Agora Energiewende. 2015. Fraunhofer Institute for Solar Energy Systems ISE, Freiburg, Germany.
- [7] D.M. Lee, "A DIRECT COMPARISON BETWEEN A CENTRAL INVERTER AND MICROINVERTERS IN A PHOTOVOLTAIC ARRAY". MSc-thesis 2011, Appalachian State University, NC, USA.
- [8] Concept paper; String Inverters for PV power plants - Crystalline Modules. Danfoss Solar Inverters A/S, May 2009. L00410489-01 Rev. date 2009-05-01.
- [9] "A Review of PV Inverter Technology Cost and Performance Projections", Navigant Consulting Inc. Burlington, Massachusetts Navigant Consulting Inc. Burlington, Massachusetts. Subcontract Report NREL/SR-620-38771, January 2006.
- [10] J. Schwartz, "Central Inverters for Utility-Scale PV Plants", *SolarPro Magazine* | Issue7.4 June/July 2014. <http://solarprofessional.com/articles/products-equipment/inverters/central-inverters-for-utility-scale-pv-plants-2014-2009> (accessed February 2016). <http://solarprofessional.com/articles/design-installation/distributed-inverter-design> (accessed February 2016).
- [11] G. Walker, "Evaluating MPPT converter topologies using a Matlab PV model". *Journal of electrical and electronics engineering*, Australia 21(1), January 2001.
- [12] V. Salas, E. Olás. A. Barrado, A. Lázaro, " Review of the maximum power point tracking algorithms for stand-alone photovoltaic systems", *Solar Energy Materials & Solar Cells* 90 (2006) 1555–1578.
- [13] T. Esram, and P. L. Chapman, "Comparison of Photovoltaic Array Maximum Power Point Tracking Techniques", *IEEE TRANSACTIONS ON ENERGY CONVERSION*, VOL. 22, NO. 2, JUNE 2007.
- [14] D. Séra, " Real-time Modelling, Diagnostics and Optimised MPPT for Residential PV systems2, PhD-thesis 2009. Aalborg Univesity, Institute of Energy Technology. ISBN: 978-87-89179-76-6
- [15] Søren B. Kjær, "Evaluation of the "Hill Climbing" and the "Incremental Conductance" Maximum Power Point Trackers for Photovoltaic Power Systems", *IEEE TRANSACTIONS ON ENERGY CONVERSION*, VOL. 27, NO. 4, DECEMBER 2012
- [16] H. Haeberlin and Ph. Schaefer, " New Procedure for Measuring Dynamic MPP-Tracking Efficiency at Grid-Connected PV Inverters", *24th European Photovoltaic Solar Energy Conference*, Hamburg, Germany, Sept. 2009.
- [17] H. Haeberlin, L. Borgna, M. Kaempfer, and U. Zwahlen, "Measurement of dynamic mpp-tracking efficiency at grid-connected pv inverters," in *21st Photovoltaic Solar Energy Conference, Dresden, Germany*, 2006.
- [18] J. Pinne, "Optimierung von PVWechselrichtern im Netzparallelbetrieb mithilfe analytischer Verhaltens- und Verlustleistungsmodelle". PhD-thesis. Kassel University Press, ISBN: 978-3-86219-924-2.
- [19] D. Kranzer, C. Wilhelm, B. Burger, "Hocheffiziente und kompakte PV-Wechselrichter mit SiC transistoren". *25. Symposium Photovoltaische Solarenergie*. Kloster Banz, Bad Staffelstein 2010. ISBN: 978-3-941785-23-6

- [20] Heinrich Häberlin, "Photovoltaik - Strom aus Sonnenlicht für Verbundnetz und Inselanlagen", ISBN-13: 9783800732050
- [21] Solar Inverters FLX Series Installation Guide. L00410568-03\_2q / Rev. date: 2014-06-20  
[http://files.sma.de/dl/24088/SMA\\_FLX\\_InstallationGuide-XX-L00410568-03\\_2q.pdf](http://files.sma.de/dl/24088/SMA_FLX_InstallationGuide-XX-L00410568-03_2q.pdf)
- [22] SMA Solar Technology AG, SUNNY TRIPOWER 20000TL HIGH EFFICIENCY datasheet.
- [23] SMA\_Sunny\_Tripower\_SiC\_stp20000tlhe-dus114013.pdf [www.sma-america.com](http://www.sma-america.com) (accessed January 2016).
- [24] MasterVolt SunMaster brochure , "Central String inverter that fits your system" .Version no. 120712EN, Article 500007560. <http://libra-energy.eu/files/ckeditor/Mastervolt/SunMaster%20CS%20%28EN%29.pdf> (accessed January 2016).
- [25] Danfoss MLX Inverter Series brochure, " The Power of Forward Thinking". ID: DKSI.PFA.205.B6.02 May 2014. [www.danfoss.com/](http://www.danfoss.com/) File: MLXsystembrochureEUDKSIPFA205B602web.pdf (accessed January 2016).
- [26] Bosch inverter datasheet. ID: Td\_Bo-BPT\_IS\_1050\_1400-DeEn-1209 Bosch\_inv\_Td\_Bo-BPT\_IS\_1050\_1400-En.pdf. <http://www.a2energie.de/start/produkte/wechselrichter/> (accessed January 2016).
- [27] S.V. Araujo and P. Zacharias, "Analysis on the potential of Silicon Carbide MOSFETs and other innovative semiconductor technologies in the photovoltaic branch". *13th European Conference on Power Electronics and Applications*, 2009. EPE '09.
- [28] R. Burkart, and J.W. Kolar, "Comparative Evaluation of SiC and Si PV Inverter Systems Based on Power Density and Efficiency as Indicators of Initial Cost and Operating Revenue", *Proceedings of the 14th IEEE Workshop on Control and Modeling for Power Electronics (COMPEL 2013)*, Salt Lake City, USA, June 23-26, 2013.
- [29] M. Mazzola," Integrating Wide Bandgap Semiconductor Technology into Microgrid Power Converters", Presentation at *CEM-UT Micro Grid Rodeo*, 20 Feb. 2014.
- [30] C. Sintamarean, F. Blaabjerg and H. Wang," Comprehensive Evaluation on Efficiency and Thermal Loading of Associated Si and SiC based PV Inverter Applications". *39th Annual Conference of the IEEE Industrial Electronics Society*, IECON 2013.
- [31] R. Erlichmann, "Distributed Inverter Design. Utilizing String Inverters in Large Commercial Systems". *SolarPro magazine* | August/September 2013
- [32] A.M. Pavan, S. Castellan, S. Quaia, S. Roitti and G. Sulligoi, "Power Electronic Conditioning Systems for Industrial Photovoltaic Fields: Centralized or String Inverters?", *International Conference on Clean Electrical Power*, 2007. ICCEP '07.
- [33] C. Weber, M. Sporleder, M. Breede, B. Engel and J. Reekers, "Multi-Megawatt PV-Grosskraftwerke mit modularer Anlagentopologie". *25. Symposium Photovoltaische Solarenergie*. Kloster Banz, Bad Staffelstein 2010. ISBN: 978-3-941785-23-6
- [34] S. Ransome and J. Sutterlueti, "THE SENSITIVITY OF LCOE TO PV TECHNOLOGY INCLUDING DEGRADATION, SEASONAL ANNEALING, SPECTRAL AND OTHER EFFECTS". *27th European Photovoltaic Solar Energy Conference and Exhibition*. EUPVSEC 2012.
- [35] G. Müetter, T. Krametz and P. Steirer, "Experiences with a Performance Package for Multi-MW PV Plants Based on Computations on Top of Monitoring". *32<sup>nd</sup> European PV Solar Energy Conference and Exhibition 2015*.
- [36] A.G. Ponze, "Experiences with a Performance Package for Multi-MW PV Plants Based on Computations on Top of Monitoring". Presentation at the *2<sup>nd</sup> Inverter and PV System Technology Forum*, Berlin, 2011.
- [37] IRENA 2012, "Solar Photovoltaics", *Renewable Energy Technologies: Cost Analysis Series Volume 1 – Power Sector, Issue 4/5*. International Renewable Energy Agency
- [38] Photovoltaics Report 2012, *FRAUNHOFER INSTITUTE FOR SOLAR ENERGY SYSTEMS ISE*. December 2012. [www.ise.fraunhofer.de](http://www.ise.fraunhofer.de) (accessed January 2016)
- [39] Photovoltaics Report 2013, *FRAUNHOFER INSTITUTEFOR SOLAR ENERGY SYSTEMS ISE*. July 2014. [www.ise.fraunhofer.de](http://www.ise.fraunhofer.de) (accessed January 2016)
- [40] Photovoltaics Report 2015, *FRAUNHOFER INSTITUTE FOR SOLAR ENERGY SYSTEMS ISE*. November 2015. [www.ise.fraunhofer.de](http://www.ise.fraunhofer.de) (accessed January 2016)

- [41] SolarEdge case study: "200kW Multi-facet Commercial Installation Trentino, ITALY"  
<http://www.solaredge.com/files/pdfs/se-case-study-Trentino-Italy.pdf> (accessed January 2016)
- [42] Kari Lappilainen and Seppo Valkealathi, "Effects of the sharpness of shadows on the mismatch losses of PV generators under partial shading conditions caused by moving clouds". *28th European Photovoltaic Solar Energy Conference and Exhibition*. EUPVSEC 2013. DOI: 10.4229/28thEUPVSEC2013-5BV.7.4
- [43] Anssi Mäki and Seppo Valkealathi , "Operation of long series connected silicon-based photovoltaic module strings and parallel connected short strings under partial shading conditions". *26th European Photovoltaic Solar Energy Conference and Exhibition*. EUPVSEC 2011.
- [44] Anssi Mäki and Seppo Valkealathi , "Mismatch losses in photovoltaic power generators due to partial shading caused by moving clouds". *27th European Photovoltaic Solar Energy Conference and Exhibition*. EUPVSEC 2012.
- [45] N.D. Kaushika and N.K. Gautam," Energy Yield Simulations of Interconnected Solar PV Arrays". *IEEE TRANSACTIONS ON ENERGY CONVERSION*, VOL. 18, NO. 1, MARCH 2003.
- [46] N.D. Kaushika and A.K. Rai, "An investigation of mismatch losses in solar photovoltaic cell networks". *Elsevier Science Direct Energy* 32 (2007) 755–759.
- [47] Francois Giraud and Ziyad M. Salameh, "Analysis of the Effects of a Passing Cloud on a Grid-Interactive Photovoltaic System with Battery Storage using Neural Networks." *IEEE Transactions on Energy Conversion*, Vol. 14, No. 4, December 1999.
- [48] Louis L. Bucciarelli, "POWER LOSS IN PHOTOVOLTAIC ARRAYS DUE TO MISMATCH IN CELL CHARACTERISTICS," *Solar Energy*, Vol. 23, pp. 277-288, Pergamon Press Ltd., 1979.
- [49] Charles E. Chamberlin et al., "Effect of mismatch losses in photovoltaic arrays." *Solar Energy*, Vol. 54, No. 3, pp. 165-171, 1995.
- [50] Lijun Gao et al., "Parallel-Connected Solar PV System to Address Partial and Rapidly Fluctuating Shadow Conditions.", *IEEE Transactions on Industrial Electronics*, Volume 56, 2009, pages 1548-1556.
- [51] Tamas Kekeres et al., "A Practical Optimization Method for Designing Large PV Plants." *IEEE JOURNAL OF PHOTOVOLTAICS*, VOL. 3, NO. 2, APRIL 2013
- [52] Anssi Mäki and Seppo Valkealathi , "Effect of Photovoltaic Generator Components on the Number of MPPs Under Partial Shading Conditions." *IEEE TRANSACTIONS ON ENERGY CONVERSION* · DECEMBER 2013. DOI: 10.1109/TEC.2013.2274280.
- [53] Anssi Mäki and Seppo Valkealathi , "Differentiation of multiple maximum power points of partially shaded photovoltaic power generators", *Renewable Energy* 71 (2014) pp. 89-99.
- [54] Björn Hermann, "Ertrag, Performance, Wirtschaftlichkeit – Parametervariationen zu diesen Größen in der Anlagenoptimierung kleiner und mittlerer PVAnlagen." *25. Symposium Photovoltaische Solarenergie*. Kloster Banz, Bad Staffelstein 2010. ISBN: 978-3-941785-23-6.
- [55] Bernhardt Beck et al., "Anlagenkonzepte für ertragsoptimierten Netzparallelbetrieb im Vergleich." *18. Symposium Photovoltaische Solarenergie*. Kloster Banz, Bad Staffelstein 2003
- [56] Danfoss Solar Inverter TrippleLynx CN Reference manual. Code L00410582-01\_02.
- [57] European Commission project "Performance Plus". EC grant agreement No 308991.  
<http://www.perfplus.eu/project-overview> (accessed February 2016)
- [58] D. Renne: "NREL data set shows clouds' effects on solar power." NREL News Release Nr. 4411, August 31 2011.
- [59] Thomas E. Hoff and Richard Perez, "Quantifying PV Power output variability", *Solar Energy* 84 (2010) 1782–1793.
- [60] Jonathan Gifford, "Tracking shadows", *PV-magazine* 10/2011
- [61] Cristina Cornaro et al., "SOLAR RADIATION FORECAST USING NEURAL NETWORKS FOR THE PREDICTION OF GRID CONNECTED PV PLANTS ENERGY PRODUCTION (DSP PROJECT)", *28th European Photovoltaic Solar Energy Conference and Exhibition*, 2013, DOI: 10.4229/28thEUPVSEC2013-5BV.4.48
- [62] Vincent P.A. Lonij, "Intra-hour forecasts of solar power production using measurements from a network of irradiance sensors", *Solar Energy* 97 (2013) 58–66.
- [63] D. Anagnostos et al., "PV Energy Yield Nowcasting Combining Sky Imaging with Simulation Models," in *30<sup>th</sup> European PV Solar Energy Conference and Exhibition*, Hamburg, Germany, 2015.

- [64] D. Anagnostos et al., "DEMONSTRATION AND VALIDATION OF AN ENERGY YIELD PREDICTION MODEL SUITABLE FOR NON-STEADY STATE NON-UNIFORM CONDITIONS", *The 6th World Conference on Photovoltaic Energy Conversion*, November 2014.
- [65] Ward T. Jewell and Timothy D. Unruh, "LIMITS ON CLOUD-INDUCED FLUCTUATION IN PHOTOVOLTAIC GENERATION", *IEEE Transactions on Energy Conversion*, Vol. 5, No.1, March 1990.
- [66] "MIT STUDY ON THE FUTURE OF THE ELECTRIC GRID", Chapter 5: The Impact of Distributed Generation and Electric Vehicles, 2011, ISBN 978-0-9828008-6-7
- [67] J. Guerrero et al., "Analysis of mismatch and shading effects in a photovoltaic array using different technologies", *Materials Science and Engineering* 59 (2014) 012007, Doi:10.1088/1757-899X/59/1/012007
- [68] B. Bletterie, R. Bruendlinger, and S. Spielauer, "Quantifying dynamic MPPT performance under realistic conditions first test results—The way forward," in *Proc. 21st Eur. Photovoltaic Solar Energy Conf. Exhibition*, 2006, pp. 2347–2351.
- [69] Bruno Burger, "Auslegung und Dimensionierung von Wechselrichtern für netzgekoppelte PV-Anlagen", 25. *Symposium Photovoltaische Solarenergie*. Kloster Banz, Bad Staffelstein 2010.
- [70] S. Armstrong and W.G. Hurley, "A thermal model for photovoltaic panels under varying atmospheric conditions", *Applied Thermal Engineering* 30 (2010), pp. 1488-1495.
- [71] Anssi Mäki and Seppo Valkealahti, "Effect of PV power generator layout on the global MPP voltage range during cloud shading events", *28<sup>th</sup> European Photovoltaic Solar Energy Conference and Exhibition 2013*.
- [72] Kari Lappilainen and Seppo Valkealathi, " Recognition and modelling of irradiance transitions caused by moving clouds", *Solar Energy* FEBRUARY 2015. DOI: 10.1016/j.solener.2014.11.018.
- [73] John Berndner, "Field Results of Energy Maximizing Distributed DC Topology – Residential & Commercial Installations". *25<sup>th</sup> European Photovoltaic Solar Energy Conference and Exhibition 2010*.
- [74] R.A. Walling and K. Clark, "Support Functions Implemented in Utility-Scale PV Systems", *Transmission and Distribution Conference and Exposition*, 2010 IEEE PES, DOI: 10.1109/TDC.2010.5484373.
- [75] Paul Denholm et al., "Land-Use Requirements of Modern Wind Power Plants in the United States", *Technical Report NREL/TP-6A2-45834*, August 2009.
- [76] David L. King et al., "Temperature Coefficients for PV Modules and Arrays: Measurement Methods, Difficulties, and Results", *26th IEEE Photovoltaic Specialists Conference*, September 29-October 3, 1997, Anaheim, California.
- [77] Scott Moskowitz, "1,500-Volt PV Systems and Components 2016-2020: Costs, Vendors, and Forecasts", GTMResearch report. <https://www.greentechmedia.com/research/report/1500-volt-pv-systems-and-components-2016-2020> (accessed February 2016).
- [78] Ingo Klute, "Technical Overview: Pros & Cons of Higher system Voltages". juwi Solar GmbH. Presentation at the *2<sup>nd</sup> Inverter and PV System Technology Forum*, Berlin, 2011.
- [79] E. Gkoutioudi. P. Bakas and A. Marinopolous, "Comparison of PV systems with Maximum DC Voltage 1000V and 1500V". *IEEE 38<sup>th</sup> Photovoltaic Specialists Conference (PVSC)*, 2013. DOI: 10.1109/PVSC.2013.6745070
- [80] T. Booth, D. Lee and D. Brearley, "Next Generation Central Inverters. Manufacturers, Specifications and Design Considerations". *SolarPro Magazine* | December/January 2009 .  
<http://solarprofessional.com/print-issue/december-january-2009> (accessed February 2016).
- [81] J. Cataldo and M. Zeballos, "Roughness terrain consideration in a wind interpolation numerical model", *11th Americas Conference on Wind Engineering*, San Juan, Puerto Rico, June 2009.
- [82] "Estimating wind speed",  
<http://www.wind-power-program.com/windestimates.htm> (accessed February 2016).
- [83] J. S. Touma, "Dependence of the Wind Profile Power Law on Stability for Various Locations", *Journal of the Air Pollution Control Association*, 27:9, 1977, 863-866, DOI: 10.1080/00022470.1977.10470503
- [84] Z. Sen, A. Altunkaynak and T. Erdik, "Wind Velocity Vertical Extrapolation by Extended Power Law", *Advances in Meteorology*, Volume 2012, Article ID 178623, DOI:10.1155/2012/178623
- [85] R.H. Touiller and U.O. Lappe, "Wind and Temperature Profile Characteristics from Observations on a 1400 ft Tower". *Journal of Applied Meteorology*, vol. 3, June 1964.

- [86] J. Counihan, "ADIABATIC ATMOSPHERIC BOUNDARY LAYERS: A REVIEW AND ANALYSIS OF DATA FROM THE PERIOD 1880-1972", *Atmospheric Environment* (1967) Volume 9, Issue 10, October 1975, Pages 871-905, DOI:10.1016/0004-6981(75)90088-8
- [87] Tatsuo Hanafusa et al., "DEPENDENCE OF THE EXPONENT IN POWER LAW WIND PROFILES ON STABILITY AND HEIGHT INTERVAL", *Atmospheric Environment* Vol. 20, No. 10, pp. 2059-2066, 1986.
- [88] J.S. Irwin, "A THEORETICAL VARIATION OF THE WIND PROFILE POWER-LAW EXPONENT AS A FUNCTION OF SURFACE ROUGHNESS AND STABILITY", *Atmospheric Environment* Vol. 13, pp. 191-194.
- [89] P. Weishaupt, "Svæveflyvehåndbogen", Chapter 4: Meteorology. 1986. ISBN: 87-87492-16-4.
- [90] K. H. Hussein, I. Muta, T. Hoshino, and M. Osakada, "Maximum photovoltaic power tracking: An algorithm for rapidly changing atmospheric conditions," *IEE Proc.—Gener., Transm. Distrib.*, vol. 142, no. 1, pp. 59-64, 1995.
- [91] Keith A. Pickering, "The Southern Limits of the Ancient Star Catalog and the Commentary of Hipparchos", *DIO The International Journal of Scientific History*, Vol. 12, September 2012. ISSN: 1041-5440.
- [92] Peter Würfel (2005), "The Physics of Solar Cells". Weinheim: Wiley-VCH. ISBN 3-527-40857-6.
- [93] Bastian Zinsser et al., "RATING OF ANNUAL ENERGY YIELD MORE SENSITIVE TO REFERENCE POWER THAN MODULE TECHNOLOGY", *IEEE 35<sup>th</sup> Photovoltaic Specialists Conference (PVSC)*, 2010, 10.1109/PVSC.2010.5614705.
- [94] "Guidelines for PV Power Measurement in Industry", *JRC Scientific and Technical Reports. JRC EUR 24359 EN report*. ISBN 978-92-79-15780-6, DOI :10.2788/90247
- [95] International Standard IEC62053 Electricity metering equipment (a.c.) –Particular requirements – Part 21: Static meters for active energy (classes 1 and 2)  
Part 22: Static meters for active energy (classes 0,2 S and 0,5 S)
- [96] Mahmoud Alahmad, Mohamed A. Chaaban and Siu Kit Lau, "An Adaptive Photovoltaic-Inverter Topology" (2011). *Architectural Engineering -- Faculty Publications*. Paper 47.
- [97] Anton Driesse, P. Jain and S. Harrison, "BEYOND THE CURVES: MODELING THE ELECTRICAL EFFICIENCY OF PHOTOVOLTAIC INVERTERS", *Photovoltaic Specialists Conference*, 2008. PVSC '08. 33rd IEEE, DOI: 10.1109/PVSC.2008.4922827
- [98] Heinz Neuenstein and Jochen Siemer, "Rundum gelungen", Test results for the Danfoss TLX 15K inverter published in the *PHOTON Profi Magazine*, April 2010.
- [99] A.B. Sproul, "Vector Analysis of Solar Geometry", Key Centre for Photovoltaic Engineering. University of New South Wales. Sydney, NSW, 2052. Australia, 2002.
- [100] Hiren Patel and Vivek Agarwal, "MATLAB-Based Modeling to Study the Effects of Partial Shading on PV Array Characteristics", *IEEE TRANSACTIONS ON ENERGY CONVERSION*, VOL. 23, NO. 1, MARCH 2008.
- [101] Elkor WattsOn Universal Power Transducer User manual.  
[www.elkor.net/pdfs/WattsOn\\_Manual.pdf](http://www.elkor.net/pdfs/WattsOn_Manual.pdf) (accessed February 2016).
- [102] Si-02 Silicon Irradiance sensor datasheet. Ingenieurbüro Mencke & Tegtmeyer GmbH, November 2012. [http://www.imt-solar.com/fileadmin/docs/en/products/Si-Sensoren\\_E.pdf](http://www.imt-solar.com/fileadmin/docs/en/products/Si-Sensoren_E.pdf) (accessed February 2016).
- [103] Article "The Learning Curve" in PHOTON The Photovoltaic Magazine, Issue 8, 2012. IV-curve tracer overview.
- [104] Ed Mohan et al., "Power Electronics: Converters, Applications, and Design", 3rd Ed. Wiley Publ., ISBN-13: 978-0471226932
- [105] Anton Driesse, "Dynamic uncertainty of Irradiance Sensors. Illustrations from a Study of 42 Radiometers", presented at the 4<sup>th</sup> PV Performance Modelling and Monitoring Workshop, TÜV Rheinland Group, Cologne, Germany, 22<sup>nd</sup> and 23<sup>rd</sup> October 2015
- [106] Eugene Hecht, "Optics". Addison-Wesley Publ., ISBN-13: 978-0133977226.
- [107] A. Spina et al., "DATA VALIDATION AND UNCERTAINTY EVALUATION OF THE ESTER OUTDOOR FACILITY FOR TESTING OF PHOTOVOLTAIC MODULES", *24th European Photovoltaic Solar Energy Conference*, 21-25 September 2009, Hamburg, Germany. DOI: 10.4229/24thEUPVSEC2009-4AV.3.89

- [108] Cristina Cornaro, "OUTDOOR PV MODULE PERFORMANCE COMPARISON AT TWO DIFFERENT LOCATIONS", Conference Proceedings of AMSE-ATI-UIT 2010.
- [109] Cristina Cornaro, "Performance analysis of PV modules of various techniques after more than one year of outdoor exposure in Rome", IEEE International Conference on Advanced Electromaterials, 2011.

## Appendix A1-A7

Appendix A1-A7 contains a list of publications made as a part of this project in conference papers and a journal.

- A1 K.M. Paasch, M. Nyman and F. Haase, “Optimization of PV-based energy production by dynamic PV-panel/inverter configuration”, *PVSAT 9 - 9th Photovoltaic Science Applications and Technology Conference*, 2013, Swansea, United Kingdom.
- A2 K.M. Paasch, M. Nyman and F. Haase, “Sensor System for Long-term Recording of Photovoltaic (PV) IV-curves”, *PVSAT 9 - 9th Photovoltaic Science Applications and Technology Conference*, 2013, Swansea, United Kingdom.
- A3 K.M. Paasch, M. Nyman and S.B. Kjær, “Distributed measurement system for long term monitoring of clouding effects on large PV plants”, *EPE'13 ECCE Europe 15<sup>th</sup> European Conference on Power Electronics and Application*, Lille, France, 2013.
- A4 K. Paasch, M. Nyman and S.B. Kjær, ”Simulation of the impact of moving clouds on large scale PV-plants”, *IEEE 40th Photovoltaic Specialist Conference (PVSC)*, 2014, Denver, USA. DOI: 10.1109/PVSC.2014.6925036
- A5 K. Paasch, M. Nyman and S.B. Kjaer, “COMPARATIVE ANALYSIS OF THE PERFORMANCE OF STRING- AND CENTRAL INVERTER TOPOLOGY AT A LARGE PV UTILITY PLANT WITH VARYING TOPOGRAPHY”. *31th European Photovoltaic Solar Energy Conference and Exhibition*. EUPVSEC 2015, Hamburg, Germany.
- A6 K. Paasch, M. Nyman and F. Haase, “Long term energy yield measurements of a string- vs. central inverter concept tested on a large scale PV-plant”, *EPE'15 ECCE Europe 17<sup>th</sup> European Conference on Power Electronics and Application*, Geneva, Switzerland, 2015.
- A7 J. Olsen, K.M. Paasch, B. Lassen and C.T. Veje, ”A new principle for underground pumped hydroelectric storage”, *Journal of Energy Storage* 2 (2015) 54–63. DOI:10.1016/j.est.2015.06.003

## Appendix A1

K.M. Paasch, M. Nymand and F. Haase, “Optimization of PV-based energy production by dynamic PV-panel/inverter configuration”, *PVSAT 9 - 9th Photovoltaic Science Applications and Technology Conference*, 2013, Swansea, United Kingdom.

### Errata.

Equation (2):

Printed:  $\theta = \cos^{-1}[\sin(\beta) \cos(\Sigma) + \cos(\beta) \sin(\gamma) \sin(\Sigma)]$

Should read:  $\theta = \cos^{-1}[\sin(\beta) \cos(\Sigma) + \cos(\beta) \sin(\gamma) \cos(\Sigma)]$

Typing error, the calculations are performed with the correct equation.

## Optimization of PV-based energy production by dynamic PV-panel/inverter configuration

Kasper M. Paasch,<sup>\*</sup> Morten Nymand and Frerk Haase<sup>\*</sup>

Univ. of Southern Denmark, Inst. of Technology and Innovation, Niels Bohrs Alle 1, DK-5230 Odense

<sup>\*</sup>Danfoss Solar Inverters A/S, Jyllandsgade 30, DK-6400 Sønderborg

Corresponding Author

### Introduction

This paper investigates the possible increase in annual energy production of a PV system with more than one MPPT (maximum power point tracker) input channels under Nordic illumination conditions, in case a concept of dynamic switching of the PV panels is used at the inputs of the inverters.

The power output of any photovoltaic (PV) system is affected not only by the irradiation level, but also by the conversion efficiency of the applied inverter. In cloudy weather, as in winter, the power generated by PV panels is fairly low compared to peak production. The inverters for a PV plant are dimensioned after the rated Wpeak value of the panels connected, but PV inverters typically have maximum conversion efficiency at a specific input power level. Thus, inverters will exhibit a conversion efficiency depending on the actual solar irradiation level. For low irradiation levels it thus seems beneficial to connect PV panels/strings in parallel to one MPPT input /inverter in order to utilize higher overall conversion efficiency. This method has been reported in literature [1] but has not yet been applied to Nordic illumination conditions, as far as we know.

### Available data set

Meteorological data used in this study have been obtained from DMI (Danish Meteorological Institute). The data contain a "average year" for 2002, including the normal direct as well as the diffuse irradiation components, temperature etc. Especially in Nordic areas, long periods of bad and cloudy weather are expected, resulting in low conversion efficiency due to low power input. The same is the case at sunrise and sunset. See figures 1 and 2 for an example of varying irradiation over one year.

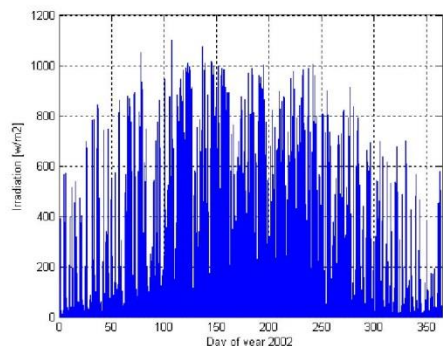


Figure 1. Direct irradiation profile for the "Danish average year 2002" [2]. Data sampled per hour.

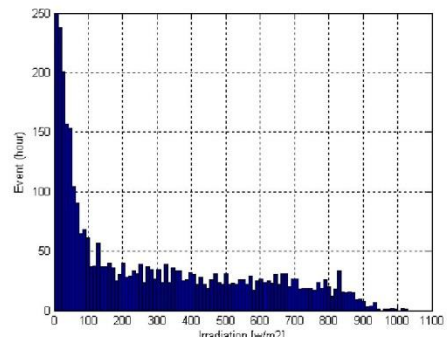


Figure 2. Histogram of the direct irradiation in the "Danish average year 2002". Night values=0 are not shown to scale.

### Basic configuration

The concept investigated is based on the allocation of strings to specific MPPT-inputs, determined by the actual irradiation level. Optimum configuration is seen as the configuration at which the inverter operates with the highest conversion efficiency. The principle is illustrated in figure 3 by combining 3 strings.

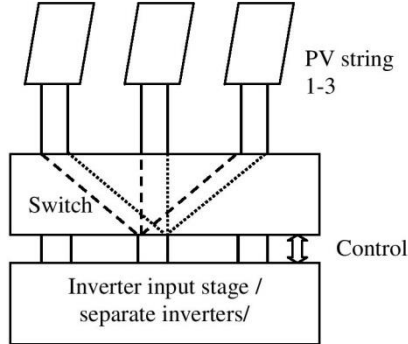


Figure 3. Principle of combining three PV-strings to increase annual power production

#### Irradiation profile

The virtual energy production for a 15 kW PV-system, consisting of 3x20 250W panels, has been simulated. This data set used in this study contains measurements of the normal direct and diffuse irradiation components on an hourly basis, as well as the position of the sun, temperature etc. Irradiation values must be adapted to the panel orientation in order to calculate the output power of the PV-panels. The approach followed here is based on [3]. See figure 4.

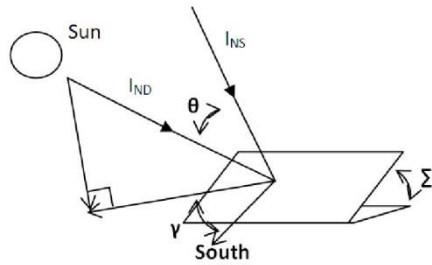


Figure 4. Panel coordinate system (after [8]).

Total solar radiation  $I_{TS}$  incident on the tilted surface can be expressed as a function of the received normal irradiation  $I_{ND}$ , the angle of incidence relative to the surface  $\theta$  the tilt angle  $\Sigma$ , the horizontal orientation  $y$  and the ground albedo  $\rho$ .  $I_{TS}$  will consist of contributions from 3 sources; the direct sunlight  $I_{NS}$ , the diffuse radiation  $I_{DS}$  and the ground reflected diffuse radiation  $I_{RS}$ .

$$I_{TS} = I_{NS} + I_{DS} + I_{RS} \quad (1)$$

$I_{NS}$  can be determined by pure geometry

$$I_{NS} = I_{ND} \cos(\theta) \quad (2)$$

where

$$\theta = \cos^{-1}[\sin(\beta) \cos(\Sigma) + \cos(\beta) \sin(\gamma) \sin(\Sigma)]$$

The addition of the diffuse irradiation component  $I_{DS}$  as well as the ground reflected radiation  $I_{RS}$  needs some consideration. A tilted surface facing the sun will in reality receive more diffuse light than if pointing in the opposite direction. Elaborate studies have been undertaken to investigate this anisotropic effect [4]. In this study the effect of diffuse light has been included through a simple model

$$I_{DS} = I_{diff} \cdot R_{diff} \quad (3)$$

where  $R_{diff}$  is the diffuse transposition factor. For diffused light evenly distributed over the whole hemisphere  $R_{diff}$  can be expressed by a simple anisotropic approximation [3,4]

$$R_{diff} = (1 + \cos(\Sigma))/2 \quad (4)$$

Eq. 4 is applied in this study. For in-depth analysis of diffuse radiation modeling, model accuracy and literature reviews, see [4-6]. The ground reflected diffuse irradiation  $I_{RS}$  is determined by the measured total ground reflection  $E$ , the albedo value  $\rho$  and the ground transposition factor  $R_r$ .

$$I_{RS} = \rho \cdot E \cdot R_r \quad (5)$$

For an ideally isotropic surface,  $R_r$  can be expressed as

$$R_r = (1 - \cos(\Sigma))/2 \quad (6)$$

The problem is generally to determine  $E$ , which is often neglected in studies due to its rather small contribution. Ground reflections are not included in this study since available data sets do not include  $E$ , and in literature, the effect of ground reflection is considered to be minor [5].

#### Inverter efficiency curves

Overall inverter efficiency is commonly used as a sales parameter; the higher the better. In order to compare this sales parameter, specific procedures have been

accepted by the EC and the Californian Energy Commission (CEC) for measurement of overall inverter efficiency [7]. Both procedures use a weighted ratio between efficiencies at specified power levels, relative to the nominal power. See Eq. 7-8 [7].

$$h_{EC} = 0.03h_{5\%} + 0.06h_{10\%} + 0.13h_{20\%} + 0.1h_{30\%} + 0.48h_{50\%} + 0.2h_{100\%} \quad (7)$$

$$h_{CEC} = 0.04h_{10\%} + 0.05h_{20\%} + 0.12h_{30\%} + 0.21h_{50\%} + 0.53h_{75\%} + 0.05h_{100\%} \quad (8)$$

It can be seen that the EC method includes the efficiency at lower power levels than the CEC standard, which has a higher weight for higher power levels. From a sales perspective, the EC method is therefore "better" for inverters intended for use in cloudy areas.

The efficiency curves for two typical inverters are shown below. It can be seen that the inverter efficiency drops off substantially at lower output power levels and it is thus anticipated that, when having a system with several inverters/inputs, an efficiency gain can be obtained by combining the inputs into one MPPT channel (and turn off the other MPPT channels). A detailed analysis will have to take the internal structure and different efficiencies of the sub-parts of a given inverter into account. This analysis only investigates an overall assumption based on a simple model.

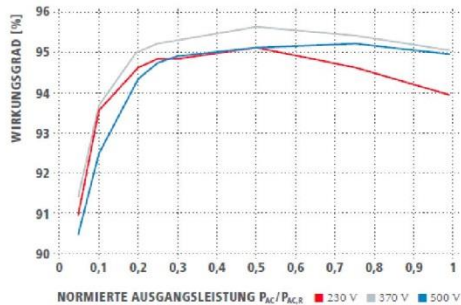


Figure 5. Inverter efficiency curves for an inverter of type Fronius IG Plus 150 V-3 [8].

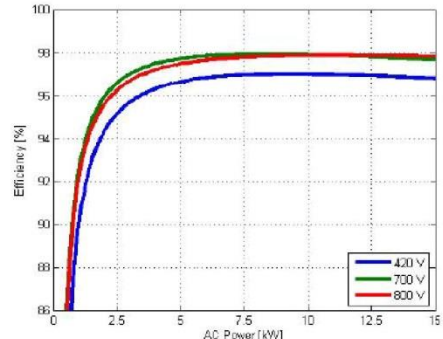


Figure 6. Inverter efficiency curves for an inverter of type Danfoss TripleLynx CN 15 kW [9].

As demonstrated, the inverter efficiency depends on the actual output power with a characteristic decline of efficiency below 0.2 times the nominal power of the inverter to efficiency levels around 85%. For output power levels higher than 0.2 times nominal power, efficiency is in the range of 96-98%. The rapid decline in efficiency when operating below 0.2 times nominal power is due to the idle power losses in the inverter (control, switching etc.).

If output power is higher than the nominal power of the inverter, power production in the inverter will be limited to the rated maximum power of the input stage.

## Simulation.

A 3-string system has been modeled in Matlab and the overall energy gain as a function of the threshold value for switching has been calculated. The simulation using the Danish data set is illustrated in figure 1 and models a system consisting of 3 strings with each 20 panels of 250W. Panel orientation is south, tilt is 37 degrees. A representative piecewise linear inverter efficiency curve, based on curves shown in figures 5 and 6, has been implemented. Since a rapid decline in inverter efficiency in general happens around a ratio of 0.2, it is expected that a potential gain in power production will happen around that level. A threshold value of 0.33 means that the PV-strings will be connected in parallel if the power from one string equals 1/3 the rated inverter power. A threshold above 0.33 implies that the inverter in operation might receive above its maximum power level and thus cannot utilize all potential power from the solar panels. A power

temperature coefficient of  $-0.4\%/\text{°C}$  has been included. The data set used contains ambient temperature measurement for each set of irradiation values, but, as they are not panel temperatures, they are not fully representative of the direct irradiation heating of the solar panels during warm periods. In the simulations this will result in a slightly higher power production during sunny periods than in a real test scenario. The curve shown in figure 7 can therefore be seen as a conservative estimate.

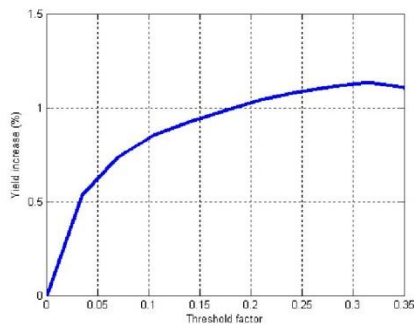


Figure 7. Simulated annual increase in power production by dynamic switching of 3x5kW strings between three inverters/inverter inputs.

In this study it is assumed that there is no power loss during the reconfiguration of the strings and that the inverter inputs behave as independent inverters. It can be seen that under the given simulation conditions an annual increase in power production in the range of 1% is to be expected. This value compares well to tests described in literature, where a gain of around 1% is reached at a 123 kW test site in Dimbach, South-West Germany [1].

### Conclusion and outlook

Based on data for a Danish average year, it has been shown that the annual power production of a solar plant under Nordic illumination conditions is expected to increase around 1% by applying dynamic switching of 3 strings of each 5 kW and a switching threshold level of 0.33. This work has been supported by the Sunrise-PV project, which is partly funded by Syddansk Vækstforum in Denmark and the European Regional Development Fund.

### References

- 1 Beck et al. *Anlagenkonzepte für ertragsoptimierten Netzparallelbetrieb im Vergleich*. 18th Symposium Photovoltaic Solar Energy, Bad Staffelstein, DE, 2003.
- 2 Danish Meteorological Institute. [www.dmi.dk](http://www.dmi.dk)
- 3 Mohamed et al. *Thermosyphon solar water distillers for remote and arid areas*. Presented on HEFAT2008, 6th International Conference on Heat Transfer, Fluid Mechanics and Thermodynamics.
- 4 Gueymard, A. *Direct and indirect uncertainties in the prediction of tilted irradiance for solar engineering applications*. Solar Energy 83 (2009), pages 432-444.
- 5 Padovan et al. *Measurement and modeling of solar irradiance components on horizontal and tilted planes*. Solar Energy 84 (2010), pages 2068-2084.
- 6 Evseev et al. *The assessment of different models to predict the global solar radiation on a surface tilted to the sun*. Solar Energy 83 (2009), pages 377-388.
- 7 W. Bower. *Performance Test Protocol for Evaluating Inverters Used in Grid-Connected Photovoltaic Systems* (draft version Oct. 2004). Sandia National Laboratories, Solar Technologies. [www.sandia.gov](http://www.sandia.gov)
- 8 Fronius IG Plus 150 V-3 datasheet.DS\_Fronius\_IG\_Plus\_M\_06\_0008\_DE\_113\_as13\_156488\_snapshot.pdf [www.fronius.de](http://www.fronius.de)
- 9 Danfoss Solar Inverter TrippleLynx CN Reference manual. Code L00410582-01\_02 [www.danfoss.com](http://www.danfoss.com)

## **Appendix A2**

K.M. Paasch, M. Nyman and F. Haase, “Sensor System for Long-term recording of Photovoltaic (PV) IV-curves”, *PVSAT 9 - 9th Photovoltaic Science applications and Technology Conference*, 2013, Swansea, United Kingdom.

## Sensor System for Long-term Recording of Photovoltaic (PV) IV-curves

Kasper M. Paasch,<sup>\*</sup> Morten Nymand and Frerk Haase<sup>\*</sup>

Univ. of Southern Denmark, Inst. of Technology and Innovation, Niels Bohrs Alle 1, DK-5230 Odense

<sup>\*</sup>Danfoss Solar Inverters A/S, Jyllandsgade 30, DK-6400 Sønderborg

<sup>\*</sup> Corresponding Author

### Introduction

The purpose of this paper is to present a recording system for long-term investigation of PV panel dynamics under partial shading conditions. The system is intended to be a low-cost system deployable for stand-alone field use and long-term data recording at PV-plants. Passing clouds will affect the energy production due to lower irradiation and the resulting induced imbalance in current/voltage characteristics [1]



Figure 1. Arduino platform; ATmega2560 board and Memoire SD/RTC-shield [2].

### Hardware platform

The solar irradiation and the resulting IV-curve of an attached PV-panel are measured and stored in one-second intervals. The recording unit is based on the low cost Arduino platform [2].

The system consists of 3 main parts: CPU unit with ADC, communication etc. (Arduino ATmega2560), SD storage shield with Real-time-clock, custom designed analog interface/sweep unit and electronic load unit, based on power MOSFETs, as well as Hall-effect based current sensor with low internal resistance in the current path ( $100\mu\Omega$ ). The use of a Hall-effect based current sensor (Allegro ACS758LBC) eliminates the need for a series resistor in the current path and allows for future extension to large currents up to and above 50A [3].

The analog power stage must comply to the power level of the PV-source to be monitored, but as the sweep time is kept short, the average power dissipation will be significantly lower than in continuous operation at the maximum power point of the source. The device presented here primarily addresses the measurement around the maximum power point of a panel, therefore no special attempt is made to measure the true short circuit current  $I_{SC}$ , which can be a difficult task in itself due to the on-resistance of transistors. See figure 2.

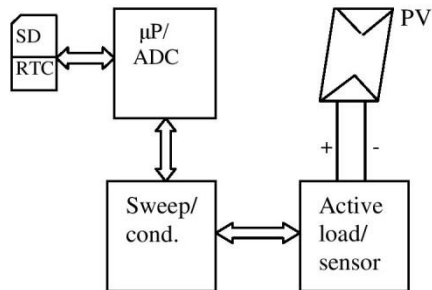


Figure 2. Basic components of the recording unit.

The recording unit is initially powered by battery, but an extended version, harvesting energy from the solar panel under test, is under development.

Due to the price and size of large heat sinks the load handling demand of the sweep unit is an important design parameter, in order to keep the overall cost of the unit to a minimum. The average power dissipation depends on the IV-curve of the panel/string to be monitored and the sweep profile (fast/slow). The needed cooling capacity will therefore depend on the sweep profile.

In order to estimate the power dissipation and thus the needed cooling requirements, a system model has been implemented,

based on the classical one-diode model of a solar cell [4] shown in figure 3.

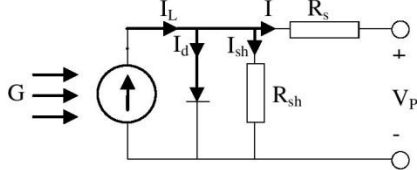


Figure 3. One-diode model of a PV-cell [4].

The one-diode model IV-characteristics of a solar cell are given by Eq. 1.

$$I = I_L - I_0 \left( e^{\frac{q(V_p + R_s I)}{n \cdot k \cdot T}} - 1 \right) - \frac{V_p + R_s I}{R_{sh}} \quad (1)$$

A closed-form exact solution of Eq. 1 for the unknown current  $I$  is not available, so numerical methods should be applied [4]. A Newton-Raphson method has been applied in this study, following the approach outlined in [4]. Knowledge of the open circuit voltage  $V_{OC}$ , the temperature dependency and the saturation current is mandatory to complete the model.

$$I_L(T) = I_L(T_{ref}) + \alpha(T - T_{ref}) \quad (2)$$

$$I_L(T_{ref}) = I_{SC}(T_{ref}) \frac{G}{G_{ref}} \quad (3)$$

$$I_0(T_{ref}) = \frac{I_{SC}(T_{ref})}{\left( e^{\frac{q \cdot V_{OC}(T_{ref})}{n \cdot k \cdot T_{ref}}} - 1 \right)} \quad (4)$$

$$V_{OC}(T) = V_{OC}(T_{ref}) + \beta(T - T_{ref}) \quad (5)$$

where  $G$  is the irradiation level,  $k$  the Boltzman's constant,  $q$  the electron charge,  $\alpha$  and  $\beta$  the temperature coefficients for the voltage and current, respectively.  $n$  is the ideality factor of the junction (between 1 and 2). For an estimation of  $R_{sh}$  and  $R_s$  see [4]. The subscript ref refers to the Standard Test Conditions (STC)  $T_{ref}=25^\circ C$ ;  $G_{ref}=1000W/m^2$  [5]. The short-circuit current  $I_{SC}$  and the open circuit voltage  $V_{OC}$  at  $T_{ref}$  are panel parameters stated by the manufacturer.

### Regulation vs. power dissipation

Examples of active loads are known from literature and the regulation schemes used can be classified as either direct or current/voltage controlled [6,7]. Both constant voltage and constant current implies the use of a regulator/control

function, as shown in figure 4 and in [6], where a direct drive on the gate terminal without feedback loop simplifies the circuitry. This study will compare the direct drive and the voltage feedback schemes.

Loads for PV-systems are typically dimensioned for continuous power, meaning that even modest power levels will require extensive cooling effort. But if the IV-curves of a panel can be measured fast, the average power requirement can be reduced, thus enabling a smaller and cheaper unit. The power dissipation as well as the required sampling rate will depend on the scheme chosen.

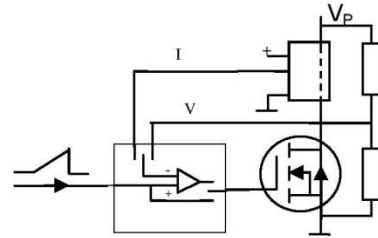


Figure 4. MOSFET/Hall-sensor based load circuit with selectable voltage, current or direct drive.

The active element chosen in this study is a HEXFET Power MOSFET of type IRF530 [8]. The threshold voltage  $V_{th}$  of a FET is in the range of a few volts and the panel voltage  $V_p$  around the MPP is typically 30-40V, so the FET will be operating mainly in the active/saturated region, where the drain current  $I_{Drain}$  is essentially independent of the drain-source voltage  $V_{DS}$  [7,9]. Thus  $I_{Drain}$  is essentially a function of the applied gate-source voltage  $V_{GS}$ .

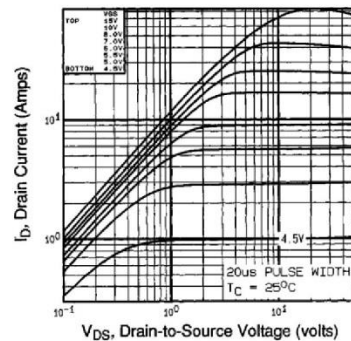


Figure 5. Output characteristics for the IRF530 MOSFET [8].

The following conditions apply:

$$V_{panel} = V_{DS}$$

$$V_{DS} \gg V_{th}$$

For operation in the active/saturated region  $I_{\text{Drain}}$  can be approximated by Eq. (6) [9].

$$I_D = \frac{K_n}{2} (V_{GS} - V_{th})^2 \quad (6)$$

where  $K_n$  is a device specific constant related to the internal FET geometry.

For operation in the ohmic region  $I_D$  can be expressed by Eq. (7).

$$I_D = k[2(V_{GS} - V_{th})V_{DS} - \frac{1}{2}V_{DS}^2] \quad (7)$$

The instantaneous power  $P_{\text{load}}$  dissipated in the FET in the active region is, for  $V_{GS} > V_{th}$ .

$$P_{\text{load}} = V_{DS} \cdot \frac{K_n}{2} (V_{GS} - V_{th})^2 \quad (8)$$

By combining the mapped IV-relationship, based on Eq. (1-5), with Eq. (6-8) the instantaneous power  $P_{\text{load}}$  can be calculated.

The average power  $P_{\text{av}}$  dissipated in the load can be calculated from the simulated IV-relationship (Eq. 1-5), the applied drive voltage and the transfer characteristic of the MOSFET.

$$P_{\text{av}} = \frac{1}{T_{\text{sweep}}} \int_0^{t_{\text{sweep}}} P_{\text{load}}(t) dt \quad (9)$$

### Simulation results

Different schemes have been simulated for a number of linear sweep rates and solar irradiation. The simulations are based on data for a commercial PV-panel (Sunpower SPR-225,  $W_{\text{peak}}=225\text{W}$ ,  $V_{\text{OC}}=0.674\text{V}$ ,  $I_{\text{SC}}=5.87\text{A}$  [9]). See figure 6.

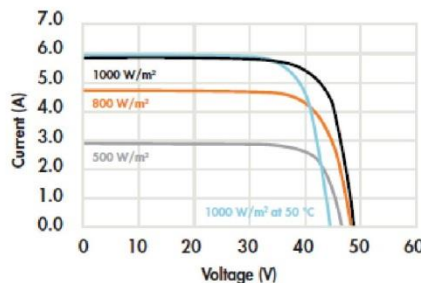


Figure 6. IV-curves for a Sunpower SPR-225 panel [10]

### Direct linear ramp drive

The result of using Eq. (8) to simulate the power dissipation in the FET, during 4 different direct linear ramp input signals on

the FET gate, is illustrated in figure 7. Ramp rates are 10-15-20-25 V/s. The irradiation level is  $1000\text{W/m}^2$ .

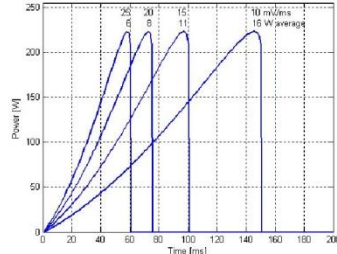


Figure 7. Power dissipation vs. time for 10-25 mV/ms sweep rates.

The power dissipation generated by varying illumination and fixed sweep rate is shown in figure 8.

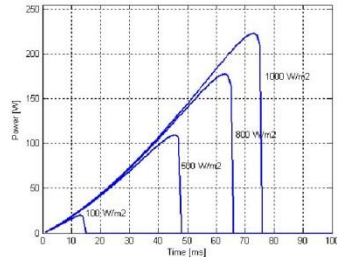


Figure 8. Power dissipation for a selected sweep-rate (20 mV/ms) as function of irradiation level (100-80-50-10% of STC).

### Voltage mode, linear ramp

Applying a voltage feedback loop ensures that the panel voltage will track the input ramp voltage. The simulated power dissipation generated by 4 linear input ramps is shown in figure 9.

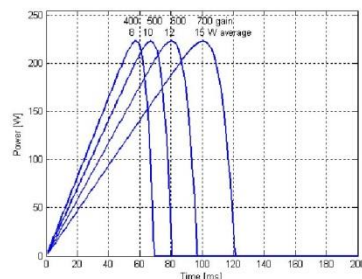
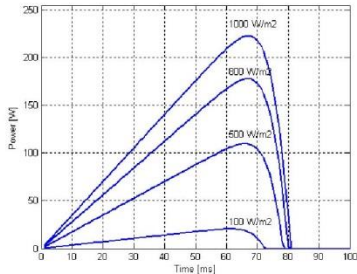


Figure 9. Power dissipation as function of time for 4 sweeps when linear voltage feedback is applied.

The simulated power dissipation generated by varying the irradiation level at a fixed input ramp is shown in figure 10.



**Figure 10.** Power dissipation for a voltage feedback system at a fixed linear sweep-rate as function of irradiation level (100-80-50-10% of STC).

By comparing figures 8 and 10 it can be observed that the voltage based regulation scheme has an advantage over the direct drive scheme regarding required sampling speed. Both schemes give comparable power dissipation as function of sweep time, but a considerable difference in the time available for recording the IV-values can be observed. A system with a direct drive mode will generate power curves, whose time duration will depend significantly on the irradiation level. As low cost microprocessor platforms have limited sample rates in general it is recommendable that scanning systems for PV-panels are not based on the direct drive scheme.

#### Initial test results

A prototype of the recording unit has been tested on a solar panel simulator with a peak power of 80W. An example of the power calculated from the logged IV-data per scan for 1 hour of continuous recording (3600 datasets) is shown in figure 11. The current and voltage values are sampled synchronously, within 200  $\mu$ s.

#### Conclusion and outlook

A stand-alone low-cost microprocessor platform including data storage has been designed for long-term recording of PV IV-characteristics. By default, the scan period is one second. During each scan 200 IV-values are measured and stored on an SD-card. Approx. 6 months of recordings can be stored on a 32 GB card. The implementation of a short scanning time lowers the demand for handling high power levels in the load circuitry, due to low average power dissipation.

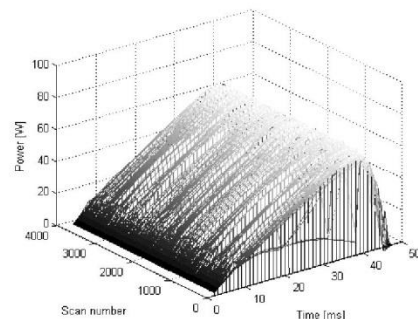


**Figure 11.** Calculated power dissipation for a direct drive scheme with a slew rate of 15 mV/ms, based on 3600 recorded scans over 1 hour on a solar panel simulator. A few bad scans, due to noise, are visible.

The real-time-clock functionality allows time stamps to be recorded as well as synchronous measurements done by several units. Future work will include wireless synchronization, supply via energy harvesting and PV-string scanning up to 15 kW.

This work has been supported by the Sunrise-PV project, which is partly funded by Syddansk Vækstforum and the European Regional Development Fund.

#### References

- 1 Quaschning et al. *Numerical simulation of current-voltage characteristics of photovoltaic systems with shaded solar cells*. Solar Energy Vol. 56, No. 6, page 513-520, 1996.
- 2 Arduino platform, Snoopdog SD card. [www.arduino.cc](http://www.arduino.cc); [www.snootlab.com](http://www.snootlab.com)
- 3 Allegro ACS758 datasheet.
- 4 Adamo et al. *Parameters Estimation of Photovoltaic Panels*. XIX IMEKO World Congress Fundamental and Applied Metrology, 2009, Lisbon, Portugal.
- 5 IEC 61215-4:2005 – Crystalline silicon terrestrial photovoltaic (PV) modules.
- 6 Garrigos . *Power MOSFET is core of regulated-dc electronic load*. EDN Network. March 17, 2005, page 91-92.
- 7 Kuai et al. *An electronic load for testing photovoltaic panels*. Journal of Power Sources no. 154, page 308–313. 2006.
- 8 IRF530 datasheet.
- 9 Mohan et al. *Power Electronics*. ISBN 978-0-473-22693-2.
- 10 SPR-225 datasheet, [www.Sunpowercorp.com](http://www.Sunpowercorp.com)

## **Appendix A3**

K.M. Paasch, M. Nyman and S.B. Kjær, “Distributed measurement system for long term monitoring of clouding effects on large PV plants”, *EPE’13 ECCE Europe 15<sup>th</sup> European Conference on Power Electronics and Application*, Lille, France, 2013.

# **Distributed measurement system for long term monitoring of clouding effects on large PV plants**

Kasper M. Paasch\*, Morten Nymand, Frerk Haase

University of Southern Denmark

Alsion 2

6400 Sønderborg, Denmark

Tel.: +45 – 65501695

Fax: +45 – 65501635

E-Mail: [paasch@mci.sdu.dk](mailto:paasch@mci.sdu.dk)

URL: <http://www.sdu.dk>

## **Keywords**

Electronic ballast, Solar cell system, Power plant performance, Thermal design

## **Abstract**

A recording system for the generation of current-voltage characteristics of solar panels is presented. The system is intended for large area PV power plants. The recorded curves are used to optimize the energy output of PV power plants, which are likely to be influenced by passing clouds and periods of overcast skies.

## **Introduction**

The system and approach presented in this paper is intended for R&D purposes and is based on the deployment of modular data storage/communication units for high speed measuring/recording of the current-voltage (IV) characteristics of PV panels/strings. The rapid price decline for photovoltaic systems has recently led to the construction of PV Power plants crossing the MW limit, so that today many plants of above 50 MWpeak (MWp) are in operation. See table I for examples. Owing to the rather low conversion efficiency of solar cells as well as local geographical conditions, PV plants of this size will occupy quite large areas of land.

## **Background**

The land area required to place a 1 MWp PV power plant using standard fixed tilt mounting and modules with 15% efficiency, varies from around 1 hectare in tropical regions to above 2 hectare in Northern Europe [1]. For comparison, wind mill farms typically require a total area of 34.5 hectare per MW on average, as shown in a study by NREL for 172 US-based wind mill farms [2]. The direct area is on average 0.3 ha/MW, but additional land between mills etc. is required. However this can eventually be used for agricultural purposes.

**Table I: Examples of large PV power plants in operation [3]**

Installed capacity	Location
97 MWp	Sarnia, Canada
84 MWp	Montaldo de Castro, Italy
82 MWp	Finsterwalde, Germany
70 MWp	Rovigo, Italy

Such large plants are thus expected to be influenced by slowly changing weather conditions, such as passing clouds, generating power production fluctuations [4]. The US National Renewable Energy Laboratory (NREL) has reported that clouds can be a challenge to large PV power plants and has initiated activities related to this field [5]. In order to model the expected annual outcome of large PV

plants, it is mandatory also to know the IV characteristics of the PV-panels used. However, to our knowledge, no datasets containing synchronized IV-curve measurements are publicly available for large PV plants. Our aim is to establish a database with measured IV-curves at different locations within the area of selected PV power plants. Designated panels inside a PV power plant are synchronously swept each second and the measured IV curves are used to optimize the annual plant energy output.

## PV plant configuration

The degree of fluctuation in energy production induced by partial shading /clouds will depend on the actual configuration of the site with respect to the wiring and inverter concept applied [6, 7]. Traditionally PVplant design follows one of two approaches: a large number of decentralized string inverters (for example with 25 PVpanels per inverter input / Max-Power-Point-Tracker (MPPT)), or with relatively few large central inverters (typically >500 kW each), each covering a large amount of solar panels. The use of many small string inverters in a single plant, such as the 5318 15 kW PV-inverters used in the 80 MWp plant Eggebek, Germany [8], is expected to be less sensitive to passing clouds due to local maximum power point tracking (3 MPPT per inverter, 20 panels per MPPT) than a plant of few large central inverters, where fluctuations will have an effect on a larger area [9, 10]. See figures 1a,b.

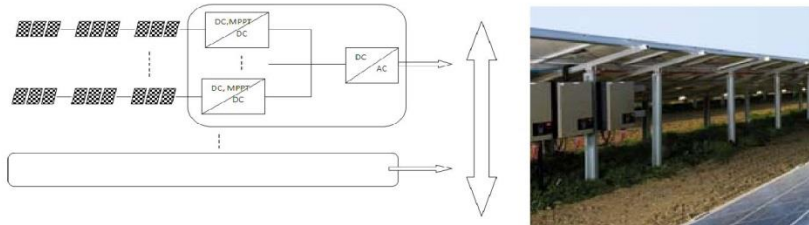


Fig. 1a,b: General concept for string inverters. Picture from Danfoss A/S

The sweep units are placed along the edge and in the center of a PV plant. See figure 2.

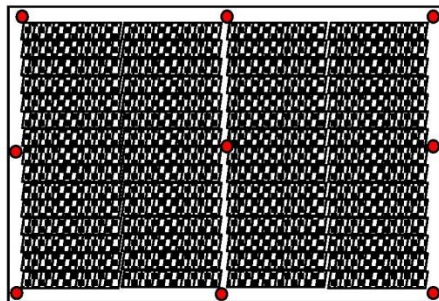


Fig. 2: Example of sensor unit placement in a large PV power plant. 9 sweep units (red) are evenly distributed along the edge and in the center.

The measurement system is intended to deliver time correlated sweep data for solar panels. The purpose is to record the current-voltage (IV)-curve of selected panels distributed over a large PV power plant by using a simple electronic load circuit. This generates a spatially distributed data set for a given test site in order to model the long term yield of the power plant.

## Design concept

The system consists of 3 main parts: A CPU-unit with Real-Time-Clock (RTC), communication means and SD storage, an analog interface/sweep unit and an electronic load unit. The main factors for choosing a suitable design are price and simplicity, due to the volume of systems expected to be deployed. The price constraints implicitly determine that the different elements including mechanics are to be kept as standard and simple as possible. General purpose CPU-platforms have over the last years become commercially available at a price level of \$100-150 for a system containing processor, analog I/O, digital I/O, onboard memory, communication means etc., as illustrated in figure 3. The first prototypes are based on low cost processor platforms including wireless communication, networking operability etc., with a custom made interface unit attached.

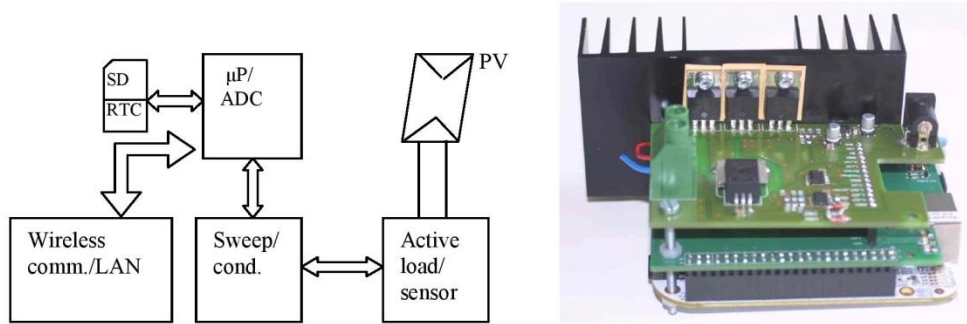


Fig. 3a,b: a) System building blocks b) Prototype sweep unit installed on the Beaglebone platform

The electronic load circuitry is based on power MOSFETs as the active load. In order to obtain short circuit current ( $I_{SC}$ ) measurement, the current is monitored by an integrated Hall-effect sensor with an insertion impedance of  $100 \mu\Omega$  [11]. Using a source resistor as an alternative would introduce a series impedance in the current path, influencing the  $I_{SC}$  measurement even when the MOSFET is driven into its on-stage. This is not critical when the focus is to analyze around the maximum power point (mpp), but the Hall-effect sensor allows a more general use due to its high current capability (50A in the implemented version). See figure 4.

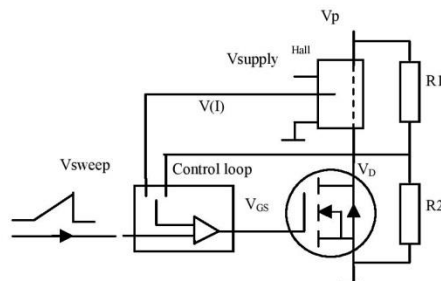


Fig. 4: Schematic view of the active load unit, showing one transistor.  $V_p$ =photovoltaic panel input, Hall = Hall effect based current sensor.

The principle of voltage controlled and current controlled feedback ( $V(I)$ ) is shown together with a triangular input sweep signal.  $R_1$  and  $R_2$  determine the feedback voltage level. The transistor illustrated symbolizes a transistor block which can consist of several transistors in parallel, depending on the resulting thermal design.

## Sweep time estimation

Special focus has been on the selection of a proper sweep time. The optimum sweep time can be determined by considering three design considerations: the average power dissipation in the active load, the error induced via the capacitance of the solar panel, and the sampling speed of the CPU-platform used.

## Power dissipation

The power dissipation of the active load will determine the physical size as well as the price of each sensor module. The aim is thus to minimize the power dissipation as much as reasonably possible by performing fast sweeps of the IV-curve. The average power dissipation can be calculated by eq. 1, where  $T_{\text{sample}}$  is the time interval between the IV-sweeps,  $P_{\text{load}}(t)$  is the time dependent power dissipation function dominated by the solar panel characteristics and  $t_{\text{sweep}}$  is the sweep time for each scan of the IV-curve.

$$P_{\text{av}} = \frac{1}{T_{\text{sample}}} \int_0^{t_{\text{sweep}}} P_{\text{load}}(t) dt \quad (1)$$

The present system is designed for scanning a 250Wp solar panel at STC (Standard Test Conditions, 1000W/m<sup>2</sup>, 25 °C) once every second. In order to minimize the average power dissipation  $P_{\text{av}}$  it is thus advantageous to keep the sweep time  $t_{\text{sweep}}$  at a minimum. In order to estimate the power dissipation and thus the needed cooling requirements, a system model has been implemented, based on the classical one-diode model of a solar cell [12] shown in figure 5.

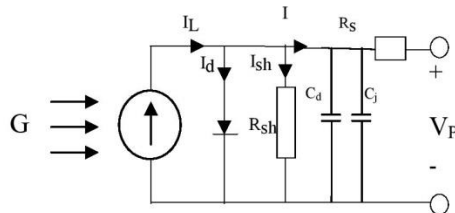


Fig. 5: One-diode model of a PV-cell [12], but modified with capacitors  $C_d$  and  $C_j$ . The capacitors are not considered in the first stage of the investigation.

The one-diode dc model IV-characteristics from figure 5 are given by Eq. 2. The capacitors are not considered at this stage.

$$I = I_L - I_0 \left( e^{\frac{q(V_p + R_s \cdot I)}{n \cdot q \cdot T}} - 1 \right) - \frac{V_p + R_s \cdot I}{R_{\text{sh}}} \quad (2)$$

$I_0$  is the diode reverse saturation bias current.  $G$  is the solar irradiation level in W/m<sup>2</sup>,  $k$  is Boltzman's constant,  $q$  is the electron charge,  $n$  is the ideality factor of the junction (between 1 and 2). For an estimation of  $R_{\text{sh}}$  and  $R_s$  see [12].  $R_s$  is normally neglected in simulations due to its small size. The short circuit current  $I_{\text{SC}}$  and the open circuit voltage  $V_{\text{OC}}$  at  $T_{\text{ref}}$  are typically stated by the solar panel manufacturer. The subscript ref refers to the Standard Test Conditions (STC:  $T_{\text{ref}}=25^\circ\text{C}$ ;  $G_{\text{ref}}=1000\text{W/m}^2$ ) [13]. A closed-form exact solution of eq. 2 for the unknown current  $I$  is not available, so numerical methods should be applied. A Newton-Raphson method has been applied in this study, following the approach outlined in [12]. It is observed that the instantaneous power  $P_{\text{load}}$  dissipated in the MOSFET can be written as presented in eq. 3, a function of the drain voltage  $V_{\text{DS}}$  ( $=V_p$ ), the gate-source voltage  $V_{\text{GS}}$ , the threshold voltage  $V_{\text{th}}$  and the MOSFET specific constant  $K_n$  related to the internal geometry [14]. The MOSFET is operated in the active region for  $V_{\text{GS}} > V_{\text{th}}$ .

$$P_{\text{load}} = V_{\text{DS}} \cdot \frac{k_n}{2} (V_{\text{GS}} - V_{\text{th}})^2 \quad (3)$$

A simulation for a voltage controlled feedback, where the panel voltage is varied linearly, is shown in figure 6 for 5 different sweep times, indicating an average power dissipation of 6-17W for sweep times between 45 and 120 ms.

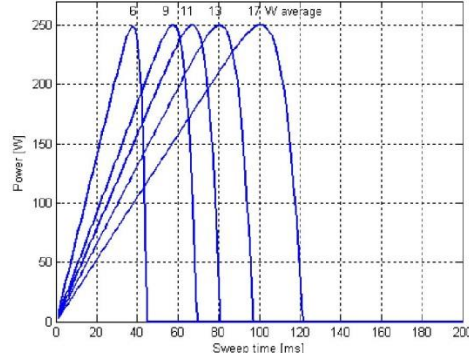


Fig. 6: Simulated power response for 5 different sweep times via voltage feedback for a 250W solar panel,  $T_{\text{sample}}=1\text{s}$ .

It can be shown that a voltage based regulation scheme has an advantage over the direct drive scheme regarding required sampling speed [14]. Both schemes give comparable power dissipation as function of sweep time, but a considerable difference in the time available for recording the IV-values can be observed. The approximate average power dissipation for a sweep time  $t_{\text{sweep}}$  can be calculated by applying eq. 1 under the assumption that  $P_{\text{load}}(t)$  can be described by the linear relationship given by eq. 4.

$$P_{\text{load}}(t) = \frac{P_{\text{panel}}}{t_{\text{sweep}}} t \quad (4)$$

The average power dissipation can then be determined via equations 1 and 4.

$$P_{\text{av}} = P_{\text{panel}} \frac{t_{\text{sweep}}}{2 \cdot T_{\text{sample}}} \quad (5)$$

The simulated response obtained by applying eq. 2-5 compared with the approximate response represented by eq. 5 for a sweep time around 45 ms are shown in figure 7. It can be observed that both methods, although not having the max power point at the same time step, give almost similar average power levels. Eq. 4 can thus be used for further analysis.

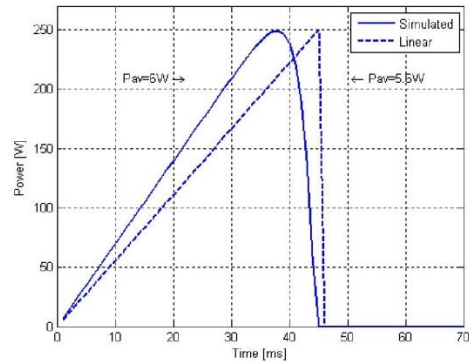


Fig. 7: Comparison of simulated and approximated response when scanning a 250W solar panel

### Panel capacitance

The average power dissipation is close to a linear function of the sweep time  $t_{\text{sweep}}$ , so a fast sweep time seems preferential. However, a minimum sweep time is determined by the other factors like available sampling rate of the CPU-unit, the ac-characteristics of the solar cell and the effective transient thermal impedance. A fast sampling speed is no problem for modern CPU-boards such as the Beaglebone from TI, but the dynamic behavior of solar cells and the transient thermal impedance (to be discussed later) must be taken into consideration. Solar panels are traditionally modeled as dc sources due to slow temporal sunlight variations, but fast scanning of solar panels need to take the module ac-characteristic into account [15]. As illustrated in figure 5, the solar cell capacitance can be modeled as a diffusion capacitance  $C_d$  in parallel with a junction capacitance  $C_j$  [16]. The solar cell capacitance can be shown to exhibit a nonlinear characteristic as a function of both the operating voltage  $V_d$  and the cell temperature [17]. Junction capacitance values for different types of Si-based solar cells have been reported in literature, ranging from 6.5 to approx. 60 nF/cm<sup>2</sup> (see table II).  $C_{j0}$  indicated  $C_j$  with zero applied voltage.  $C_j$  can be approximated from  $C_{j0}$  via eq. 6, where  $V_d$  is the solar cell voltage and  $V_{bi}$  is the built-in potential of the PN-junction.

$$C_j = \frac{C_{j0}}{\sqrt{1 - \frac{V_d}{V_{bi}}}}; V_d < V_{bi} \quad (6)$$

**Table II: Capacitance data compiled from literature**

Cell/panel type	$C_{ix}$ [ $\mu$ F]	Area[cm <sup>2</sup> ]	$C_{ix}/\text{area}$ [nF/cm <sup>2</sup> ]	Note	Ref.
Poly	12.5	240	52.1	$C_{j0}$	[16]
Mono	5.0	240	20.8	$C_{j0}$	[16]
BC-Mono	1.0	153	6.5	$C_{j0}$	[16]
Mono	4.50	--	--	$C_{j0}$	[16]
Mono	5.70	--	--	$C_{j0}$	[16]
Mono	5.30	--	--	$C_{j0}$	[16]
Mono	4.70	--	--	$C_{j0}$	[16]
Panel, Mono	1.43	--	--	4 cells, $C_{j0}$	[16]
Si		78.5	50	$C_{j,mpp}$	[17]
Panel, Si	0.166	--	--	27 cells, $C_{j,mpp}$	[17]

Figure 8 presents compiled solar cell capacitance values found in literature, as function of the cell voltage. Values have been extracted from plots. Calculated  $C_j$ -values (eq. 6) for the 20.8 nF/cm<sup>2</sup> mono-crystalline cells shown in table II are inserted for comparison.

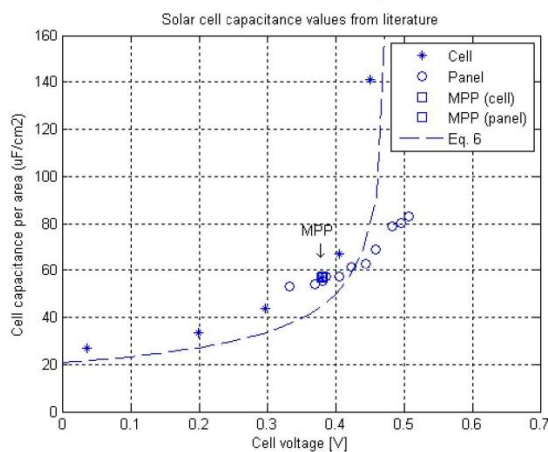


Fig. 8: Solar cell capacitance data from literature [17]. \*: single cell o: extracted from panel data; □: max-power-points, --:  $C_j$  values from eq. 6 for  $c_{j0}=20.8$  nF/cm<sup>2</sup> [16].

It can be observed that the capacitance at mpp is approx. twice the value of  $C_{j0}$ . At  $V_{oc}$ , the value can be as high as 25 times  $C_{j0}$ .

The junction capacitance  $C_j$  dominates the resulting cell capacitance and the analysis performed on the published data indicate that for a mono-crystalline cell capacitance in the order of  $50-100 \text{ nF/cm}^2$  around the mpp is to be expected. The value for a poly-crystalline cell will be about twice as high. The capacitance of a solar panel with  $n$  cells in series can thus be calculated as  $n$  capacitors of value  $C_{j,mpp}$  connected in series. The resulting panel capacitance  $C_{panel,mpp}$  around mpp can thus be calculated as

$$C_{panel,mpp} = \left[ \sum_{i=1}^n \frac{1}{C_{j,i}} \right]^{-1} \quad (7)$$

Inserting eq. 6 and assuming that all cells are equal yields

$$C_{panel,mpp} = \frac{1}{n} \frac{C_{j0}}{\sqrt{1 - \frac{V_{mpp}}{V_{bi}}}}; V_d < V_{bi} \quad (8)$$

Taking as an example a 250W mono-crystalline panel consisting of 72 silicon cells of approx.  $12 \times 12 \text{ cm}$  ( $144 \text{ cm}^2$ ), the panel will at the max-power-point exhibit a capacitance in the order of  $100-200 \text{ nF}$ . The scanning of the panel IV-curve will be influenced by the module capacitance, depending on the slope/direction of the scan [18]. This effect is shown in figure 9, where the effect is simulated in SPICE-based software (Multisim 12) using a 1-diode model in parallel with a  $200 \text{ nF}$  capacitor. It has further been shown that for fast scans (in the low ms range) the IV-curve will exhibit significant hysteresis around the mpp and thus generate a measurement error compared to a quasi static value [16]. Note that for the 25 ms situation there is no hysteresis visible on the IV-curve.

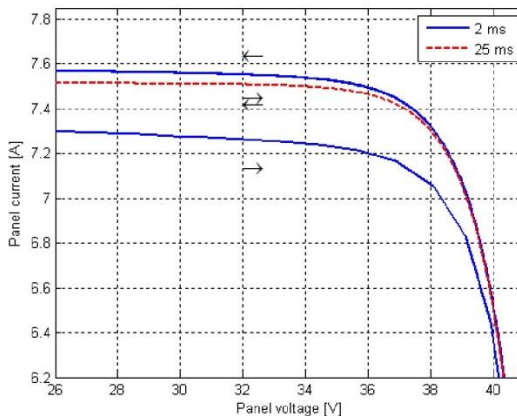


Fig. 9: Simulated IV-curves for a 72 cell solar panel with hysteresis due to an internal  $200 \text{ nF}$  module capacitance for a high irradiation level of approx.  $800 \text{ W/m}^2$ . A 1-diode model is applied. A saw tooth shaped sweep pattern with equal rise- and fall times has been applied. Red curve: 25 ms. Blue curve: 2 ms. Arrows indicate sweep direction.

Simulations of both dynamic sweep characteristics and comparable point-to-point quasi static measurement have been analyzed in [16]. It has been shown that a resulting error in the range of 9% from the quasi-static values around mpp can be expected under low irradiation conditions. In order to obtain a measurement error below 0.5%, the minimum allowed sweep time has to be in the order of 5 ms for poly-silicon cells, 10 ms for mono-silicon cells and 50 ms for backside connected mono-silicon cells. The effect of the irradiation level on the resulting error also has to be considered and when

sweeping the IV-curve, the RC time constant  $\tau_C$  should be taken into account. A simplified equation for  $\tau_C$ , assuming  $R_{SH} \gg R_S$  has been derived in [16].

$$\tau_C = \frac{\tau_d}{2} \frac{I_{dl}}{(I_{dl} + \frac{V_T}{R_s})}; V_d < V_{bi} \quad (9)$$

$\tau_d$  is the base minority carrier lifetime of the cell,  $I_{dl}$  is the current thru diode D1,  $R_s$  is the shunt resistance and  $V_T$  is the thermal voltage. This time constant, although as small as in the 40-50  $\mu s$  range, has an impact on the measurement error. It has further been shown that although the time constant decreases with decreasing irradiation, the total measurement error and thus the optimal scan time will be moderately increased. It is argued that a moderate increase of error at lower irradiance levels should be expected, due to the charging/discharging conditions. At the imposed limit of 0.5% up to 32% increase for polycrystalline silicon solar cells at irradiance levels of 200  $W/m^2$  is to be expected, compared to 1100  $W/m^2$ . As the sweep unit is intended for measuring any standard panel up to 250 W, the estimated measurement error approach for a backside connected mono-silicon panel is applied. The minimum sweep time as function of allowed error has been compiled from graphical data published. The average power dissipation (eq. 5) is shown in figure 10 as function of sweep time, together with vertical lines representing the estimated measurement error for selected sweep times. As stated earlier an error of 0.5% imply a minimum sweep time of around 50 ms.

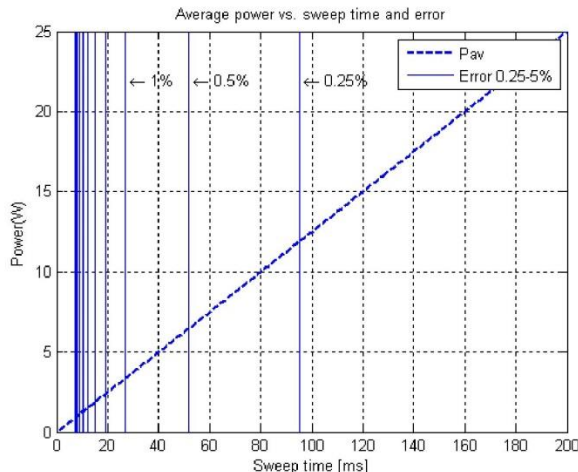


Fig. 10: Average power dissipation as function of sweep time. Vertical lines represent the estimated measurement error for the given sweep time in the range of 0.25-5%.  $P_{panel}=250W$ ,  $T_{sample}=1s$ .

In order to keep the error below 0.5% it is advisable to keep the sweep time as high as reasonably possible above the 50 ms range. A sweep time of 50 ms will under STC thus generate an average power dissipation of around 7W. As the load pattern has an impulse like shape is it further required to include the effective transient thermal coefficient  $Z_{0JC}$  in the calculation of the thermal requirements for the load circuit / heat sink [19]. Therefore the allowable sweep time not just has a lower bound owing to the module ac-characteristics (dominated by the capacitance) and a higher bound is set by the allowed average power dissipation  $P_{av}$ . The maximum allowed junction temperature  $T_J$  determines the allowed impulse energy via the effective transient thermal coefficient  $Z_{0JC}$  for the given transistor.

An average power level of 7W in a TO220 housing with  $R_{0JC}=0.5$  could be expected to be handled by applying a heat sink with a thermal resistance  $R_\theta$  of approx.  $4^\circ C/W$  for  $T_{ambient}=40^\circ C$ , giving a  $T_J$  and a  $T_{case}$  in the order of  $80^\circ C$  and  $70^\circ C$ , respectively. But the load circuit will for a 250W panel under STC in the given application experience a transient impulse of around 30 ms (duty cycle 0.03, 7.5 Joule), resulting in a  $Z_{0JC}$  in the order of  $0.5^\circ C/W$  for a typical MOSFET with TO220 housing. Due to the

transient nature of the sweep the maximum junction temperature  $T_J$  must be determined from the peak pulse power  $P$  and  $Z_{0JC}$  via eq. 10 [19] and not from the calculated average power level of 7W.

$$T_J = P \cdot Z_{0JC} + T_{case} \quad (10)$$

$T_J$  will acc. to eq. 10 be in the order of 195°C for a 7.5 Joule impulse per second, assuming a  $T_{case}$  of 70°C. This will destroy a standard Si-transistor.  $T_J$  is thus dominated by the peak power and not the average power level, so a single transistor load with a TO220 housing is not sufficient. It can be shown that a maximum allowed junction temperature  $T_J$  of 110°C implies the parallel use of 3 transistors, dividing the power equally between them. A control loop per transistor is necessary to ensure proper current splitting during the transient. A high-current transistor with a large chip like the IRFP4468 in a TO247AC housing with a  $Z_{0JC}$  in the range of 0.2°C/W is marginally capable of handling the transient power in the present application. The number of transistors needed in this application is thus determinated not only by the average power dissipation but also by the effective transient thermal coefficient  $Z_{0JC}$ .

## Test results

Initial testing performed on a basic solar panel simulator circuit setup has been done. Figure 11a shows data measured/ recorded for a scanning sequence of approx. 1 hour with one sweep per second. Figure 11b shows a comparison between the established model and a selected power curve.

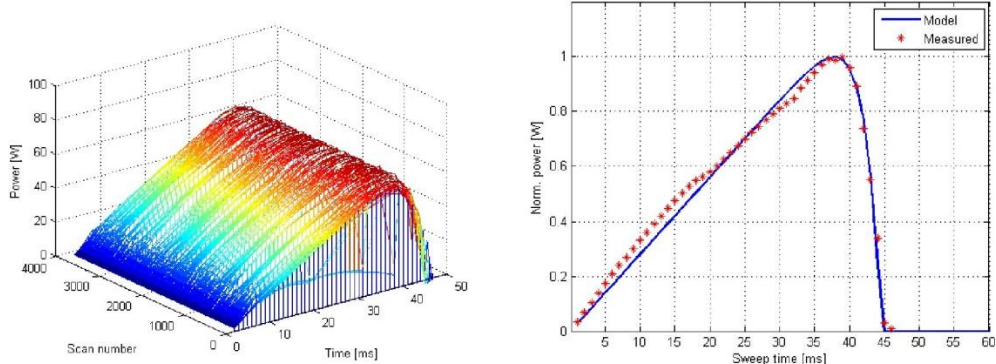


Fig. 11a,b: a) Approx. 1 hour of scanning data with 1 scan per second. b) Comparison of simulated IV-curve vs. measured curve on a simulator (1 min average).

## Conclusion

The concept presented in this paper enables fast monitoring of the fluctuations induced by clouds passing large PV plants as well as residential units. Low cost off-the-shelf microprocessor based hardware platform are suitable as platforms for IV-scanning units. These observations enable investigation of the performance of MPPT algorithms and inverter concepts under varying illumination conditions. The low cost distributed measurement system designed contains a number of operational PV sweep units, capable of scanning and recording IV-curves from a solar panel with nominal power rating in the order of 250W. The design of the analog load/sweeping unit has been optimized regarding average power dissipation and thus price and it has been shown that the average power dissipation can be limited to around 1/20 of the rated PV module power. But the transient nature of the swept power curve implies the use of the transient thermal impedance of the transistor housing, being a dominant factor for the actual circuit design. Further reduction in average power via faster scanning time will, due to a hysteresis effect caused by the internal capacitance of the solar panel, increase the theoretical measurement error.

## References

- [1] Wolfe, P.: Solar photovoltaic projects in the mainstream power market. Oxford: Earthscan; Routledge. ISBN: 978-0-415-52048-5.
- [2] Denholm P. et al.: Land-use requirements of modern wind power plants in the United States. Technical Report NREL/TP-6A2-45834, August 2009. National Renewable Energy Lab., USA.
- [3] Top 100 PV plants map. PV balance of system conference & exhibition, Berlin. 28-29 June 2011.
- [4] Jewell Ward T. et al.: Limits on cloud-induced fluctuation in photovoltaic generation. IEEE Transactions on energy conversion., Vol. 5, 1990, pp. 8-14.
- [5] NREL News Release NR-4411, NREL data set shows clouds' effects on solar power. August 31, 2011.
- [6] Gao L. et al.: Parallel-connected solar PV system to address partial and rapidly fluctuating shadow conditions. IEEE Transactions on industrial electronics, vol. 56, 2009, pp. 1548-1556.
- [7] Grumpos Peter et al.: A generic approach to the shadow effect of large solar power plants. Solar cells, vol. 22, 1987, pp. 29-46.
- [8] Onze, A.G.: Optimized System layout – the practical experience of 80 MW Eggebek plant realized with a multiple MPPT string inverter concept. Presented at the 2<sup>nd</sup> PV inverter forum, Berlin, 2012.
- [9] Xiaoli Z. et al.: Design of MPPT Algorithm under Partial Shadows. IEEE international conference on electric information and control engineering (ICEICE) 2011.
- [10] Patel H. et al.: MATLAB-based modeling to study the effects of partial shading on PV array characteristics. IEEE Transactions on energy conversion, vol. 23, 2008, pp. 302-310.
- [11] Allegro ACS758xCB data sheet. Thermally enhanced, fully integrated, Hall effect-based linear current sensor IC with 100  $\mu\Omega$  current conductor.
- [12] Adamo et al.: Parameters estimation of photovoltaic panels. XIX IMEKO world congress fundamental and applied metrology, 2009, Lisbon, Portugal.
- [13] IEC 61215-4:2005 – Crystalline silicon terrestrial photovoltaic (PV) modules.
- [14] Paasch Kasper et al.: Sensor system for long-term recording of photovoltaic (PV) IV-curves. PVSAT-9 conference, 2013, Swansea, UK.
- [15] Chenvidhya D.: PV module dynamic impedance and its voltage and frequency dependencies. Solar energy materials & solar cells journal, 2004, Vol.86, Issue2, pp.243-251.
- [16] Herman M. et al.: Optimal I-V curve scan time of solar cells and modules in light of irradiance level. International journal of photoenergy, vol. 2012, article ID 151452.
- [17] Kumar R. et al.: Effect of solar array capacitance on the performance of switching shunt voltage regulator. IEEE transactions of power electronics, vol. 21, no. 2, March 2006.
- [18] Merhej P. et al.: Effect of capacitance on the output characteristics of solar cells. 2010 Conference on Ph.D. research in microelectronics and electronics (PRIME), Berlin. ISBN: 978-1-4244-7905-4.
- [19] Mohan et al.: Power electronics. 3<sup>rd</sup> ed.. ISBN: 978-0-471-22693-2.

## **Appendix A4**

K. Paasch, M. Nyman and S.B. Kjær, "Simulation of the impact of moving clouds on large scale PV-plants", *IEEE 40th Photovoltaic Specialist Conference (PVSC)*, 2014, Denver, USA.  
DOI: 10.1109/PVSC.2014.6925036

# Simulation of the impact of moving clouds on large scale PV-plants

Kasper M. Paasch, Morten Nyman and Søren B. Kjær

University of Southern Denmark, Alsion 2, 6400 Sønderborg, Denmark  
University of Southern Denmark, Niels Bohrs Allé 1, 5230 Odense, Denmark  
Danfoss Solar Inverters A/S, Nordborgvej 81, 6400 Sønderborg, Denmark

**Abstract** — A tool for the impact of moving clouds on the power production large scale PV plants has been developed. Focus is on the comparison of different inverter topologies (string vs. central) under real time weather conditions. The effect of a given clouding situation can be simulated and the resulting available DC output power and maximum power point variation, as well as the resulting AC production during passage can be analyzed for a range of representative clouding situations. The developed model include PV plant surface topology (individual panel orientation), irradiation level, panel temperatures, panel mismatch and inverter efficiency characteristics.

**Index Terms** — numerical simulation, photovoltaic system, photovoltaic cells, power system modeling.

## I. INTRODUCTION

This paper presents an approach for modeling the effect of moving clouds on the energy production of large PV plants. The land area required to place a PV power plant using standard fixed tilt mounting and modules with around 15-20% efficiency varies from around 1 hectare ( $10,000\text{m}^2$ ) per MWp in tropical regions to above 2 hectare per MWp in Northern Europe [1]. Large PV plants in the MW range are thus expected to be influenced by passing clouds, generating power production fluctuations [2]. The US National Renewable Energy Laboratory (NREL) has reported that clouds can be a challenge to large PV power plants and has initiated activities related to this field [3].

The degree of fluctuation in energy production induced by clouds is expected to depend on the actual configuration of the PV plant with respect to the wiring and inverter concept applied [4]-[7]. PV plant design traditionally follows one of two approaches: a large number of decentralized string inverters (for example with 24 PV panels per inverter input / Max-Power-Point-Tracker (MPPT)), or with fewer large central inverters (typically  $>500$  kW each), each covering a large amount of solar panels. See Fig. 6 and 7.

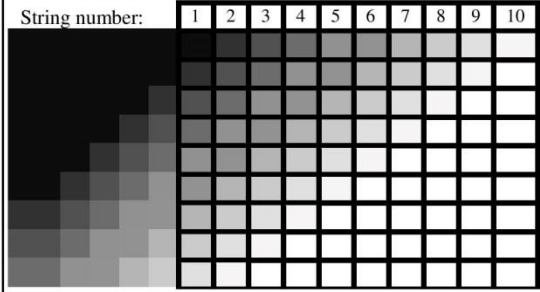
The use of many small string inverters in a single plant, like the 5318 15 kW PV-inverters used in the 84 MWp plant Eggebek, Germany [8], is expected to be less sensitive to passing clouds due to local maximum power point tracking, compared to a plant of few large central inverters where fluctuations will have an effect on a larger interconnected area [9].

## II. MODELING

Non-uniform irradiation conditions of PV plants have earlier been studied in literature [4], but the effect of fast moving clouds on the Max Power Point Tracking performance has not been identified. The model developed compares the power production of a groups of PV-strings, each with its own string inverter, with the same number of strings paralleled to one central inverter. The simulation is performed on module level and bypass as well as blocking diodes are included in the model. Due to the given voltage limit of 1000 volt per string/array the number of panels in a series connection has initially been limited to around 24 panels when standard 250W panels with  $U_{oc}$  @STC around 40V are considered. The model is based on the approach presented in [10], whose algorithms constitute the core of the simulations. The proposed approach is optimized to include an arbitrary cloud pattern (represented by a sliding shading matrix) moving in any direction resulting in a decrease of irradiation at module level. A simple linear shadow front is illustrated in table 1.

Any parameter having an effect on the resulting power

String number:	1	2	3	4	5	6	7	8	9	10



production of each panel, such as temperature, angles of orientation etc. can be modelled by adding additional sliding matrices. It is thus possible to compare the PV power production of different inverter configurations under arbitrary ambient conditions.

#### A. PV cell model

The simulation is based on the classical one-diode model of a solar cell [4] shown in Fig. 1.

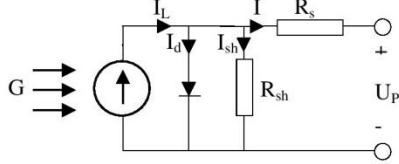


Fig. 1. One-diode model of a PV-cell [4].

The model IV-characteristics ( $I, U_p$ ) of a solar cell are described by (1)-(5), where  $G$  is the solar irradiation level,  $k$  the Boltzmann's constant,  $q$  the electron charge,  $n$  is the ideality factor of the junction (1-2). Knowledge of the open circuit voltage  $V_{oc}$ , the temperature constants  $\alpha$  (current) and  $\beta$  ( $U_{oc}$ ) and the saturation current is mandatory to complete the model.

$$I = I_L - I_0 \left( e^{\frac{q(U_p + R_s \cdot I)}{n \cdot k \cdot T}} - 1 \right) - \frac{U_p + R_s \cdot I}{R_{sh}} \quad (1)$$

$$I_L(T) = I_L(T_{ref}) + \alpha(T - T_{ref}) \quad (2)$$

$$I_L(T_{ref}) = I_{SC}(T_{ref}) \frac{G}{G_{ref}} \quad (3)$$

$$I_0(T_{ref}) = \frac{I_{SC}(T_{ref})}{\left( e^{\frac{qU_{OC}(T_{ref})}{n \cdot k \cdot T_{ref}}} - 1 \right)} \quad (4)$$

$$U_{OC}(T) = U_{OC}(T_{ref}) + \beta(T - T_{ref}) \quad (5)$$

$R_{sh}$  and  $R_s$  are the equivalent shunt and series resistances and are derived from panel data [11]. A closed-form exact solution of (1) for the unknown current  $I$  is not available and a Newton-Raphson numerical method has been applied in this study.  $G_{ref}$  and  $T_{ref}$  are STC reference values STC (Standard Test Conditions; 1000 W/m<sup>2</sup>, ATM 1.5, 25°C) [12].

#### B. System topology

The input for the simulations include arbitrary cloud pattern/shading profile and irradiation level, panel temperature (both static and as function of shading), aging effect as well as the site topology itself. The orientation of a given PV panel is likely to follow the surface topology of the land (due to the costs related to planning an area) and thus cause small differences in irradiation on the interconnected panels. These differences will generate differences in the individual IV-characteristics and thus cause mismatch between the panels. Fig. 2 illustrates the curvature of a part of the new 2.1 MW Danfoss Solar Park in Denmark.



Fig. 2. Topology of a section of the 2.1 MW Danfoss Solar Plant at the Danfoss A/S corporate headquarter on the island of Als in Denmark.

### III. RESULTS

Different PV systems layouts have been simulated with respect to DC power generation as function of shadow fronts.

The concept has been tested on a small 4x4 PV array, consisting of 100W mono crystalline panels (type Prevent SM636-100), located on the roof of the SDU Photovoltaic test site at the Mads Clausen Institute in Sønderborg, Denmark. Measurement of the IV-characteristics of the 4x4 matrix by applying artificial shadowing of individual panels has been compared to the simulation of the same system. The shadowing is applied from the lower left corner of the matrix. Fig. 3 illustrates the shading method, applying multiple layers of shading material. The transparency of the foils covering each panel is given in table II.



Fig. 3. Test panels with partially covered modules, interconnected in a 4x4 matrix. The inserted photo shows a close-up of shading foil layers on a panel.

The applied test patterns are shown in table II, each shading type represents a specific attenuation factor.

TABLE II  
TEST PATTERN FOR THE 4x4 MATRIX

	Pos. 1	Pos. 2
100%		
92%		
84%		
73%		
67%		
	Pos. 3	Pos. 4

The measured PV-curves as well as the simulated curves are shown in Fig. 4. It can be observed that the simulation follow the measured PV-curves well. The curves are recorded at different temperatures, causing minor displacements of the curves. The PV sweep instrument used is a SOLIAMetre.

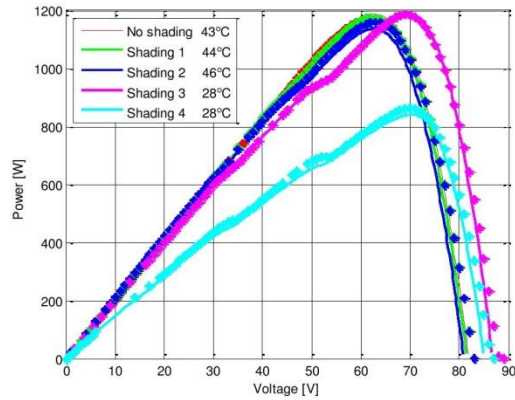


Fig. 4. 4x4 test matrix. Measured (--) and simulated (\*) PV-curves for different partial shading conditions and temperatures, acc. to Table II.

The measured PV-curves are for visual comparison recalculated to STC and normed to the max-power-point of the curve obtained under uniform illumination. See Fig. 5. Partial shading will generate a deviation from the curve for uniform illumination and this is confirmed by both the measured and the simulated results. Calculating the measured data back to STC, as shown in figure 5, clearly show the expected behavior. The test of the developed model on a 4x4 matrix of 100W PV panels has shown the validity of the model and the simulation platform tested above has further been applied for the simulation of two larger PV-structures with varying shading conditions. A custom system for long term recording of IV-curves of selected panels has been suggested and will be implemented in future tests [13].

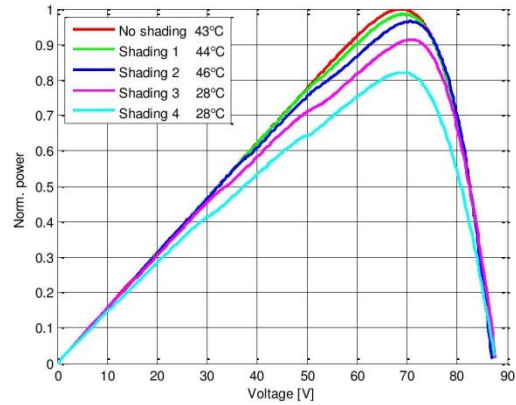


Fig. 5. Measured power/voltage curve of the 4x4 panel matrix, data recalculated to STC.

A simulation of a small PV system, consisting of 90 220W modules is shown below. See Fig. 6 and 7.

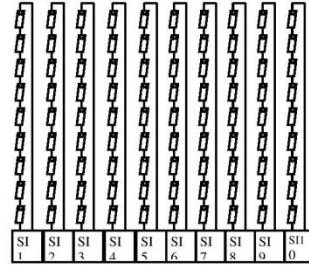


Fig. 6. PV-configuration with 10 strings and 10 independent inverters/MPP.

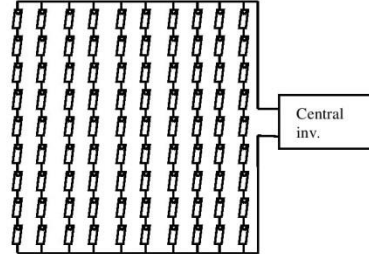


Fig. 7. Configuration with 9x10 panel array and one central inverter.

The resulting power output of the panels in the two configurations has been simulated, based on the approach described above. The diagonal shading pattern shown in Table I has been applied, arriving from west (equivalent to a straight shadow front from North-West (NW) with a transmission

factors linearly distributed from 1 (no shading) to 0.3 (heavy shading) with steps of 0.035.

The initial intensity and temperature is for the shown simulation held at Standard Test Conditions. Fig. 8 illustrates the available DC input power for the string inverter and the central inverter configurations during the passing of a heavy shading front as illustrated in Table 1 (finally leaving the panels in uniform shaded conditions).

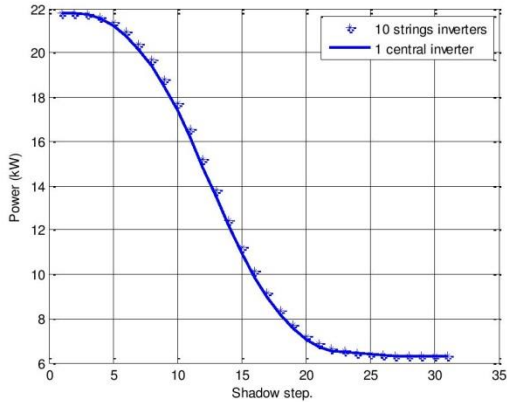


Fig. 8. Power production for the 2 configurations (10 string inverters versus one central inverter).

The percentage difference between the power productions for both systems is shown in Fig. 9.

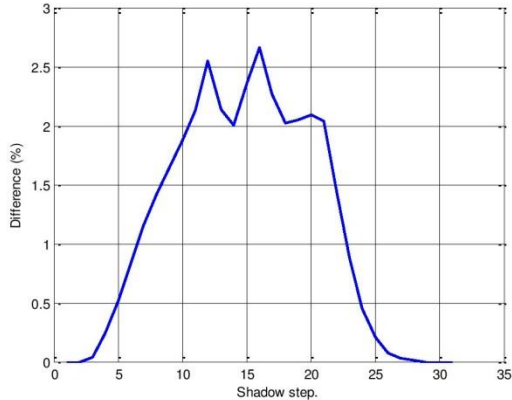


Fig. 9. Percentage gain in DC power production by using a string inverter concept, compared to a central inverter concept, as function of shadow front position.

For the string inverter concept each inverter independently will follow the 10 different max-power-points per individual string, but the central inverter will follow the combined IV-curve of the whole array of panels as shown. The example above show that the difference in this example peaks around

2% (equal to 350 Watt), showing the expected advantage for the string inverter concept.

As another example the available DC power for a 108 kWp system has been simulated for a fast change in irradiation over around 1 minute. The irradiation profile used was measured on October 15, 2014, at the SDU PhotoVoltaic test site, with a temporal resolution of 1 second. See Fig. 10 and 11. Note the fast changing irradiation pattern due to moving clouds in Fig. 10, showing more than 3 hours of irradiation data. The peak indicated by the arrow is extended in Fig. 11 and used for the simulation.

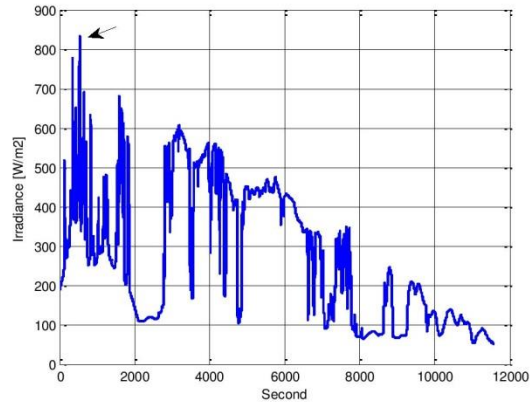


Fig. 10. Irradiation profile for the afternoon of October 15, 2013.

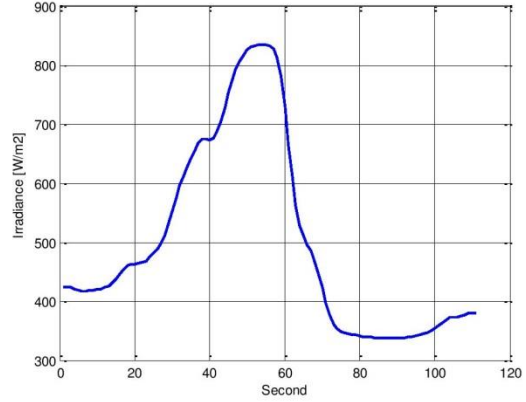


Fig. 11. Selected irradiation profile section used in the simulation.

The system has again been modeled in two configurations: a) with string inverters (20 strings with 24 panels per string) and b) with a central inverter connected to an array of 24x20 panels. The panel type used in the simulation is Sharp ND-225R1J, as mounted in the Danfoss Solar Park.

Two weather situations have been simulated, the intensity profile approaching perpendicular from left (west:  $270^\circ$ ) and from southwest ( $225^\circ$ ) to the string orientation.

Fig. 12 and 13 show the results of the profile approaching from west. It can be observed that the string and central inverter concept with an intensity profile approaching from left generate very similar power profiles. This was expected, due to the uniform illumination across each string by applying a profile perpendicular to the orientation of the strings

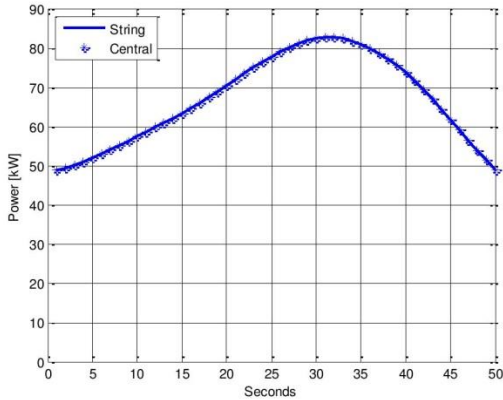


Fig. 12. Power production for the 2 configurations (20 string inverters versus one central inverter).

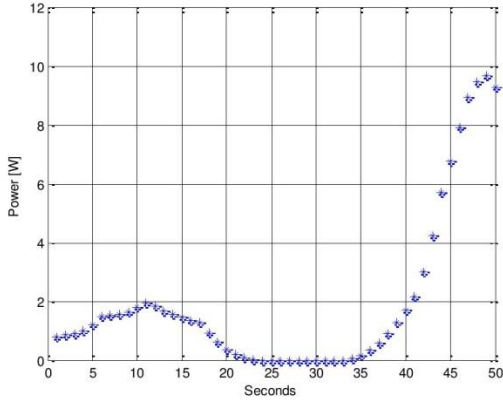


Fig. 13. Difference in DC power production by using a string inverter concept, compared to a central inverter concept, as function of intensity profile passing.

Fig. 14 shows the result of the same intensity profile approaching from southwest. Applying the same intensity profile from Southeast result in a much higher difference between the string inverter and the central inverter concept, with a peak difference in the order of 40%. This clearly shows the advantage of the string inverter concept compared to the central inverter concept under the intensity profile applied.

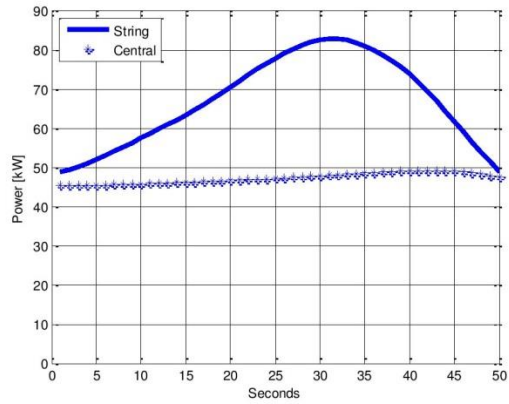


Fig. 14. DC power production by using a string inverter concept and a central inverter concept, as function of intensity profile passing in diagonal direction.

Any implemented MPP algorithm in an inverter will need time to locate the new MPP, thus losing power during the process. The variation of the MPP voltage as function of the shadow front position in the central inverter configuration has been analyzed under dynamic conditions. The actual speed of the shadow front over ground and the tracking behavior of the implemented MPP algorithm will have an effect on the PV plant energy production.

Additional losses such as DC cabling losses as well as detailed inverter efficiency characteristics can be included in the model to estimate the annual difference in energy production for the different inverter topologies.

#### IV. CONCLUSION

A modeling approach for the investigation of the effect of partial shading such as for example a moving cloud pattern, on the power generation of a large PV plant has been developed. Partial shadowing of PV panels in a 4x4 configuration has been used to validate the concept.

Examples of the differences between a string-based inverter concept and a central inverter system has been analyzed with respect to the effect of moving clouds on the available DC power for a string based and a central inverter based topology.

The examples used show clear differences in the power generation under different dynamic shading conditions. The effect of the clouds on the power production as function of time has been quantified and it can be seen that the difference depends strongly on the direction of the movement of the shadow front with respect to the orientation of the panel strings.

Future work will analyze the difference between the string and the central configuration as function of shading profile, inclination angle / areal topology and include inverter efficiency characteristics.

## REFERENCES

- [1] P. Wolfe, "Solar photovoltaic projects in the mainstream power market." Oxford: Earthscan; Routledge. ISBN: 978-0-415-52048-5.
- [2] W. T. Jewell, and T. D. Unruh, "Limits on cloud-induced fluctuation in photovoltaic generation.", *IEEE Transactions on energy conversion*, vol. 5, pp. 8-14, 1990.
- [3] NREL News Release NR-4411, "NREL data set shows clouds' effects on solar power," August 31, 2011..
- [4] L. Gao, R. A. Dougal, S. Liu and A. P. Iotova, "Parallel-connected solar PV system to address partial and rapidly fluctuating shadow Conditions," *IEEE Transactions on industrial electronics*, vol. 56, pp. 1548-1556, 2009.
- [5] P. P. Groumpas and K. Khouzam, "A generic approach to the shadow effect of large solar power plants". *Solar cells*, vol. 22, pp. 29-46. 1987.
- [6] K.M. Paasch, M. Nyman and F. Haase, " Optimization of PV-based energy production by dynamic PV-panel/inverter configuration." *PVSAT-9 conference*, 2013, Swansea, UK.
- [7] K.M. Paasch, M. Nyman and S.B. Kjær, "Distributed measurement system for long term monitoring of clouding effects on large PV plants." *EPE'13 ECCE Europe 15<sup>th</sup> European Conference on Power Electronics and Application*, Lille, France, 2013.
- [8] A. G. Onze, "Optimized System layout – the practical experience of 80 MW Eggebek plant realized with a multiple MPPT string inverter concept". 2nd PV inverter forum, Berlin, 2012.
- [9] W. M. Z. Xiaoli, L. Xiaoqin, D. Zhengang and Y. Jun, "Design of MPPT Algorithm under Partial Shadows," *IEEE international conference on electric information and control engineering (ICEICE)*, 2011.
- [10] H. Patel and V. Agarwal, "MATLAB-based modeling to study the effects of partial shading on PV array characteristics.," *IEEE Transactions on energy conversion*, vol. 23, pp. 302-310, 2008.
- [11] F. Adamo, F. Attivissimo, A. D. Nisio, A. M. L. Lanzolla and M. Spadavecchia, "Parameters Estimation of Photovoltaic Panels". *XIX IMEKO World Congress*.
- [12] IEC 61215-4:2005 – Crystalline silicon terrestrial photovoltaic (PV) modules.
- [13] K.M. Paasch, M. Nyman and F. Haase, "Sensor System for Long-term Recording of Photovoltaic (PV IV-curves",. Portugal, 2009. *PVSAT-9 conference*, 2013, Swansea, UK.

## **Appendix A5**

K. Paasch, M. Nymand and S.B. Kjaer, "COMPARATIVE ANALYSIS OF THE PERFORMANCE OF STRING- AND CENTRAL INVERTER TOPOLOGY AT A LARGE PV UTILITY PLANT WITH VARYING TOPOGRAPHY". *31th European Photovoltaic Solar Energy Conference and Exhibition*. EUPVSEC 2015, Hamburg, Germany.

## COMPARATIVE ANALYSIS OF THE PERFORMANCE OF STRING- AND CENTRAL INVERTER TOPOLOGY AT A LARGE PV UTILITY PLANT WITH VARYING TOPOGRAPHY.

Kasper M. Paasch\*, Morten Nymand and Soren B. Kjær●  
 University of Southern Denmark, Campusvej 55, DK-5230 Odense  
 ● Danfoss Solar Inverters A/S, Nordborg, Denmark  
 \* Corresponding Author

**ABSTRACT:** This paper presents new results from a long term measurement campaign involving synchronous high speed recording of performance data from a series of PV-strings on a 2.1 MW PV utility plant with uneven topography. The focus in this study is the performance of a series of string inverters (15 kW, 3 MPPT) and a series of small central inverters (60 kW, 1 MPPT) in the same PV plant under varying irradiation conditions and also including the potential detrimental effect of the horizontally tilt of the solar panels due to area topography variation. It has been shown that the gain from using multiple MPPTs is low, but that the effect of topographical variations can be substantial. The effect of a varying topography has been analyzed and it is shown that even a minor topographical variation has a noticeable effect on energy production. The results are compared to a simulated future PV strings with 1500V string voltage.

Keywords: PV System, Simulation, System Performance.

### 1 INTRODUCTION

This paper presents new results from a long term measurement campaign involving synchronous recording of performance data from 12 strings on a 2 MW PV utility plant. The focus in this study is the potential detrimental effect of horizontally tilted solar panels in a PV string on the energy production over a sunny day.

Panel strings presently consist of a maximum of around 24 solar panels in series, to avoid string voltage to exceed 1000V. However, a future increase of string voltage to 1500V is to be expected [1]. Higher string voltage will require longer strings (typ. 36 panels) and are expected to be more influenced by the topographical variation of the site.

### 2 PV PLANT CONFIGURATION

#### 2.1 Test plant description

Data from the Danfoss Solar Plant, a large PV utility plant of 2.1 MW with both string inverters and central inverters, is used in this analysis. The PV utility plant used for testing is the 2.1 MW plant located at the corporate headquarter of Danfoss A/S in Nordborg, Denmark. It consists of a total of 9216 panels of 225/230W mounted in 35 rows with 3 sub rows in each. See Fig. 1 a,b. The voltage limit of max. 1000 volt per string/array has limited the number of panels in series connection to 24 panels [1]. Inverters are of type Danfoss/SMA FLX 15K (each with 3 MPPT) [2] and the Danfoss/SMA MLX 62 kW (1 MPPT) [3].



Figure 1 a,b. Overview and topography of a section of the 2.1 MW Danfoss Solar Plant in Denmark.

The rows in the plant are up to 96 panels long (4 groups of 24 panels; around 160m) and each row has its own topography profile. Each group of 24 panels has its own MPPT (Max Power point Tracker). See Fig. 2. Several inverters were in 2015 replaced with MLX 60 kW inverters.

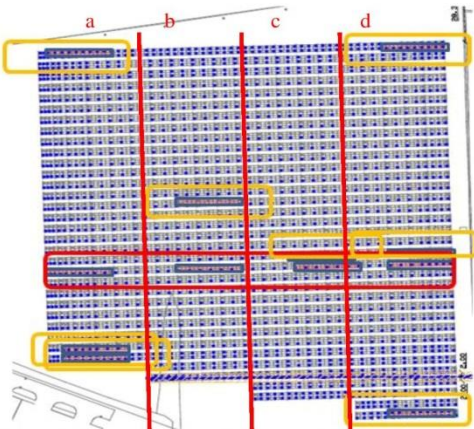


Figure 2. Plant string configuration, 35 rows. Dark areas indicate monitored strings of 3x24 panels. The red box show the placement of the 4 primary FLX test inverters. The yellow boxes show the location of monitored test inverters. a,b,c,d indicate panel sections.

#### 2.2 Stringing of the inverters

The traditional string layout of the panel rows is shown in Fig. 3. Each inverter covers  $\frac{1}{4}$  (3x96 panels) of a full row with individual MPPT for the 3 sub-rows. This setup gives a minimum of geographical distribution of the interconnected panels and has a clear advantage when inter-row shadowing is occurring. To investigate shading on a larger geographical distribution of panels 2 primary test inverters in row 21 have been rewired to different panel groups. See Fig. 3 and 4. This is performed as part of a larger study regarding the optimization of large PV plants [4,5]. Two inverters (ID 235 and 236) have each 3 strings attached, distributed over the whole length of a row, one inverter with 3 independent MPPTs and one inverter with strings in parallel fed to only one MPPT.



Figure 3. Traditional string layout concept for the Danfoss PV utility plant. 1 inverter per section (1-4).

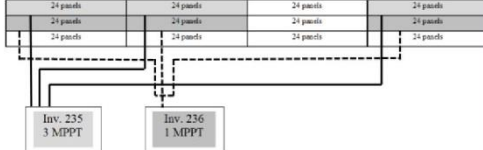


Figure 4. Modified string layout in the test string for two of the test inverters in row 21. Each inverter has panels distributed over approx. 160 meter.

### 3 SITE TOPOLOGY

The tilt of individual panel in a PV plant can be obtained by two methods. By extraction form surveying CAD data during site preparation (if they exist) or via the measurement of the tilt of each panel by an inclinometer (time consuming). Both methods have been applied here, as surveying data were not available for row 1-5. See Fig. 5.

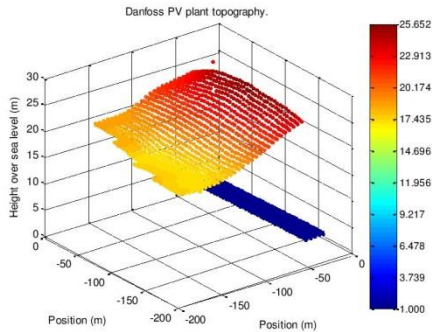


Figure 5. Topography extracted from available CAD data.

The maximum horizontal tilt variation for the analyzed rows is shown in table 1. The panel tilt of row 21 was both calculated and measured for comparison of the methods and it can be seen that both methods give comparable results. See Fig. 6.

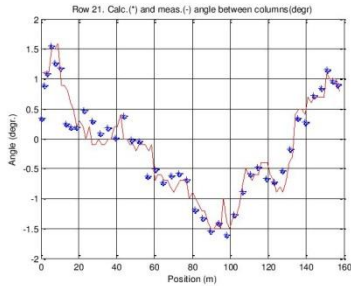


Figure 6. Comparison of tilt angle measurements (\*) and calculation from CAD data (-) for row 21, section a.

In Table I the min. and max. tilt angles for each section are shown, as well as the hypothetical angles in case the rows were configured for 1500V (2 strings of 36 panels in a row).

**Table 1.** Comparison of tilt angle measurements (\*) and calculation from CAD data (-) for row 21, section a.

TABLE I  
HORIZONTAL TILT ANGLE VARIATION ( $^{\circ}$ )

Row	Section @ 1000V				Section @ 1500V	
	a	b	c	d	a	b
1	-6.4 -2.2	-1.9 0.6	0 0.8	0.3 3.3	-6.4 0.6	0.0 0.8
2	-6.2 -1.7	-1.5 0.7	0.3 1.1	0.7 2.9	-6.2 0.2	-0.1 1.1
3	-7.0 -1.6	-1.8 0.8	0.4 1.1	0.4 3.1	-7.0 0.0	-0.4 1.1
4	-6.0 -1.7	-1.5 0.8	0.5 1.6	0.6 3.0	-6.0 -0.2	-0.2 1.6
5	-6.0 -1.8	-1.5 0.9	0.5 1.3	0.7 3.3	-6.0 -0.6	-1.0 1.3
21	-1.1 -0.2	-0.2 1.0	0.4 1.5	0.9 -1.1	-1.6 0.2	0.4 1.5

### 4 IRRADIATION PROFILE MODEL

The model is based on the calculation of the position of the sun at any given time and its effect on a curved string of 24 panels. The method described in [6] for finding solar azimuth and elevation angles has been implemented in this work. The irradiation on a panel with an arbitrary tilt can be determined via the dot inner vector product of the solar vector  $\mathbf{S}$  and the unit vector of the illuminated surface (panel)  $\mathbf{n}$ . See Fig. 7 a and b.

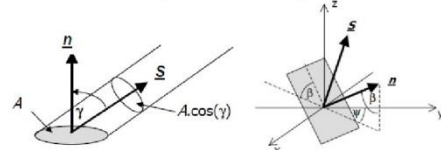


Figure 7 a,b . Irradiation geometry [4].

For any given time we have

$$P_{direct} = I_{direct} A \cos(\gamma) \quad (1)$$

$$I_{surface} = \frac{P_{direct}}{A} = I_{direct} \cos(\gamma) \\ = I_{direct} \bar{S} \cdot \bar{n} \quad (2)$$

It can further be shown [7] that

$$\bar{S} \cdot \bar{n} = \cos(\alpha) \sin(\beta) \cos(\Psi - \Theta) + \sin(\alpha) \cos(\beta) \quad (3)$$

where  $\alpha$ =solar elevation,  $\Theta$ =solar azimuth,  $\beta$ =panel elevation,  $\psi$ =panel azimuth. The irradiation  $I_{direct}$  can now be calculated by introducing the elevation dependent Air Mass (AM) [6,7].

$$I_{direct}(z) = I_0 e^{-c * \sec(z)^S} \quad (4)$$

$$I_{direct}(\alpha) = 1.353(0.7^{AM(\alpha)^{0.678}}) \quad (5)$$

Where  $z$ =solar zenith angle,  $I_0=1353 \text{ w/m}^2$ ;  $c=0.357$ ;  $S=0.678$ . The Air Mass (AM), expressed as the secant of the solar zenith angle  $z$  in (4), is estimated via an

interpolative function as function of the solar elevation angle  $\alpha$  [8].

$$AM(\alpha) = \frac{1}{\sin(\alpha + 244/(165 + 47\alpha^{1.1})} \quad (6)$$

The panel elevation angle  $\beta$  is held constant, but each panel on a curved area has its own horizontal tilt angle  $\delta_x$ , where  $x$  identifies the individual panel. The panel azimuth angle  $\Psi$  thus must be modified as

$$\Psi_x = \Psi + \delta_x \quad (7)$$

The irradiation on each panel in a string is calculated via (1-6). For each time step  $t$  the irradiation (and thus potentially generated DC current  $I_x(t)$ ) for each of the  $q$  panels in the string. A discretized time step dependent current vector  $I_{panel}(t)$  can be defined as

$$\bar{I}_{panel}(t) = [I_1(t) \ I_2(t) \ I_3(t) \dots I_q(t)] \quad (8)$$

The effective string current  $I_{string}$  can be found as

$$I_{string}(t) = \min(I_{panel}(t)) \quad (9)$$

The generated string power  $P_{string}(t)$  can then be calculated via the IV-characteristic of the given panel, giving the panel voltage  $V_x(t)$  at current  $I_x(t)$

$$P_{string}(t) = 24 \cdot V_{panel}(t) \cdot I_{string}(t) \quad (10)$$

A simulated response for row 1 is shown in Fig. 8.

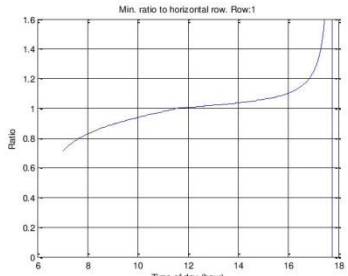


Figure 8. Simulated power ratio as function of time for row 1, section a, for July 29, 2014. 20% diffuse light is assumed.

## 5 TEST RESULTS

The DC power generated as function of time for the string was analyzed for July 29, 2014 and normalized to a flat row response (row 21). See Fig. 9.

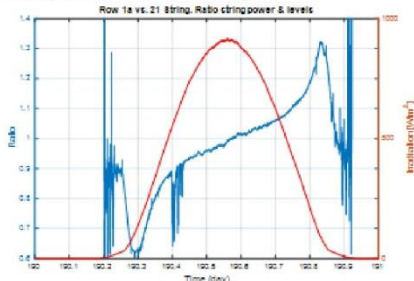


Figure 9 Measured variation of generated DC power (blue) for day 190 (July 29), normalized to row 21. Red

curve illustrated recorded solar irradiation.

The ratio between the power levels of the strings as function of time clearly indicate that the high tilt variation of row 1a affect the energy production. Before noon there is a lower power production and after noon (when the sun is facing towards the panels tilted westward (neg. angle)) is the power production higher (late afternoon, where the irradiation level is low) than for the relatively flat reference string. But the increase in power production after lunch is not high enough to compensate for the losses before noon, so the large horizontal variation effectively has a negative effect on the accumulated energy production. The calculated ratio curves for section 1-4 are shown in Fig. 10.

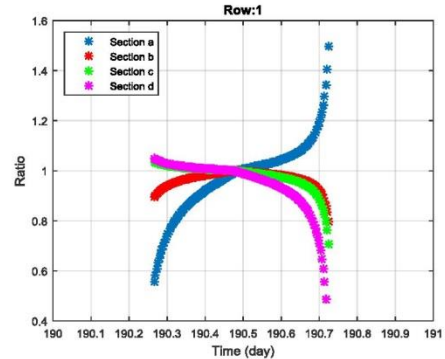


Figure 10 Measured variation of generated PV power in all segments of row 1 in day 190 (July 29, 2015), normalized to the response from a flat/horizontal row.

By comparing the calculated ratio curves in Fig. 12 with the data presented in Table I it can be observed that row 1 section a, which has the largest angle spread (-6.4° to -2.2°, blue curve) also show the largest variation. With only negative angels was it expected that the output power would be above the normal after noon, as measured. The other segments (b-c-d) of row 1 are more centered around 0° which are not generating a large effect in the afternoon. Row 2-4 show a similar behavior.

The accumulated energy production for the row with high horizontal tilt variation has a 2.5% lower energy production (40.5 kWh) than the other segments monitored (41.5 kWh). The accumulated DC power generated for strings of 24 panels in different rows is shown in Fig. 11.

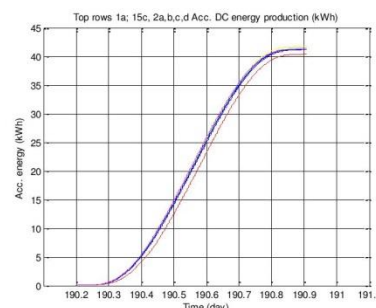


Figure 11. Calculated accumulated energy for the monitored single strings.

## 6 MLX CENTRAL INVERTER TEST

After several month of operation with FLX inverters were several of the inverters replaced with 60 kW MLX inverters for test purposes (1 MLX replaces 4 FLX). The new layout of a small part of the park is shown in Fig. 12.



Figure 12. Part of the PV plant layout with MLX inverters. Red boxes show MLX inverter 1-4, each covering 4 strings in parallel.

The measured DC power for MLX inverter 1-4 (covering section c-d of row 1-8 and 9-10) and MLX 8 (covering section c-d of row 20-21) for a sunny day are shown in Fig. 13. Inverter MLX 8 (not shown in Fig. 12) is acting as a reference inverter due to the relative flatness of the strings.

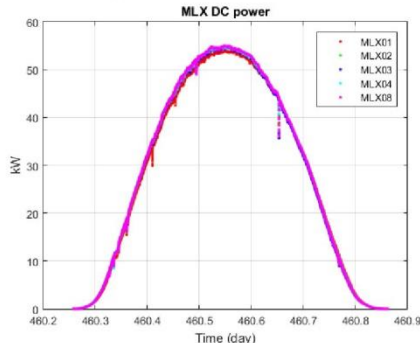


Fig. 13. MLX inverter 1-4 and 8 DC energy levels for April 25, 2015 (day 460).

The relative DC power ratio for the MLX inverter 1-4, relative to inverter 8, is shown in Fig. 14. It can be observed that the ratio is centered around 1 and that only MLX 1 shows a variation of up to 10% during morning and evening.

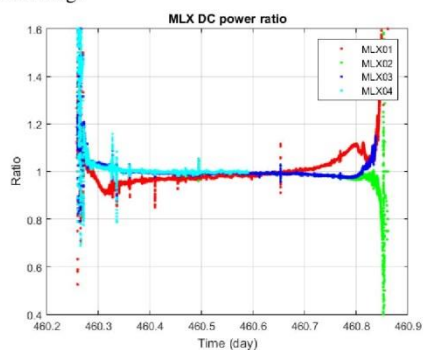


Fig. 14. MLX inverter 1-4 DC energy levels relative to MLX 8 reference inverter for April 25, 2015 (day 460).

The difference in energy production, due to the topographical influence is below 1% between the inverters.

## 7 CONCLUSION

Results from a long term measurement campaign on a large PV utility plant with different inverter configurations have been used to quantify the effect of topographical variations in large PV parks. A modeling approach for the investigation of the effect of topographical conditions on the DC power generation of a large PV plant has been developed, taking into account the solar position and the individual panel orientations. It has been shown both theoretically and experimentally that topographical variations over a given area can result in a noticeable loss of energy production during a sunny day, due to the series connection of PV panels and uneven illumination, compared to flat PV string, where only the variation in the panel data will generate a mismatch factor and thus a power loss. An energy loss in the range of 2.5% is observed on a sunny day for a PV string with an angular variation between -6.4 and -2.2° from horizontal. Extrapolation of the obtained results to potential future 1500V system indicate that the negative effect will increase due to the longer strings (36 panels) in areas with topographical variations. The data obtained from the 60 kW MLX inverters, having 4 strings in parallel, show that the topographical effect is visible, but to a lower extend than for the string inverters. An almost symmetrical morning/evening deviation of up to 10% has been recorded for a sunny day.

## 8 REFERENCES

- [1] E. Gkoutioudi, P. Bakas and A. Marinopoulos, "Comparison of PV systems with maximum DC voltage 1000V and 1500V". IEEE Photovoltaic Specialist Conference 2013, pp. 2873 – 2878.
- [2] Danfoss Solar Inverter FLX Pro 17k data sheet "FLX Inverter Series. When experience meets innovation". DKSI.PFP.204.B3.02. Published December 2013.
- [3] MLX inverter data sheet. "MLX Inverter Series. The Power of Forward Thinking". DKSI.PFA.205.B6.02. Published May 2014.
- [4] K. Paasch, M. Nyman and F. Haase, "Long term energy yield measurements of a string- vs. central inverter concept tested on a large scale PV-plant", IEEE European Conference on Power Electronics and Applications, EPE. 2015.
- [5] K. Paasch, M. Nyman and S.B. Kjær, "Simulation of the impact of moving clouds on large scale PV-plants". Photovoltaic Specialist Conference (PVSC), 2014 IEEE 40th, DOI: 10.1109/PVSC.2014.6925036
- [6] K. Paasch, M. Nyman and S. Kjær, "Distributed measurement system for long term monitoring of clouding effects on large PV plants", IEEE European Conference on Power Electronics and Applications, EPE. 2013.
- [7] A.B. Sproul, "Vector analysis of solar geometry". Proceedings of Solar 2002- Australian and New Zealand Solar Energy Society.
- [8] A.B. Meinel and A.J. Meinel, "Applied Solar Energy. An introduction". Addison Wesley Publ. Company 1976. ISBN: 0-201-04719-5. 7.

## **Appendix A6**

K. Paasch, M. Nyman and F. Haase, “Long term energy yield measurements of a string- vs. central inverter concept tested on a large scale PV-plant”, *EPE’15 ECCE Europe 17<sup>th</sup> European Conference on Power Electronics and Application*, Geneva, Switzerland, 2015.

# **Long term energy yield measurements of a string- vs. central inverter concept tested on a large scale PV-plant.**

Kasper M. Paasch\*, Morten Nymand, Søren B. Kjær  
University of Southern Denmark  
Alcion 2  
6400 Sønderborg, Denmark  
Tel.: +45 – 65501695  
Fax: +45 – 65501635  
E-Mail: [paasch@mci.sdu.dk](mailto:paasch@mci.sdu.dk)  
URL: <http://www.sdu.dk>

## **Keywords**

Solar cell system, PV Power plant performance, Solar inverter, Partial shading

## **Abstract**

High speed long term recording of inverter data has been performed on a utility scale PV plant and two different configurations of panel groups are compared. The recorded impact of partial shading due to moving clouds on a sting based and a central inverter based concept is analyzed.

## **Introduction**

This paper investigates the effect of moving cloud on the performance on large PV utility plants. It presents initial results of a long term measurement campaign involving quasi-synchronous recording of performance data from a total of 12 string inverters mounted at a 2.1 MW PV utility plant. Inverter data were monitored for almost one year at targeted 1 Hz sampling rate. PV utility plants differ from residential plants in installed module power (typ. >1 MW vs. <20 kW) as well as shading conditions. Small residential PV plants can suffer from unavoidable partial shading due to trees, light posts, chimneys etc., where objects casting shadows are typically removed from the vicinity of large utility plants. But all PV plants can experience periods of partial shading due to the movement of clouds. The net effect of moving clouds is however not well understood [1,2] and it is not well known how a string based inverter with independent MPPTs performs to an identical system with only one MPPT and the strings connected in parallel.

## **Background**

The deployment of PV utility plants in cloudy areas such as Northern Europe raises the question of the actual effect of fast cloud patterns on the annual energy yield of such PV plants. Studies about non-uniform irradiation conditions of PV plants are found in literature [3,4,5,6], but documented effects of fast moving clouds on the energy production due to panel shading in different inverter configurations have not been identified in literature. Large PV power plants are thus expected to be influenced by changing weather conditions, such as fast clouds, generating fluctuations in power production.

## **PV test site description**

The PV utility plant selected as test site is a new 2.1 MW plant located at the corporate headquarter of Danfoss A/S in Nordborg, Denmark. It consists of a total of 9216 Sharp ND225E1J 225W polycrystalline panels, initially distributed on 128 FLX Pro 17k string inverters from Danfoss Solar Inverters A/S, each having 3 MPPT inputs [7]. The panels are mounted in 35 rows each with 3 panels horizontally stacked. Each MPPT input is connected to panel strings mounted either in the top, middle or bottom row. See Fig. 1a,b. The plant is designed for a small amount of inter-row shading to happen on the lower sub-rows during December. The topography of the occupied area is uneven and the plant is following the contours of the area, resulting in panel rows with horizontal tilt angles from -3.3° to +6.3° [8]. The panel inclination is 15° and the panel orientation is -3° from geographical south. Annual production is estimated at 2000 MWh.



Fig. 1a,b: The Danfoss A/S 2.1 MW utility PV plant in Nordborg, Denmark.

### Data recording system

The implemented data recording system is based on the internal recording of parameters in the individual FLX inverters. A locally installed field PC is scanning/retrieving data from the 12 selected inverters each second as well as from a weather station (Davis VantagePro2 Plus, recording temperature, wind speed, wind direction etc.). A large amount of parameters (19 from the weather station and 28 per inverter) are recorded by the PC connected to the internal Ethernet bus of the plant and streamed to the university server each night. The recorded individual inverter parameters are listed in table 1. A sensor kit mounted on one inverter supplies irradiance and temperature measurements.

**Table I: Inverter parameters logged**

PV voltage 1	PV voltage 2	PV voltage 3	PV current 1	PV voltage 3	PV voltage 3
PV power 1	PV power 2	PV power 3	Grid voltage L1	Grid voltage L2	Grid voltage L3
Grid volt L1-L2	Grid volt L2-L3	Grid volt L3-L1	Grid current L1	Grid current L2	Grid current L3
Grid power L1	Grid power L2	Grid power L3	Grid power sum	Grid freq. L1	Grid freq. L2
Grid freq. L3	Grid freq. mean	kWh today	kWh total		

The location of the inverter strings/panels monitored is illustrated i Fig. 2.

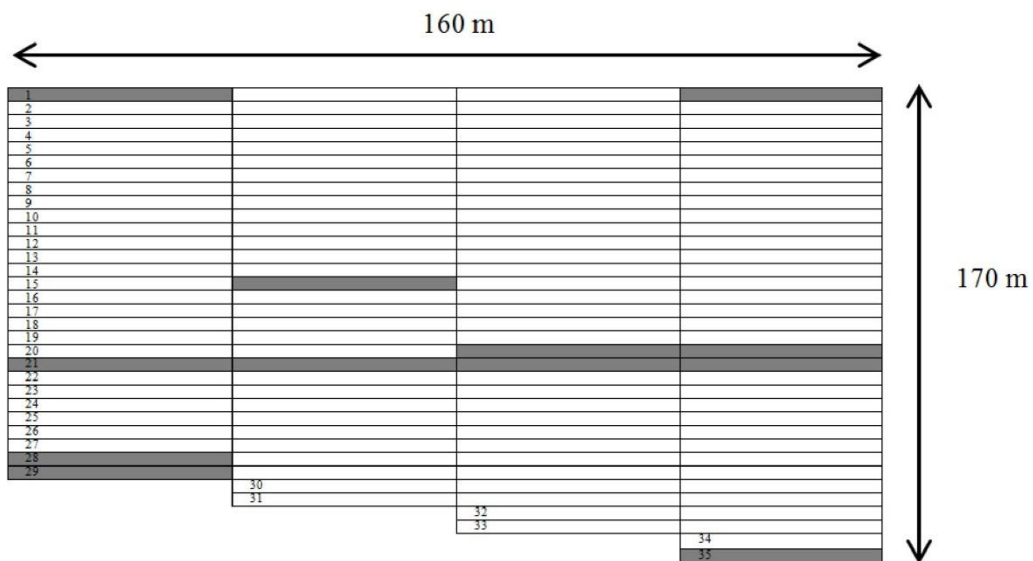


Fig. 2: Monitored string areas of the Danfoss PV plant. Row 21 is the main test row.

Four of the 12 inverters have modified panel configurations and, as primary test inverters, need to be monitored with high accuracy, but as inverters in general are not specified for net metering it is to be

anticipated that the internal AC power measurement circuit cannot be expected to comply with general net metering standard accuracy. To assure a high accuracy of the AC power measurement of said inverters, 4 external power monitoring modules [9] (compliant to IEC62503 [10,11], 0.2%) have been installed on said 4 inverters and used for a periodic calibration. The accumulated DC energy production is calculated by numerical integration of the recorded DC string voltages. The FLX inverters apply the Incremental Conductance type of MPPT. Gain errors in the voltage and current measurements will have no influence on the MPPT performance and it has been shown that this type of MPPT is comparable to the Hill Climbing method and show similar performance under same real atmospheric conditions (a perturbation step size of 2% of the MPP voltage result in about 0.1% loss for both methods) [12].

## String layout

The traditional string layout of the panel rows is shown in Fig. 3. Each inverter covers  $\frac{1}{4}$  of a full row (3x96 panels), with individual MPPT for the 3 sub-rows. This setup gives a minimum of geographical distribution of the interconnected panels and has a clear advantage when inter-row shadowing is occurring. To investigate shading on a larger geographical distribution of panels the 4 primary test inverters have been rewired to different panel groups. See Fig. 4. Two inverters (ID 235 and 236) have each 3 strings attached, distributed over the whole length of a row, one inverter with 3 independent MPPTs and one inverter with strings are in parallel fed to only one MPPT.

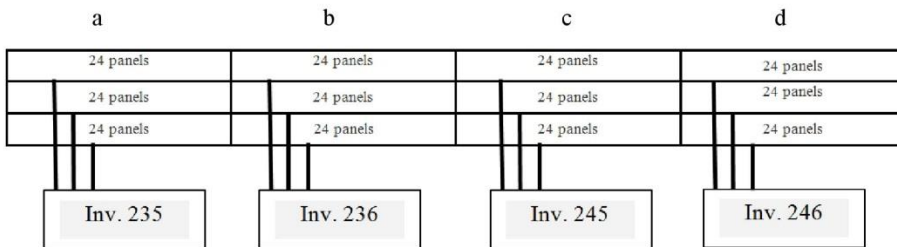


Fig. 3: Traditional string layout concept for the Danfoss PV utility plant. 1 inverter per section (1-4).

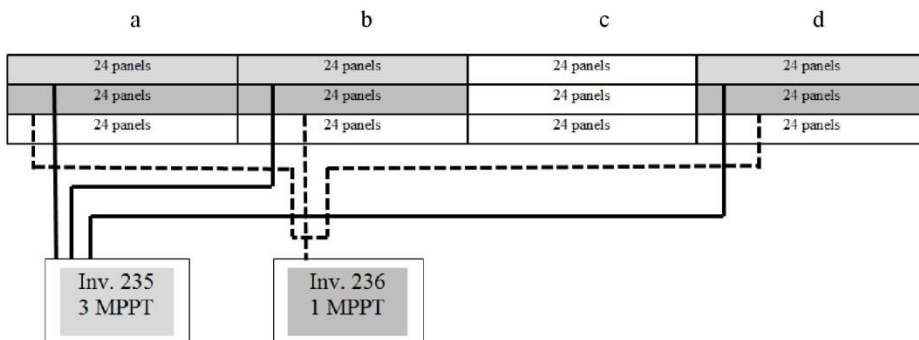


Fig. 4: Modified string layout in the test string for two of the test inverters. Each inverter has panels distributed over approx. 160 meter.

## Characterization of the PV strings

For this study the steady state response is not of primary interest, compared to the potential dynamic response caused by passing clouds. But the communication with the inverters via Ethernet cannot assure fixed response times (and thus exact timing of the measurements) so that any instant reading from two inverter might not be within 1 sec. To circumvent this problem the accumulated energy production has been used to evaluate differences in performance of the two string configurations, but this requires the compensation of any slow effect causing string differences under steady state

conditions via compensation during steady state levels. Two long term parameters have been investigated: the expected steady state string mismatch loss due to variations in the panel data and the topographical effect (the solar panels follow the curvature of the field). As shown in Fig. 4 one inverter is connected to three individual strings and the other has 3 strings in parallel. The initial differences in string parameters [13] has been analyzed via available flash data for all PV panels in the plant [14], listing the variation in PMPP, IMPP and VMPP via the method described in [15]. All 288 solar panels in row 21 have been identified by their serial numbers; see Fig. 5 for the variation in the current IMPP for each row divided into the 4 row sections (a-b-c-d).

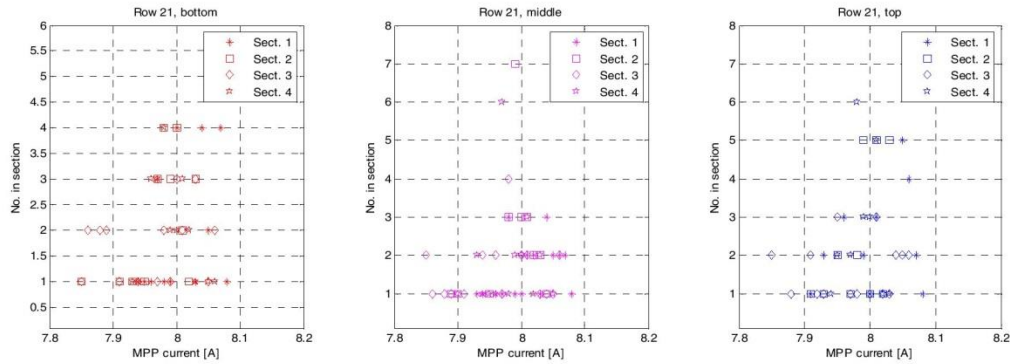


Fig. 5: Distribution of the MPP current for all 288 panels in row 21, divided into bottom, middle and top sub rows.

The method for mismatch analysis developed in [16] has been applied for the strings in question and the mismatch loss factor is found to be <0.2%. All strings in row 21 have the same angular tilts in each section. The angle of each panel in row 21 has been measured and the minimum and maximum values are presented in table II. The section angle distribution varies with around 1.2 degree for section a and b and with 2 degrees for section d (section c is not part of the test setup).

**Table II: Row 21 Panel section angles**

	Section a	Section b	Section c	Section d
Maximum angle	-1.1°	-0.2°	0.4°	0.9°
Minimum angle	-0.2°	1.0°	1.5°	-1.1°

The angular difference between the panels is very low and the influence on the differential power production can be estimated to be <0.2% at full sunlight, following the method described in [16]. This effect has therefore not been considered further in this analysis.

## Analysis of long term data

The parameter of primary interest in this study is the difference in energy production from the two string combinations. As the available PV plant is also a test plant for an inverter manufacturer some interference with the data recording was to be expected and this has also been observed. The data recorded for 353 days (starting early summer 2014) have been analysed and the data from days showing clear and explainable abnormal behaviour have been excluded from the analysis. All data removed from the analysis could be related to non-operational conditions such as software updates, inverter tests and communication error due to network issues. See Fig. 6. The calculated average difference for the filtered days is 0.1%.

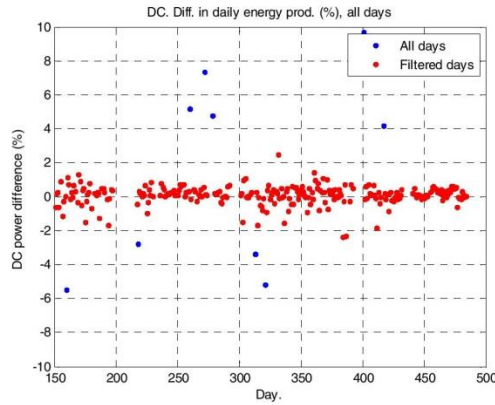


Fig. 6: Difference in energy production between the inverters per day. Only days with differences <10% are shown.

### Measured steady state response

The steady state measurement offset between inverter 235 and inverter 236 has been analysed by identifying all measurements with stable illumination ( $d(\Delta P)/dt$  is centred around 0). The ratio for the power generation during stable illumination levels is shown in Fig. 7. The ratio is distributed around 0.997, indicating that both inverters/strings seem to produce within 0.3% of power during stable illumination and indicating almost identical string parameters, taking measurement uncertainties into account.

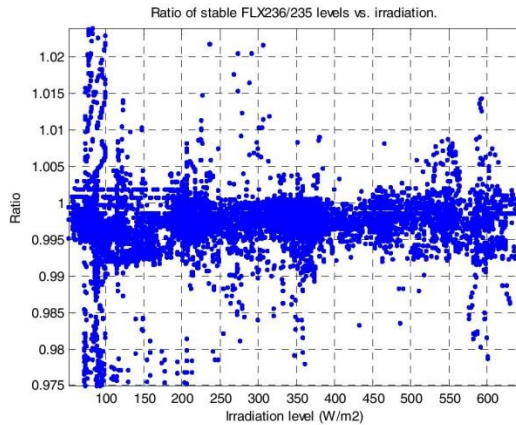


Fig. 7: Ratio of steady state response for inverter FLX235 and FLX236 vs. irradiation level.

The calculated difference in accumulated energy production between the two primary test inverters FLX235 (3 MPPT) and FLX236 (1 MPPT) for a selected day with rapid changes (day 283) is shown in Fig. 8. It can be seen that the difference in energy production is 0.12%, and below the guaranteed accuracy of the applied power meters / test system.

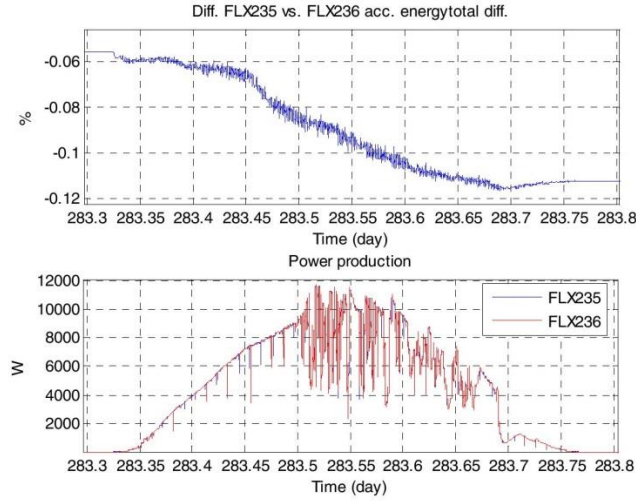


Fig. 8: Difference in recorded accumulated energy production for day 283.

The recorded data includes wind direction and velocity from a weather station placed at the north-western corner of the PV site. The recorded dominant wind direction and velocity for each day can be seen in Fig. 9a,b,c. A worst case scenario is for shading patterns to arrive from west ( $270^\circ$ ) as the panels are placed horizontally towards south. That condition would generate the largest change in the irradiation distribution on the strings under test.

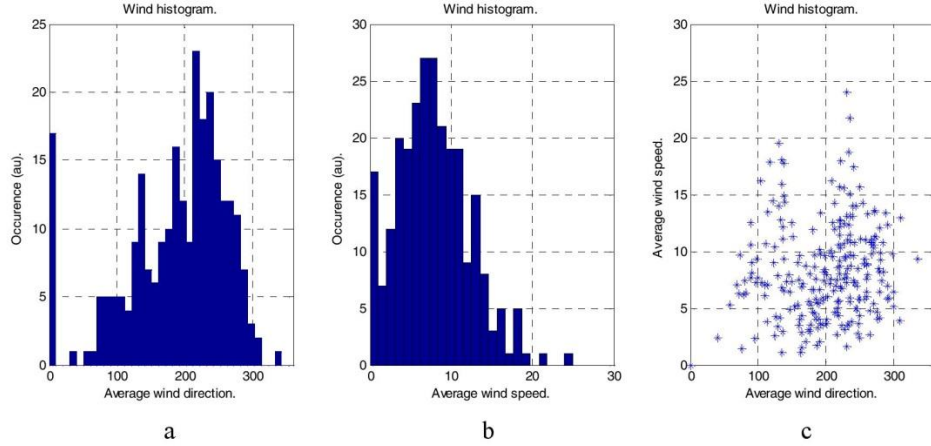


Fig. 9: Histogram of a) dominant wind direction, b) average velocity and c) their correlation for the filtered days.

The cloud direction as well as velocity might differ from the data recorded by the ground-based weather station due to varying wind conditions in the atmosphere. This has been taken into account in the analysis by performing a time correlation of the measurements between the recorded inverter data. The analysis showed only minor deviations from the weather station recordings and it is thus in this analysis assumed that the wind data measured is representative for the direction and speed of the moving clouds, knowing that cloud direction and surface wind direction might differ under extreme circumstances.

A high resolution density plot of the recorded wind speed and direction data for the whole measurement period (353 days, with sub minute resolution) is shown in Fig. 10, generated from approx.  $20 \times 10^6$  recordings. The color map applied in Fig. 10 represent the occurrence of a given wind speed and direction combination. The color map is logarithmically scaled ( $\log_{10}$ ) and it can be observed that the dominant wind direction is around 230 degrees (SSW) and the dominant wind speed in said direction is in the range of 5-15 m/s.

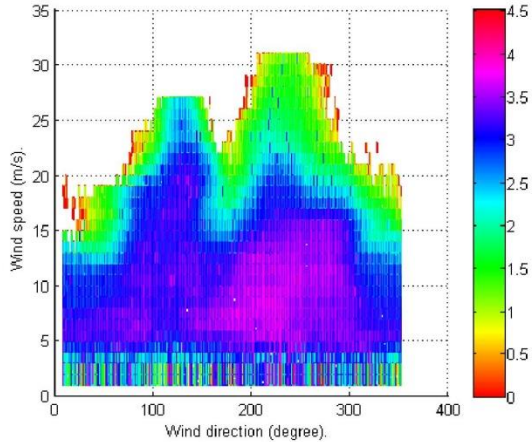


Fig. 10: Density plot of the wind speed and wind angle combinations recorded with  $\log_{10}$  color scaling of the occurrence for each combination.

For a 39 meter long string (24 panels), this implies that a shadow front will pass in around 2.5-8 seconds and for the distributed string layout in 10-32 seconds. This means that any effect due to partial shading will only be visible during that short time period. Fig. 11 shows the calculated differences in daily energy production correlated to the recorded wind direction and average wind velocity and it must be concluded that no distinct effect can be identified.

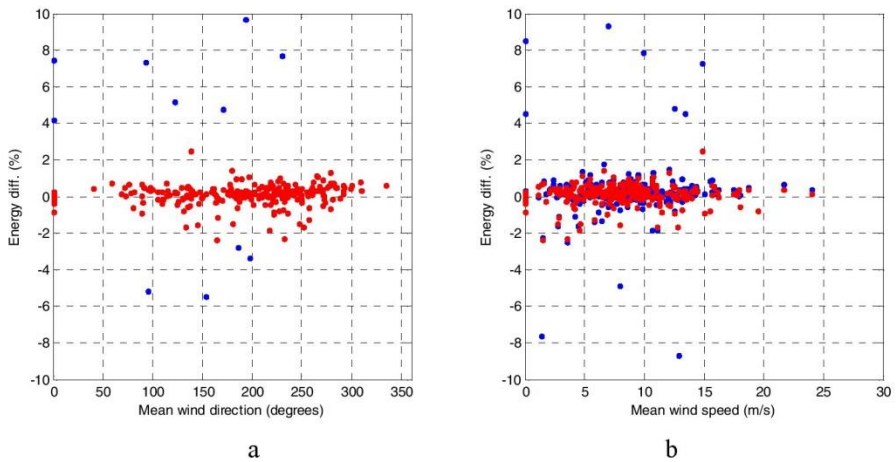


Fig. 11: Energy difference per day as function of a) wind direction b) wind velocity. Red indicates valid data set.

## MLX central inverter

Data from a 60 kW central inverter of type MLX [17] with strings physically located close to row 21 has been compared to the results obtained with the string inverters for the cloudy day (day 318). The inverter is connected to 12 parallel strings and the inverter thus operated with only one MPPT. Since each FLX test inverter only has 3 strings, the DC power recordings of the MLX inverter have been divided by a factor 4. The comparison shows that the power production of the MLX closely follows that of the FLX inverters. See Fig. 12. The analysis of the MLX data is ongoing.

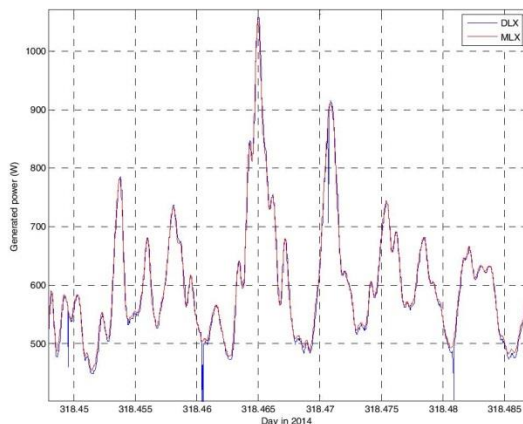


Fig. 12: Scaled MLX response compared to FLX test inverters for section of day 318 (Nov. 11, 2014).

## Conclusion

The test setup and data presented in this paper analyze long term cloud induced differences in accumulated energy production from a large scale PV utility plant by comparing two different string configurations. The study applies data recorded for almost a year from selected inverters at the Danfoss 2.1 MW PV utility plant. The analysis show that passing clouds on two different string inverter configurations has no clearly identifiable impact on the long term energy production and also that the accuracy of the measurement system so far is the limiting factor. The induced mismatch between the strings in a configuration with one MPPT and 3 parallel strings of each 24 solar modules does not result in a noticeable long term degradation of the energy production. It must be concluded that a potentially long term net gain in energy from an inverter in the range of 17 kW, using 3MPPTs, connected to PV-strings spatially distributed over 160 m is negligible, compared to using only one MPPT under similar real weather conditions. In case a PV plant layout is designed for periods with inter-row shadowing during winter, the use of multiple MPPTs are still considered to be beneficial.

This work was in part supported from the Danish Sunrise-PV project, ERDFD-09-0069, financially supported by Syddansk Vækstforum and The European Regional Development Fund.

## References

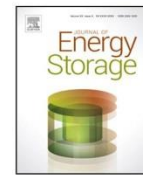
1. Giraud et al.: Analysis of the Effects of a Passing Cloud on a Grid-Interactive Photovoltaic System with Battery Storage using Neural Networks. *IEEE Transactions on Energy Conversion*, vol. 14, 1999, pp. 1572-1577
2. News Release NR-4411 NREL data set shows clouds' effects on solar power August 31, 2011 <http://www.nrel.gov/news/press/2011/1575.html>

3. Large-Scale Photovoltaic Power Plants Ranking 1-50  
<http://www.pvresources.com/PVPowerPlants/Top50.aspx>
4. Kern et al.: Cloud effects on distributed photovoltaic generation ; Slow transients at the Gardner, Massachusetts photovoltaic experiment. IEEE Transactions on Energy Conversion, vol. 4, 1989, pp. 184-190
5. Ruiz, A.: System aspects of large scale implementation of a photovoltaic power plant. Thesis 2011, KTH Royal Institute of Technology, Stockholm, Sweden
6. Paasch, K.. M.; Nyman, M. ; Kjaer, S.B.: Simulation of the impact of moving clouds on large scale PV-plants. Photovoltaic Specialist Conference (PVSC), 2014 IEEE 40<sup>th</sup>, DOI: 10.1109/PVSC.2014.6925036
7. Danfoss Solar Inverter FLX Pro 17k data sheet "FLX Inverter Series. When experience meets innovation". DKSI.PFP.204.B3.02. Published December 2013
8. Paasch, K. M.; Nyman, M.; Kjaer, S.B.: Comparative Analysis of the Performance of String- and Central Inverter Topology at a Large PV Utility Plant with Varying Topography. Accepted for publication at EUPVSEC 2015, September 2015, Hamburg, Germany
9. WattsOn\_Universal\_Power\_transducer.pdf. Retrieved from [www.Elkor.net](http://www.Elkor.net) May 2015
10. IEC62053-22: Electricity metering equipment (a.c.) – Particular requirements – Part 22: Static meters for active energy (classes 0.2 S and 0.5S)
11. American National Standard for Electricity Meters – 0.2 and 0.5 Accuracy classes (ANSI C12.20 Class 0.2)
12. Kjær, S. B.: Evaluation of the "Hill Climbing" and the "Incremental Conductance" Maximum Power Point Trackers for Photovoltaic Power Systems. IEEE TRANSACTIONS ON ENERGY CONVERSION, VOL. 27, NO. 4, DECEMBER 2012
13. Chamberlin, Charles E. et al. Effects of mismatch losses in photovoltaic arrays. Solar Energy, vol. 54 no 3, pp. 165-171. 1995
14. Flashtestliste Danfoss.pdf. List received November 25, 2015 from Helge Andersen, Solarpark DK, Småenget 10, 6240 Logumkloster, Denmark
15. Webber, J. and Riley, E.: Mismatch Loss Reduction in Photovoltaic Arrays as a Result of Sorting Photovoltaic Modules by max-Power parameters. ISRN Renewable Energy, Vol. 2013, Article ID 327835
16. Bucciarelli, L. L. jr.: Power loss in photovoltaic arrays due to mismatch in cell characteristics. Solar Energy, vol. 23, no. 4 pp. 277-288, 1979
17. MLX inverter data sheet. MLX Inverter Series. The Power of Forward Thinking. DKSI.PFA.205.B6.02. Published May 2014

## **Appendix A7**

J. Olsen, K.M. Paasch, B. Lassen and C.T. Veje, "A new principle for underground pumped hydroelectric storage", *Journal of Energy Storage* 2 (2015) 54–63.

Doi:10.1016/j.est.2015.06.003



## A new principle for underground pumped hydroelectric storage



Jan Olsen <sup>a</sup>, Kasper Paasch <sup>b</sup>, Benny Lassen <sup>b</sup>, Christian T. Veje <sup>c,\*</sup>

<sup>a</sup> JolTech ApS, Langbrogade 3, DK-6400 Sønderborg, Denmark

<sup>b</sup> Mads Clausen Institute, University of Southern Denmark, Alision 2, DK-6400, Denmark

<sup>c</sup> Centre for Energy Informatics, Mærsk Mc-Kinney Møller Institute, University of Southern Denmark, Campusvej 55, DK-5230, Denmark

### ARTICLE INFO

#### Article history:

Received 2 February 2015

Received in revised form 18 June 2015

Accepted 18 June 2015

Available online 14 July 2015

#### Keywords:

Energy storage

Underground pumped hydro storage

Hydro energy

Structural mechanics model

### ABSTRACT

This paper presents the basic idea, design considerations and field test results for a novel concept of an energy storage system. The system is of the underground pumped hydro storage (UPHS) type where energy is stored by lifting a mass of soil through the pumping of water into an underground cavity. The cavity is formed by two impermeable membranes welded along the edges. A simple model captures the dynamics of the system revealing the importance of both visco-elastic and plastic effects for the cyclic loading of the soil. The results indicate that the efficiency of this new concept will be very close to that of the traditional pumped hydro storage (PHS) technology and the energy lost by deformation of the soil will be between 0.04 and 0.12% for a full scale system of 30 MW power and 200 MWh capacity. A key feature of the concept is the relatively price efficient design where the main cost is movement of soil. A cost analysis indicates that a full scale system will be economically viable when connected to the European power grid where the main revenue will come from selling ancillary services. The storage cost for a full scale 30 MW/200 MWh system is estimated to be approximately 5.3 EUR cent/kWh. The estimated cost of installed power is 1111 EUR/kW and the related cost of installed storage capacity is 208 EUR/kWh.

© 2015 Elsevier Ltd. All rights reserved.

## 1. Introduction

For a number of years it has been evident that large scale energy storage will be necessary for leveling the intermittencies of an electricity grid supplied largely from renewable and intermittent or periodic energy sources [1]. Currently more than 30% of the Danish electric power is produced by wind turbines [2] and photovoltaics covering a minor share. On a larger scale, Europe is aiming to meet the 20% goal for energy production by renewable energy in the 2020 EU Climate and energy package [3].

Ideally it is desirable to be able to store and extract large amounts of electrical energy with fast response and high efficiency. At the same time such a system should be realizable in the actual topographical surroundings available. Large scale storage systems for electric energy are typically of the pumped hydro storage (PHS), compressed air or large scale battery types [1,4]. Of these, the PHS is the technology that is the most mature and covers almost the entire global energy storage capacity [5,6]. One reason is that PHS systems are applicable in systems where fast response and high power rates are necessary.

Frequency controlled ancillary services<sup>1</sup> for up and down regulation can be delivered to the grid within few seconds upon frequency deviations. PHS is indeed capable of injecting and extracting power from the grid within this timescale [4].

A typical requirement for a PHS system is the availability of relatively large height differences between the two water reservoirs. The pressure delivered for power generation is provided directly by the hydrostatic pressure obtained from this height difference. In situations where such a height difference is not topographically available, concepts of the underground pumped hydro storage (UPHS) type have been proposed [7–9]. The conventional concept here is to facilitate the height difference by placing the lower reservoir in an underground cavity. Recently concepts where the water pressure at large depth in oceans can act as the driving force in a PHS system have been presented [10,11]. A challenge for such systems is the necessity to create a high pressure chamber at large depths at a reasonable price.

<sup>1</sup> The glossary of ENTSO-E Operation Handbook defines ancillary services as Interconnected Operations Services identified as necessary to effect a transfer of electricity between purchasing and selling entities (TRANSMISSION) and which a provider of TRANSMISSION services must include in an open access transmission tariff. [<https://www.entsoe.eu/publications/system-operations-reports/operation-handbook/>].

\* Corresponding author. Tel.: +45 20585161.  
E-mail address: [veje@mmtm.sdu.dk](mailto:veje@mmtm.sdu.dk) (C.T. Veje).

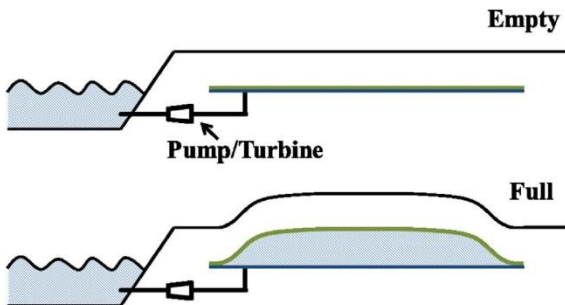


**Fig. 1.** Sketch of the energy membrane underground energy storage concept (EM-UPHS). Water is pumped into a cavity bounded by two impermeable membranes and the soil on top is lifted. Blue and green are top and bottom membrane respectively. (For interpretation of the references to color in this figure legend, the reader is referred to the web version of the article.)

Countries like Denmark have only a few hilly areas suitable or available for PHS systems. This paper presents a novel idea for a PHS system which is based on a storage reservoir, where water is enclosed in a membrane placed underground as shown schematically in Fig. 1 – the energy membrane-underground pumped hydro storage system (EM-UPHS). The overlaying soil gives the necessary pressure to run a pump/turbine and store large amounts of electrical energy. This system is independent of the local topology and can be placed close to a water reservoir – sea, lake, or river – with little or no height difference. The pump/turbine machinery is based on the well known technology of conventional PHS systems which typically has an efficiency of 70–85% [12]. The concept seeks to facilitate a PHS system in a geographical/geological setting where the topology does not allow for a conventional PHS system.

A special application for such an EM-UPHS may also arise in a stand alone wind turbine power supply which is not strongly connected to a power grid/PV power plant (e.g. island operation of wind turbines). This application is of special interest for wind turbine manufacturers as well as to remote societies/habitations or uninterrupted disconnected power supplies for remote technical installations.

In this paper the concept and initial results of this novel EM-UPHS system are presented. The intention is to examine the technical aspects of the concept with a reservoir of  $50\text{ m} \times 50\text{ m}$ , based on experience from a preliminary smaller proof of concept and a field test trial. The availability, use and operation of the pumps and turbines needed are well known and poses no particular problem in terms of the applicability of this system. The primary question is first of all a proof of concept, specifically addressing the mechanical stability of the system and evaluation of the relative magnitude of the losses associated with the soil deformation in the shear zone being developed along the perimeter of the system. Possible problems in the construction of the overlying soil layers and the load of the membrane are highlighted. In addition the aim is to ascertain whether the expected attainable efficiency and economics can become acceptable compared with already known PHS technologies.

## 2. System concept and design

In a conventional PHS or UPHS system the energy is stored as potential energy by lifting a mass of water into an upper reservoir. The amount of stored energy is roughly proportional to the lift height between the lower and upper reservoir, the density of water and the volume of water stored. The novel concept presented here is shown in detail in Fig. 2. It consists of an inflatable cavity (A) filled with water which is pumped in through a connecting pipe (B)

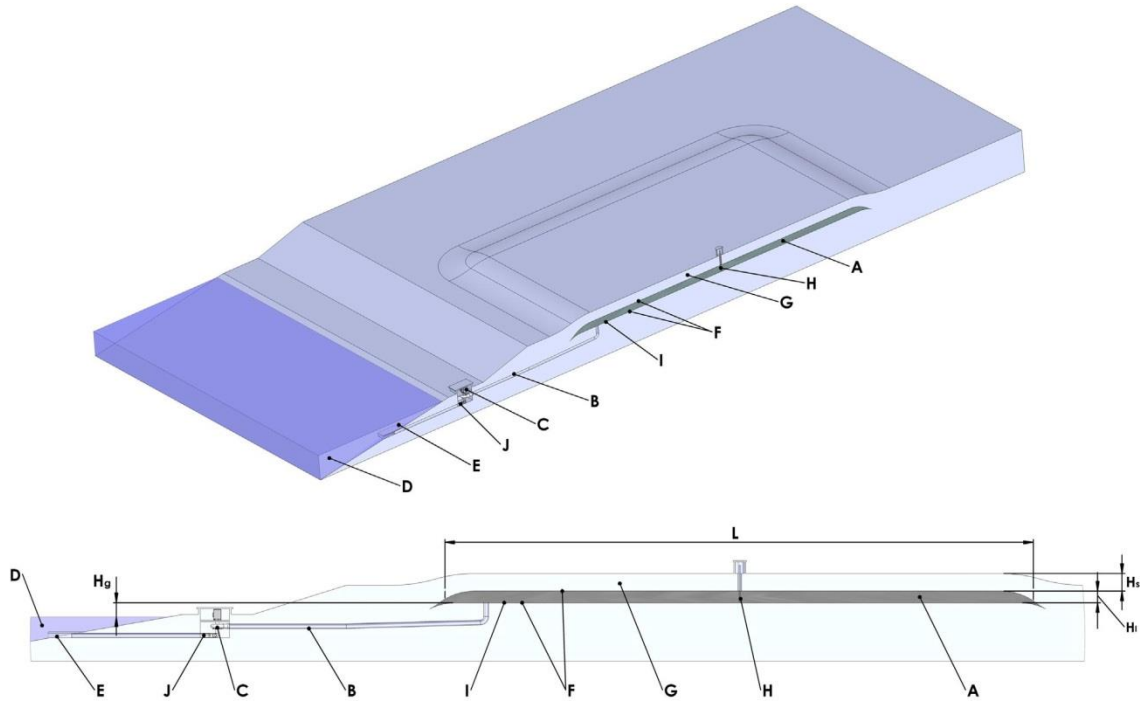


**Fig. 2.** Schematic representation of the underground energy storage concept. Top: isometric view of the  $L \times L = 50\text{ m} \times 50\text{ m}$  field test plant. Bottom: section view showing details of the design. (A) Inflatable cavity, (B) connecting pipe, (C) pump system, (D) water reservoir, (E) strainer, (F) lower membrane (G) top soil, (H) level meter, (I) pressure gauge, and (J) flow meter.

by a pump system (C) connected to a water reservoir (D). A strainer placed at the intake (E) ensures that larger objects do not enter the pump system. The cavity is formed by an upper and a lower membrane (F) (1 mm Wepelen, LDPE membrane) placed on the ground before soil (G) is placed on top of the membranes. The membranes are welded along the edges to form an inflatable volume. The inflation of the cavity lifts the soil placed on top of the upper membrane. The amount of energy stored is here roughly proportional to the lift height and the lifted mass of soil.

**Fig. 2** (bottom) shows a cross-section view of the system. The characteristic dimensions of the system are the edge length  $L$ , the maximum lift height  $H_l$  and the soil layer thickness  $H_s$ . Neglecting the hydrostatic pressure in the cavity, hydrodynamic losses and the possible effects of energy stored in the soil edge zone, the total energy to be stored in the system can be roughly estimated by

$$E_{\text{storage}} = g \rho_s H_s L^2 H_l, \quad (1)$$

where  $g$  is the gravitational acceleration and  $\rho_s$  is the soil density. If a system is scaled up by a factor of  $k$  in each geometric length in Eq. (1) it becomes evident that the stored energy increases by a factor of  $k^4$ . Since the overwhelming plant cost is related to moving soil the capacity to cost ratio will scale linearly in  $k$  which will become important for up-scaling estimates.

For comparison it is noted that if topographical possibilities of a conventional PHS system exist in the vicinity, the conditions for such a conventional PHS system to be able to store more energy than the EM-UPHS can be estimated. Assuming soil to have the double density of water a rough estimate will result in the bottom reservoir height difference of the PHS needs to exceed  $H_s + H_l + H_{gl}$  where the latter quantity is the ground level height of the empty EM-UPHS system relative to sea surface. In general  $H_{gl}$  can be negative. Thus, as stated, the present UPHS solution is only of particular relevance when such topographical opportunities are not available.

There are not many locations in Denmark with an elevation of more than 50 m near the coast, with can be used as location for an upper reservoir in a conventional PHS system. Denmark has approximately 7000 km coast line and with large areas near the coast in use by agriculture today. This gives many possible locations for an EM-UPHS plant and the surface area of the storage can be continued to be used for agriculture. For conventional PHS systems, the use of seawater in an upper reservoir creates a high environmental risk, as even a small leak from the reservoir has the potential to contaminate the groundwater in a large area. And the upper reservoir will have a high visibility in the landscape, with a highly fluctuating surface level. The underground reservoir of an EM-UPHS system can be located near the coast close to sea-level, where a leak of seawater from the reservoir will have no

environmental consequence and the underground reservoir will not be visible in the landscape after the constructions phase is completed.

A proof of concept laboratory test of  $5 \text{ m} \times 5 \text{ m}$  dimension was conducted and showed that it was feasible to implement the principle. A conclusion from this test study was that the energy loss in the soil layer was approximately  $100 \text{ J/m}^3$  [13]. Extrapolating these results it was expected that the energy loss in the layer of soil of a  $50 \text{ m} \times 50 \text{ m}$  field test plant will constitute  $<0.5\%$  of the total amount of energy stored.

Tests on the  $50 \text{ m} \times 50 \text{ m}$  system were performed in two stages for two different designs, the first from February 2011–July 2012, and the second from August 2012 to October 2013. A picture of the layering of the two membranes during construction is shown in **Fig. 3** (left). In the first test run there appeared an indication of a small leak in the membrane. The leak got progressively larger by repeated filling of the cavity. Inspection showed that the leak was localized at the edge where the two membranes are welded together. These preliminary investigations showed that the welded edge constitutes a weak point in the design. Some points on the edge of the upper membrane have been displaced along the outward direction. When the displacement is getting too large the upper membrane tear off at the inside of the weld and thereby causes a leak. Repeatedly inflating and deflating the system caused the upper membrane to buckle in the edge zone due to the relative movement and compaction of the soil in this area as shown in **Fig. 3** (right). A detailed two dimensional mathematical model of the system was developed in order to aid the design of the edge zone and to further evaluate the energy storage and optimization of the system [14]. The model is based on a structural analysis of the membranes and the soil, and implemented in the commercial finite element software Comsol using plastic deformation and creep. Material properties for the membrane material are found in the datasheet and for the soil the Drucker–Prager with elliptical cap constitutive relation was used [15]. For the creep model a Norton flow function was used as described in [16] for the viscous behavior of clay. Soil properties from the specific test site were extracted through geotechnical laboratory tests comprising classification and triaxial tests [17]. For further basic reading on plasticity and soil behaviour please see [18,19].

**Fig. 4** shows the effective creep strain in the soil after 10 cycles inflating the cavity. **Fig. 4** (top) shows the creep strain in the soil for the initial design where membranes are placed primarily in a horizontal plane as in the preliminary tests. The stresses and maximum strains are located on the edges close to the welding lending support to the conclusion that this will cause the buckling and rupture of the membrane at the edge. To alleviate this problem the edges of the top and bottom membranes were drawn down as shown in **Fig. 4** (bottom). This was in order to reinforce the edge



**Fig. 3.** Left: laying of the two  $50 \text{ m} \times 50 \text{ m}$ , 1 mm thick LDPE membrane during construction with the initial design for the edge zone. Right: preliminary results showing folding and buckling close to the welded edge of the membranes. These caused failure in the membrane leading to leaks and decreased efficiency.

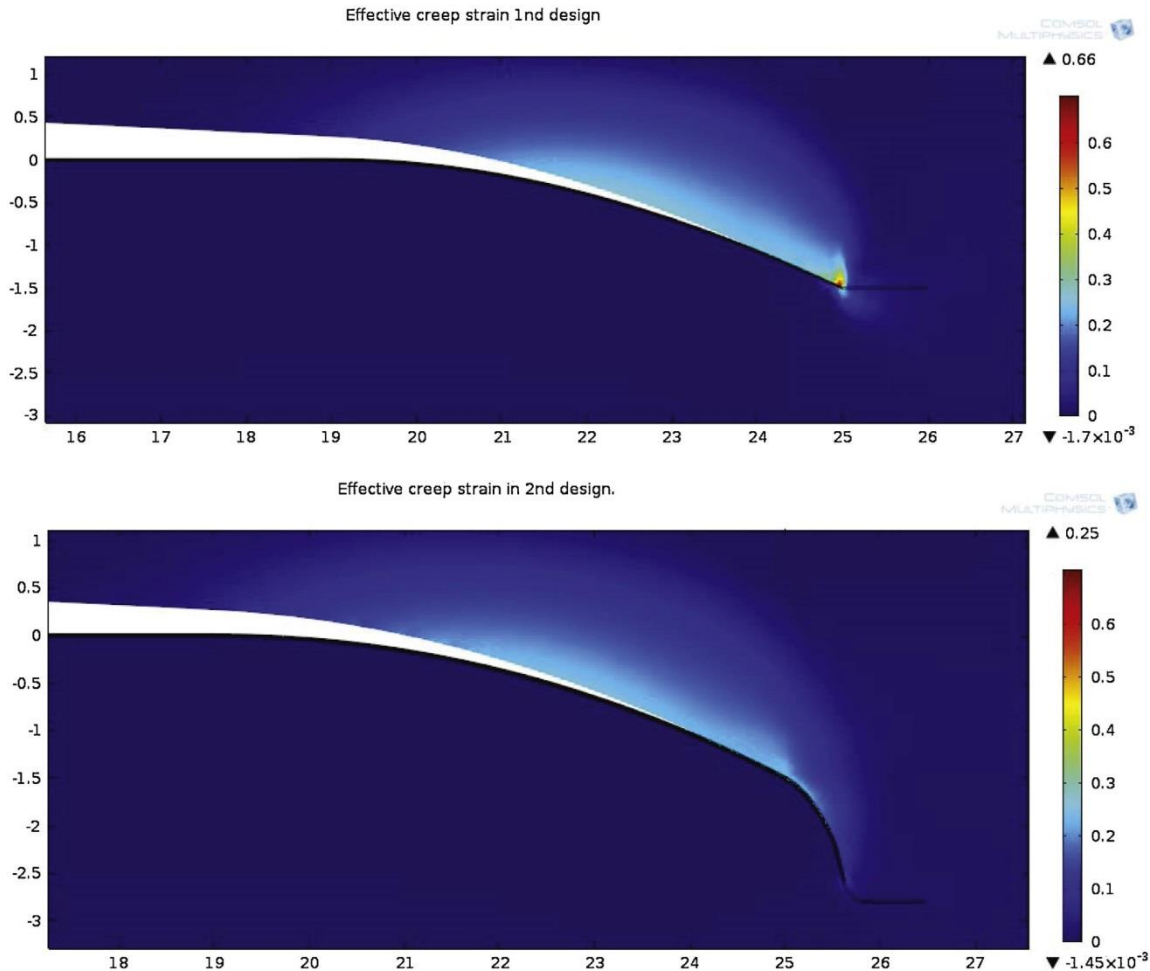


**Fig. 4.** Results from the finite element model showing the effective creep strain in the soil after 10 cycles inflating the cavity. Top: the initial design for the edge zone. The max effective creep strain is located close to the edge welding and the relative difference movement of top and bottom membrane causes the top membrane to buckle. Bottom: in the 2nd design the strain is drawn away from the edge and extended over a larger area. This alleviates the buckling problem since relative movement between bottom and top membrane is allowed due to separation by the water layer.



**Fig. 5.** The 2nd design of the edge zone with a reinforcement geotextile over the top membrane.

using the soil pressure and to displace the maximum strain of the membrane to a point further from the edge. Maximum stress and strain are now located away from the membrane welding edge and will be absorbed by the elasticity of the membrane. This alleviates the buckling problem since relative strain between bottom and top membrane is allowed due to separation by the water layer. Also the energy dissipation due to soil movements during load cycles can be predicted using this model. These results will be discussed later.

Fig. 5 shows a picture of the construction using the second design. In addition to the design change a geotextile Stablinka 150 was layered over the edge in order to reinforce the area under maximum creep strain.

### 3. Field test setup

After the initial tests and optimization of the design, a number of test runs were conducted on the 50 m × 50 m system. The 3 m soil layer contains approximately 15,000 tons of soil, which has an expected average lift of 0.6 m corresponding to a maximum cavity volume of 1500 m<sup>3</sup>. The schematic drawings of the field test setup are shown in Fig. 2. The center lift height is measured by a rod (H)

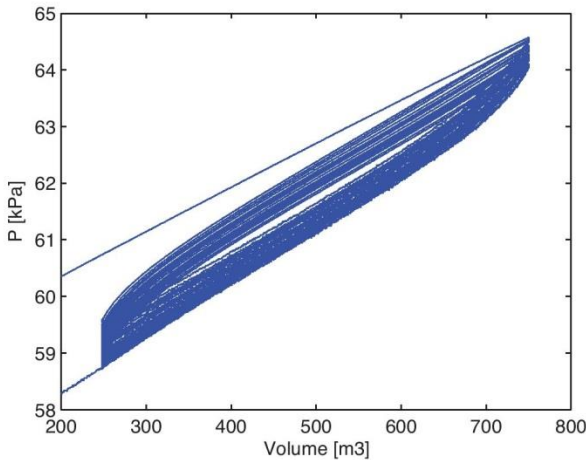


**Fig. 8.** Pressure–volume representation of the CT-3 data set. The swept area in each cycle represents the cycle losses.

and we cannot speculate to correlate these finding against soil or ambient temperature.

**Table 1** shows the design parameters for the 5 m × 5 m Lab Test, the 50 m × 50 m Field Test and a 500 m × 500 m Full Scale plant. A factor 10 up-scaling of side length of the membrane will result in an approx. factor 10,000 increase in stored energy. This was shown technically possible by the up-scaling of the 5 m × 5 m Lab Test to the 50 m × 50 m Field Test. A further factor 10 up-scaling to a 500 m × 500 m Full Scale plant will also be technically possible with technology available today. The head of a full scale 30 MW EM-UHPS will be 50–60 m and the pressure drop in the 300 m 4 m pipe, contribute approx. 4% (2% each way) to the energy loss. 30 MW is in the mid-size range for Francis pump-turbines. Variable speed Francis pump turbines can be optimized for high efficiency (93%) in both pump and turbine operation mode, and are commercially available in a number of standard sizes [20]. The challenge to build a 500 m × 500 m Full Scale plant lies in the logistics to transport the large volumes of soil, and to the secure the funding for such a project.

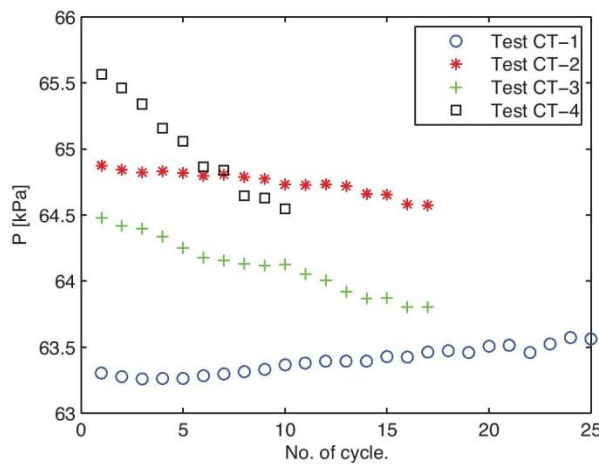


**Fig. 9.** Maximum pressure for each cycle as function of cycle number.

**Table 2**

Summary of the field test trials. A total of 80 cycles was conducted for different conditions, 74 of these are presented here. Average cycle loss is determined by Eq. (2).

Cyclic test ID.	No. of cycles	Volume change (m <sup>3</sup> )	Average cycle loss (%)
CT-1	25	250–750	0.4
CT-2	17	250–750	0.7
CT-3	17	250–750	1.0
CT-4	10	250–1000	1.2
CT-5	1	500–750	0.4
CT-6	1	500–1000	0.6
CT-7	1	250–1250	0.8
CT-8	2	500–1500	1.0

#### 4.1. Soil displacement

The long term deformation of the soil layer has been analyzed with respect to average height deformation and average horizontal deformation (creep) using the DGPS system. The resulting horizontal displacement is on the order of a few cm and the vertical displacement is of the same order of magnitude as the estimated uncertainty. The soil displacement in the horizontal x-y direction after all performed cycles (spanning a period of 200 days from December 29, 2012, for each coordinate point in the mesh, is shown in **Fig. 10**. The average length of the displacement vector as function of time is shown in **Fig. 11**. The first part of the test is intensive in cycling and the latter part is less cycle intensive. There is a correlation between the average displacement vector and the number of days between the data set indicating that the soil layer is approaching a steady-state value.

#### 4.2. Plastic and viscoelastic model

To gain further knowledge of the governing effects of the process and to model the motion and the energy storage of the membrane and top soil layer, a simple mathematical model has been developed. The system is described through a zero dimensional model neglecting the local deformations but focusing on the average dynamics. This is done using a simple approach including the main effects that come into play; the elastic energy storage in the soil, the viscous losses associated with the displacement and the plastic deformations due to yielding of

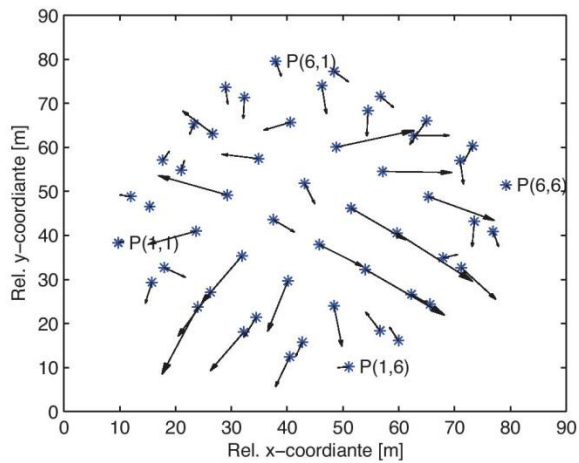


**Fig. 10.** Soil displacement in the x-y plane as measured by DGPS after 200 days of field test trials. Displacement vectors are magnified by a factor of 100 for enhanced visibility.

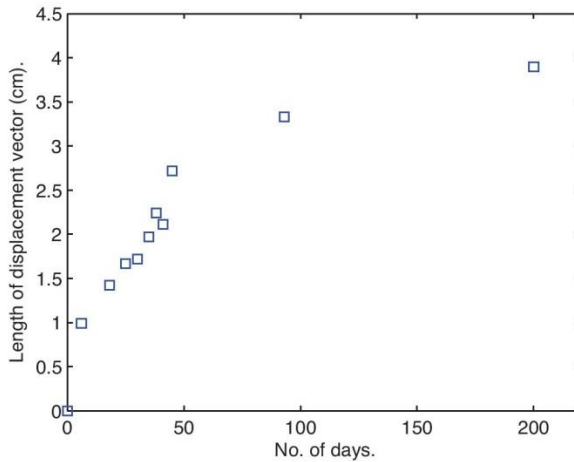


Fig. 11. The average horizontal displacement as function of time.

the soil. The soil layer is considered as a square block attached by a structural contact model on each side. In Fig. 12 a schematic of the contact model is shown.

To account for the geometry of the system and the fact that the stretching of the soil layer is not vertical the contact model is connected in parallel with an initial length and angle to the horizontal plane given by the size of the membrane and the thickness of the soil layer, see Fig. 13.

The dynamical equations for the forces and displacements are as follows

$$\begin{aligned} \mu_1 \dot{\epsilon}_1 &= \sigma_{\max} \left( \frac{|\sigma - \sigma_{\max}|}{\sigma_{\max}} \right)^N \\ E_2 \sigma + \mu_2 \dot{\sigma} &= E_1 E_2 \epsilon_2 + \mu_2 (E_1 + E_2) \dot{\epsilon}_2 \\ \epsilon &= \epsilon_1 + \epsilon_2. \end{aligned}$$

Here  $\epsilon_1$  is the strain due to the yielding of the material and  $\epsilon_2$  is the strain due to the viscoelastic behavior,  $\epsilon$  is the total strain,  $\sigma$  is the stress,  $\sigma_{\max}$  is the yielding stress,  $\mu_1$  is the viscosity of the clay associated with yielding,  $N$  is related with the shape of the stress after yielding,  $E_1$  and  $E_2$  are stiffness parameters, and  $\mu_2$  is the viscosity of the soil before yielding takes place. The initial length is

$$x_0 = \sqrt{L_1^2 + z_0^2},$$

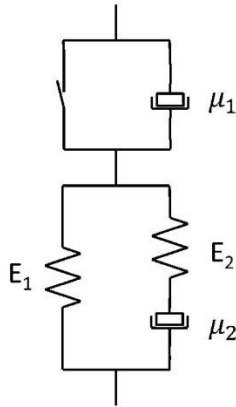


Fig. 12. A schematic representation of the zero dimensional model for the contact forces on each side of the model soil block.

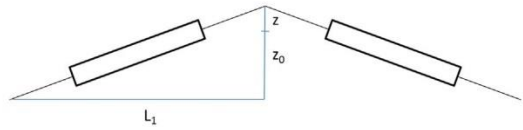


Fig. 13. A schematic representation of the zero dimensional model. Each contact is attached to each side of the solid block.  $L_1 = L/2$ . Only two of the four sides represented.

with  $z_0 = 1.5$  m obtained from measurements on the test plant. The deformed length is

$$x(t) = \sqrt{L_1^2 + (z_0 + z(t))^2},$$

where  $z$  is the height of the membrane at time  $t$ . The strain of the four zero-dimensional models is then given by

$$\epsilon = \frac{x - x_0}{x_0}.$$

#### 4.3. Model validation

The parameters of the model were found by making a least square fit to the experimental time-pressure data CT-8 in Table 2. The data together with the model results are presented in Fig. 14. The results show an excellent fit (blue line) to the experimental data (black line) and underlines that this simple model is indeed capable of capturing the dynamics of the system. The model parameters found from this fit are given in Table 3. The  $P_{\text{offset}}$  parameter has been added to account for the pressure at the bottom of the membrane before water is pumped into the membrane. In order to determine the impact of the yielding (plastic part of the model) we also show results of a model leaving out the yielding component (red line). From the figure we see that we indeed get a better agreement with the experimental results from the plastic model indicating yielding to have a small but noticeable impact.

The model is verified by comparing model results (predictions) and data found in another experiment carried out over a longer time span running multiple cycles (experimental data set CT-4). The experimental data and the model predictions are shown in Fig. 15. The model fits the experimental data nicely during the first 3–4 cycles, however, the discrepancy increases for the subsequent

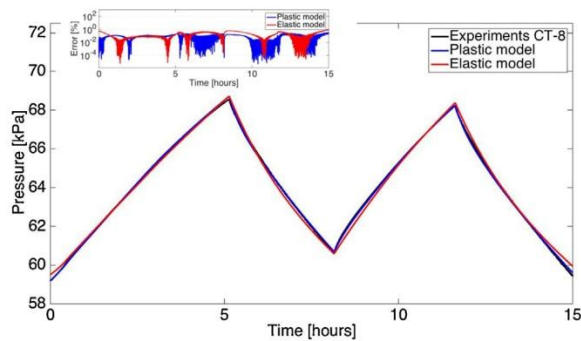


Fig. 14. Comparison between experimental data (black line), plastic model results (blue line), and elastic model results (red line) achieved by a least square fit between model and experiments using data set CT-8. Both pressure and the error is presented in terms of gauge pressure. (For interpretation of the references to color in this figure legend, the reader is referred to the web version of the article.)

**Table 3**

Model parameters found by least square fit to experimental data using data set CT-8.

Parameter	Value	Unit
$E_1$	$1.335 \times 10^8$	[Pa]
$E_2$	$1.508 \times 10^8$	[Pa]
$\mu_1$	$1.359 \times 10^{10}$	[Pas]
$\mu_2$	$2.4391 \times 10^{11}$	[Pas]
$\sigma_{max}$	$90.28 \times 10^3$	[Pa]
$N$	1.3955	[–]
$P_{offset}$	244.4	[Pa]

cycles. In order to capture the longer time scale behavior of the system another dashpot could be introduced in a further refinement of the model. This would again enable a better agreement between model and experiments also on long time-scales, however, this extension of the model is outside the scope of this paper.

### 5. Economic viability

A full scale EM-UPHS plant connected to the Danish power grid would get its main revenue by delivering ancillary services to the control reserves market. In Denmark the transmission system operator (TSO) has the responsibility to ensure that the physical balance in the electricity system is maintained. In order to do this, the TSO needs regulating power and control reserve capacity. Control reserve capacity is either production capacity or consumption which is offered in advance to the TSO in return for an availability payment. The TSO buys various types of reserve capacity that differ with respect to response rate, etc. The term “ancillary service” is a general term for the reserve capacity bought by a TSO in order to ensure a reliable and efficient operation of the electricity system [22]. The market price for the ancillary services varies with many factors, and cannot be predicted reliably over a longer time frame. An estimate of the construction and operating cost of a 500 m × 500 m full scale EM-UPHS is presented in Table 4. Pricing information of grid scale energy storage systems, like those listed in Table 4 and shown in Fig. 16 should be taken with some caution. Of the technologies compared only few (PHS, CAES and Flywheel), has actually been implemented on grid scale and been in successful operation for a significant amount of time. Table 5 shows an overview of the Control Reserves Market – Western Denmark in the period from January 2011 to July 2013. With the historical data it is possible to

**Table 4**

Estimation of the construction and operating cost of a 500 m × 500 m full scale EM-UPHS.

Full scale EM-UPHS system construction and operating cost		
Transporting 7.5 million m <sup>3</sup> soil at EUR 20.0 million		
EUR 2.67/m <sup>3</sup>		
30 MW pump/turbine <sup>a</sup>	EUR 6.7 million	
Membrane and 300 m Ø4 m pipe	EUR 6.7 million	
Total plant construction cost	EUR 33.4 million	
Annual return	7%	EUR 2.3 million
Purchase price for 1 kWh	EUR 0.04	
Expected efficiency	80%	
Expected operating days per year (days)	280	
Expected pump/turbine operating hours per day (h)	8	
Pump/turbine size (MW)	30	
Max. storage capacity (MWh)	200	
Annual purchases of electricity (MWh)	67,200	
Annual costs of electricity		EUR 2.7 million
Total annual costs		EUR 5.0 million
Annual sales of electricity (MWh)	53760	
Sales Price for 1 kWh to cover total annual cost	EUR 0.09	
Capital cost per unit of power rating (EUR/kW)	EUR 1111	
Capital cost per unit of storage capacity (EUR/kWh)	EUR 208	

<sup>a</sup> The cost include a complete installed delivery consisting of: pump turbine, turbine control, 2 valve, generator, control system, switching station and transformer.

estimate the annual revenue from a full scale EM-UPSH plant, as if it had been operating in Control Reserves Market of Western Denmark, in the time period of the data. An EM-UPHS plant would bid into the market for Primary and Secondary Control Reserves, where the earnings potential ranged from 13,000 to 26,000 EUR/MW per month for primary control reserves, and from 10,000 to 13,000 EUR/MW per month for Secondary Control Reserves. The estimated annual revenue would have been between 8.3 and 14 million EUR.

A comparative study of the capital cost of a selection of grid scale energy storage systems [22], with the proposed EM-UHPS system inserted, is shown in Fig. 16. It can be seen that an EM-UHPS system is expected to have both lower capital costs per unit of power rating and capital cost per unit storage capacity than battery based systems regardless of type. The capital costs are comparable to the capital costs of a Compressed Air Energy Storage (CAES) system.

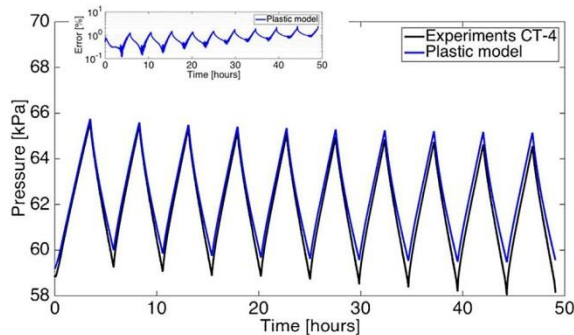


Fig. 15. Comparison between model results and extended experimental test using data set CT-4. Both pressure and the error are presented in terms of gauge pressure.

**Table 5**

Earnings potential of a Full Scale EM-UPHS plant in the Control Reserves Market. Ref. [22]. Minimum bid: minimum effect size for the control reserves. Load factor: percentage of the actual delivered power in the availability period.

#### Control Reserve Market Western Denmark 2011–2013

- Primary Control Reserves
  - Daily auctions, minimum bid: 0.3 MW
  - Response time 30/150 seconds, very low energy supplied (load factor ≈0.2%)
  - Earnings potential (avg. 2011–2013): 13,000–26,000 EUR/MW per month
- Secondary Control Reserves
  - Monthly auctions, minimum bid: 1 MW
  - Response time up to 15 min, moderate energy supplied (load factor 10–20%)
  - Earnings potential (avg. 2011–2013): 10,000–23,000 EUR/MW per month
- Tertiary Control Reserves
  - Daily auctions (hour for hour), minimum bid: 10 MW
  - Response time up to 15 min, large energy supplied (load factor >90%)
  - Earnings potential (avg. 2011–2013): 130–1300 EUR/MW per month

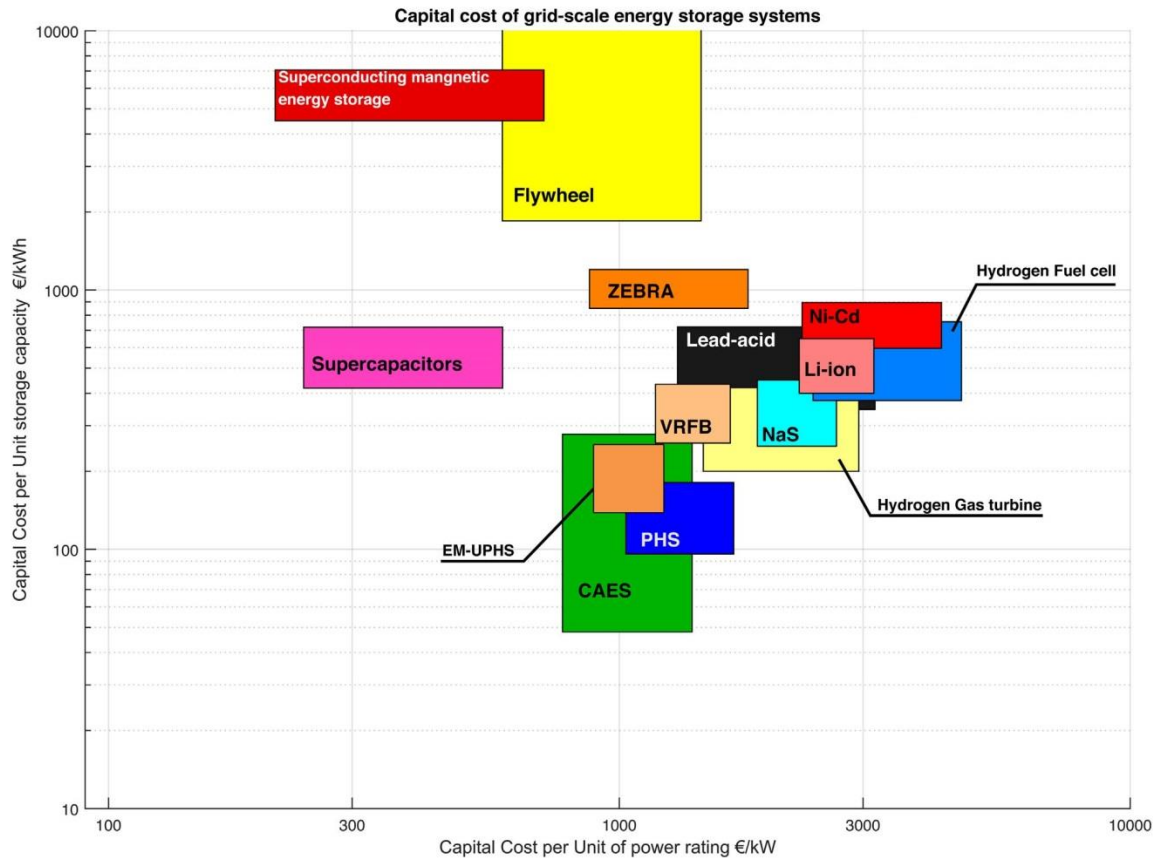


**Fig. 16.** Diagram showing a comparative study of the capital cost of a selection of grid scale energy storage systems [22].

## 6. Conclusion

The field tests demonstrate that the EM-UPHS system is a feasible system for energy storage with response similar to conventional PHS technology. The results indicate that the storage efficiency of this new technology will be very close to that of traditional and existing PHS technology. The experiments show that the energy lost by deformation of the soil/sand is between 0.4 and 1.2% with an average of 0.76%. The test results combined with the theoretical modeling done on the system are indicating that viscoelastic effects through stress relation by creep are the main mechanism for energy loss in the soil layer. The energy loss in the soil layer is low compared to energy loss by friction in the piping and the pump/turbine.<sup>2</sup> By virtue of Eq. (1), scaling up to a 10 times larger EM-UPHS system, the cycle energy loss in the soil is therefore expected to be less than 0.1% of the stored energy on average. Based on such extrapolations from the field tests and cost estimation for moving soil and equipment, the price per installed power will be 1111 EUR/kW and the price per installed storage capacity 208 EUR/kWh for a 500 m × 500 m installation.

A very large percentage of the cost for building an EM-UPHS is related to moving soil. This will be contracted locally and hence the cost of an EM-UPHS will depend very much on local cost of land, soil and manpower. Also the availability of a water reservoir

is another factor to be considered. In the coastal zones EM-UPHS has a high potential whereas in central Europe other sources of water limit the possibility for EM-UPHS. In Europe it will be possible to build EM-UPHS in the coastal areas where sea water may be used.

The TSO in Denmark, EnergiNet.dk, expect that the total installed wind power capacity in Denmark will increase, from 4893 MW in 2014, to 6700 MW in 2025 [22]. In 2014, the wind power generation corresponded to 39% of the electricity consumption. In the course of the next 10 years, the share is expected to increase to 61%. The TSO expect that there will be room for 5–10 full scale EM-UPHS plants in a 10 year timeframe with the current development of renewable energy, and the corresponding increase in the demands for ancillary services. The main function of the EM-UPHS plants will be to deliver ancillary services to the control reserves market and the achievable size of the proposed storage plant is well suited for buffering both wind and PV solar utility installations in coastal areas.

## Acknowledgements

The EM-UPHS project was financed through the ForskEL research program under EnergiNet.dk. The authors would like to thank all the project participants: EnergiNet.dk, JolTech ApS, GODEvelopmet ApS, RisøDTU, DTU Byg, SDU/MCI, GEO, Syd Energi, Danfoss A/S, Arkil A/S, Lean Energy Cluster, Sloth-Møller A/S and Sønderborg Kommune.

<sup>2</sup> Approximate losses in pump turbine/electrical system 15% and losses in the pipes 5%.

## References

- [1] W.F. Pickard, A.Q. Shen, N.J. Hansing, Parking the power: strategies and physical limitations for bulk energy storage in supply-demand matching on a grid whose input power is provided by intermittent sources, *Renew. Sustain. Energy Rev.* 13 (8) (2009) 1934–1945, <http://dx.doi.org/10.1016/j.rser.2009.03.002>.
- [2] C. Energystrelsen, Energistatistik 2012. 2012 (in Danish). <http://www.ens.dk/info/tal-kort/statistik-nogletal/arlig-energistatistik>.
- [3] Directive of the european parliament and of the council on the promotion of the use of energy from renewable sources, COM(2008) 19 final 2008/0016 (COD).
- [4] F. Diaz-Gonzalez, A. Sumper, O. Gomis-Bellmunt, R. Villafafila-Robles, A review of energy storage technologies for wind power applications, *Renew. Sustain. Energy Rev.* 16 (4) (2012) 2154–2171, <http://dx.doi.org/10.1016/j.rser.2012.01.029>.
- [5] J.P. Deane, B.P.O. Gallachoir, E.J. McKeogh, Techno-economic review of existing and new pumped hydro energy storage plant, *Renew. Sustain. Energy Rev.* 14 (4) (2010) 1293–1302, <http://dx.doi.org/10.1016/j.rser.2009.11.015>.
- [6] DOE global energy storage database, US Department of Energy. <http://www.energystorageexchange.org>.
- [7] S.W. Tam, C.A. Blomquist, G.T. Kartsounes, Underground pumped hydro storage – an overview, *Energy Sources* 4 (4) (1979) 329–351, <http://dx.doi.org/10.1080/00908317908908068>.
- [8] H.H. Chiu, L.W. Rodgers, Z.A. Saleem, R.K. Ahluwalia, G.T. Kartsounes, F.W. Ahrens, Mechanical energy storage systems: Compressed air and underground pumped hydro, *J. Energy* 3 (3) (1979) 131–139, <http://dx.doi.org/10.2514/3.62426>.
- [9] W. Pickard, The history, present state, and future prospects of underground pumped hydro for massive energy storage, *Proc. IEEE* 100 (2) (2012) 473–483, <http://dx.doi.org/10.1109/JPROC.2011.2126030>.
- [10] Packing some power, *The Economist*. <http://www.economist.com/node/21548495>.
- [11] A. Slocum, G. Fennell, G. Dundar, B. Hodder, J. Meredith, M. Sager, Ocean renewable energy storage (ores) system: analysis of an undersea energy storage concept, *Proc. IEEE* 101 (4) (2013) 906–924, <http://dx.doi.org/10.1109/JPROC.2013.2242411>.
- [12] J.S. Tietjen, Pumped Storage Hydroelectricity, *Encycl. Energy Eng. Technol.* (2007) 1207–1212.
- [13] Energilager - nedgravet pumpelager/energimembran (in Danish), Energinet.dk – PSO Project No. 010216. <http://www.energiforsknig.dk>.
- [14] J. Olsen, Structural model for soil mechanics and creep in a periodically loaded underground energy storage system, 2015 (unpublished).
- [15] D.C. Drucker, W. Prager, Soil mechanics and plastic analysis for limit design, *Q. Appl. Math.* 10 (2) (1952) 157–165.
- [16] G. Qu, S.D. Hinchberger, K.Y. Lo, Evaluation of the viscous behaviour of clay using generalised overstress viscoplastic theory, *Geotechnique* 60 (10) (2010) 777–789.
- [17] O. Hedeland, Laboratory tests on reconstituted clay, geotechnical data report, revision 1.1, Technical University of Denmark, DTU, 2012, August (unpublished).
- [18] E. Neto, D. Peric, D. Owen, Computational Methods for Plasticity – Theory and Applications, 2008.
- [19] D. Wood, Soil Behaviour and Critical State Soil Mechanics, 2007.
- [20] J. Krenn, H. Keck, M. Sallaberger, Small and mid-size pump-turbines with variable speed, *Energy Eng.* 5 (2013) 48–54.
- [21] B. Zakeri, S. Syri, Electrical energy storage systems: a comparative life cycle cost analysis, *Renew. Sustain. Energy Rev.* 42 (0) (2015) 569–596, <http://dx.doi.org/10.1016/j.rser.2014.10.011>.
- [22] H. Parbo, Seminar om Energilagring den 28. august 2013, EnergiNet.dk. <http://www.energinet.dk/EN/El/Engrosmarked/Viden-om-engrosmarkedet/Sider/Reserver-og-regulerkraft.aspx>.

## 8 Appendix A8 Selection of PV test plant

This appendix describes the selection of a suitable MW-size test plant and the developed test concepts. Data of PV irradiation and power generated with a time resolution <1 minute could not be accessed and it was decided to produce data on the second-level and to construct a local database containing said data.

### 8.1 PV test plant requirements

A major goal during the first part of the project was the identification a suitable large PV utility plant for field testing. The selected plant should be suitable for modification regarding string/central inverter configuration and associated test equipment as well as easily accessible and have a suitable size / geographical extension. See table A8.1.

Table A8.1 Initial requirements set up for selecting a PV utility test park.

Parameter	Value/type etc.	Importance	Comment
Installed PV power	>1 MWp	Medium	Will depend on geographical distribution of strings
String inverter type	DSI TLX / FLX string inverter types	High	Communication via Danfoss proprietary inverter protocol
Additional central inverters	>3 parallel strings	Medium	For comparison to string inverter concept
Topography	Flat	Medium	Curvature will complicate analysis
Rewiring to central concept	>50 m between strings	High	Crucial for shadow analysis
Mounting of PVSweeper units	1 panel of max. 250W	Medium	Can be tested externally
Access to mains power	230V AC	(High)	At least temporary for external test equipment.
In operation	Not later than early 2014	High	Time for at least one year measurements 2014-2015
Sample rate	1 sec. sampling	High	For temporal resolution
Mounting of weather station	Davies Vantage Pro+	High	Part of the Sunrise data logger concept
IP access	High speed internet	High	For data upload to SDU server
Mounting of field PC	Enclosure with mains power	High	Part of the Sunrise data logger concept
Distance from SDU	Preferably within 2 hour driving distance	Medium	Frequent visits are foreseen, esp. in the start-up phase

## 8.2 Selection of primary PV test plant

The PV test plant selection priority list and the main conclusions are shown in table A8.1.

Table A8.2 PV test plant selection priority

Priority	Plant operation	Evaluation
1	Utility scale PV-plant equipped with both string-inverters and a central inverters with equal characteristics.	Such plant could not be identified.
2	Utility scale PV-plant equipped with both string-inverters and a central inverters with comparable characteristics.	Such plant could not be identified.
3	Mounting of string inverters on selected strings on a plant equipped with at least one central inverter.	A plant with central inverters could not be located for long term testing
4	Mounting of a central inverter on a part of a plant equipped with string inverters.	Complicated for practical/legal reasons (grid connection).
5	Modify parts of a plant with string inverters so emulate a central inverter	Possible.

A plant with combined string and central inverters could not be identified and mounting a central inverter which need connection to the medium voltage grid) would be difficult/expensive and require permission from local energy companies.

Rewiring of a utility size PV plant to simulate a central inverter concept was selected and 3 detailed concepts were planned.

- Emulating a central inverter setup via string inverters
- High speed recording of inverter and weather parameters
- Recording of IV-scans over a distributed area / alternatively to monitor single panel externally.

### 8.2.1 Evaluated PV utility plants.

The PV Utility plants listed in table A8.3/A8.4 were investigated in detail. Contacts to the owner/operators of the parks in Langenbogen, Zappendorf and Edersleben ( H. Hron GmbH) and Busenwurth (Möhring GmbH) were established via Danfoss Solar Inverters A/S.

Table A8.3 Technical data from investigated PV utility plants.

PV plant	Power (MWp)	Inverter type	In operation
Edersleben/Hutdeckel, DE	2.748	163xTLX 17Pro+	2011
Edersleben/Tongrube, DE	4.053	TLX15/12.5	2011
Langenbogen, DE	0.969	TLX15/12.5k	2011
Busenwurth, DE	12.217	744x TLX17Pro+	2011
Zappendorf, DE	1.510	TLX15/12.5	2011
AFB Skrydstrup, DK	0.6	35xTLX17Pro+	05-2014
AFB Karup, DK	1.2	70xTLX17Pro+	05-2014
Danfoss Solar Park, DK	2.1	128xFLX17Pro+*	01-2014

Colour code: OK () Restrictions apply Minor issue Major issue

\*Several inverters were replaced with 60kW MLX-inverters during 2015.

All plants except Langenbogen and AFB Skrydstrup were above 1 MW. As illustrated in table A8.3 were none of the Danish parks accessible for test before 2014 and access for installing test systems in the Danfoss Solar Park could not be granted until May 2014. All parks have a suitable physical size and TLX/FLX inverters, but the possibilities for rewiring rows, the layout and topography vary.

The distance to the parks (relevant for service, inspection and modification etc. of test equipment) was part of the decision base, as shown in table A8.4. The mounting of a weather station and a field PC was allowed at all parks listed.

Table A8.4 Decision matrix of the major parameters.

PV plant	Rewiring of strings	Wiring between rows	PV sweep allowed	1sec. sampling	IP access	IP/Mains power	Plant Topography	Driving distance
Edersleben/Hutdeckel, DE	✓	(✓)	✓	✓	✓	✓	Minor curvature	≈540 km
Edersleben; Tongrube, DE	✓	(✓)	✓	✓	✓	✓	Minor curvature	≈540 km
Langenbogen, DE	✓	(✓)	✓	✓	✓	✓	Minor curvature	≈540 km
Zappendorf, DE	✓	X	X	✓	✓	✓	Minor curvature	≈570 km
Busenwurth, DE	✓	X	✓	✓	✓	✓	Flat	151 km
FW Skrydstrup, DK	✓	X	✓	X	✓	(✓)	Flat	74 km
FW Karup, DK	✓	X	✓	X	✓	(✓)	Flat	219 km
Danfoss Solar Park, DK	✓	X	✓	✓	✓	(✓)	Medium curvature	19 km

Colour code: ✓ OK (✓) Restrictions ■ Minor issue ■ Major issue X Not acceptable

Detailed plans for using the Edersleben/Hutdeckel plant near Halle, Germany, were made early 2013, but after a decision by Danfoss A/S to establish the Danfoss Solar Park the plants were put on hold. The PV plants owned by the Royal Danish Airforce (FW=Fighter Wing) could not be equipped with the intended sampling system as the monitoring of the sites were outsourced to an external company. Negotiations to access/sample in parallel were not successful. Access to the PV-plants was restricted (but possible) due to their location inside operational military units.

### 8.2.2 Conclusion regarding selection of a test park

The Danfoss Solar Park was selected as the primary test park due to the easy possibilities for rewiring, sampling and ease of access. Danfoss A/S was very helpful in all matters regarding access to the park, which at the same time was used as a test park for Danfoss Solar Inverters A/S. The medium curvature of parts of the park proposed a challenge due to the varying irradiation over the individual panels in some of the row segments, causing additional mismatch/power loss between the panels. The subject is addressed in detail in chapter 5. The layout of the Danfoss Solar Park is shown in figure A8.1.

The construction of the Danfoss Solar Park was initiated 2013 and was completed early 2014. Construction started more than a year later than initially planned, due to an unclear situation regarding national feed-in tariffs.

The Danfoss plant was the main test plant and irradiation data from a 62.5kW PV plant at SDU Alsion in Sønderborg, Denmark, was added for comparison of irradiance measurements and for IV-curve sweeping. The 62.5 kWp PV plant at the Mads Clausen Institute at the University of Southern Denmark in Sønderborg (54°54'47''N, 9°46'44''E) is situated on the roof of a 4 storage building, housing a concert hall in connection with the University. The plant consist of 250 polycrystalline

250W panels of type Simax New Green Energy (SM660-250) mounted vertically with a tilt of 15° and an 45° orientation (Southwest).

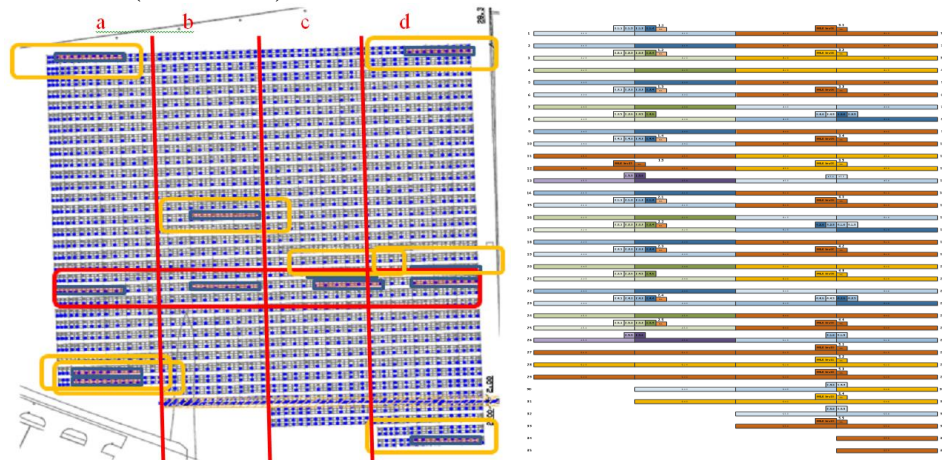


Figure A8.1 Danfoss solar park layout. Left: with 128 string inverters, boxes indicate test inverters. Red box shows test row 21. Right: With 60 kW MLX inverter mounted (brown row segments) during 2015.

The basic parameters of the test parks are listed in table A8.5.

Table A8.5 Basic parameters for the selected PV plants.

Parameter	Danfoss Solar Park	SDU Alsion PV plant	
Inverter capacity	1,920 kW	60 kW	
Module capacity	2,076,840 Wp	62,500Wp	
Plant area	4 ha	800 m <sup>2</sup>	
Panel area	2.45 ha	408 m <sup>2</sup>	
Inverters (until spring 2015)	128 x FLX 15kPro (3 MPPT)*	4x FLX12.5Pro+ (3 MPPT) 1xFLX10kPro+ (3 MPPT)	
Module manufacturer	ND-225-230-235-240R1J_EN	Hanwha SolarOne, Ltd.	
Module rating	8568x225W; 648x230W	250Wp	
Cell type	Polycrystalline	Polycrystalline	
Total no. of modules	9216	250	
Module types	ND225R1J NDR225A2 NDR230A2 ND230R1J	7308 panels 1260 panels 198 panels 450 panels	SM660-250
Module sorting scheme	Random	Random	
Grid connection	5x400kW low voltage grid	3Phase 380V 50Hz mains	
Est. production	Est. 1.957 MWh/year	Est. 52.530 MWh/year	
Panel angle	15°	15°	
Panel orientation	SSE, 3° from S	SW, 45° from S	
Topography	Uneven, up to ±7° tilt	Flat, within 1° tilt	
No of panels per inverter MPPT	24	23/21	
No of rows	36 (uneven length)	12 (uneven length)	
No of panels per row (row 1-29)	3x96	12	

\*Changed during 2015, replaced by 60kW MLX-inverters

### 8.2.3 Danfoss Solar Park panel statistics

The Danfoss Solar Park is equipped with 9216 PV panels. Flash-test data documentation for all panels have been obtained from the Danish developer of the PV plant and analysed.

#### 8.2.3.1 Test row statistics

The row 21 of the Danfoss Solar Park is of particular interest, as this row has been rewired for test purposes. The distributions of the  $I_{MPP}$  and the  $P_{MPP}$  values for the panels in the different row sections for the top, middle and bottom row are shown in figure A8.2-A8.3.

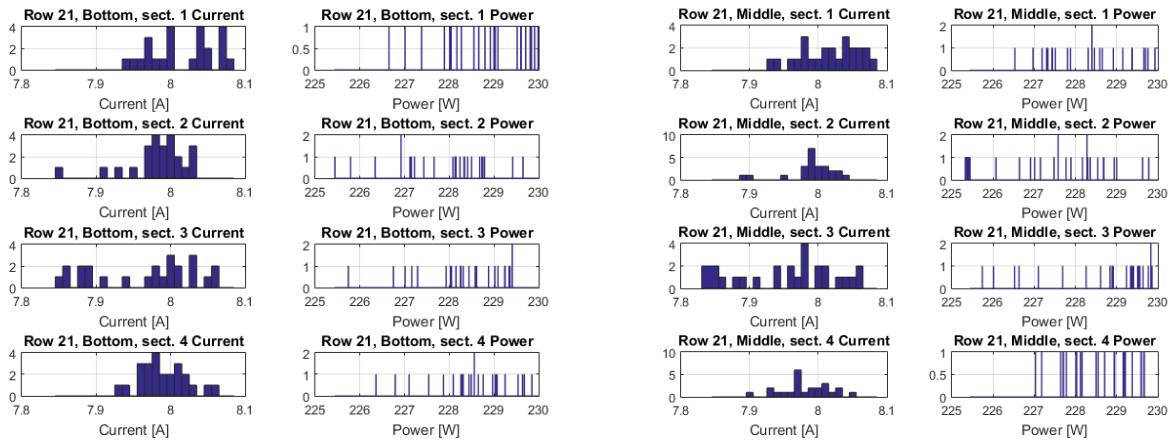


Figure A8.2

Row 21 Bottom (left) and middle (right) row, section 1-4.

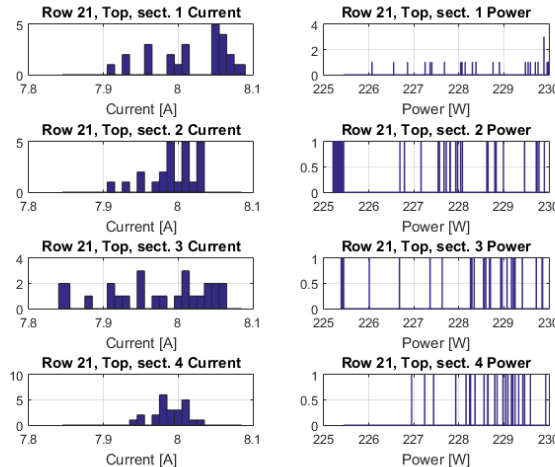


Figure A8.3 Row 21 Top row, section 1-4.

All panels in Row 225 have a  $P_{MPP}$  value  $< 230\text{W}$ . The  $I_{MPP}$  currents are widely distributed for all row segments and sections. Top row section 21 has the most narrow  $I_{MPP}$  distribution and a  $P_{MPP}$  variation from 227.0-229.6W.

#### 8.2.3.2 Panel statistics

The distribution of the MPP current, MPP voltage and the rated panel power is for all 9216 panels mounted at the Danfoss Solar Park are shown in figure A8.4.

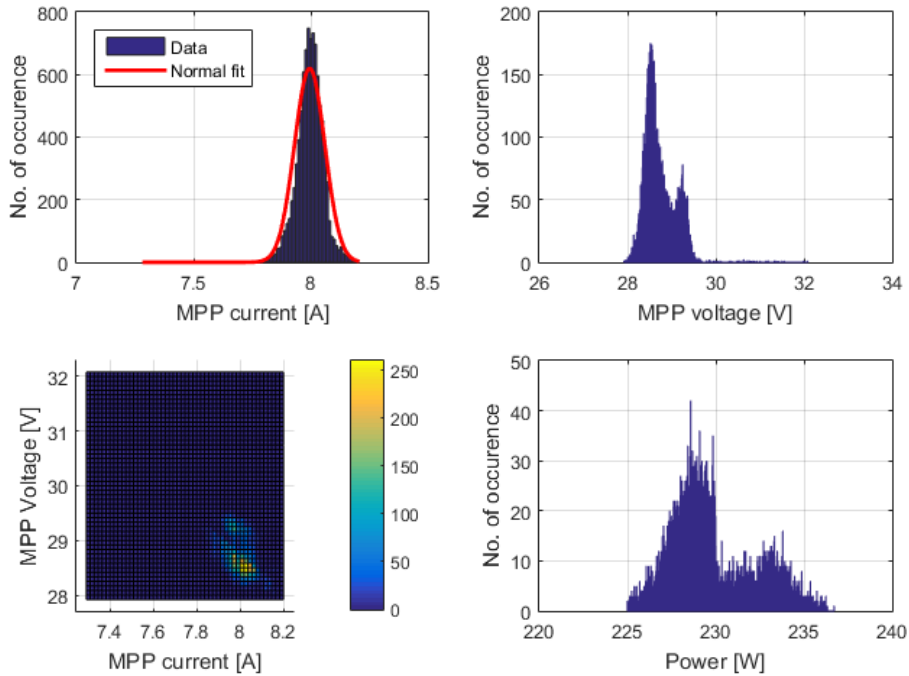


Figure A8.4 Panel statistics for all panels mounted in the Danfoss Solar Plant. Top left:  $I_{MPP}$  with normal fit ( $\mu=8.00$ ,  $\sigma=0.065$ ), A Least Square amplitude fit was applied. Top right:  $V_{MPP}$ . Bottom left:  $I_{MPP}$  vs.  $V_{MPP}$  distribution. Bottom right:  $P_{MPP}$  histogram.

The current  $I_{MPP}$  values are almost uniformly distributed around 8A but the voltage  $V_{MPP}$  values are distributed around two centres.

The distribution of  $P_{MPP}$  is shown in figure A8.5 for the 4 different types of panels mounted, as well as the sorted  $P_{MPP}$  values of all panels. The differences between the labelled  $P_{MPP}$  and product  $I_{MPP} \cdot V_{MPP}$  are for all panels below  $\pm 0.15\text{W}$ . The analysis of the power ratings distribution according to panel type show that there is a clear difference between the panel types.

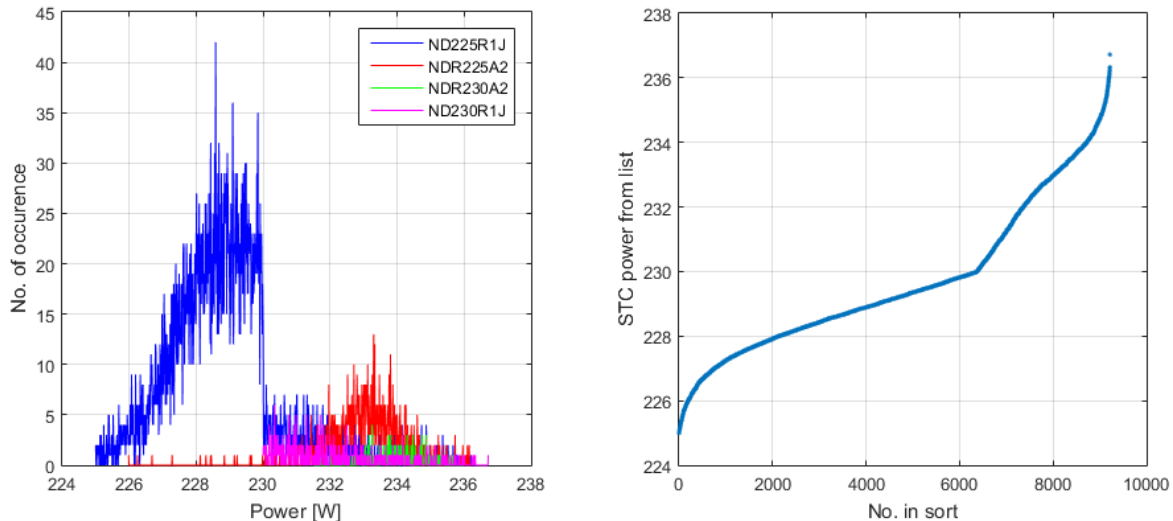


Figure A8.5 Left: Panel distribution histogram, acc. to panel type. Right: Sorted panel  $P_{MPP}$  values.

It can be observed that the dominant panel type is ND225R1J, dominating up to 230W, where a sorting by the manufacturer seem to have limited the number of panels above. The panel of type

NRD225A2 is acc. to its label a 225W panel, but the actual  $P_{MPP}$  value is mainly distributed around 233W. The other panel types are all distributed above 230W.

The panels are randomly distributed over the entire site, but the 225W and 230W groups are not mixed. This means that the group of 225W-type panels (types ND225R1J and NDR225A2) in reality consist of more a mixture of 225W and 230W range panels. The Danfoss Solar Park has a total of  $9216/24=384$  individual string input/MPPT of which 256 are connected to 225W type panels. It can be concluded that the Danfoss Solar Park consist of 6379 panels in the 225-230W range and 2837 panels in the 230-237W range (but only 648 panels acc. to the type number), according to the available flash-test data.

#### 8.2.4 Energy storage/stabilization

The storage of energy from renewable energy sources like PV plants and windmills is related to the optimization of a PV utility plant in term of both short term and long term supply stability. Local energy storage can be beneficial for a PV utility plant in case of inverter breakdown and stabilization of the power grid. An operational advantage of string inverters is that they are easily replaced by local personnel who can have some inverters for replacement in stock. If a central inverter breaks down there is a risk of longer periods with loss of energy production and it can take time for larger central inverters to be repaired or replaced<sup>7</sup>.

Moving clouds are known to be the cause of voltage flicker on the electric grid, requiring additional voltage regulation capability on the electric grid [66]. Local buffering of energy is an emerging concept due to the development of new storage technologies and according to [74] it is both practical and desirable to consider inclusion of grid support functionality in utility-scale PV plants. The explosive growth in PV and wind power units worldwide in recent years has generated an increased interest in storage solutions of which many are entering the market, being for example battery storage, pressured air, hydrogen, power-to-gas, flywheel or gravitational storage.

An activity related to the study of a novel concept of gravitational storage suitable for fluctuating sources of electricity like wind power and photovoltaics are peripherally included in this study via concept evaluation, data analysis and co-authorship of the publication listed in appendix [A7]. The system is of the UPHS (Underground Pumped Hydro Storage) type where energy is stored by lifting a mass of soil through the pumping of water into an underground cavity formed by two 1 mm thick membranes below the soil layer, therefore called EM-storage for Energy Membrane storage. The estimated storage cost for a full scale 30 MW storage plant with 200 MWh storage capacity is estimated to be approximately 0.053 EUR /kWh. It is shown that the EM-UHPS energy storage plants are a suitable solution for coastal areas. Details are presented in appendix [A7].

---

<sup>7</sup> Information regarding central inverters received via personal communications with the operator of MW PV-plants in Ukraine (Gerhard Mütter, Technical director at AES GmbH, Vienna (A)), via the EC Performance Plus project [57].

### 8.3 Emulating a central inverter setup via string inverters

The logged inverters are illustrated in figure A8.6. A distribution over the whole site has been attempted. The string connections in row 20/21 have been changed in order to emulate a central inverter location (long distances between strings). The location of the inverter strings/panels monitored is shown as dark/red areas in figure 2. Row 21 (red) is the main test row. The details about the monitoring instrumentation are available in the published work [A3].

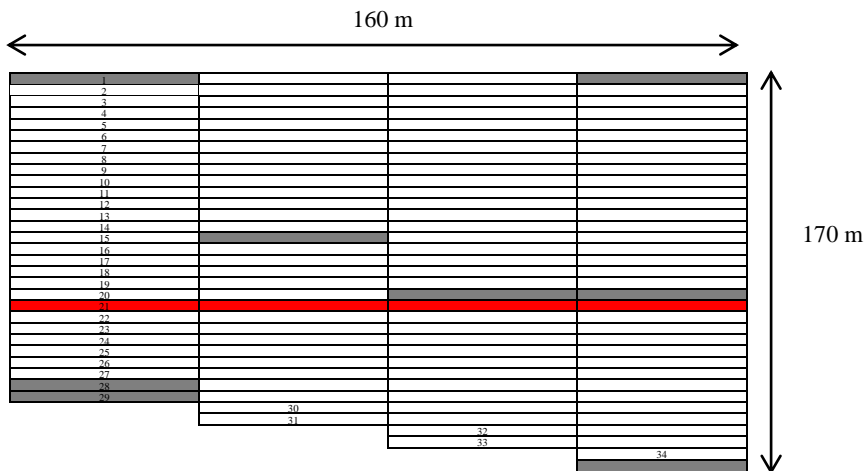


Figure A8.6 Monitored string areas of the Danfoss PV plant.

#### 8.3.1 String modification

The traditional string layout of the panel rows is shown in figure A8.7. Each inverter covers  $\frac{1}{4}$  of a full row (3x96 panels), with individual MPPT for the 3 sub-rows. This setup gives a minimum of geographical distribution of the interconnected panels and has a clear advantage when inter-row shadowing is occurring. To investigate shading on a larger geographical distribution of panels the 4 primary test inverters have been rewired to different panel groups. See figure A8.8.

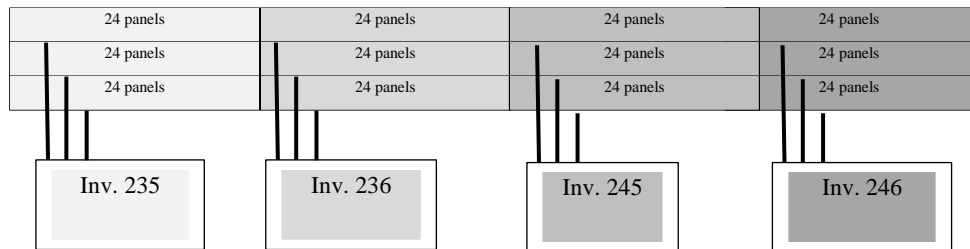


Figure A8.7 Traditional string layout concept for the Danfoss Solar Park.  
There is one inverter per section (1-4).

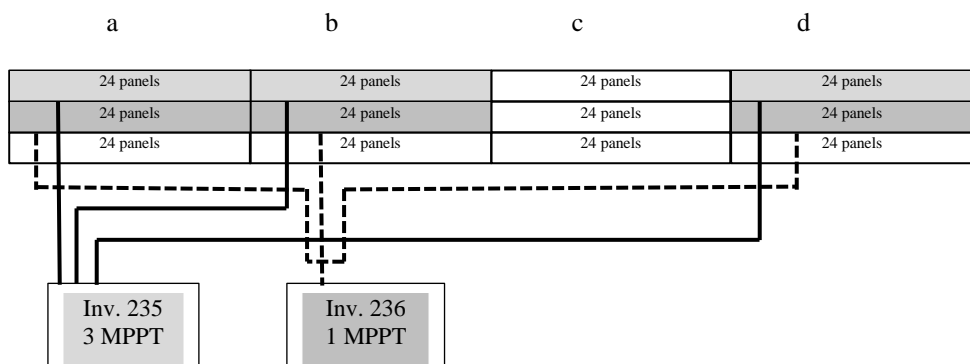


Figure A8.8 Modified string layout in the test string for two of the test inverters. Each inverter has panels distributed over approximately 160 meter.

Two inverters (ID 235 and 236) each have 3 strings attached, distributed over the whole length of a row, one inverter with 3 independent MPPTs and one inverter with strings are in parallel fed to only one MPPT.

The wiring to the solar panels are extended by approximately 80 m to each string with 8 mm copper wire. The estimated power loss in the cable during STC condition (8A) is calculated to 27 mΩ per wire and a power loss of <2W.

### 8.3.2 Inverter replacement to type MLX 60kW

The layout of part of the park was during 2015 changed in order to mount a series of 60kW inverter. This implied that several of the original inverters on the Eastern end of the plant were replaced and strings were parallelized. The test tow 21 was not affected by the replacement.

## 8.4 High speed recording of inverter and weather parameters

The identified need for data over long periods of time with high temporal resolution was addressed by implementing a data recording system as described below.

### 8.4.1 Data logger system concept

The purpose of this section is to describe the data logger system implemented at the 2.1 MW Danfoss Solar Park and at the 62 kW SDU Alsion PV plant. Both sites are equipped with DSI TLX/FLX type inverters, an irradiance/temperature sensor kit and a Davies Vantage Pro weather station. The data connection/storage is controlled by a field-PC, handling and storing data via the internet, see figure A8.9.

The data were stored locally during each day and around midnight transferred to the data server at the University of Southern Denmark. Firewall issued required the intermediate use of a file storage facility ([www.dropbox.com](http://www.dropbox.com)) during download. Details regarding setup, functionality etc. is documented in an internal report. The data communication/download functionality was implemented by engineering students.

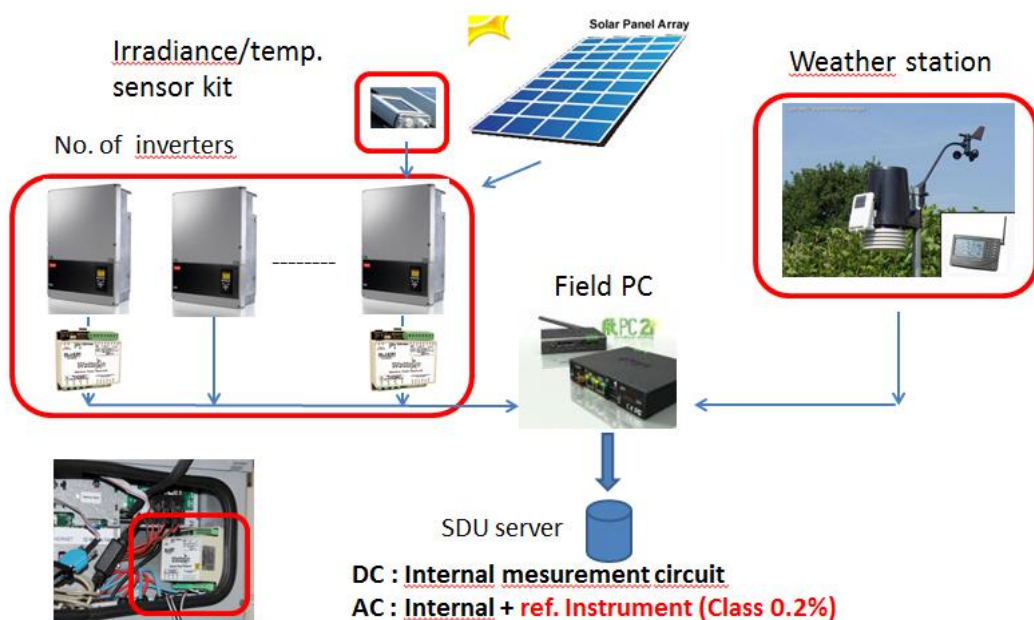


Figure A8.9 Implemented data logger system. Lower red square: High precision 3-phase AC meter, class 0.2%. TLX-inverters are shown.

#### **8.4.1.1 AC external calibration/monitoring**

The inverter series manufactured by Danfoss Solar Inverters A/S (TLX, FLX and MLX) are commercial products in a very competitive market and therefore details about the internal construction of the inverters could not be disclosed to the project. As the inverters are not intended to comply to a net metering standards e.g. [95] and measurement inaccuracies higher than 0.2% were expected [105].

4 of the test inverters (Row 21, inverter no 9 (2.3.5), 10 (2.3.6), 11 (2.4.5), 12 (2.4.6) ) have been equipped with high precision external AC energy meters for periodic comparison of type ELKOR WattsOn [101] as indicated by the lower red square in figure A8.9.

The calibration factors for the test inverters shown in table A8.6 have been identified as an average over a 5 day test period with continuous parallel logging of data from the inverters and the ELKOR energy meters.

Table A8.6 Calculated AC calibration factors.

Inverter ID	Cal. factor
Inverter 9 (2.3.5)	1.0077
Inverter 10 (2.3.6)	1.0062
Inverter 11 (2.4.5)	1.0064
Inverter 12 (2.4.6)	1.0083

#### **8.4.1.2 Inverter DC calibration**

The DC power values measured internally in the inverters are not factory calibrated and are in principle only indicative. Field test equipment suitable for the DC calibration of the inverters were not available at it was decided to perform a relative calibration between the two inverters by comparing the DC input levels on a clear day.

The method was applied to compare the recorded DC levels from test inverter 10, having one MPPT, with the recorded DC levels from inverter 9 and then to determine an average calibration factor. The DC input levels compared during a day with clear sky are shown in figure A8.10.

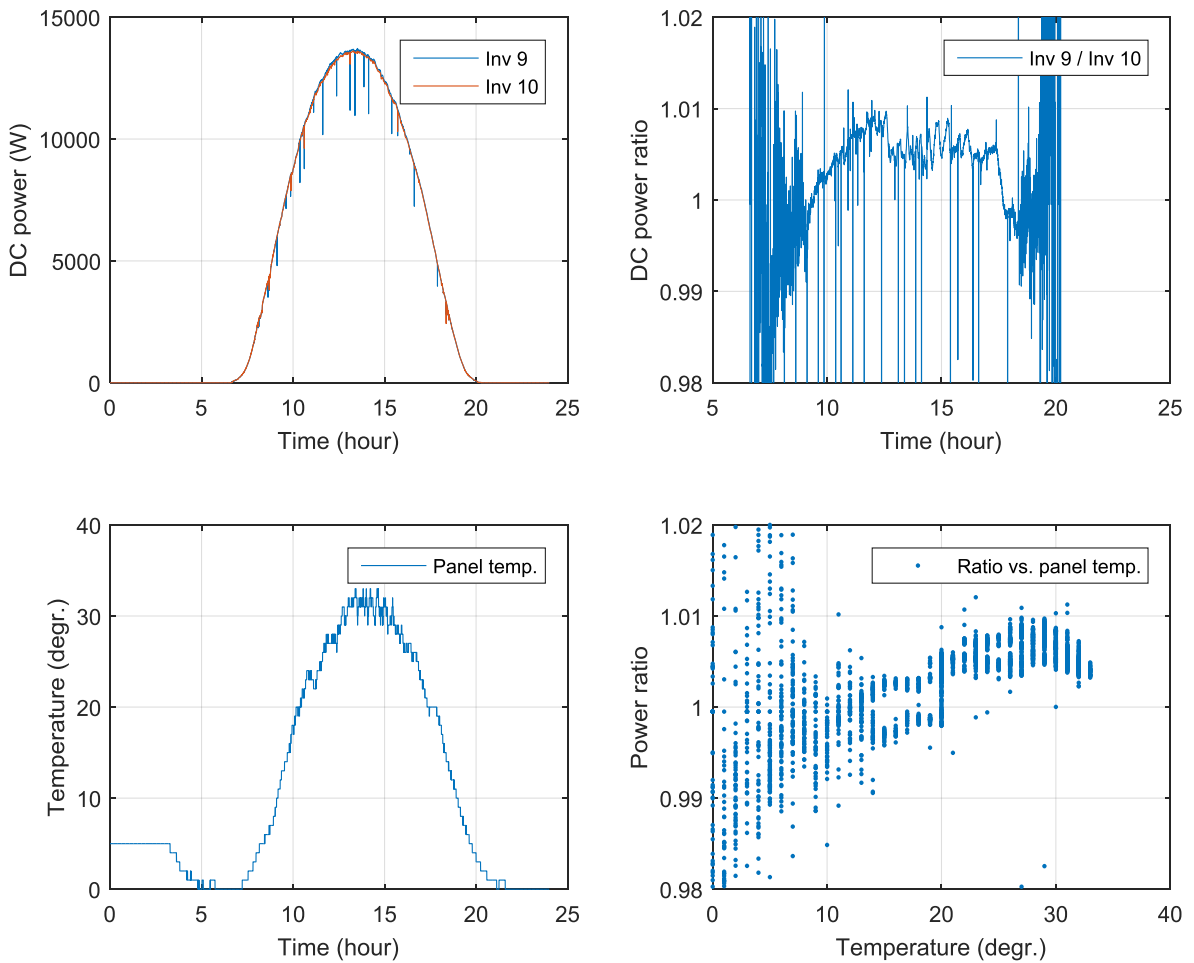


Figure A8.10 Top left: Power profile for a selected very clear day (day 460) for inverter 9 and inverter 10. Peaks are due to internal scans in the inverters. Top right: Ratio between the power levels of inverter 9 and inverter 10. Bottom left: Panel temperature. Bottom right: Power ration vs. temperature.

The topological effect identified in section 5.4 is visible and must be compensated. It can be observed that the ratio between the power levels of the two primary test inverters for a very clear day without clouds has a ratio which is temperature dependent but the change is within 1% for 33°C variation. The DC calibration factor between the two inverters has, based on the energy production per inverter that specific day, been set to **1.003**. This calibration factor is applied in the calculation of the distribution of the DC energy differences in this thesis.

The DC energy is calculated numerically via the Matlab *trapz*-function (available in Release 2015b, introduced before R2006b) for trapezoidal numerical integration. The accuracy of the integration method was tested by applying recorded AC power values and comparing the result with the accumulated data from the certified ELKOR AC meters. A difference of <0.04% was calculated and the *trapz*-function was considered valid for use.

#### 8.4.1.3 Data logger specifications

The basic specification listed in table A8.7 is derived from the intended usage and knowledge about the inverter data available.

Table A8.7 Primary design considerations.

Parameter	Value	Comment
Inverter data retrieval frequency	1 Hz	Will depend on reply time from the inverters and the network.
Weather station data retrieval frequency	1 Hz	Will depend on reply time from the weather station and the network.
Weather station data	Table A8.8	19 parameters
No. of inverters logged	5/12	Full Alsion plant, selected Danfoss plant inverters
Inverter data per inverter	Table A8.8	415 parameters (12 inverters / Danfoss) 184 parameters (5 inverters / Alsion)
Scan time	≈1s	Will depend on reply time from the inverters and the network.
File content	1 hour data	To avoid too large files for handling
Fine storage local	24 hour	Mini-PC / USB / local backup
File storage remote	Permanent	University server / backup
File format	.csv	Comma separated values, for Matlab interface
File name	Date	YYYY_MM_DD_HH.csv
Data directory structure	Day	One directory per day
AC reference meter	3-phase mains voltage	Compliant to IEC62053-22
Irradiation sensor data		Via master inverter
Ambient temperature		Via master inverter
Panel temperature		Via master inverter
Operating temperature	-20°C to 60 °C	Outdoor in enclosure all year

The recorded parameter together with the respective index is shown in table A8.6. The “index” parameter is used for localization of the parameter inside each data file.

Table A8.8 Index of stored variables for Danfoss Solar Park / Alsion PV plant log files.

Parameter	IP	1	2	3	4	5	6	7	8	9	10	11	12
Weather station	Inverters												
Date	Parameter	1	20	53	86	119	152	185	218	251	284	317	350
Time		2	21	54	87	120	153	186	219	252	285	318	351
Barrend		3	22	55	88	121	154	187	220	253	286	319	352
Barometer		4	23	56	89	122	155	188	221	254	287	320	353
Insidetemp		5	24	57	90	123	156	189	222	255	288	321	354
Outsidetemp		6	25	58	91	124	157	190	223	256	289	322	355
Inside humidity		7	26	59	92	125	158	191	224	257	290	323	356
Outside humidity		8	27	60	93	126	159	192	225	258	291	324	357
Wind		9	28	61	94	127	160	193	226	259	292	325	358
Wind average 10 min		10	29	62	95	128	161	194	227	260	293	326	359
Wind direction		11	30	63	96	129	162	195	228	261	294	327	360
UV-index		12	31	64	97	130	163	196	229	262	295	328	361
Solar radiation		13	32	65	98	131	164	197	230	263	296	329	362
Rain rate		14	33	66	99	132	165	198	231	264	297	330	363
Daily rain		15	34	67	100	133	166	199	232	265	298	331	364
Monthly rain		16	35	68	101	134	167	200	233	266	299	332	365
Yearly rain		17	36	69	102	135	168	201	234	267	300	333	366
Sunrise		18	37	70	103	136	169	202	235	268	301	334	367
Sunset		19	38	71	104	137	170	203	236	269	302	335	368
			39	72	105	138	171	204	237	270	303	336	369
IIPI=192.168.2.44			40	73	106	139	172	205	238	271	304	337	370
IIPI=192.168.2.27			41	74	107	140	173	206	239	272	305	338	371
IIPI3=192.168.2.114			42	75	108	141	174	207	240	273	306	339	372
IIPI4=192.168.2.121			43	76	109	142	175	208	241	274	307	340	373
IIPI5=192.168.2.118			44	77	110	143	176	209	242	275	308	341	374
IIPI6=192.168.2.95			45	78	111	144	177	210	243	276	309	342	375
IIPI7=192.168.2.141			46	79	112	145	178	211	244	277	310	343	376
IIPI8=192.168.2.91			47	80	113	146	179	212	245	278	311	344	377
IIPI9=192.168.3.10			48	81	114	147	180	213	246	279	312	345	378
IIPI10=192.168.3.11			49	82	115	148	181	214	247	280	313	346	379
IIPI11=192.168.3.16			50	83	116	149	182	215	248	281	314	347	380
IIPI12=192.168.3.17			51	84	117	150	183	216	249	282	315	348	381
			52	85	118	151	184	217	250	283	316	349	382
													415

Grey=same parameter for all inverters.

For example the

*wind direction*

has index 11

*inverter 9 PV power input string 1*

has index 290

*solar irradiance level*

has index 310

The same index structure apply to the SDU Alsion PV data, up to index 184 as there are only 5 inverters monitored. Indexes 310-316 are replaced by index 46-52 due to the position of the irradiance/temperature sensor kit on inverter 1.

The concept of the applied data logger system was developed as part of an earlier project and further developed and implemented via this project. The purpose was to remotely monitor solar inverters of type TLX and FLX from Danfoss Solar Inverter A/S via their internal data recording circuit. DSI had their own data recording system for monitoring / R&D their inverters and data files initially were obtained by assistance from DSI. But as long term fast and reliable data logging was of vital importance it was decided to implement a customized recording system working in parallel with the DSI logging.

#### 8.4.1.4 Post-processing

Up to 200MB of data is stored per day (during summer) from the Danfoss Solar Park PV site onto the SDU server. These files are too large for continuously being handled for data analysis over longer time periods, see figure A8.11. Therefor are all data, for a selected time interval, post processed/extracted into \*.mat-variable files to make access and handling of them more feasible. Presently the files are up to 200 MB in size each.

Each variable/parameter is stored in each own file, so any variable can be called via just one parameter (the index from table A8.8). A corresponding time-vector is generated (index = 0), assuring the correct time for each recording.

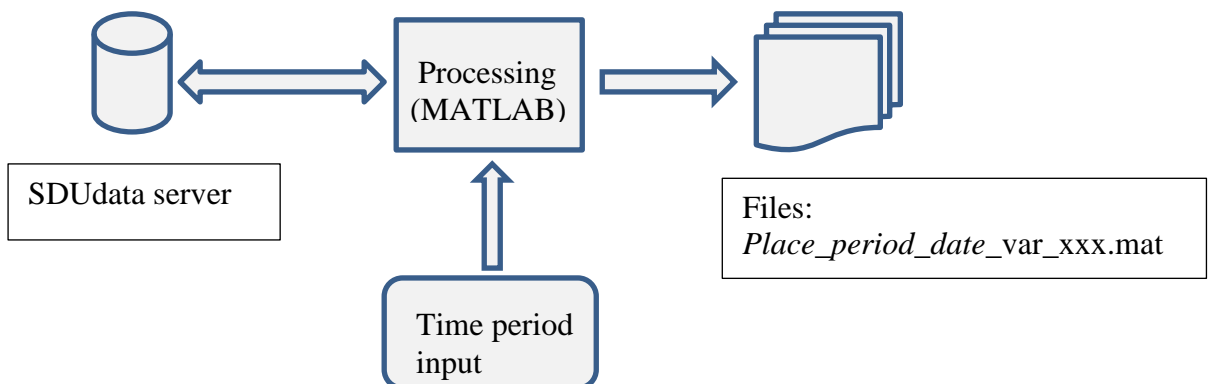


Figure A8.11 Principle of data file post processing for a specific time period.

*Examples:*

The file name for the irradiance signal until 31/8 2015 is *DN\_period3\_to\_20150731\_var\_310.mat* “310” refer to the index in table A8.8.

Inverter data are available as raw \*.csv files and as post-processed \*.mat variable files for a period of more than a year. Due to HW breakdown, communication /firewall issues, internal test periods etc. by Danfoss Solar Inverters are minor periods / days missing.

Over 25 mill. datasets of 415 parameters are recorded from the Danfoss Solar Park and approximately 13 mill. data sets of 184 parameters from the SDU Alsion PV plant during the test period.

## 9 Appendix 9 Irradiation statistics

The weather data recorded during the test periods are in this appendix presented in graphical form. All plots display the occurrence of a given parameter/ratio/function as a function of the recorded wind speed and wind direction.

### 9.1 Data set 1, SDU Alsion 150 days weather data

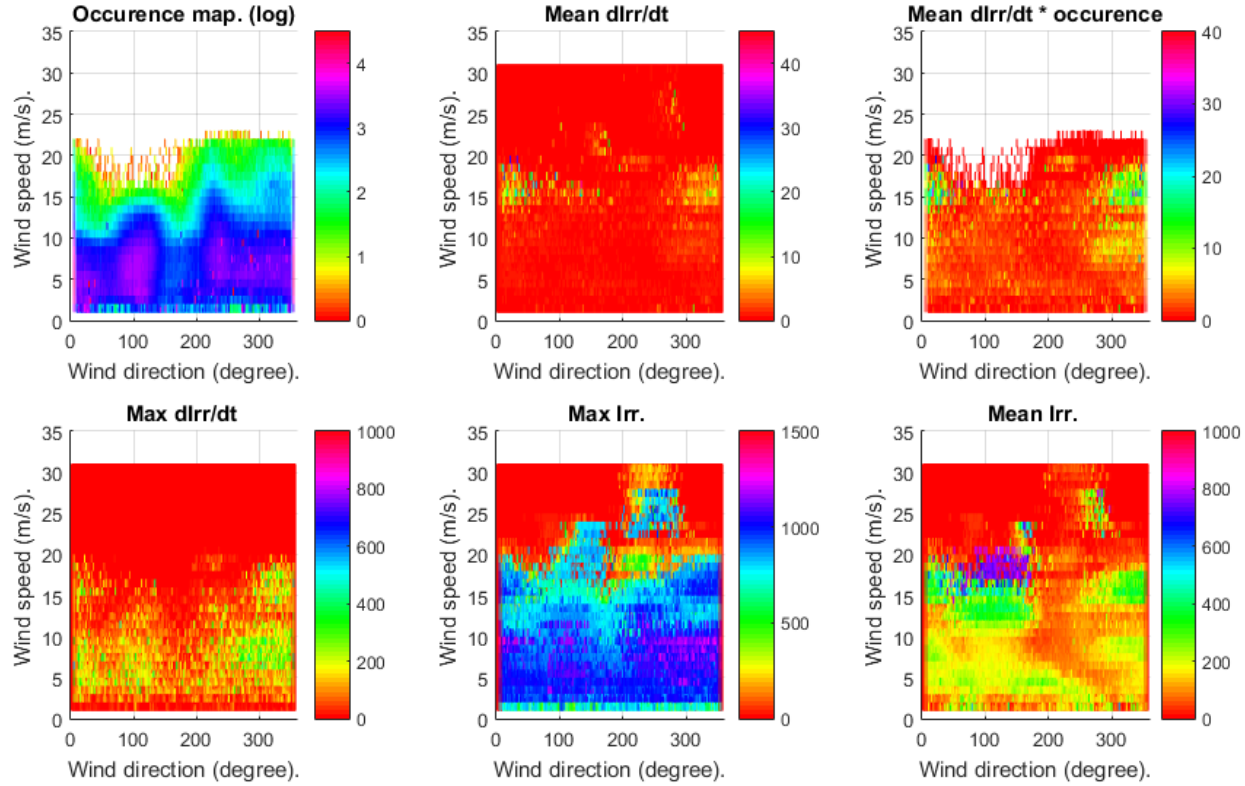


Figure A9.1 Maps for the irradiation level occurrence, mean( $dIrr/dt$ ), mean( $dIrr/dt * occurrence$ ), max( $dIrr/dt$ ), max( $Irr$ ) and mean( $Irr$ ) as a function of wind speed and wind direction for the 5 month of data from the SDU Alsion test plant.

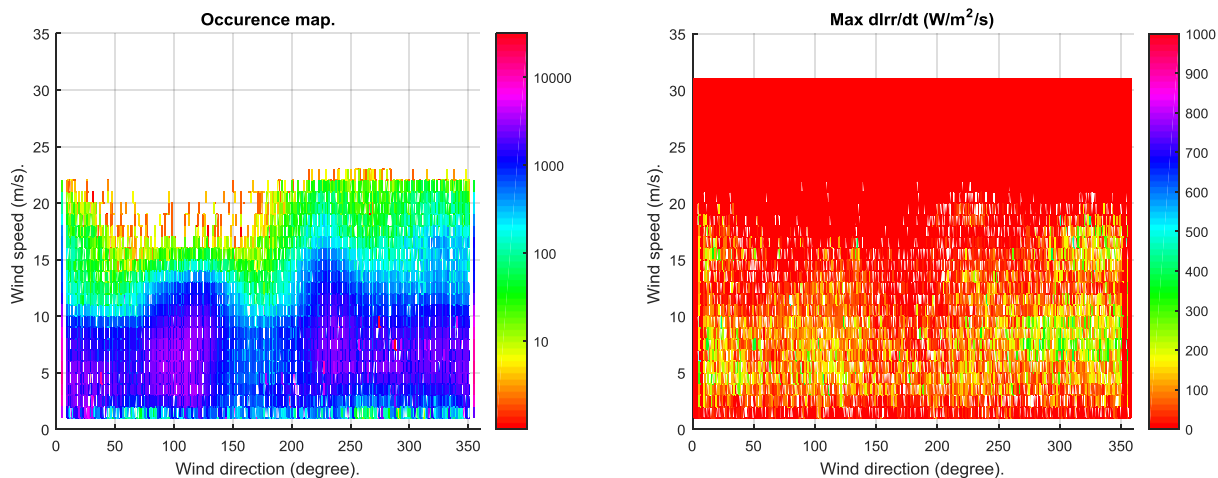


Figure A9.2 Maps for the irradiation level and maximum slope occurrence as a function of wind speed and wind direction for the one year of data from the SDU Alsion test plant.

## 9.2 Data set 2, SDU Alsion one year weather data

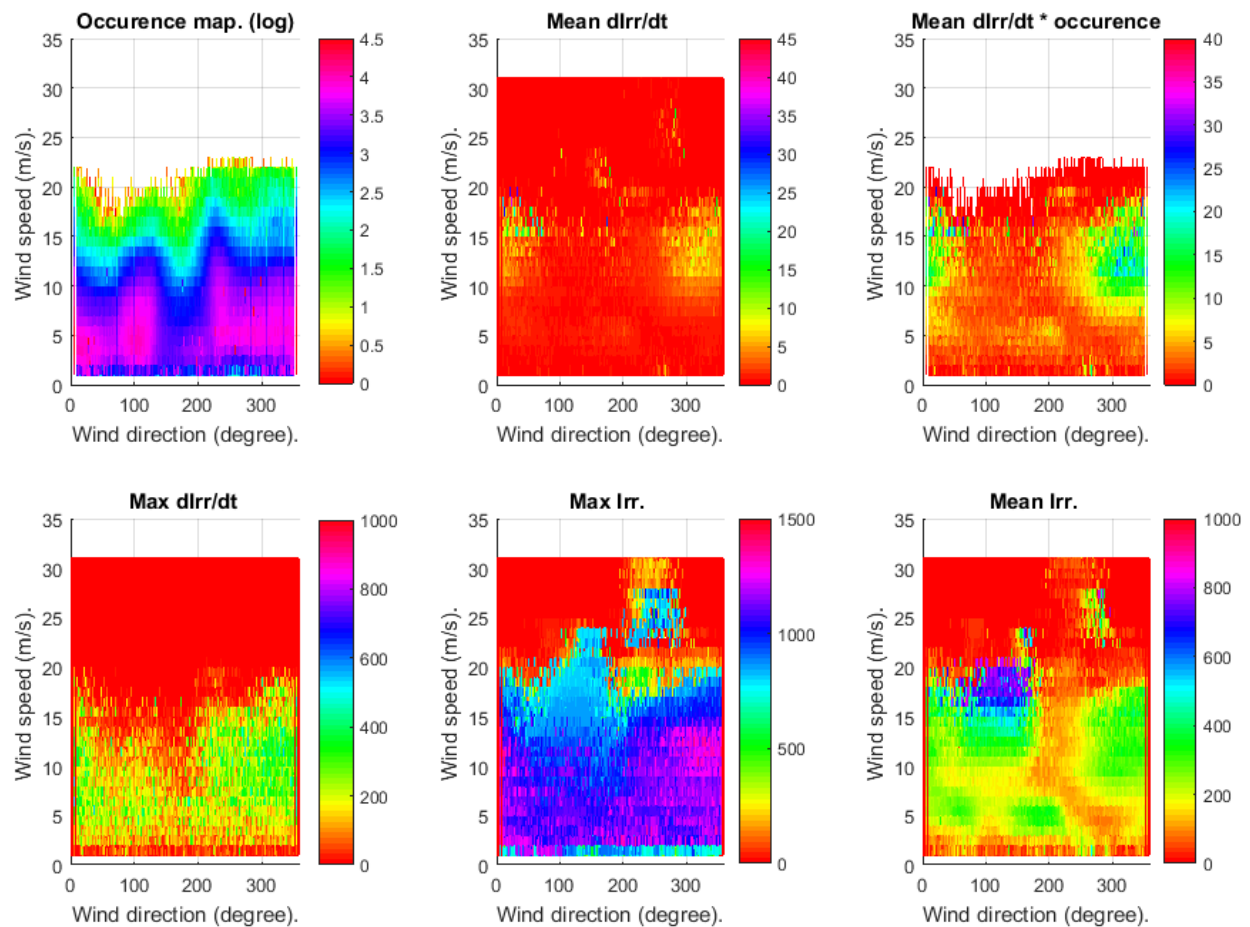


Figure A9.3 Maps for the irradiation level occurrence, mean( $dIrr/dt$ ), mean( $dIrr/dt * occurrence$ ), max( $dIrr/dt$ ), max( $Irr$ ) and mean( $Irr$ ) as a function of wind speed and wind direction for the one year of data from the SDU Alsion test plant.

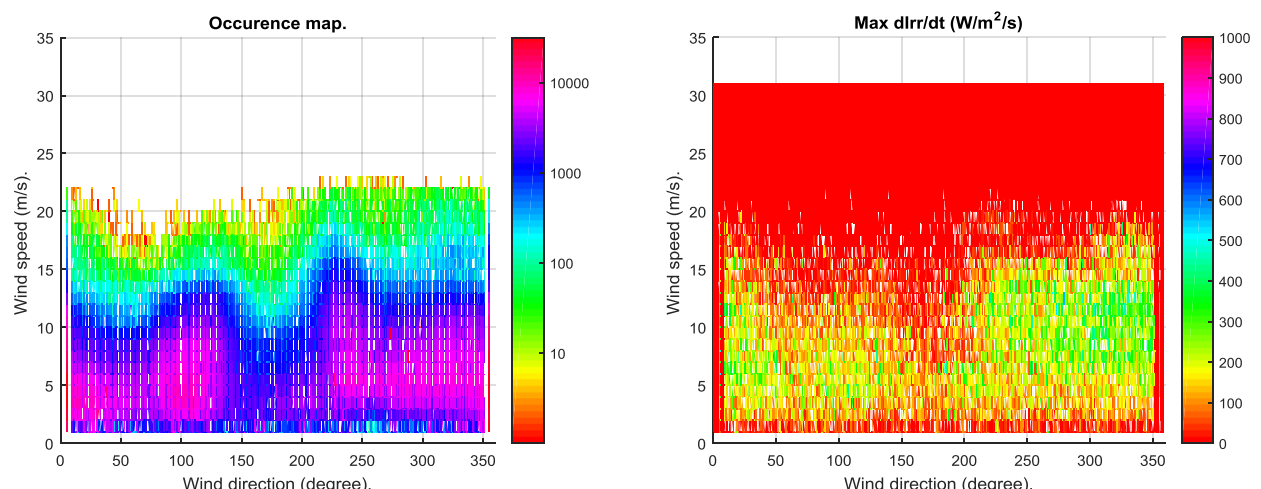


Figure A9.4 Maps for the irradiation level and maximum slope occurrence as a function of wind speed and wind direction for the SDU Alsion test plant.

### 9.3 Data set 3, Danfoss Solar Park one year weather data

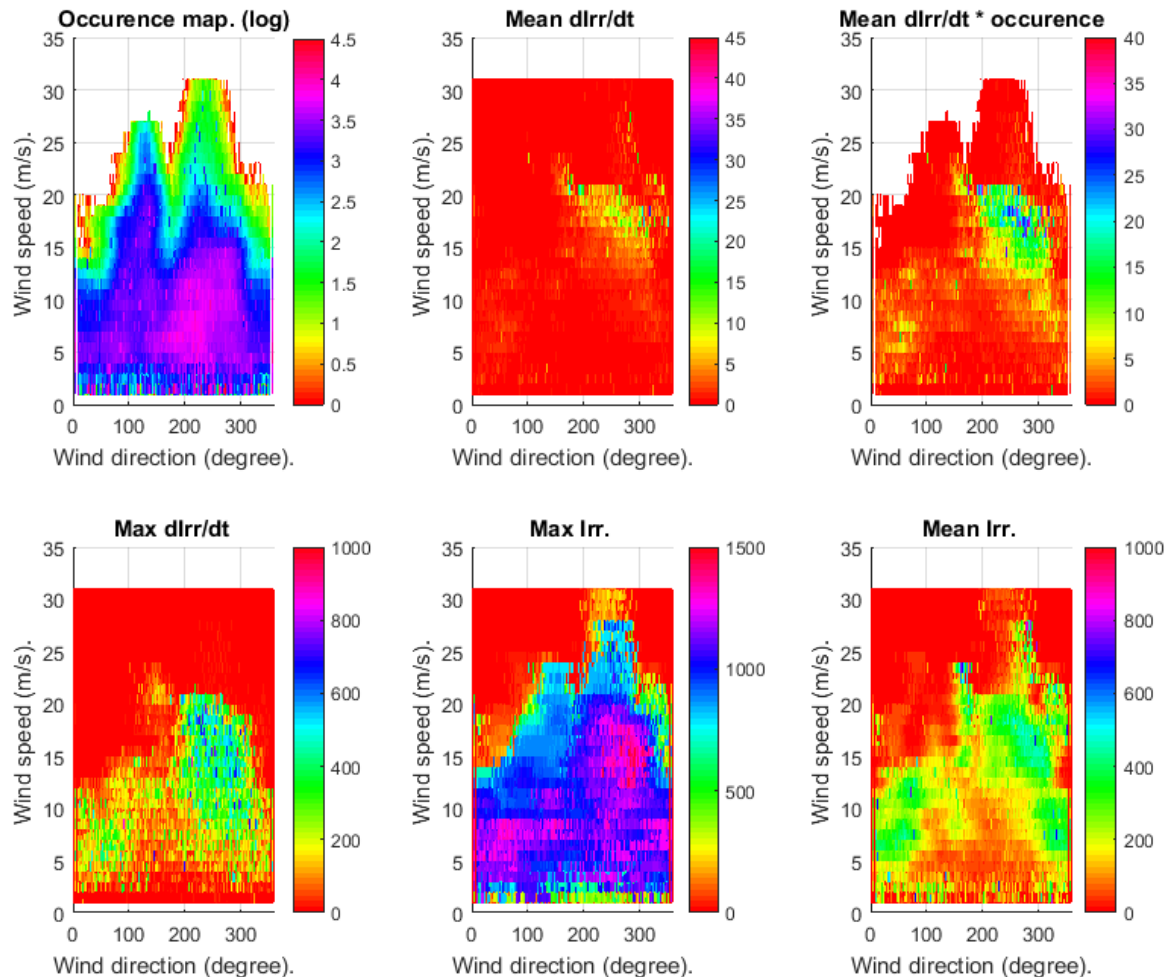


Figure A9.5 Maps for the irradiation level occurrence, mean( $dIrr/dt$ ), mean( $dIrr/dt * occurrence$ ), max( $dIrr/dt$ ), max( $Irr$ ) and mean( $Irr$ ) as a function of wind speed and wind direction for the one year of data from the Danfoss Solar Park.

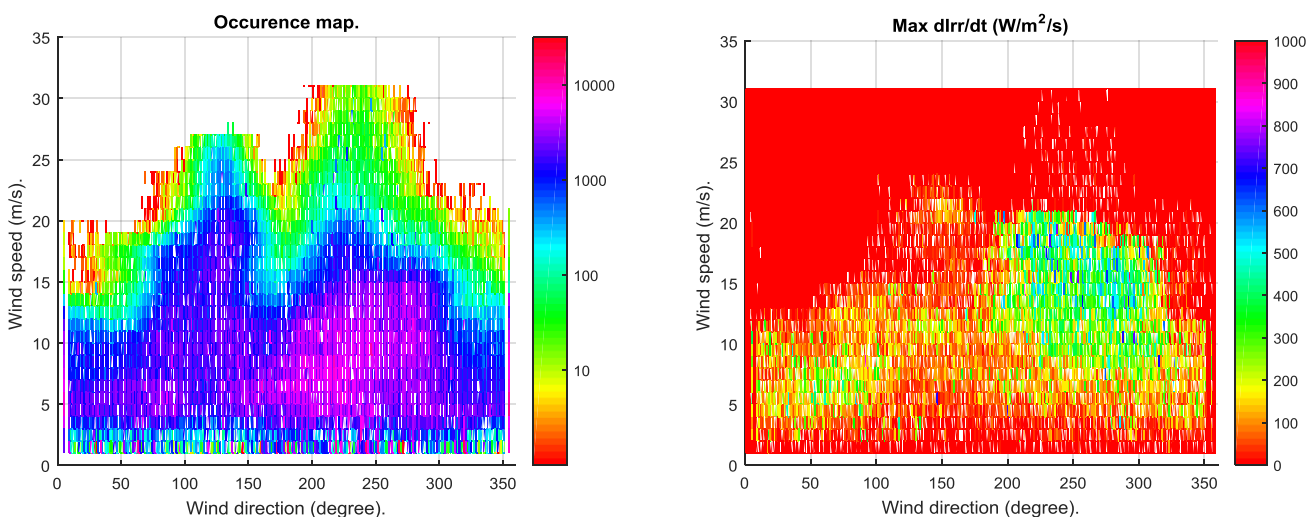


Figure A9.6 Maps for the irradiation level and maximum slope occurrence as a function of wind speed and wind direction for the Danfoss Solar Park.

### 9.3.1 Clouds speed estimation via time correlation between inverter data

The availability of (almost) synchronously sampled data from inverter distributed over an area of 170x160m gives the possibility to use time correlation to estimate the speed-over-ground (SOG) wind speed and the direction of passing clouds. An approach to calculate the average wind speed and direction via time correlation of the recorded power levels from the inverters located at the corners of the Danfoss Solar Park is ongoing, see A9.7

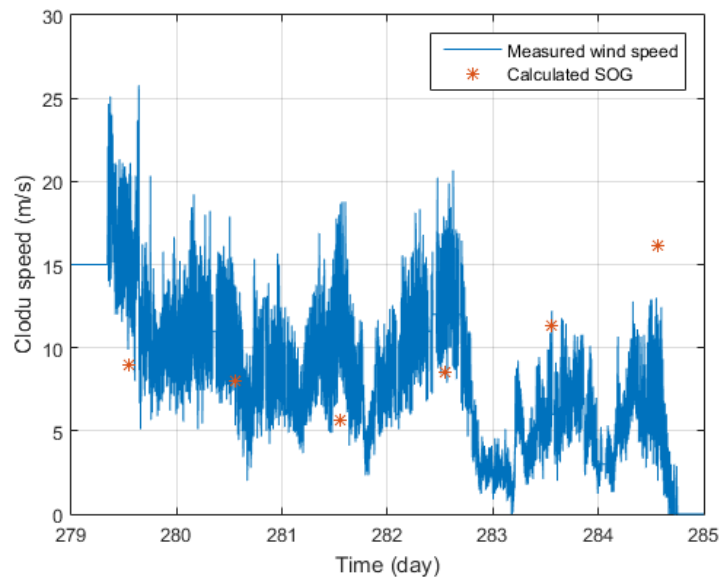


Figure A9.7 Example of calculated average speed over ground (SOG) and cloud directions for specific days.

The time correlation analysis applied by using the data from the distributed inverters result in cloud speed and direction close to the measured values from the ground based weather station.

It cannot be concluded that the Q-factor estimated earlier is too large as there is no sky-camera available to give information of actual cloud movements. Q=3 should be seen as a worst case situation. This investigation is ongoing.

## 10 Appendix 10 PV panel measurement

A panel of same type as mounted in the Danfoss Solar Park was monitored for approximately 6 months at the outdoor ESTER Outdoor PV monitoring station in Rome as a larger variation in irradiation level and temperature was expected there than in Denmark. The panel was monitored with the developed IV-curve tracer instrument to obtain IV-sweep data every second from March 2015 to October 2015).



Figure A10.1 Danfoss Solar Park PV-panel under test at ESTER in Rome. Red arrow: The locations of the PVSweeper and the panel are indicated.

### 10.1 Panel under test

Detailed information about the design, construction and calibration of the IV-curve tracer platform is located in appendix [A11]. The raw current and voltage values recorded by the IV-curve tracer system (called PVSweeper) are compensated for the influence of ambient temperature and nonlinearity of the current measurement circuit, as described in appendix [A11]. The panel under test is a 225W polycrystalline panel of type ND-225R1J from the company SHARP. The main panel data are listed in table A10.1.

Table A10.1 Panel data<sup>8</sup>

Panel Type	SHARP Solar Module ND-225R1J		
Serial no.	134459494		
	STC	NOCT	Unit
Nom. power	225	162.1	W
V <sub>oc</sub>	36.6	35.8	V
I <sub>sc</sub>	8.28	6.68	A
V <sub>MPP</sub>	29.3	26.1	V
I <sub>MPP</sub>	7.68	(6.21) <sup>1</sup>	A

<sup>1</sup> Calculated value.

#### 10.1.1 PV panel sweep data

The developed PVSweeper unit records a scan consisting of 100 measurement points every second, as well as the panel temperature, ambient temperature and solar irradiation level. Via data post processing are the P<sub>MPP</sub>, V<sub>MPP</sub> and I<sub>MPP</sub> values extracted. As an example are the recorded PV-curves during the solar equinox on March 20, 2015, shown in figure A10.2.

<sup>8</sup> Solar panel datasheet. SunFields\_SHARP\_Datasheet\_ND-225-230-235-240R1J\_EN.pdf ID: SolarND60R1J\_E0412.

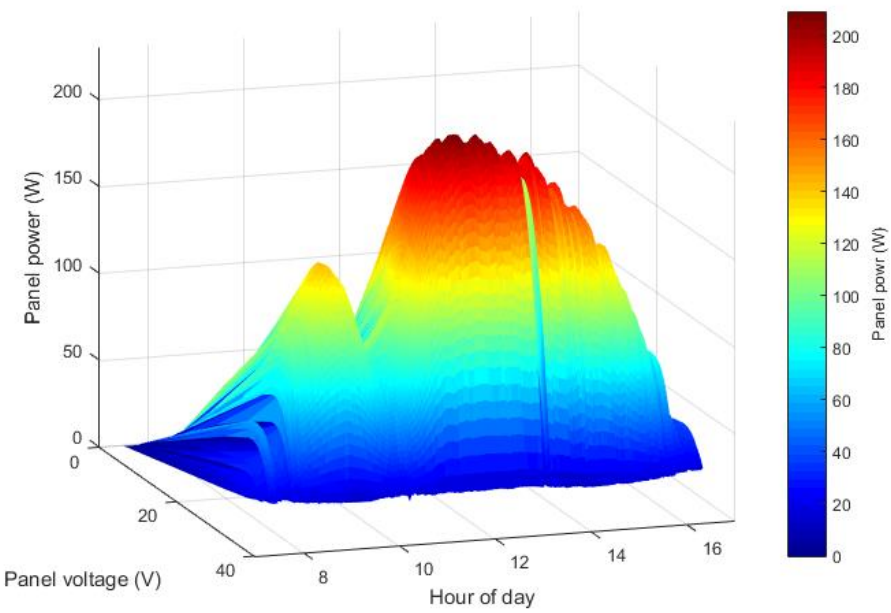


Figure A10.2 Recorded PV sweeps for March 19, 2015, during a solar eclipse, based on the recorded IV-values. 1 minute averaging is applied.

## 10.2 STC/NOCT analysis

### 10.2.1 ESTER Outdoor PV monitoring station in Rome, Italy

The occurrence of combinations of irradiation level and panel temperature for the tests performed with the developed PVsweeper at the ESTER Test facility in Rome is shown in figure A10.3. It can be observed that the STC condition is outside the main area of operation but also that the irradiation/temperature distribution is different from the other test plants as more irradiation around the level of  $1000 \text{ W/m}^2$  is present.

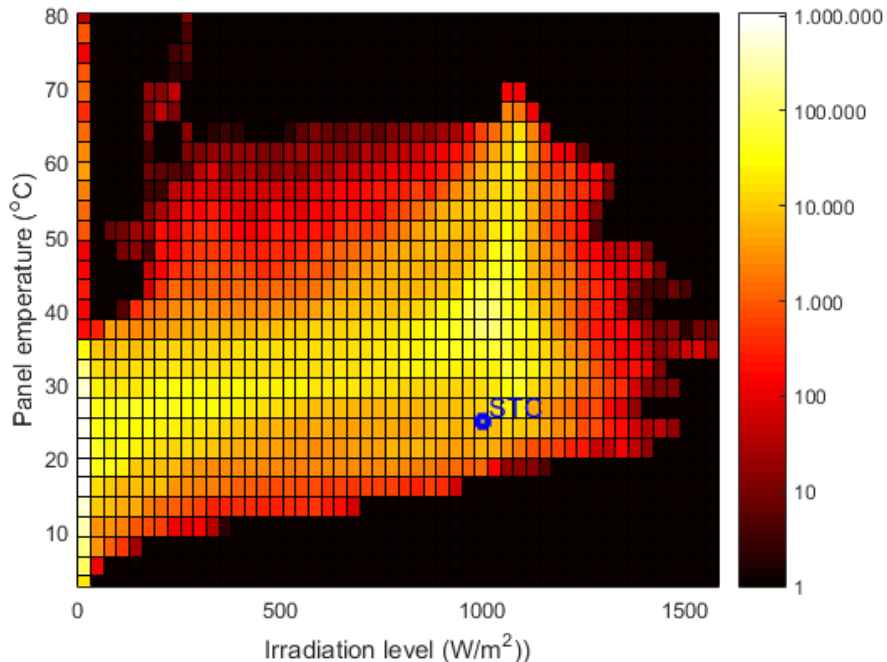


Figure A10.3 Distribution of panel temperature and irradiation level for day 30-100 of the observation period. A total of approximately 13 mill. measurements pairs are presented in the plot.

## 10.2.2 Panel temperature analysis

The temperature coefficient  $\tau$  for a the specified series of irradiance levels  $Irr$  can be determined by fitting a series of suitable functions to the power and irradiance data measured at a specific temperature  $T$ . A power law function of the form given in eq. A10.1 was chosen.

$$P(Irr, T) = 10^{k(T)} * (Irr)^{v(T)} \quad (\text{A10.1})$$

A set of  $(k, v)$  coefficients are calculated for each chosen temperature  $T$ . In figure A10.4 are the extracted  $P_{MPP}$  values shown as a function of the air mass range 1.0-3.0 as well as the fitted power law function for each temperature. The solar elevation and corresponding air mass factor was calculated for each sample time, using the actual time stamp of each measurement and applying the modified procedure introduced by [91], see section 4.2.1 for details. The air mass interval of 1.0-3.0 has been accepted to obtain sufficient data points, even if the variation is solar elevation / air mass introduces a potential spectral dependency due to varying atmospheric absorption spectra. The STC location is marked with a red dot.

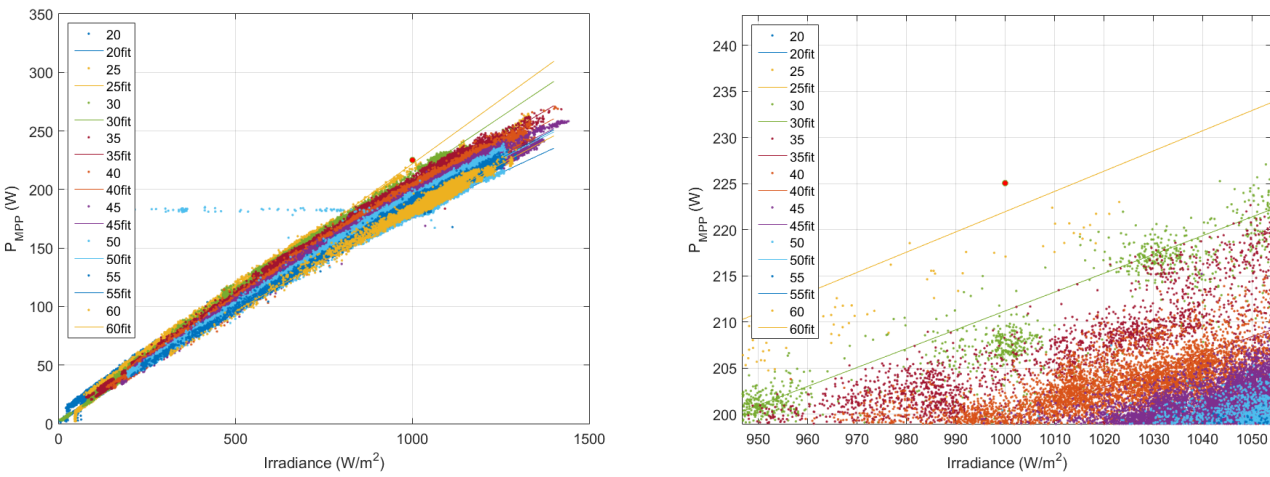


Figure A10.4 Left: Calculated PMPP levels as a function of solar irradiance in steps of 5°C with fitted polynomials of 1<sup>st</sup> order. Data from day 30-100 applied, AM interval 1-3. A total of approximately 418,000 out of 13 mill. data points are shown.  
Right: Zoomed. The red dot indicated the location of the STC regarding irradiance, temperature and panel MPPT-rating.

Environmental conditions at or close to STC regarding temperature ( $25\pm0.5^\circ\text{C}$ , irradiation  $1000\pm2\text{W/m}^2$ , air mass  $\text{AM}1.5\pm0.1$ ) are not present in the recorded dataset. For an extended interval around STC ( $25\pm1^\circ\text{C}$ ,  $1000\pm5\text{W/m}^2$ ,  $\text{AM}1.5\pm0.2$ ) only 4 sets of data are found. The average  $P_{MPP}$  value of these data sets was 218W.

The linear fit for  $T_{\text{panel}}=25^\circ\text{C}$  for the interval 100-1400  $\text{W/m}^2$  shown in figure A10.4 indicate that for an irradiation level of  $1000 \text{ W/m}^2$  a  $P_{MPP}$  level of 222W for the monitored panel is fitted. This is 1.4% below the nominal  $P_{MPP}$  level of 225.0 W, but the nominal power loss due to aging of the panel is not known and the data sheet guarantees max. 4% loss during the first year of operation. The panel under test has been in operation for approximately 1.5 year in total.

The fitted functions are used to calculate the temperature coefficients  $\tau$  for each temperature combination  $(T_a, T_b)$  and irradiance level  $Irr$  via eq. A10.2.

$$\tau_{T_a T_b}(Irr, \Delta T_{a,b}) = \frac{P_{T_a}(Irr) - P_{T_b}(Irr)}{P_{T_b}(Irr) \Delta T_{a,b}} \quad (\text{A10.2})$$

for  $a=1:n$  and  $b=1:n$ ,  $n$  being the number of temperature intervals.

The analysis is performed for  $T=20^\circ\text{C}, 25^\circ\text{C} \dots 60^\circ\text{C}$ . An average temperature coefficient  $\tau_{\text{Irr}}$  for each selected irradiance level  $Irr$  was found by averaging all valid calculated combinations for said level  $Irr$ . The calculated values are shown in figure A10.5. Temperature coefficients obtained at irradiance values below 200  $\text{W/m}^2$  were discarded due to a low number of actual measurements at some temperatures.

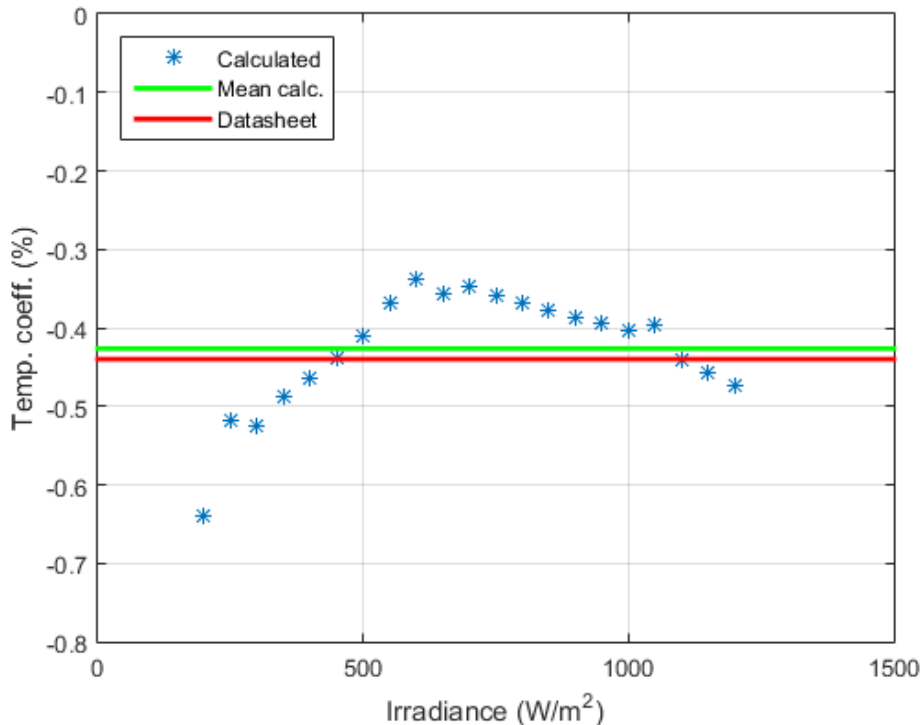


Figure A10.5 Calculated averaged temperature coefficients for the tested SHARP PV panel as a function of irradiance level.

The average temperature coefficient, estimated on the basis of the fitted functions for the interval 200-1200  $\text{W/m}^2$ , is  $-0.43 \pm 0.07\%$ , close to the data sheet value of  $-0.440\%$ . An apparent dependency of the irradiation level is observed which is to be expected as  $P_{\text{MPP}}$  is the product of  $I_{\text{MPP}}$  and  $V_{\text{MPP}}$ , both of which vary with temperature and irradiance, acc. to (A10.3) [76].

$$\frac{dP_{\text{MPP}}}{dT} = V_{\text{MPP}} \frac{dI_{\text{MPP}}}{dT} + I_{\text{MPP}} \frac{dV_{\text{MPP}}}{dT} \quad (\text{A10.3})$$

The measured values are average values over all temperatures for a given irradiation interval. The data sheet information of a temperature coefficient of  $-0.440\%/\text{C}$  is only to be seen as an average coefficient.

This observed dependency is subject of an ongoing investigation as more data becomes available from the running measurement program in Rome.

### 10.2.3 Mapping of $V_{MPP}$ , $I_{MPP}$ and $P_{MPP}$ recording

The distribution of the recorded  $V_{MPP}$ ,  $I_{MPP}$  and  $P_{MPP}$  values for the test period is shown in figures A10.6 and A10.7.

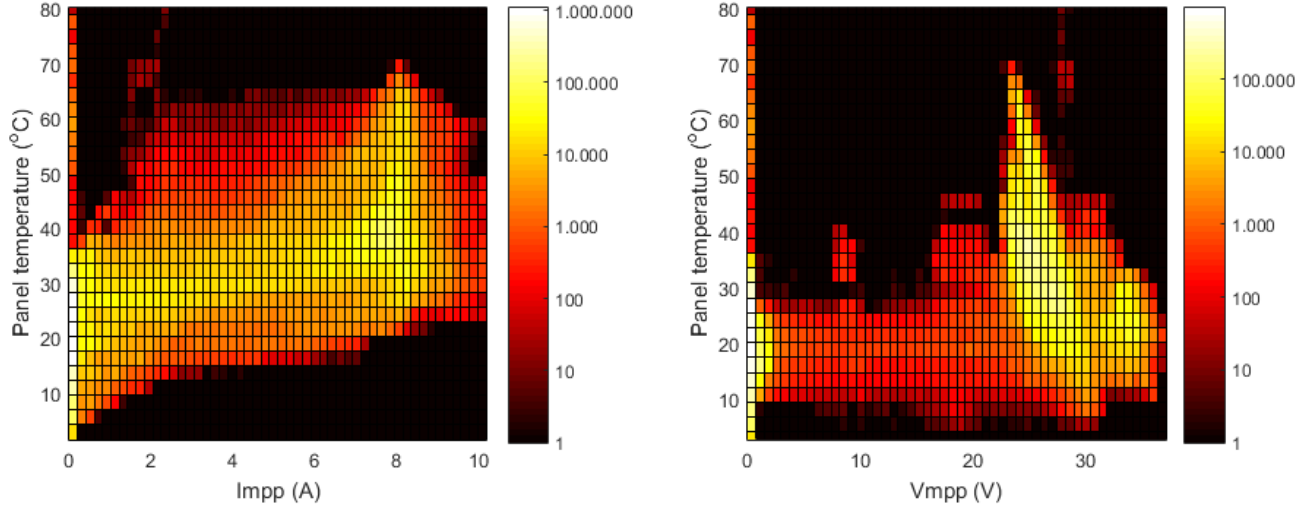


Figure A10.6 Distribution of panel temperature and  $I_{MPP}$  level (left) and  $V_{MPP}$  level (right) for day 30-100 of the observation period. A total of approximately 13 mill. measurements pairs are presented in each plot.

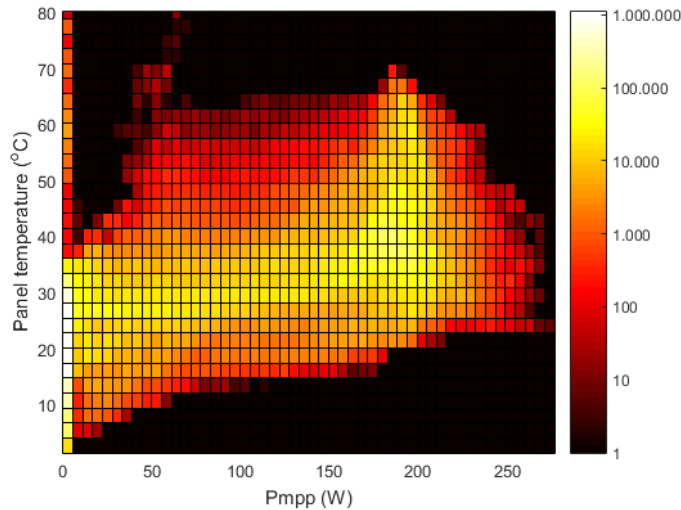


Figure A10.7 Distribution of panel temperature and  $P_{MPP}$  level for day 30-100 of the observation period. A total of approximately 13 mill. measurement pairs are presented in the plot.

### 10.3 Thermal effects due to fast change in irradiation

An abrupt change in irradiation will either let the panel cool down or warm up, depending on the direction of the change. The thermal mass of the panel will delay the panel temperature to adapt to the new thermal equilibrium for the panel, resulting in a power deviation of the power production under MPPT relative to the instant irradiance. The thermal effect has been addressed in the literature, i.e. [70], stating a thermal time constant in the range of 7-10 minutes for a laminated (85W) PV panel and even longer time constants for larger panels with thicker back plates, up to twice as long. This thermal effect has been observed in the recorded IV-curves, see figure A10.8 and A10.9.

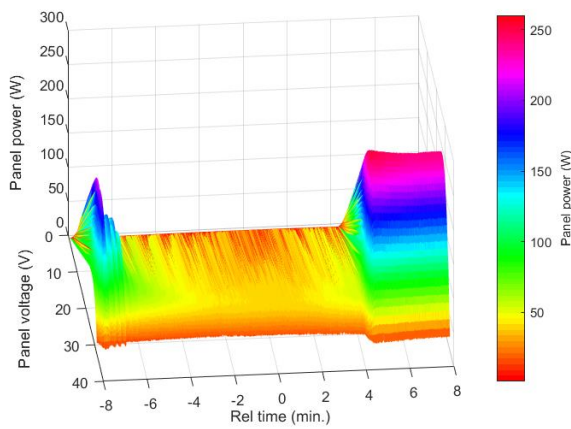


Figure A10.8 IV scans around an event with fast change in irradiation level, recorded April 17, 2015.

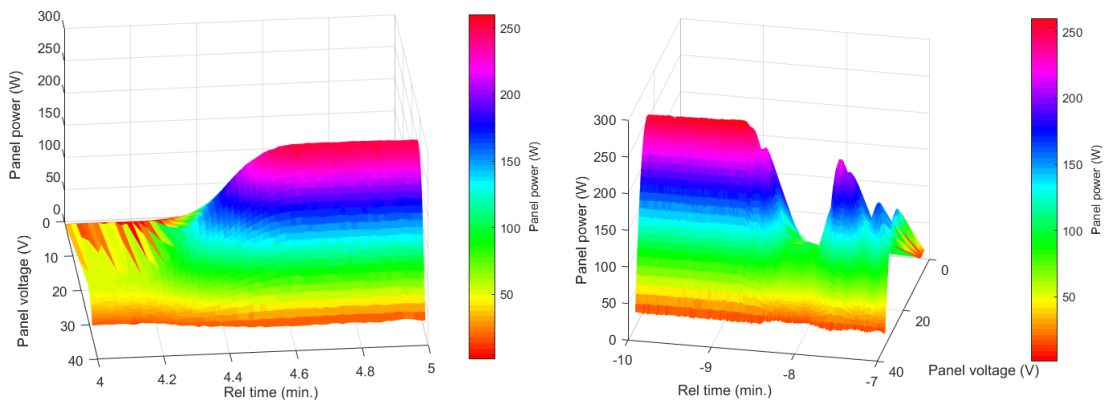


Figure A10.9 IV scans around the transitions areas. Left: Downwards. Right: Upwards.

The extracted  $P_{MPP}$  values and the irradiation levels are shown in figure A10.10.

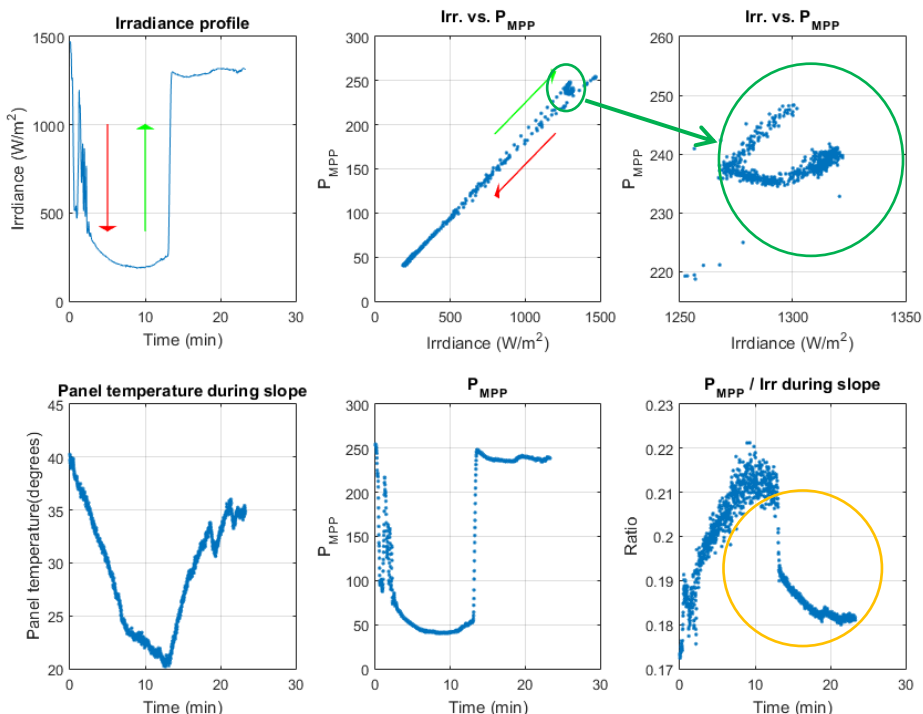


Figure A10.10 Extracted plots with irradiation and  $P_{MPP}$  data.

The irradiance profile is shown top-left. The arrows indicate the direction of the change. The plot located top-center shows the decline from 236 W power level @ 1300 W/m<sup>2</sup> to around 40 W @ 200 W/m<sup>2</sup> and back up to 248 W @ 1300 W/m<sup>2</sup> (green circle). The panel cools down from 40 to 20 during the shadowing and then warms up during the next 10 minutes. The temperature effect can be observed in the ratio between the PMPP and the irradiation, shown in the plot bottom-right (orange circle). An estimate for the time constant of the PV panel is 10 minutes.

# 11 Appendix 11 PVSweep system evaluation, design and test

The purpose of this appendix is to describe the following:

- Specification of requirements and evaluation of available IV-curve tracers.
- The development and testing of the developed PVSweeper system.
- Temperature analysis and calibration of the PVSweeper system.
- Irradiance sensor calibration at the ESTER Outdoor PV monitoring station in Rome.

The PVSweeper is intended for field use and long term monitoring of selected PV-panels via fast IV-sweeps. Data is stored on a SD-card for later post processing. The PVSweeper system was tested mainly under laboratory conditions regarding temperature calibration at the University of Southern Denmark and under field test conditions at the ESTER Outdoor PV monitoring station at the Tor Vergata University in Rome, Italy.

## 11.1 IV-curve tracer specifications

The initial specifications listed in table A11.1 have been derived from the intended usage and the performance of comparable instruments commercially available [103].

Table A11.1 Primary design specifications.

Parameter	Value	Comment
Max. PV DC current	10A	Single panel operation
Max. PV DC voltage	50V	Above panel voltage (60 cell panel).*
Maximum power point level	250W	Typical power level for a standard 60-cell panel.*
Irradiance level recording	0-1500W/m <sub>2</sub>	Irradiance level likely to occur in main Europe.
Scan rate	1 Hz	
Accuracy of MPP-level	<1%	
Scan rate	> 30 ms	Avoiding splitting of IV curves, limited by power dissipation.
Battery operation	>1 week	Internal battery
Mains operation	Optional	For long term use
Protection class	IP65	Housing, outdoor under roof/panel. IEC standard 60529.
Irradiance sensor interface	Analog	Compliant to DSI irradiance sensor Si-02
Ambient temperature sensor	±0.5°C	Analog sensor interface
Panel temperature sensor	±0.5°C	Analog sensor interface
Data storage period	>2 weeks	On SD card
Timing	< 0.1 sec	RTC on-board (for later sync.)
File structure	1 file/hour	Time stamp in name
File format	Text	.csv format for Matlab interface
Operating temperature	0-40°C	Temp. comp. by post processing allowed
Max. surface temp.	74°C	Metal surface of heatsink acc. to IEC60601-1 3 <sup>rd</sup> ed., table 23.

\*Must be easy to modify in future versions.

A selection of reviewed curve tracers is listed in table A11.2 together with their main parameters.

Table A11.2 A selection of the reviewed curve tracers.

Instrument	Sweep time	Sweep repetition	No of sweeps	Battery operation	Price/unit (approx.)
Primary specification	<100ms	1 sec	>10 <sup>6</sup>	1 week	€500
Solaimetre	10/100 ms	1 min	999	8h	€3,500
Stratasense IV	300ms	>15s	PC	Panel	€1,000/node
Tritec Trika Fly	15-30s	>1 min	>16k	6h	€3,000
HT Instr. Solar I-V	3-7 s	>10s	>200	>3h	€3,500
Solmetric PVA-680	3s	>10s	PC	6h	€3,500

No curve tracer with variable sweep time and sweep repetition time was identified as being available. The Stratasense IV system was closest to the specs, but was not able to scan fast enough or repeat scans fast enough. An approximate price target in the range of €1000 per unit was initially set for each sweeper unit/node as the deployment of > 10 unites were

## 11.2 Design aspects

The different versions of the PVsweeper are shown in Table A11.3. The initial prototype version 0.1 of the PVsweeper, as published in appendix [A1], was further developed via student activities at SDU. Version 0.1 and 0.2 were field tested at Alsion. The design has developed over the project, starting with a TO-220 cased IRD530 N-channel MOSFETs as the active load and a simple Real-Time-Clock (RTC) to a system with a high-power IXTH15N50L2 transistor, capable of handling the peak power. An ongoing redesign is including more parallel active load units, both to expand the current range and to lower the transient thermal stress on the transistors, network operation and other improvements. For version 0.2 and 0.3 research assistants / engineering students have been involved in the development. Version 0.3 consists of the main building blocks shown in figure A11.1.

Table A11.3 PVsweeper versions

Version	Version	Main features / issues
0.1	First prototype	Basic functionality verified, unstable Arduino Uno platform. High side current sensing. Analog sweep generator.
0.2	Improved prototype	PCB layout, ADC board. Arduino ATMEGA platform, 3xIRF530.
0.3	Improved prototype	Improved RTC, DAC sweep control, IXYS MOSFET, Combined battery/mains supply. Implemented at ESTER.
0.4	BA project (2016)	Networking / data transfer, higher power level, improved accuracy, power harvesting (for long term battery operation), Raspberry PI HW platform, modular design, production ready. High side current sensing.

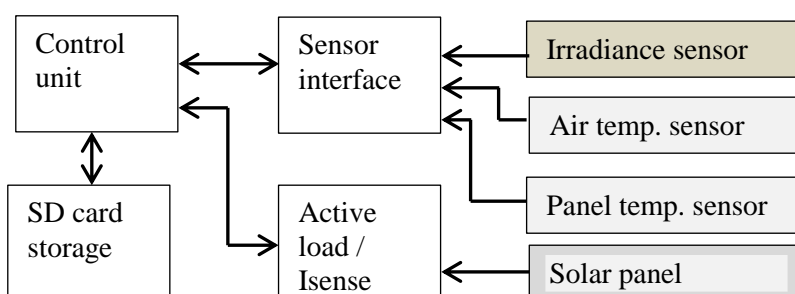


Figure A11.1 Main building blocks of PVsweeper v0.3.

Attached external sensor:

Irradiation sensor: Si-02 from Mencke & Tegtmeyer Ingeniörbüro GmbH [102].

Air/panel temp. sensors: Texas Instrument LM35<sup>9</sup>.

Solar panel: Solar panel under investigation, max 250W (in present sweeper version).

### 11.2.1 Thermal design

During the sweep of a PV panel in the linear region of the load circuit power will be dissipated in the load circuit, as demonstrated in publication [A2]. Passive cooling of the power component via a heat sink was chosen due to the demand of low power consumption / battery operation and therefore excluding Peltier-based cooling and forced air flow / ventilation).

#### 11.2.1.1 Power dissipation

The temperature of the transistor case surface  $T_{\text{case}}$  and the heat sink surface  $T_{\text{heatsink}}$  were measured via an infrared camera during a range of different DC power levels as displayed in figure A11.2. The present design showed a measured maximum heatsink temperature below 40°C @ room temperature. The maximum allowed surface temperature  $T_{\text{heatsink}}$  for a heatsink touchable by humans is 74°C ([IEC60601-1 3<sup>rd</sup> ed., table 23] for human skin contact, limiting the allowed worst case temperature increase to  $T_{\text{heatsink}} - T_{\text{ambient,max}} = 34^\circ\text{C}$ . The surface of the MOSFET reached 39°C for 10W dissipated via the heat sink and the internal case temperature increases by approximately 0.2°C.

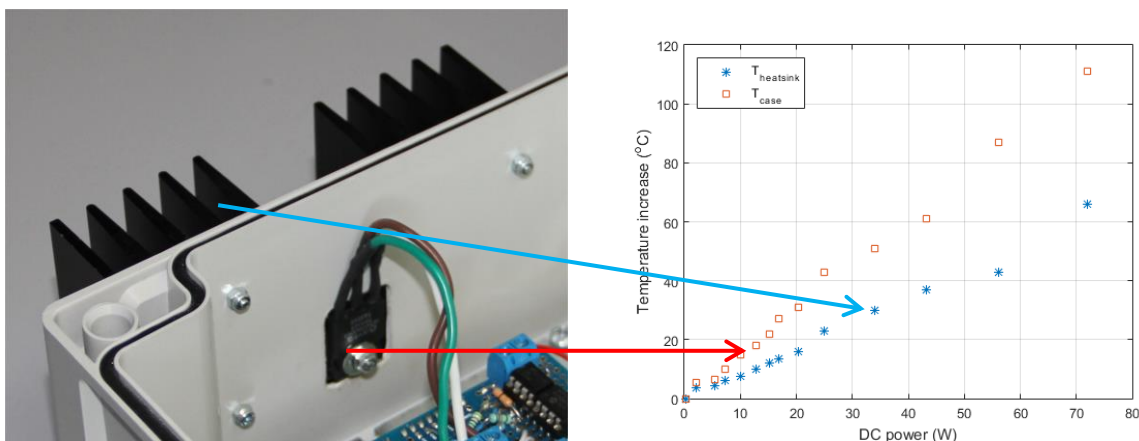


Figure A11.2 Left: The active load transistor mounted on heatsink. Right: Temperature increase of  $T_{\text{case}}$  and  $T_{\text{heatsink}}$  as a function of applied DC power for an IXTH15N50L2<sup>10</sup> MOSFET mounted on the heatsink.

The requirements for ambient temperature and surface temperature, allowing a temperature rise of 34°C limit the allowed dissipated power to 22W. The corresponding allowed increase of  $T_{\text{case}}$  is approximately 35°C, giving a  $T_{\text{case,max}} = 75^\circ\text{C}$ . But the requirements for  $I_{\text{peak}}$  and scan time (10A, >50ms) further reduces the allowed  $T_{\text{case,max}}$  due to the transient thermal impedance of the transistor, see figure A11.3-4. The maximum dissipated power during STC conditions will be in the order of 7W, resulting in a  $T_{\text{case}}$  increase of 10°C above ambient = 50°C maximum.

<sup>9</sup> <http://www.ti.com/lit/ds/symlink/lm35.pdf> (accessed February 2016).

<sup>10</sup> [http://ixapps.ixys.com/DataSheet/DS100054B\(IXTA-TH-TP15N50L2\).pdf](http://ixapps.ixys.com/DataSheet/DS100054B(IXTA-TH-TP15N50L2).pdf) (accessed February 2016).

Fig. 12. Maximum Transient Thermal Impedance

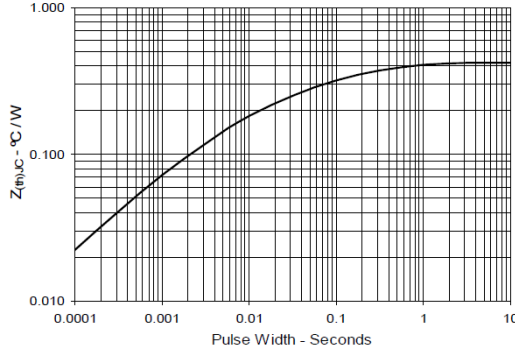


Figure A11.3 Maximum transient thermal impedance of an IXTH15N50L2 MOSFET.

Fig. 13. Forward-Bias Safe Operating Area  
@  $T_c = 25^\circ\text{C}$

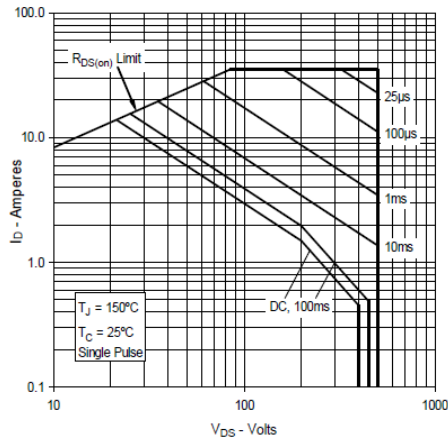


Fig. 14. Forward-Bias Safe Operating Area  
@  $T_c = 75^\circ\text{C}$

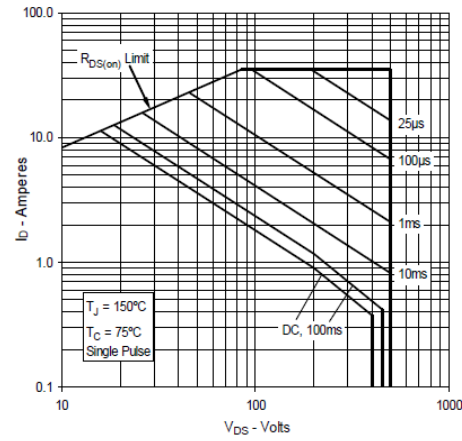


Figure 11.4 Forward biased safe operating area (FBSOA) for an IXTH15N50L2 MOSFET.

An average power level of 7W in a TO220 housing with  $R_{θJC}=0.5$  is thus expected to be handled by applying a heat sink with a thermal resistance  $R_\Theta$  of approximately  $4^\circ\text{C}/\text{W}$  for  $T_{\text{ambient}}=40^\circ\text{C}$ , giving a  $T_J$  and a  $T_{\text{case}}$  in the order of  $80^\circ\text{C}$  and  $70^\circ\text{C}$ , respectively. Due to the transient nature of the sweep the maximum junction temperature  $T_J$  must be determined from the peak pulse power  $P_{MPP}$  and  $Z_{θJC}$  via eq. A11.1 [104] and not from the calculated average power level of 7W.

$$T_{J,\max} = P_{MPP} \cdot Z_{θJC} + T_{\text{case}} \quad (\text{A11.1})$$

The load circuit will, for a 250W panel under STC in the given application, experience a transient impulse of around 30 ms (duty cycle 0.03, 7.5 Joule), resulting in a  $Z_{θJC}$  in the order of  $0.5^\circ\text{C}/\text{W}$  for a typical MOSFET with TO-220 housing.  $T_J$  will acc. to eq. A11.1 be in the order of  $175^\circ\text{C}$  for a 7.5 Joule impulse per second, assuming a  $T_{\text{case}}$  of  $50^\circ\text{C}$ . This will most likely destroy a standard Si-transistor.  $T_J$  is thus dominated by the peak power and not the average power level, so a single transistor load with a TO-220 housing is not sufficient. It can be shown that a maximum allowed junction temperature  $T_J$  of  $110^\circ\text{C}$  implies the parallel use of 3 TO-220 transistors, dividing the power equally between them as well as control loops necessary to ensure proper current splitting during the transient event. A high-current transistor with a large chip like the presently implemented IXTH15N50L2 in a TO247AC housing with a  $Z_{θJC}$  in the range of  $0.25^\circ\text{C}/\text{W}$  is marginally capable of handling the transient power in the present application. The number of transistors needed is thus determined not only by the average power dissipation but also by the effective transient thermal coefficient  $Z_{θJC}$ .

The present design version 0.3 operates with one IXTH15N50L2 and has performed well during the tests in Rome and at SDU.

### 11.2.1.2 Self-heating of the PVSweeper inside the housing

The temperature inside the housing is not recorded in the present version. The power consumption of the electronic circuit, except the FET, is 1.25 W. The active load (FET) was initially designed to dissipate a maximum of around 7W during max. PV current, mainly dissipated to the outside via a heatsink. The rest is dissipated as heat inside the housing (via the transistor surface etc.) adding to the heat from the electronics. The measured worst case rise (no wind) due to self-induced heating inside the enclosure (a type FIBOX5814009, ABS material, vol. 10 L was selected) is shown in figure A11.5, as a function of the applied power.

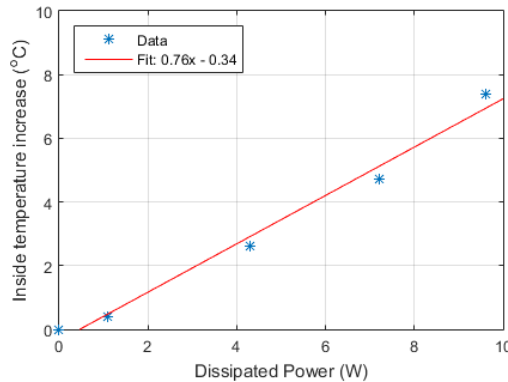


Figure A11.5 Temperature rise due to self-induced heating inside the selected enclosure as a function of dissipated power.  $T_{\text{ambient}}=23^{\circ}\text{C}$ . No ambient air flow = worst case scenario.

The temperature increases by  $0.75^{\circ}\text{C}$  per watt dissipated. The active load added approximately  $0.2^{\circ}\text{C}$  during maximum load, determining the maximum increase of the inside temperature of the housing to be around  $1^{\circ}\text{C}$ .

### 11.2.2 Active load & current sensing

The current flow is in version 0.3 monitored on the low voltage side via the voltage drop over a  $0.10\Omega$  resistor in series with the FET, as shown in figure A11.6. A MOSFET of type IXTH15N50L2 was chosen, due to its large forward biased safe operation area (FBSOA) and low transient thermal resistance. The initial version 0.1 was modified as the use of the implemented Hall Effect based current sensor showed to be problematic. As the main purpose of the PVSweeper is to monitor around the main operating conditions (mainly the Max-Power-Point) and not to measure true  $I_{\text{SC}}$  (in itself a difficult task) was the inclusion of a  $0.10\Omega$  monitoring resistor in the PV current path accepted. For multiple MOSFETs in parallel for version 0.4 and  $I_{\text{SC}}$  detection must high side sensing be considered due to multiple current paths on the low side, even if the circuit complexity is increased.

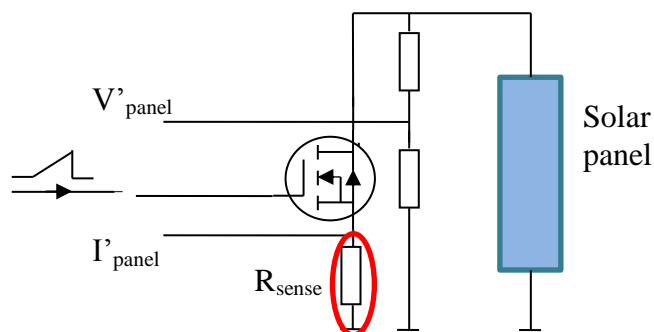


Figure A11.6 Low side current sensing implemented on PVSweeper v0.3 with  $0.10\Omega$  sense resistor  $R_{\text{sense}}$  (red circle).  $V'_\text{panel}$  and  $I'_\text{panel}$  represent panel voltage and current.

### 11.2.2.1 Sensing resistor power level

The system has been tested by applying different power levels to the sensing resistor  $R_{sense}$  in the active load. The average maximum power dissipation was designed to be below 10 watt for the active load (FET), but only 0.25W for the sensing resistor (<10% sweep time, 10A peak (5A average) during a linear sweep). A 5W type resistor as sensing resistor was selected to have a wide safety margin. The resistor load factor is <5% and a temperature increase below 30°C is expected. For verification the temperature of the  $0.1\Omega$  sensing resistor was measured by means of an infrared camera at different power levels. The result is shown in figure A11.7.

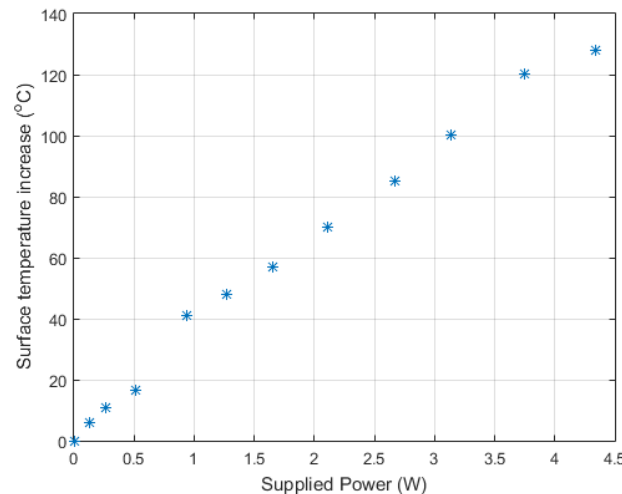


Figure A11.7 Surface temperature of the sensing resistor as a function of dissipated power.  
Ambient temperature= 25°C.

The temperature increase of the resistor is approximately 30°C per Watt dissipated. The resistor changes its value from  $0.1029\Omega$  to  $0.1042\Omega$  from 0-4W dissipated, resulting of a variation of the current measurement in the range of 0.4%/W. As the sweeper was designed for an average power dissipation in the sensing resistor < 0.25W the error of the current measurement due to variation of resistor value is expected to be in the order of 0.1%.

### 11.2.2.2 Linearity of the current sensing

The current recording has been investigated by applying constant current from a power supply and monitoring the recorded current levels on the SD-card at 25°C constant ambient temperature. See figure A11.8.

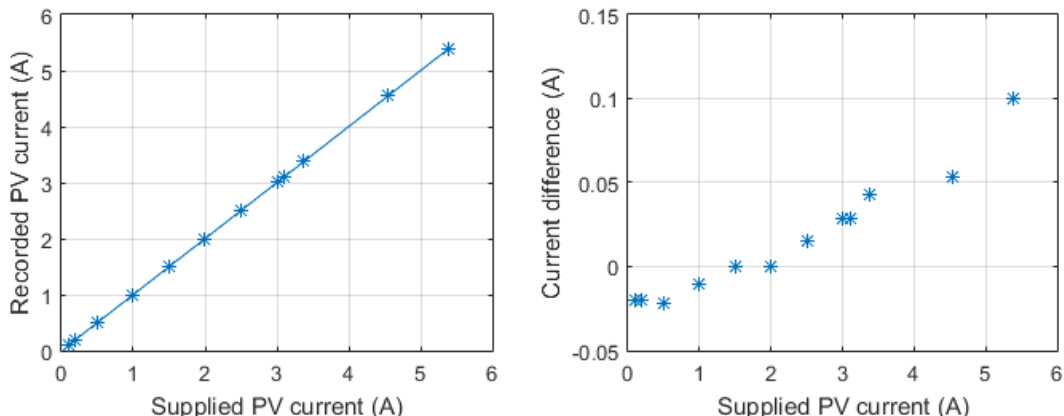


Figure A11.8 Left: Relationship between applied and recorded PV current  $I_{PV}$  under laboratory test conditions with a current generator as source. Right: Difference.

The percentage deviation as a function of PV current  $I_{PV}$  is shown in figure A11.9, together with a fitted function and the resulting deviation after compensation. A power law function of the form (eq. A11.2).

$$I(I_{PV}) = 10^a * (I_{PV})^b + k \quad (\text{A11.2})$$

was fitted for the calculated percentage error, resulting in coefficients  $a=-0.8422$   $b=-0.4946$ ,  $k=-5$ .

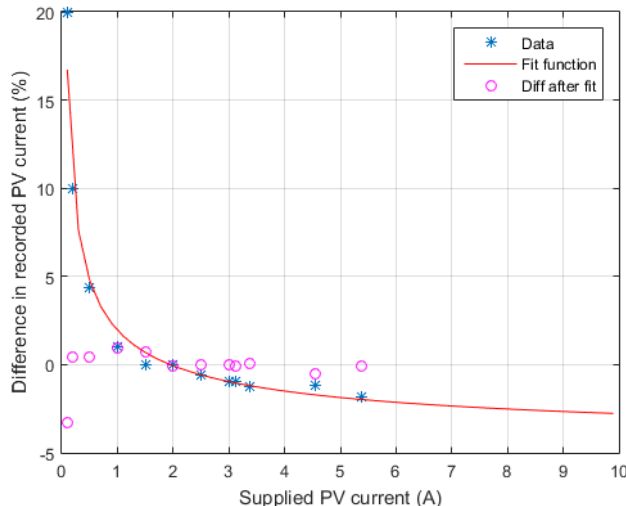


Figure A11.9 Calculated deviation between applied and recorded PV-current (\*), interpolated power function (-) and the resulting deviation (o).

By correcting the measured current values with the adapted function the residual error is reduced to below  $\pm 0.5\%$  from 0.2-5.5A PV current. Testing for higher currents than 5.5A was not possible, due to the overheating of the sensing resistor.

### 11.2.3 Temperature sensor interface

The voltage output from the irradiation sensor is buffered and amplified to utilize the ADC voltage input range of 0-5V. The temperature sensors of type LM35 (Texas Instruments), have a linear output voltage as a function of temperature and  $\pm 0.5^\circ\text{C}$  accuracy.

### 11.2.4 Irradiance sensor analysis

The type of irradiance sensor used cannot be considered having reference quality (datasheet specifies  $\pm 5\%$ ) [105] and the characteristic of the applied irradiation sensor are crucial for the evaluation. The sensor performance has been compared with the instrumentation at ESTER. The sensor has initially been tested for the linearity at low light levels. Malus law, known from the field of Optics, was applied by using two linear polarizers to perform a spectrally independent attenuation of incoming light [106]. Malus law states that the intensity ( $I$ ) of light passing through two crossed linear polarizers with angle difference  $\Theta$  will be proportional to  $\cos^2\Theta$  (eq. 11.3)

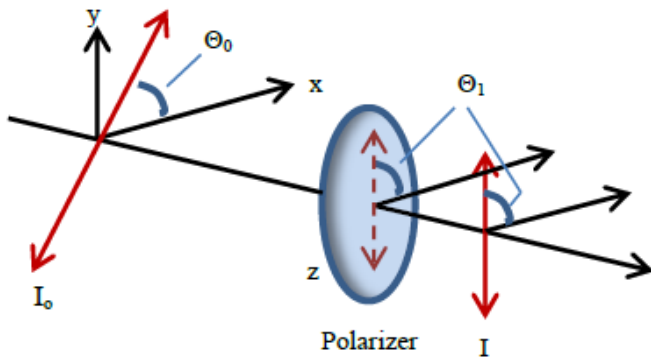


Figure A11.10 Schematic view of a polarizer setup.  $I_0$  is the intensity of the incoming linearly polarized irradiation with polarization angle  $\Theta_0$ .  $\Theta_1$  is the polarizer angle.  $I$  is the intensity passing the polarizer.

$$I = I_0 \cos^2(\Theta_0 - \Theta_1) \quad (\text{A11.3})$$

The correlation between the measured and calculated irradiance level is shown in figure A11.11.

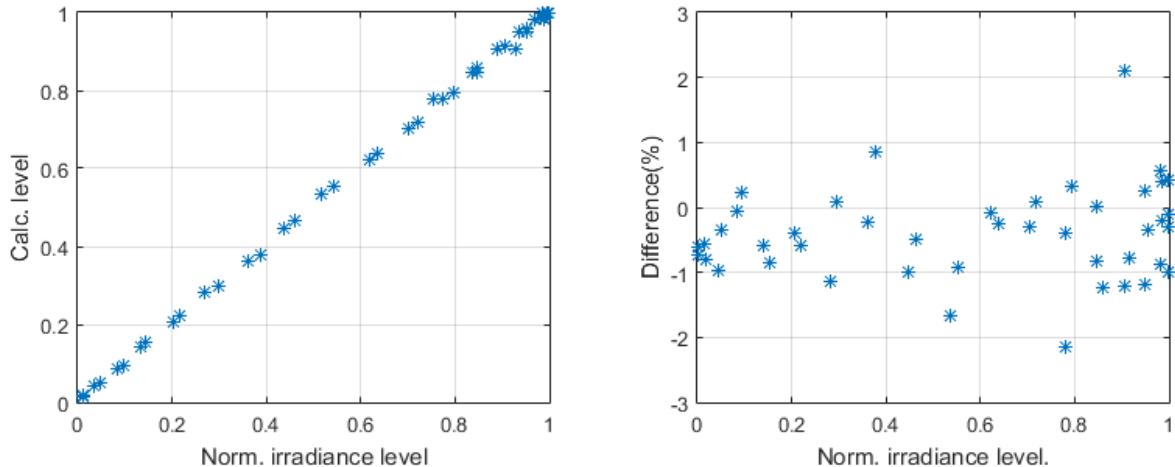


Figure A11.11 Left: Correlation between the  $\cos^2$ -function and the recorded signal levels. The levels are normalized. Right: Difference between the normalized levels.

The analysis showed that the sensor can be considered linear < 1% (limited by the test setup) at low light levels.

### 11.2.5 Calibration at the ESTER sensor system

The developed PVSweeper system was together with a PV panel mounted at the ESTER Outdoor PV monitoring station at the Tor Vergata University in Rome. The panel tested was of same type as mounted at the 2.1 MW Danfoss Solar plant in Nordborg, Denmark. The purpose of the tests was to characterize the panel under higher irradiation conditions than expected to occur in Denmark and to compare the PVSweeper system with State-of-the-Art irradiation measurement equipment as available at the ESTER PV test facility. A second purpose was to record fast changes in irradiation level.

#### 11.2.5.1 The ESTER Outdoor PV monitoring station

The ESTER system records intensity measurements from a range of sensors (a polycrystalline reference cell, a monocrystalline reference cell and a pyranometer as well as the optical spectrum

[107-109]. See figure A11.12. The ESTER irradiance data are recorded once per minute, where the PVSweeper sweeps recorded once per second. The uncertainty of the measured irradiation levels has been addressed in [107] and a difference of 2.2% has been identified between the ESTER outdoor measurements and the indoor measurements performed at the ISAAC facility at SUPSI in Lugano, CH [108]. Deviations between the ESTER sensors are in the range of  $\pm 4\%$  @  $1000 \text{ W/m}^2$  are documented and have also been observed by the tests performed.



Figure A11.12 Left: ESTER PV test platform with the sensors mounted. Right: Close-up.

The PVSweeper system was mounted at ESTER from medio March 2015. The recorded values for March 20, 2015, during a solar equinox, are shown below for the ESTER sensors and the SDU irradiation sensor. It can be observed that the 3 ESTER reference sensors differ in amplitude by a few percent between approximately 8 and 16 o'clock, see figure A11.13.

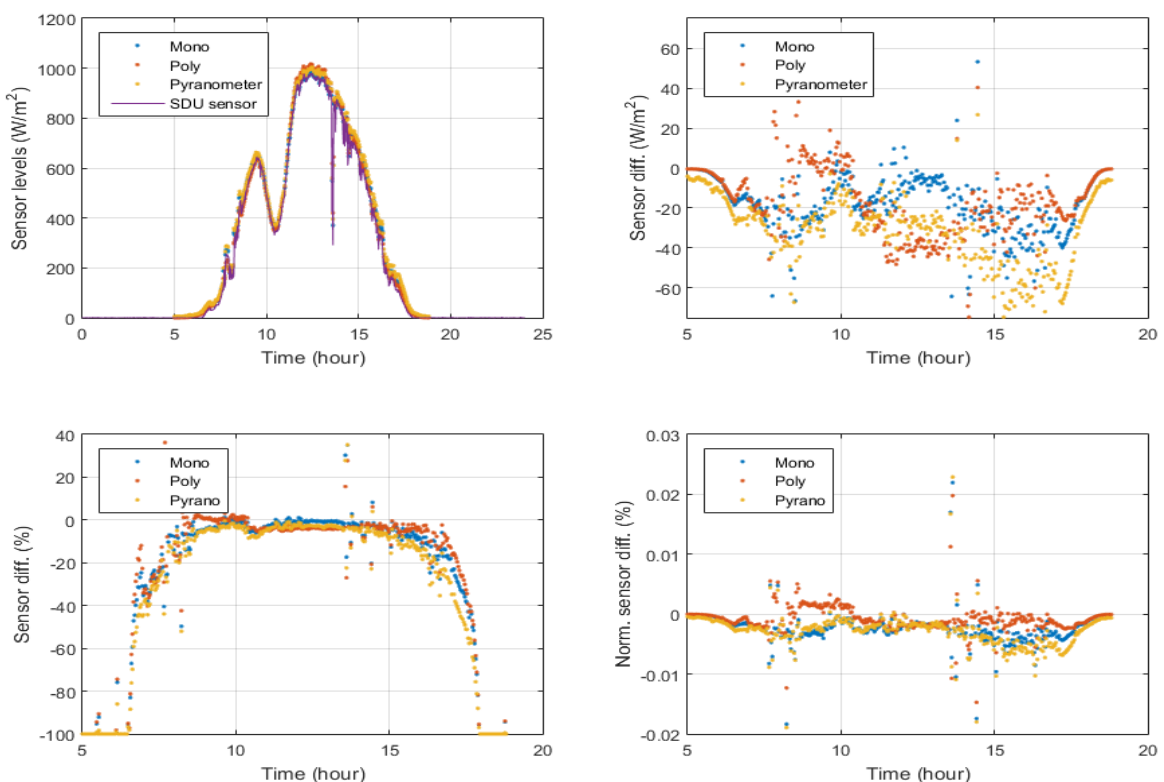


Figure A11.13 Top left: Recorded irradiance levels for March 20, 2015. The SDU sensor level is scaled to the ESTER mono ref. cell. Top right: Sensor difference in  $\text{W/m}^2$ . Bottom left: Sensor difference in %. Bottom right: Sensor difference in % between normalized levels. Right: Difference plots.

The temporal variation of the ratio between the normalized sensor levels (figure A11.13, bottom right) indicates a small spectral dependency, but the investigation of this effect is outside the scope of this analysis.

### 11.2.5.2 Comparison of the 3 ESTER irradiance sensors

The relationships between the irradiation levels recorded by the PVsweeper and the 3 ESTER sensors are shown below, together with the calculated polynomial fit of 1<sup>st</sup> order. See figure A11.14.

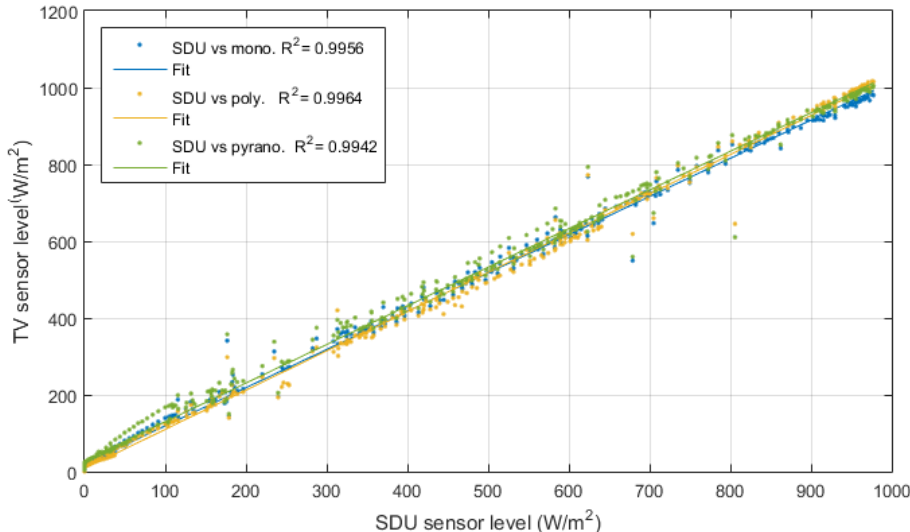


Figure A11.14 Irradiance data from the ESTER station relative to the PVsweep irradiance measurements.

All linear fits shows a  $R^2$ -value  $>0.99$ . It is concluded that the intensity measurement of the PVsweeper has an acceptable degree of correlation with the sensor systems mounted at ESTER. The relationship between the ESTER mono sensor and the other ESTER sensors for March 21, 2015 (a very clear day) is shown in figure A11.15.

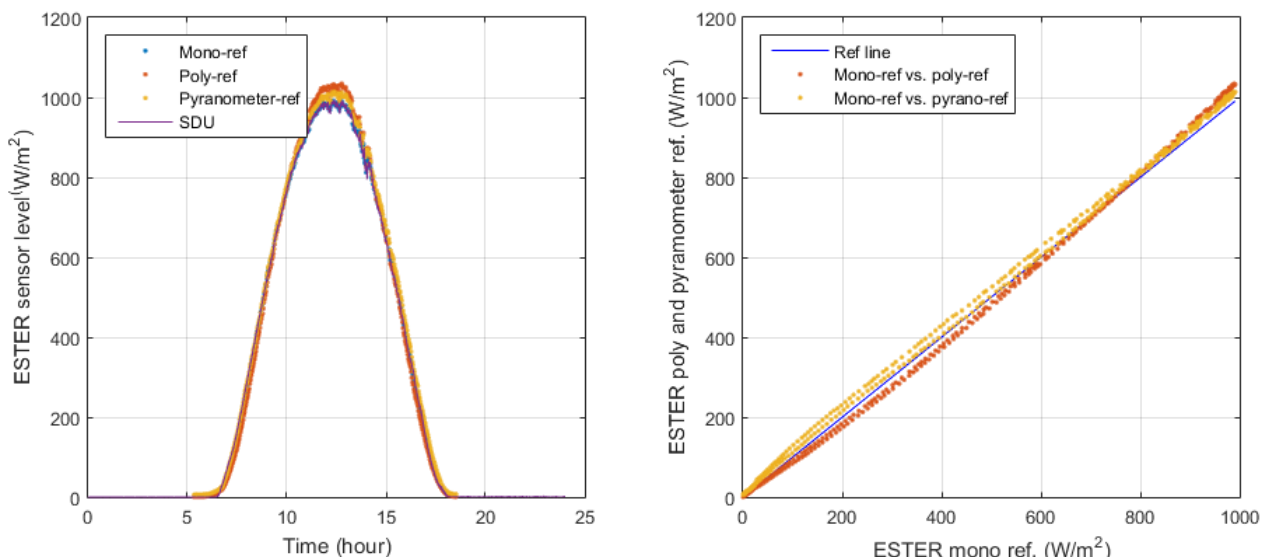


Figure A11.15 Recorded differences between ESTER sensors and the Sensor attached to the SDU PVsweeper unit for March 20, 2015 in Rome.

It can be observed that the pyranometer for all irradiance levels give a higher reading than the mono sensor and the polycrystalline sensor and that the polycrystalline sensor for levels below 800 W/m<sup>2</sup>

gives a lower reading, but a higher reading above that level. The irradiation measurements from the SDU irradiance sensor were used to scale the sensor output to the ESTER mono crystalline reference cell, due to the same crystal type and comparable performance.

### 11.2.6 PVSweeper $P_{MPP}$ vs. panel temperature analysis

The PVSweeper measuring capability has been tested by comparing the response from the irradiation detector and the calculated  $P_{MPP}$  value for each sweep. The calculated  $P_{MPP}$  values have been obtained at different temperatures from the recorded IV-curves and have been corrected for temperature in order to compare the correlation between the irradiance sensor measurements and the  $P_{MPP}$  recordings. See figure A11.16. Both the Irradiance data and the recorded  $P_{MPP}$  values have been temperature compensated (irradiation sensor temp. coefficient  $\approx 0.0005/^\circ\text{C}$  [102]; PV panel temp. coefficient  $-0.440\%/\text{C}$  (the observed dependency if irradiation level is not applied)).

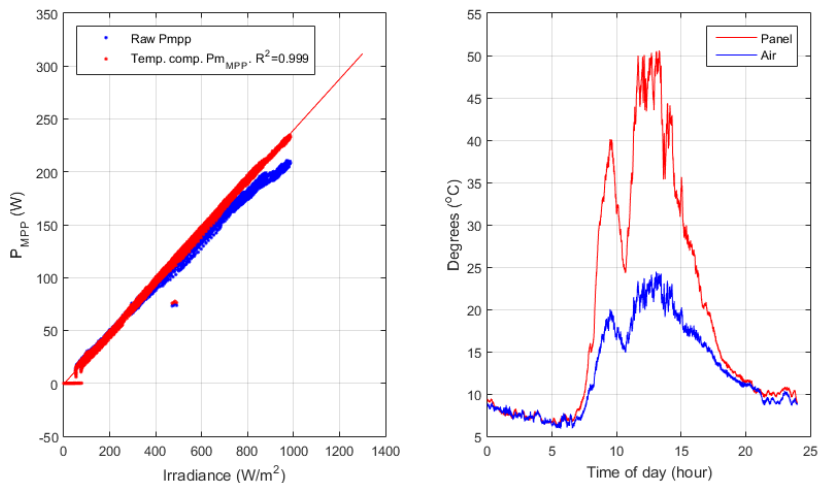


Figure A11.16 Left: Raw and temperature corrected  $P_{MPP}$  values for March 20, 2015, as a function of the recorded solar irradiance. Right: Recorded ambient and panel temperatures.

It can be observed that the expected linear dependency between the solar irradiance and the  $P_{MPP}$  values only is observed if the  $P_{MPP}$  values are temperature corrected for ambient and panel temperature, respectively. The normalized irradiation sensor levels and  $P_{MPP}$  values versus time are shown in figure A11.17 for the uncompensated as well as the compensated case.

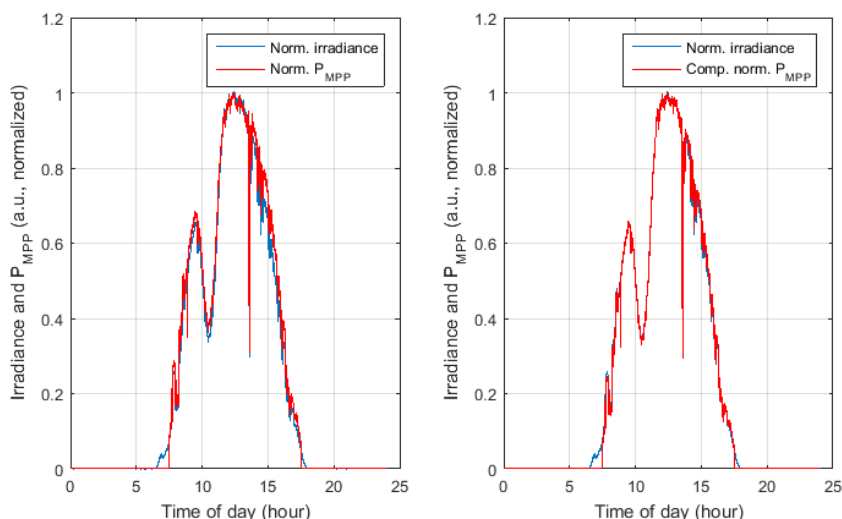


Figure A11.17 Normalized irradiance and  $P_{MPP}$  levels for March 20, 2015. Left: Without temperature correction. Right: With temperature correction applied to the  $P_{MPP}$  values.

## **11.3 Temperature sensitivity analysis**

The temperature dependency of the PVSweeper instrument as a system was investigated, as its intended use was to be mounted outside and thus subject to ambient temperature variations as well as varying internal power dissipation (electronics, active load). The effect of the ambient temperature variations has been investigated for two situations: influence of the PV current on the sensing resistor and the overall influence on the stored measurements.

### **11.3.1 Circuit temperature sensitivity**

The overall system temperature sensitivity (including the active load, the analogue interface and the Arduino ATMEGA system) has been investigated by simulating a constant irradiation (by disconnecting the MOSFET and applying a constant power level of 0.5W to the sensing resistor) and varying the ambient temperature from 0-60°C in a climate chamber. A voltage in the range of the  $V_{MPP}$ -voltage of a standard 60-cell panel (25V) was applied to the PV input. The irradiation sensor input was connected to 54 mV<sub>DC</sub>, equivalent to the input level for 1000W/m<sup>2</sup> for the monocrystalline reference sensor used.

The temperature sensors were tested by using a reference temperature source and a climate chamber and the recorded  $V_{MPP}$  and  $I_{MPP}$  values shows temperature coefficients of 0.015 %/°C and 0.034 %/°C respectively. The test also showed an offset of -1.9 °C for the panel temperature sensor and 0.2°C for the ambient temperature sensor.

## **11.4 Conclusion on the construction and test of the IV-curve tracer**

The following can be concluded on circuit design and temperature/current compensation:

- Calibration of the irradiance sensor is crucial.
- The increase of the sensing resistor due to temperature variations is negligible.
- The internal temperature increase due to self-heating is in the range of 1°C.
- The ambient temperature sensor must be offset with 0.2°C.
- The panel temperature sensor must be offset with 1.9°C.
- The measured PV currents recorded on the SD-card must be compensated for the non-linearity of the current measurement system. Applying a power law function is suggested.
- The recorded voltage and current values must be temperature compensated by the ambient temperature added the temperature increase due to self-heating (1°C). Care must be taken to ensure mounting of the PVSweeper in shade and to compensate the raw measurements with the elevated temperature. For the relevant test period at ESTER the ambient temperature stayed below 35°C.
- By performing active temperature compensation on the recorded data, as well as a correction for the nonlinearity/offset of the measured current, the measurement error on the irradiance level, compared to the ESTER mono crystalline sensor, is expected to be reduced to below 1%.
- Future versions of the PVSweeper should include internal temperature measurement for compensation before storage as well as improved analogue circuitry for lower temperature drift.

*Accurate computation,  
the gateway to knowledge of all things and dark mysteries.*

*The Rhind Mathematical Papyrus  
Egypt, around 1650 BC*

British Museum inventory number 10058  
Reg no. 1865,0218.3

**THE END**